

The Synthesis and Application of Highly Efficient Catalysts for Electrochemical Water Splitting

A thesis presented for the award of the degree of Doctor of Philosophy

From

University of Technology Sydney

Faculty of Science

By Yufei Zhao, B. Eng.

August 2017

DEDICATION

This thesis is dedicated to my beloved husband, my parents and my sisters

CERTIFICATION

I, Yufei Zhao, declare that the work in this thesis has not previously been submitted for a degree nor has it been submitted as part of requirements for a degree except as fully acknowledged within the text.

I also declare that the thesis has been written by me. Any help that I have received in my research work and the preparation of the thesis has been acknowledged. In addition, I declare that all information sources and literature used are indicated in the thesis.

This thesis is the result of a research candidature conducted jointly with Beijing Institute of Technology as part of a collaborative Doctoral degree.

Yufei Zhao

Production Note:

Signature removed prior to publication.

Sydney,

Australia

08, 2017

ACKNOWLEDGEMENTS

I would like to express my deep appreciation to my supervisor, Prof. Guoxiu Wang director of Centre for Clean Energy Technology, for his encouragement, understanding, invaluable advice and constant support during my study in University of Technology Sydney (UTS). I appreciate the chance he gave to me for pursuing my PhD in UTS and the innovative ideas for my research.

I am very grateful to Dr Hao. Liu, my co-supervisor, for his constantly rendering helps during my research work. Special thanks for Dr. Yueping (Jane) Yao for her support in the lab, provide me lots of supports. I have my thanks to many people in my research group for their encouragement and brilliant ideas during the period of this research. Dr. Bing Sun, Dr. Dawei Su, Dr. Zhimin Ao, Dr. Shuangqiang Chen, Dr. Xiuqiang Xie, Dr. Anjon Kumar Mondal, Dr. Xiaodan Huang, Mr. Kefei Li, Mr. Jinqiang Zhang, Ms. Jing Xu, Ms. Katja Kretschmer, Mr. Xin Guo and Mr. Weizhai Bao.

I also wish to thank Dr. Ronald Shimmon and Dr. Linda Xiao from School of Mathematical and Physical Sciences in UTS for their friendly support. I would like to give my thanks to Katie McBean and Mark Berkahn from the Microstructural Analysis Unit in UTS for their help on material characterization. I take this chance to mention my cordial thanks to China Scholarship Council (CSC) and Australian Research Council (ARC).

Finally, I would like to thank my husband, Mr. Jinqiang Zhang, and my whole family for their love, understanding, moral support and encouragement during my PhD study. Their love is the mental strength that supported me to

achieve my study abroad.

Yufei Zhao

TABLE OF CONTENTS

A thesis presented for the award of the degree of Doctor of Philosophy	1
DEDICATION	I
CERTIFICATION	II
ACKNOWLEDGEMENTS	III
TABLE OF CONTENTS	V
LIST OF FIGURES	XII
LIST OF ABBRIEVIATIONS	XXIV
LIST OF PUBLICATIONS	XXV
ABSTRACT	XXIX
INTRODUCTION	XXXII
Chapter 1: Literature review	1
1.1 Introduction	1
1.2 Electrochemistry of water splitting	2
1.2.1 The mechanism of electrochemical water splitting	2
1.2.2 Electrochemical parameters for the evaluation of HER and OER catalytic activity.....	4
1.2.3 Evaluation criteria of HER and OER catalysts.....	7
1.3 Electrochemical hydrogen evolution reaction	7
1.3.1 Mechanism of electrochemical hydrogen evolution reaction.....	8
1.3.2 Catalysts for HER	9
1.4 Electrochemical oxygen evolution reaction	20
1.4.1 Mechanism of electrochemical oxygen evolution reaction.....	20

1.4.2 Catalysts for OER	21
1.4.2.2 Transition metals oxides.....	22
1.5 Bifunctional catalysts for HER and OER.....	31
Chapter 2 experimental method and characterization.....	34
2.1 Overview	34
2.2 Material preparation.....	35
2.2.1 Hydrothermal method	36
2.2.2 Wet-chemical synthesis.....	36
2.2.3 Chemical redox reaction.....	37
2.2.4 Hard template method	37
2.2.5 Electrospinning technique	38
2.3 Materials characterization	38
2.3.1 X-ray diffraction analysis (XRD)	38
2.3.2 Scanning electron microscopy (SEM)	40
2.3.3 Transmission electron microscopy (TEM).....	41
2.3.4 Raman spectroscopy	42
2.3.5 Brunauer Emmer Teller (BET).....	42
2.3.6 Thermogravimetric analysis (TGA).....	43
2.3.7 X-ray photoelectron spectroscopy (XPS).....	44
2.4 Electrode preparation	44
2.4.1 Glassy carbon electrode	44
2.4.2 Rotating ring-disk electrode	45
2.5 Electrochemical performance characterization	46

2.5.1 Linear sweep votammograms (LSV)	46
2.5.2 Cyclic voltammetry (CV).....	47
2.5.3 Electrochemical impedance spectroscopy (EIS)	47
2.5.4 Stability	48
2.5.5 Turnover Frequency (TOF)	48
Chapter 3 MoS ₂ nanosheets supported on 3D graphene aerogel as a highly efficient catalyst for hydrogen evolution	49
3.1 Introduction	49
3.2 Experimental.....	51
3.2.1 Synthesis of graphene hydrogel.....	51
3.2.2 Synthesis of graphene hydrogel-MoS ₂	51
3.2.3 Synthesis of the comparison materials	52
3.2.4 Structural Characterization.....	52
3.2.5 Electrochemical Measurements	52
3.3 Results and Discussion.....	53
3.3.1 The characterization of the catalysts	53
3.3.2 The electrochemical performance test of the catalysts	59
3.4 Conclusion.....	65
Chapter 4 Graphene-Co ₃ O ₄ nanocomposite as electrocatalyst with high performance for oxygen evolution reaction	66
4.1 Introduction	66
4.2 Experimental.....	68
4.2.1 The preparation of G-Co ₃ O ₄	68

4.2.2 The preparation of Co_3O_4	68
4.2.3 The preparation of Ru/C	68
4.2.4 Structural Characterization	68
4.2.5 Electrochemical Measurements	69
4.3 Results and discussion	70
4.3.1 The characterization of the catalysts	70
4.3.2 The electrochemical performance test of the catalysts	74
4.4 Conclusion	79
Chapter 5 Porous graphene wrapped CoO nanoparticles for highly efficient oxygen evolution	80
5.1 Introduction	80
5.2 Experimental	81
5.2.1 Synthesis of porous graphene catalysts (PGE)	81
5.2.2 Synthesis of PGE-CoO catalyst	82
5.2.3 Synthesis of the comparison catalysts	82
5.2.4 Structural Characterization	82
5.2.5 Electrochemical Measurements	83
5.3 Results and discussion	83
5.3.1 The characterization of the catalysts	84
5.3.2 The electrochemical performance test of the catalysts	88
5.4 Conclusions	95
Chapter 6: Ultrathin CoMn_2O_4 nanosheets with abundant Oxygen Vacancies vertically aligned on Functionalized Carbon Nanofibers as High-Performance Catalyst for Oxygen Evolution	97

6.1 Introduction	97
6.2 Experimental.....	98
6.2.1 Synthesis of Nitrogen-doped CNFs (NC)	98
6.2.2 Synthesis of Cobalt/Nitrogen doped CNFs (CoNC)	99
6.2.3 Synthesis of CoMn ₂ O ₄ nanosheets on CoNC (CoMn ₂ O ₄ -CoNC)	99
6.2.4 Synthesis of MnO ₂ nanosheets on NCNFs (MnO ₂ -NC)	99
6.2.5 Synthesis of Co ₃ O ₄ nanoparticles on CoNC (Co ₃ O ₄ -CoNC)	100
6.2.6 Characterization	100
6.2.7 Electrochemical Measurements	101
6.3 Results and discussion.....	102
6.3.1 The characterization of the catalysts	102
6.3.2 The electrochemical performance test of the catalysts	114
6.4 Conclusion.....	119
Chapter 7: Facile Synthesis and Evaluation of Hierarchical Fe ₃ C based Catalyst for High Efficient Oxygen Evolution Reaction	121
7.1 Introduction	121
7.2 Experimental.....	122
7.2.1 Synthesis of Nitrogen-doped CNFs (NCNFs)	122
7.2.2 Synthesis of Fe ₃ C@NCNTs-NCNFs	123
7.2.3 Characterization	123
7.2.4 Electrochemical Measurements	124
7.3 Result and discussion	125
7.3.1 The characterization of the catalysts	126

7.3.2 The electrochemical performance test of the catalysts	134
7.4 Conclusion.....	139
Chapter 8 Electrospun Cobalt Embedded in Porous Nitrogen Doped Carbon Nanofibers as an Efficient Catalyst for Water Splitting	140
8.1 Introduction	140
8.2 Experimental.....	142
8.2.1 Synthesis of Co-PNCNFs.....	142
8.2.2 Synthesis of NCNFs.....	143
8.2.3 Synthesis of the comparison materials.....	143
8.2.4 Characterization	143
8.2.5 Electrochemical Measurements	144
8.3 Results and discussion.....	145
8.3.1 The characterization of the catalysts.....	145
8.3.2 The electrochemical performance test of the catalysts	151
8.4 Conclusions	159
Chapter 9 CONCLUSIONS	161
9.1 General Conclusion.....	161
9.1.1 MoS ₂ nanosheets based material as a highly efficient catalyst for hydrogen evolution	161
9.1.2 Cobalt oxide based material as a highly efficient catalyst for oxygen evolution.....	162
9.1.3 Iron carbide based material as a highly efficient catalyst for oxygen evolution.....	163

9.1.4 Carbon based material as highly efficient bi-functional catalyst for water splitting	164
9.2 Outlook.....	164
Reference.....	167

LIST OF FIGURES

Figure 1-1 Schematic diagram of an electrolyzer.....	3
Figure 1-2 The mechanism of hydrogen evolution on the surface of an electrode in acidic solutions.....	8
Figure 1-3 Elements that are used for constructing HER electrocatalysts.....	9
Figure 1-4 A volcano plot of experimentally measured exchange current density as a function of the DFT-calculated Gibbs free energy of adsorbed atomic hydrogen.	10
Figure 1-5 Structure and characterization of atomically thin MoS ₂ . (a) Three-dimensional schematic of the atomic structure of MoS ₂ . (b) AFM height profile of monolayer MoS ₂ ; inset is the corresponding AFM image.....	11
Figure 1-6 Typical AFM image of exfoliated nanosheets of WS ₂ . Scale bar, 500 nm. (b) High-resolution STEM images of an as-exfoliated WS ₂ monolayer showing regions exhibiting the 1T superlattice. Scale bar, 1 nm.	13
Figure 1-7 Electrochemical measurements of transition metal dichalcogenide films grown on glassy carbon electrodes. (a) Polarization curves of transition metal disulfides, (b) the corresponding Tafel plots.	13
Figure 1-8 (a) Scheme of the process of WCNCs grown on the tips of VA-CNTs. (b) TEM images of an individual NCs, (c) HER voltammograms of WC-CNTs synthesized at different temperatures in 0.5 M H ₂ SO ₄ (pH = 0).....	16
Figure 1-9 (a) SEM image of Mo-WP/CC, (b) Polarization data for Mo-W-P/CC in 0.50 M H ₂ SO ₄ electrolyte, along with plots of MoP/CC, WP ₂ /CC and Pt/C/CC for comparison.....	18

Figure 1-10 (a) Preparation process of MPSA/GO-1000 via cooperative assembly and pyrolysis, (b) Polarization curves of various samples for hydrogen evolution in 0.5 M H ₂ SO ₄	19
Figure 1-11 (a) Synthetic route for the γ -CoOOH nanosheets. (b) TEM image and (c) AFM image for the γ -CoOOH nanosheets. The inset in (b) shows the HRTEM image for the γ -CoOOH nanosheets. (d) XRD pattern for the γ -CoOOH nanosheets. The patterns of bulk γ -CoOOH and bulk and nanosheet α -Co(OH) ₂ are also displayed for comparison.....	22
Figure 1-12 (a) Schematic of the spatially confined hybrids and crosssectional TEM image of a sheet of nNiFe LDH/NGF electrocatalyst. (b, c) polarization curves and Tafel slope of nNiFe LDH/NGF and other samples for comparison. (d) Figures of merit with respect to both kinetics (Tafel slope) and activity (the overpotential required to achieve 10 mA cm ⁻²), with references all measured in 0.1 M KOH electrolyte.	25
Figure 1-13 polarization curves of Mn-based catalysts towards OER.	26
Figure 1-14 (a) A unit cell in perovskite showing relative positions of different ions, (b) The relation between the OER catalytic activity, defined by the overpotentials at 50 mA cm ⁻² _{ox} of the OER current, and the occupancy of the e _g -symmetry electron of the transition metal (B in ABO ₃).	27
Figure 1-15 (a) Molecular cobalt complexes, (b) CV of 5 recorded in phosphate buffer solution (0.1 mM, pH 9.2) with a scan rate of 50 mV s ⁻¹ (red), and a blank scan without 5 under the same conditions (black).	28
Figure 1-16 Structures of nicke(II) complexes used as precatalysts.	29
Figure 1-17 (a-c) SEM and TEM images of the N/C, (d) Oxygen evolution activities of the N/C, N/C-NiO _x , IrO ₂ /C (20 wt%) and Pt/C (20 wt%) electrodes with KOH electrolyte (pH 13).	30

Figure 1-18 (a) Polarization curve showing the bifunctionality of CP@Ni-P toward both HER and OER. (b) Polarization curve in a two-electrode configuration. (c) Chronopotentiometric curve of water electrolysis at several different current densities. (d) Energy efficiency of the CP@Ni-P electrolyzer as a function of current density. (e) Long-term durability tests made at 10 and 20 mA cm ⁻² . (f) A digital photograph showing the evolution of H ₂ and O ₂ gas from the electrodes at 20 mA cm ⁻²	32
Figure 2-1 Schematic illustration for materials preparations, characterizations and applications.	34
Figure 2-2 Autoclaves for hydrothermal synthesis.....	36
Figure 2-3 The electrospinning instrument for the experiment.....	38
Figure 2-4 The Bruker D8 Discover XRD instrument.....	39
Figure 2-5 The field emission scanning electron microscopy in a mode of Supra 55 VP produced by Zeiss and equipped with EDS detector.	40
Figure 2-6 Transmission electron microscopy (TEM, Model JEM-2011, JEOL).	41
Figure 2-7 The Renishaw inVia Raman microscope equipped with a Leica DMLB microscope (Wetzlar, Germany) and a 17 mW at 633 nm Renishaw helium neon laser.	42
Figure 2-8 The 3 Flex surface characterization analyser instrument produced by Micromeritics.	43
Figure 2-9 The three-electrode system.....	44
Figure 2-10 The Pine rotating ring-disk electrode (RRDE) instrument.	45
Figure 3-1 Schematic illustration for the synthesis procedure of GA-MoS ₂ composite.....	53
Figure 3-2 Electron microscope characterization of GA and GA-MoS ₂ : a, b) low and high magnification SEM images of GA, c, d) low and high magnification SEM images of GA-MoS ₂ , e, f) low and high magnification TEM images of GA-MoS ₂	54

Figure 3-3 SEM image and EDS elemental mappings of GA-MoS ₂ , (a) SEM image of GA-MoS ₂ , (b) EDS profile, (c) element of O, (d) element of S, (e) element of Mo, (f) element of C.....	55
Figure 3-4 (a) XRD patterns and (b) Raman spectra of GA and GA-MoS ₂	56
Figure 3-5 (a) XPS survey spectrum of GA-MoS ₂ composite, high-resolution XPS spectra of GA-MoS ₂ c) Mo 3d, d) S 2p. (d) thermogravimetric analysis in air of GA-MoS ₂ and MoS ₂ in air, used for calculating the content of MoS ₂ in GA-MoS ₂ composite.....	57
Figure 3-6 SEM images of (a) G-MoS ₂ and (b) pure MoS ₂	58
Figure 3-7 Nitrogen adsorption/desorption isotherm of (a) GA, (b) GA-MoS ₂ , (c) G-MoS ₂ , (d) pure MoS ₂	59
Figure 3-8 Electrochemical performance of the HER catalysts in 0.5 M H ₂ SO ₄ : a) polarization curves for GA-MoS ₂ , G-MoS ₂ , MoS ₂ and GA loaded onto GC electrodes; b) Tafel curves of GA-MoS ₂ , G-MoS ₂ and MoS ₂	60
Figure 3-9 Electrochemical capacitance measurements: Cyclic voltammograms are performed in 0.5 M H ₂ SO ₄ solution in a potential window without faradaic processes and the scan rate from 10 to 100 mV s ⁻¹ , (a) GA-MoS ₂ , (b) G-MoS ₂ , (c) MoS ₂ . (d) scan rate dependence of the average capacitive current densities at open circuit potential for GA-MoS ₂ , G-MoS ₂ and MoS ₂	61
Figure 3-10 (a) Nyquist and (b) Bode plots for GA-MoS ₂ hybrid modified GC electrode recorded at various HER overpotentials in 0.5 M H ₂ SO ₄ ; (c) Nyquist and (d) Bode plots for G-MoS ₂ hybrid. (e) Equivalent electrical circuit used to model the HER process on GA-MoS ₂ and G-MoS ₂ modified GC electrodes at various overpotentials, (f) the square symbols are experimental data and the red solid line are modelled by (e).....	63
Figure 3-11 (a) stability test of GA-MoS ₂ through potential cycling, polarization curves before and after 2000 potential cycles, (b) polarization curves of GA-MoS ₂ at different scan rates, and the inset of d) shows the	

corresponding data of the current density (at -0.2 V vs SHE) vs scan rate.....	64
Figure 4-1 A schematic illustration for preparing G-Co ₃ O ₄ nanocomposite with a sandwich-architecture.....	70
Figure 4-2 Microscope observation of the G-Co ₃ O ₄ composite. (a) Low and high magnification SEM images of G-Co ₃ O ₄ . (b) Low magnification TEM image of G-Co ₃ O ₄ . (c) High resolution TEM (HRTEM) image of G-Co ₃ O ₄ , showing a sandwich-like microstructure. (d) HRTEM image of Co ₃ O ₄ nanocrystals and SAED pattern of G-Co ₃ O ₄	71
Figure 4-3 The SEM image of pristine Co ₃ O ₄	72
Figure 4-4 The characterization of the G-Co ₃ O ₄ composite: (a) XRD patterns of Co ₃ O ₄ and G-Co ₃ O ₄ composite. (b) Raman spectra of Co ₃ O ₄ and G-Co ₃ O ₄ composite catalyst.....	73
Figure 4-5 Electrochemical performance: (a) Polarization curves of G-Co ₃ O ₄ and Ru/C catalysts on GC electrodes in 0.1 and 1 M KOH. (b) The Tafel curves of G-Co ₃ O ₄ in 0.1 and 1 M KOH. (c, d) Chronoamperometric responses (percentage of current retained versus operation time) of G-Co ₃ O ₄ and Ru/C catalysts in 1 M and 0.1 M KOH electrolytes.	74
Figure 4-6 Electrochemical performance of G-Co ₃ O ₄ composite OER catalyst: (a) LSV and Tafel slope of G-Co ₃ O ₄ in neutral solution, (b) OER stability test of G-Co ₃ O ₄ , the initial and 1000th polarization curves in neutral solution.....	76
Figure 4-7 Electrochemical performance: Polarization curves of G-Co ₃ O ₄ , G+Co ₃ O ₄ , the pristine Co ₃ O ₄ and graphene in (a) 1 M and (b) 0.1 M KOH solutions.....	77
Figure 4-8 Nyquist plots of the G-Co ₃ O ₄ , the G+Co ₃ O ₄ and the pristine Co ₃ O ₄ modified electrodes in 1M KOH solution.....	78
Figure 4-9 (a, c) Electrochemical capacitance measurements: typical Cyclic voltammograms (CV) of G-Co ₃ O ₄ and G+Co ₃ O ₄ measured in 1 M	

KOH solution in a potential window without faradaic processes (scan rate: 10, 30, 50, 70, 90 mV/s); (b, d) Average capacitive current obtained from center of potential window (-0.12 V vs Ag/AgCl) as a function of scan rate for G-Co ₃ O ₄ and G+Co ₃ O ₄ electrodes.	78
Figure 5-1 SEM image of silica nanorod templates for the synthesis of PGE.	84
Figure 5-2 Schematic illustration for the synthesis procedure of PGE-CoO materials.	84
Figure 5-3 (a) Nitrogen adsorption/desorption isotherm of PGE, (b) SEM image of PGE.	85
Figure 5-4 The characterization of PGE-CoO hybrid: (a, b) low and high magnification SEM images of PGE-CoO, (c, d) TEM images of PGE-CoO.	86
Figure 5-5 (a, b) SEM images of pure CoO and GE-CoO, (c, d) Nitrogen adsorption/desorption isotherm of PGE-CoO and GE-CoO.	87
Figure 5-6 (a) XRD patterns of PGE-CoO and PGE, high-resolution spectra XPS (b) Co 2p, (c) O 1s, (d) thermogravimetric analysis in air of PGE-CoO.	88
Figure 5-7 Electrochemical performance of the OER catalysts: (a) polarization curves for PGE-CoO, GE-CoO, CoO and PGE on GC electrodes in 0.1 M KOH. (b) Tafel curves of PGE-CoO, GE-CoO and CoO in 0.1 M KOH. (c) Nyquist plots of the PGE-CoO, GE-CoO and CoO modified electrodes in 0.1 M KOH solution. (d, e) electrochemical capacitance measurements: cyclic voltammograms (CV) were performed in 0.1 M KOH solution in a potential window without faradaic processes. (f) scan rate dependence of the average capacitive currents at -0.08 V vs Ag/AgCl for PGE-CoO and GE-CoO.	90
Figure 5-8 (a) Nyquist and (b) Bode plots for the PGE-CoO hybrid modified GC electrode recorded at various OER overpotentials in 0.1 M KOH, (c) the square symbols are experimental data and the red solid line are	

modelled by the Equivalent electrical circuit shown in the inset, (d) the low-frequency charge transfer resistance (R_{ct}) and constant phase element (C_{dl}) as a function of the OER overpotentials for PGE-CoO-modified GC electrode in 0.1 M KOH.	91
Figure 5-9 (a) The stability of PGE-CoO and GE-CoO modified electrodes before and after LSV testing for 1000 cycles, (b, c) SEM images of PGE-CoO and GE-CoO after stability test.	93
Figure 5-10 (a) Polarization curves for PGE-CoO in various KOH concentrations. (b) current densities at 0.7 V vs. Ag/AgCl for PGE-CoO in solutions with various KOH concentrations.	95
Figure 6-1 schematic illustration for the fabrication process of CoMn ₂ O ₄ -CoNC.	102
Figure 6-2 (a, b) SEM and TEM images of CoNC; (c) XRD pattern of CoNC...	103
Figure 6-3 (a, b) the low and high magnification SEM images of CoMn ₂ O ₄ -CoNC.	103
Figure 6-4 (a-c) low and high magnification TEM images of CoMn ₂ O ₄ -CoNC; STEM element mapping of CoMn ₂ O ₄ -CoNC: (d) high angle annular dark field (HAADF) image showing the area of mapping, (e-g) element mapping in STEM mode for Mn, Co and O elements.....	104
Figure 6-5 (a, b) XRD and Raman spectra of CoMn ₂ O ₄ -CoNC.	105
Figure 6-6 (a) XPS survey spectra of CoMn ₂ O ₄ -CoNC, high resolution XPS spectra of CoMn ₂ O ₄ -CoNC, (b) N 1s, (c) Mn 2p, (d) Co 2p, (e) O 1s.	106
Figure 6-7 (a) Nitrogen adsorption/desorption isotherm and (b) pore size distribution of CoMn ₂ O ₄ -CoNC.....	107
Figure 6-8 (a) SEM image of pure NCNFs, (b) SEM image, (c) XRD spectrum, (d) XPS survey spectrum of MnO ₂ -NC.	108

Figure 6-9 Typical SEM images of the products after reaction for (a, e) 20 min, (b, f) 1 h, (c, g) 4 h and (d, h) 8 h. (i) Schematic illustration of the formation procedure of CoMn ₂ O ₄ -CoNC composite.	109
Figure 6-10 (a, b) SEM images of CoMn ₂ O ₄ -CoNC obtained after 15 h reaction.	110
Figure 6-11 (a) XRD and (b) Raman spectra of CoMn ₂ O ₄ -CoNC obtained at different time.....	111
Figure 6-12 (a) XPS survey spectra, high resolution XPS spectra of (b) Co 2p, (c) Mn 2p, (d) O 1s of CoMn ₂ O ₄ -CoNC obtained at different time.....	112
Figure 6-13 Low and high SEM images of NiMn ₂ O ₄ -NiNC.	113
Figure 6-14 (a) polarization curves and (b) corresponding Tafel plots of CoMn ₂ O ₄ -CoNC, MnO ₂ -NC, Co ₃ O ₄ -CoNC, NC and RuO ₂	114
Figure 6-15 Cyclic voltammograms (CV) of (a) CoMn ₂ O ₄ -CoNC, (b) Co ₃ O ₄ -CoNC and (c) MnO ₂ -NC, in 1 M KOH solution in a potential window without faradaic processes. (c) Scan rate dependence of the average capacitive current densities at open circuit potential for CoMn ₂ O ₄ -CoNC, Co ₃ O ₄ -CoNC and MnO ₂ -NC.	115
Figure 6-16 Nyquist plots of the as-prepared samples modified electrodes recorded at a constant overpotential of 250 mV.....	116
Figure 6-17 Stability test of CoMn ₂ O ₄ -CoNC through potential cycling, the inset shows the time dependence of catalytic current density during electrolysis at a static potential.	117
Figure 6-18 (a) Evidence of O ₂ generated from CoMn ₂ O ₄ -CoNC catalyst using RRDE measurements (1600 rpm) (disk potential: 1.48 V, ring potential: 0.45 V vs. RHE), with inset showing the continuous OER → ORR process initiated on the RRDE. (b) Disk and ring current of CoMn ₂ O ₄ -CoNC catalyst on an RRDE (1600 rpm) with a ring potential of 1.5 V (vs. RHE).....	118

Figure 7-1 (a) Schematic illustration for the fabrication process of Fe ₃ C@NCNTs-NCNFs. (b) low and (c, d) high magnification SEM images of Fe ₃ C@NCNTs-NCNFs.....	126
Figure 7-2 (a) TEM image of a single fibrous Fe ₃ C@NCNTs-NCNF. (b) HRTEM image of Fe ₃ C@NCNTs aligned on NCNF. (c) high resolution TEM image of a single Fe ₃ C@NCNT. (d) a Fe ₃ C nanoparticle wrapped by multilayered graphitic carbon, the enlarged area as denoted in the white box, displaying an interplanar spacing of 0.239 nm. (e-i) STEM elemental mapping of Fe ₃ C@NCNTs-NCNFs. (j-l) two different phases of Fe ₃ C@NCNTs-NCNFs, (k) C, (l) Fe ₃ C.	127
Figure 7-3 (a,b) SEM and (c,d) TEM images of NCNFs.....	129
Figure 7-4 (a) SEM and (b-d) TEM images of Fe ₃ C-NCNFs.	129
Figure 7-5 (a, b) XRD pattern of Fe ₃ C@NCNTs-NCNFs and Fe ₃ C-NCNFs.....	130
Figure 7-6 Raman spectra of Fe ₃ C@NCNTs-NCNFs, Fe ₃ C-NCNFs and pure NCNFs.	131
Figure 7-7 (a) XPS survey spectrum of Fe ₃ C@NCNTs-NCNFs. high resolution XPS spectra of (b) C 1s, (c) Fe 2p and (d) N 1s of Fe ₃ C@NCNTs-NCNFs composite.	132
Figure 7-8 (a) Nitrogen sorption isotherm Fe ₃ C@NCNTs-NCNFs. (b) Thermogravimetric analysis of Fe ₃ C@NCNTs-NCNFs in air.	133
Figure 7-9 (a) polarization curves and (b) corresponding Tafel plots of Fe ₃ C@NCNTs-NCNFs, Fe ₃ C-NCNFs, NCNFs and RuO ₂	134
Figure 7-10 Cyclic voltammograms (CV) of (a) Fe ₃ C@NCNTs-NCNFs, (b) Fe ₃ C-NCNFs, (c) NCNFs, both in 1 M KOH solution in a potential window without faradaic processes. (d) Scan rate dependence of the average capacitive current densities at open circuit potential for Fe ₃ C@NCNTs-NCNFs, Fe ₃ C-NCNFs and NCNFs.....	135
Figure 7-11 EIS spectra of Fe ₃ C@NCNTs-NCNFs, Fe ₃ C-NCNFs and NCNFs modified electrodes with an overpotential of 250 mV.....	136

Figure 7-12 Stability test of Fe ₃ C@NCNTs-NCNFs (a) through potential cycling. (b) time dependence of catalytic current density during electrolysis at a static overpotential.....	136
Figure 7-13 (a) Disk and ring current of Fe ₃ C@NCNTs-NCNFs catalyst on an RRDE (1600 rpm) with a ring potential of 1.50 V (vs. RHE). (b) Evidence of O ₂ generated from Fe ₃ C@NCNTs-NCNFs catalyst using RRDE measurements (1600 rpm) (disk potential: 1.48 V, ring potential: 0.45 V vs. RHE), with inset showing the continuous OER → ORR process initiated on the RRDE.	137
Figure 8-1 Schematic illustration for the preparation of Co-PNCNFs nanofibers by electrospinning.	146
Figure 8-2 SEM image of Co-NCNFs (before acid treatment), showing the cobalt nanoparticles on the surface of CNFs.	146
Figure 8-3 Electron microscopy characterization of Co-PNCNFs. (a) low magnification and (b) high magnification SEM images of Co-PNCNFs. (c) EDS analysis of Co-PNCNFs, showing homogenous distribution of C, N, Co elements in fibrous structure. (d) TEM image of a single fibrous Co-PNCNF. (e) Enlarged TEM image of a single Co-PNCNF, demonstrating the structure of dispersed nanoparticles embedded in porous carbon fiber. (f) HRTEM image of a Co nanoparticle wrapped in carbon. The inset is the enlarged area as denoted in the white box, displaying an interplanar spacing of 0.205 nm.	147
Figure 8-4 (a, b) Low and high magnification SEM images of NCNFs, (c, d) Low and high magnification TEM images of NCNFs.	149
Figure 8-5 (a) XRD patterns of NCNFs and Co-PNCNFs. (b) Raman spectra of NCNFs and Co-PNCNFs. (c) XPS spectrum of Co-PNCNFs composite. High resolution XPS spectra of (d) Co 2p and (e) N 1s. (f) Nitrogen sorption isotherm of Co-PNCNFs, inset shows the pore size distribution of Co-PNCNFs.	150

- Figure 8-6** Electrochemical performance of the catalysts towards OER in 1 M KOH solution: (a) Polarization curves for Co-PNCNFs, NCNFs, RuO₂, Pt/C and pure GC. (b) The corresponding Tafel plots of catalysts. ... 152
- Figure 8-7** Cyclic voltammograms (CV) of (a) Co-PNCNFs, and (b) NCNFs, both in 1 M KOH solution in a potential window without faradaic processes. (c) Scan rate dependence of the average capacitive current densities at open circuit potential for Co-PNCNFs and NCNFs. (d) Nyquist plots of Co-PNCNFs and NCNFs modified electrodes. 153
- Figure 8-8** (a) Stability test of Co-PNCNFs through potential cycling, displaying polarization curves of initial one, after 1000 and 5000 potential cycles. Inset shows the chronoamperometric stability test over 12 h. (b) SEM image of Co-PNCNFs after stability test (60 h), displaying the carbon matrix and porous structure were maintained. 154
- Figure 8-9** (a) The ring current of Co-PNCNFs on a RRDE (1600 rpm) in a N₂-saturated 1 M KOH solution (ring potential: 0.45 V *vs.* RHE). (b) Disk and ring current of Co-PNCNFs on a RRDE (1600 rpm) with a disk potential of 1.55 V (*vs.* RHE) and ring potential of 1.50 V (*vs.* RHE) in 1 M KOH solution. 155
- Figure 8-10** Catalytic activities of (a) Co-PNCNFs, Ni-PNCNFs, Fe-PNCNFs and pure NCNFs, and (b) Co-PNCNFs, Co-PCNFs and NCNFs. All these catalytic activity of CNFs based materials towards OER were tested in 1 M KOH solution, showing the electrocatalytic improvements promoted by metal or N functionalization. 156
- Figure 8-11** Electrochemical performance of the catalysts towards HER in 1 M KOH solution: (a) polarization curves for Co-PNCNFs, NCNFs, Pt/C and bare GC. (b) The corresponding Tafel plots. 158
- Figure 8-12** Electrochemical performance test of Co-PNCNFs deposited on nickel foam towards (a) OER and (b) HER in 1 M KOH solution. (c) Optical photograph of Co-PNCNFs based electrolyzer. (d) LSV of water

electrolysis using Co-PNCNFs as both OER and HER catalysts. The inset shows the stability test at the potential of 1.66 V over 10 h.... 159

LIST OF ABBREVIATIONS

Abbreviation	Full name
<hr/>	
a.u.	Arbitrary unit
nm	Nanometer
cm	Centimeter
LSV	Linear sweep voltammetry
CV	Cyclic voltammetry
EIS	Electrochemical impedance spectroscopy
RRDE	Rotating ring-disk electrode
GC	Glassy carbon electrode
RHE	Reversible hydrogen electrode
GC	Glassy carbon electrode
Eq.	Equation
JCPDS	Joint committee on powder diffraction standards
SAED	Selected area electron diffraction
SEM	Scanning electron microscopy
TEM	Transmission electron microscopy
XPS	X-ray photoelectron spectroscopy
BET	Brunauer Emmett Teller
TGA	Thermogravimetric analysis
XRD	X-ray diffraction
FT-IR	Fourier transform infrared spectroscopy
DMF	Dimethylformamide
DMDMS	Dimethoxydimethylsilane
TEOS	Tetraethyl orthosilicate
CTAB	Hexadecyl trimethyl ammonium bromide
OCP	Open circuit potential
HER	Hydrogen evolution reaction
OER	Oxygen evolution reaction

LIST OF PUBLICATIONS

- [1] **Zhao, Y.**; Zhang, Y.; Yang, Z.; Yan, Y.; Sun, K. Synthesis of MoS₂ and MoO₂ for their applications in H₂ generation and lithium ion batteries: a review. *Science and Technology of Advanced Materials* 2013, 14, 043501.
- [2] **Zhao, Y.**; Chen, S.; Sun, B.; Su, D.; Huang, X.; Liu, H.; Yan, Y.; Sun, K.; Wang, G. Graphene-Co₃O₄ nanocomposite as electrocatalyst with high performance for oxygen evolution reaction. *Scientific reports* 2015, 5, 7629.
- [3] **Zhao, Y.**; Yang, Z.-Y.; Zhang, Y.-X.; Jing, L.; Guo, X.; Ke, Z.; Hu, P.; Wang, G.; Yan, Y.-M.; Sun, K.-N. Cu₂O decorated with cocatalyst MoS₂ for solar hydrogen production with enhanced efficiency under visible light. *The Journal of Physical Chemistry C* 2014, 118, 14238-14245.
- [4] **Zhao, Y.**; Xie, X.; Zhang, J.; Liu, H.; Ahn, H. J.; Sun, K.; Wang, G. MoS₂ Nanosheets Supported on 3D Graphene Aerogel as a Highly Efficient Catalyst for Hydrogen Evolution. *Chemistry—A European Journal* 2015, 21, 15908-15913.
- [5] **Zhao, Y.**; Sun, B.; Huang, X.; Liu, H.; Su, D.; Sun, K.; Wang, G. Porous graphene wrapped CoO nanoparticles for highly efficient oxygen evolution. *Journal of Materials Chemistry A* 2015, 3, 5402-5408.
- [6] **Zhao, Y.**; Zhang, J.; Li, K.; Ao, Z.; Wang, C.; Liu, H.; Sun, K.; Wang, G. Electrospun cobalt embedded porous nitrogen doped carbon nanofibers as an efficient catalyst for water splitting. *Journal of Materials Chemistry A* 2016, 4, 12818-12824.
- [7] Jing, L.; Yang, Z.-Y.; **Zhao, Y.**; Zhang, Y.-X.; Guo, X.; Yan, Y.-M.; Sun, K.-N. Ternary polyaniline–graphene–TiO₂ hybrid with enhanced activity for visible-

- light photo-electrocatalytic water oxidation. *Journal of Materials Chemistry A* 2014, 2, 1068-1075.
- [8] Yang, Z.-Y.; **Zhao, Y.**; Xiao, Q.-Q.; Zhang, Y.-X.; Jing, L.; Yan, Y.-M.; Sun, K.-N. Controllable growth of CNTs on graphene as high-performance electrode material for supercapacitors. *ACS applied materials & interfaces* 2014, 6, 8497-8504.
- [9] Wang, X.; Yang, Z.; Zhang, Y.; Jing, L.; **Zhao, Y.**; Yan, Y.; Sun, K. MnO₂ Supported Pt Nanoparticels with High Electrocatalytic Activity for Oxygen Reduction Reaction. *Fuel Cells* 2014, 14.
- [10] Zhang, W.; Zhang, Y.; Tian, Y.; Yang, Z.; Xiao, Q.; Guo, X.; Jing, L.; **Zhao, Y.**; Yan, Y.; Feng, J. Insight into the capacitive properties of reduced graphene oxide. *ACS applied materials & interfaces* 2014, 6, 2248-2254.
- [11] Yang, Z.; Zhang, L.; Zhang, Y.; **Zhao, Y.**; Jing, L.; Yan, Y.; Sun, K. Rational design of CuO@ Cu nanostructure with tuneable morphology and electrochemical properties. *RSC Advances* 2014, 4, 8121-8124.
- [12] Sun, B.; Huang, X.; Chen, S.; **Zhao, Y.**; Zhang, J.; Munroe, P.; Wang, G. Hierarchical macroporous/mesoporous NiCo₂O₄ nanosheets as cathode catalysts for rechargeable Li-O₂ batteries. *Journal of Materials Chemistry A* 2014, 2, 12053-12059.
- [13] Huang, X.; **Zhao, Y.**; Ao, Z.; Wang, G. Micelle-template synthesis of nitrogen-doped mesoporous graphene as an efficient metal-free electrocatalyst for hydrogen production. *Scientific reports* 2014, 4, 7557.

- [14] Chen, S.; **Zhao, Y.**; Sun, B.; Ao, Z.; Xie, X.; Wei, Y.; Wang, G. Microwave-assisted synthesis of mesoporous Co_3O_4 nanoflakes for applications in lithium ion batteries and oxygen evolution reactions. *ACS applied materials & interfaces* 2015, 7, 3306-3313.
- [15] Xu, J.; Su, D.; Bao, W.; **Zhao, Y.**; Xie, X.; Wang, G. Rose flower-like NiCo_2O_4 with hierarchically porous structures for highly reversible lithium storage. *Journal of Alloys and Compounds* 2016, 684, 691-698.
- [16] Kretschmer, K.; Sun, B.; Su, D.; **Zhao, Y.**; Wang, G. Scalable Preparation of LiFePO_4/C Nanocomposites with sp^2 -Coordinated Carbon Coating as High-Performance Cathode Materials for Lithium-Ion Batteries. *ChemElectroChem* 2015, 2, 2096-2103.
- [17] Zhang, J.; Sun, B.; Xie, X.; **Zhao, Y.**; Wang, G. A Bifunctional Organic Redox Catalyst for Rechargeable Lithium-Oxygen Batteries with Enhanced Performances. *Advanced Science* 2015, 3, 1500285.
- [18] Zhang, J.; Sun, B.; McDonagh, A. M.; **Zhao, Y.**; Kretschmer, K.; Guo, X.; Wang, G. A multi-functional gel co-polymer bridging liquid electrolyte and solid cathode nanoparticles: An efficient route to Li-O_2 batteries with improved performance. *Energy Storage Materials* 2017, 7, 1-7.
- [19] Guo, X.; Xie, X.; Choi, S.; **Zhao, Y.**; Liu, H.; Wang, C.; Chang, S.; Wang, G. $\text{Sb}_2\text{O}_3/\text{MXene}$ ($\text{Ti}_3\text{C}_2\text{T}_x$) hybrid anode materials with enhanced performance for sodium-ion batteries. *Journal of Materials Chemistry A* 2017, 5, 12445-12452.

- [20] Zhang, J.; Sun, B.; **Zhao, Y.**; Kretschmer, K.; Wang, G. Modified Tetrathiafulvalene as an Organic Conductor for Improving Performances of Li-O₂ Batteries. *Angewandte Chemie International Edition* 2017, 56, 8505-8509 .

ABSTRACT

Hydrogen (H_2) is an abundant and renewable clean fuel that is regarded as a promising energy carrier to replace fossil fuels in the future. Electrocatalytic water splitting to produce H_2 seems to be one of the cleanest and most sustainable methods for large-scale H_2 production. The catalysts are of extreme significance for the electrochemical performances of water splitting.

The composite of layered MoS_2 nanosheets supported on a 3D graphene aerogel network (GA- MoS_2) has been synthesized by two-step hydrothermal method. The flexible graphene sheets partially overlap in 3D space to form an interconnected porous microstructure, which greatly prevents serious restacking of graphene, and further provides large surface area for growing MoS_2 nanosheets. GA- MoS_2 maintains an excellent porous structure and assembles with MoS_2 nanosheets around the edge of the pores, providing relatively large amounts of exposed edge sites for hydrogen evolution. The 3D structure of the catalyst can also supply efficient conducting network for rapid electronic transport during the electrocatalytic process, offsetting the poor intrinsic conductivity of MoS_2 , facilitating fast electron transfer. Therefore, GA- MoS_2 exhibits high catalytic performance and strong stability for electrocatalytic HER application.

Graphene- Co_3O_4 composite with a unique sandwich-architecture is successfully synthesized and applies as an efficient electrocatalyst towards OER. The graphene nanosheets act as a binder to link neighboring Co_3O_4 particles together and Co_3O_4 nanocrystals are homogeneously attached on both sides of graphene nanosheets. The existence of graphene highly increases the conductivity of the composite. The obtained composite shows enhanced

catalytic activities in both alkaline and neutral electrolytes. The current density of 10 mA cm^{-2} has been achieved at the overpotential of 313 mV in 1 M KOH and 498 mV in phosphate buffer solution, respectively. Furthermore, there is no obvious current density decay after the stability test.

An active catalyst composed of porous graphene and cobalt oxide (PGE–CoO) has been synthesized, demonstrating high porosity, large specific surface area and fast charge transport kinetics. The catalyst also exhibits excellent electrochemical performance towards OER with a low onset potential (504 mV vs. Ag/AgCl) and high catalytic current density (overpotential of 348 mV for 10 mA cm^{-2}). The enhanced catalytic activity could be ascribed to porous structure, high electroactive surface area and strong chemical coupling between graphene and CoO nanoparticles. Moreover, CoO nanoparticles are wrapped by the porous graphene, inhibiting the corrosion phenomenon, thus this OER catalyst also shows good stability in the alkaline solution. The high performance and strong durability suggest that the porous structured composite is favorable and promising for water splitting.

We develop ultrathin CoMn_2O_4 nanosheets with abundant oxygen vacancies vertically aligned on cobalt and nitrogen co-functionalized carbon nanofibers ($\text{CoMn}_2\text{O}_4\text{-CoNC}$) as an efficient OER catalyst by a facial spontaneous redox reaction. The inner CoNC serves as sacrificed template and high conductive substrate to provide fast electronic transportation, and the aligned ultrathin nanosheets rich in oxygen vacancies act as active sites. Benefiting from the collaborative advantages of high effective surface areas, fast charge transfer kinetics and strong synergistic coupled effect, $\text{CoMn}_2\text{O}_4\text{-CoNC}$ composite exhibits excellent catalytic activity and good durability for

water oxidation, reaching 10 mA cm^{-2} at an overpotential of 307 mV.

Fe_3C nanoparticles encapsulated at the tip of nitrogen-enriched carbon nanotubes (NCNTs) is investigated as catalyst for OER, which are aligned on one dimensional (1D) nitrogen doped carbon nanofibers ($\text{Fe}_3\text{C}@\text{NCNTs-NCNFs}$) by a scalable electrospinning technique, as a high performance OER catalyst. The unique 3D hierarchical architecture of $\text{Fe}_3\text{C}@\text{NCNTs-NCNFs}$ leads to highly exposed active sites, enhanced electron transfer properties and strong synergistic coupled effects. $\text{Fe}_3\text{C}@\text{NCNTs-NCNFs}$ exhibits outstanding catalytic performance with a high current density (10 mA cm^{-2} at an overpotential of 284 mV), a low Tafel slope (56 mV dec^{-1}), a low charge transfer resistance and strong durability in 1 M KOH solution.

We report the successful synthesis of cobalt nanoparticle embedded porous nitrogen doped carbon nanofibers (Co-PNCNFs) by a facile and scalable electrospinning technology. The electrospun Co-PNCNF composite exhibits a low onset potential of 1.45 V (vs. RHE) along with high current density (overpotential of 285 mV for 10 mA cm^{-2}) towards OER. The exceptional performance could be ascribed to the bi-functionalized CNFs with nitrogen doping and cobalt encapsulation, which can convert the inert carbon into active sites. Moreover, the porous structure and synergistic effect further provide a highly effective surface area and facilitate a fast electron transfer pathway for the OER process. Interestingly, the Co-PNCNF composite also displays the capability for the hydrogen evolution reaction (HER) in alkaline solution. A water electrolyzer cell fabricated by applying Co-PNCNFs as both anode and cathode electrocatalysts in alkaline solution can achieve a high current density of 10 mA cm^{-2} at a voltage of 1.66 V.

INTRODUCTION

The rapid development of global economy has led to serious energy and environmental problems. With increasing demand for renewable energy, there are intense efforts to develop various types of energy storage and conversion systems. Hydrogen is considered to be one of the most promising new energy. The efficient electrochemical and photo/photoelectrochemical conversion of water to hydrogen by catalysts offers an attractive way to store energy. The water splitting reaction can be divided into two half-reactions: the hydrogen evolution reaction (HER) and oxygen evolution reaction (OER). Water splitting is mainly hindered by the oxidation process, due to its sluggish kinetics derived from a multistep proton-coupled electron transfer process. Currently, typical catalysts used for HER and OER in electrolysis cells are still precious metal-based materials (Pt, RuO₂, and IrO₂). However, their scarcity and high cost are the major barriers for the global-scale applications. Therefore, replacing noble metal-based electrocatalysts with highly efficient and inexpensive non-noble metal-based hydrogen and oxygen electrocatalysts is critical for the practical applications of these technologies. Although significant progress has been achieved in the past few years, there are lots of challenges still to overcome.

The purpose of this doctoral work is to design different materials as catalysts to improve the efficiency of water splitting and to provide possible opportunities for future research directions. A series of nanostructure materials were successfully prepared, such as one-dimensional nanofibers, two dimensional nanosheets and three dimensional porous structures. Several approaches are used to fabricate the above materials, including hydrothermal method, hard template method, wet-chemical synthesis and electrospinning

technique. The morphology and composition of the materials were characterized by Scanning electron microscopy, Transmission electron microscopy, X-ray diffraction and X-ray photoelectron spectroscopy. The electrochemical performance towards water splitting of the as-prepared materials was evaluated by various electrochemical measurements.

In this thesis, we have summarized the catalysts used for the electrocatalytic hydrogen and oxygen evolution reaction. We have designed the MoS₂ based materials as the catalysts for facilitating the electrocatalytic hydrogen evolution. We studied transition metal oxides and transition metal carbides, especially cobalt-based oxides and iron carbide, as catalysts to reduce the OER energy barrier and to further accelerate the overall water splitting process. Additionally, carbon based material have been reported as a bifunctional catalyst to simultaneously generate H₂ and O₂ in alkaline solution.

An outline of the content is briefly presented as follows:

1. A literature review of water splitting, including HER and OER, is presented in Chapter 1. In this chapter, the basic concepts and principles of water splitting are described. This chapter reviews the importance and history of renewable energy, especially hydrogen as the clean energy. The basic parameters for characterizing the catalytic performance of water splitting are also presented. Recent achievements, including the catalysts for HER and OER and the performance they achieved, for water splitting are shown in this chapter.
2. Experimental section, including material preparation, material characterization and electrochemical performance measurements, is presented in Chapter 2. We have introduced five different synthesis

approaches for synthesizing the catalysts. A variety of characterization methods to identify the morphology and composition of the as prepared catalysts. Finally, different measurement approaches are used to evaluate the electrochemical performance of these as prepared catalysts towards water splitting.

3. In chapter 3, we have prepared an active catalyst composed of MoS₂ nanosheets and 3D architectural graphene aerogel (GA-MoS₂) by two-step hydrothermal method. GA with 3D network, highly porous structure provides a stable skeleton and large specific surface area for loading layer MoS₂ nanosheets around the edge of the pores, which maximizes exposing the active sites of MoS₂ nanosheets. The macropores in this nanoarchitecture provide easy access to the electrolyte for the catalysts, enhancing the communication between the electrolyte and the catalysts and further accelerating the HER reaction.
4. In chapter 4, we report a simple method to prepare a unique sandwich-architected catalyst composed of graphene and Co₃O₄ (G-Co₃O₄). Co₃O₄ is a typical spinel oxide, is an attractive oxygen evolution catalyst. The unique sandwich-architecture of G-Co₃O₄ composite leads to large amount loading of the active Co₃O₄ nanocrystals on both sides of graphene sheets. Moreover, the strong bond between graphene and Co₃O₄ nanoparticles highly enhances the electron transfer kinetics during the OER process. These merits ensure the excellent electrochemical performance of G-Co₃O₄ as an OER catalyst.
5. Porous graphene with controlled porous textures have garnered more interests compared to the nonporous graphene because of their attractive

properties such as ordered pores, large pore volume and good conductivity. In this chapter, we developed an active catalyst, CoO nanoparticles wrapped by porous graphene sheets (PEG-CoO). When PEG-CoO is applied as catalyst for OER, the highly porous structure and the excellent chemical and electronic coupling between the composite material lead to the superior OER activity with a low overpotential and high catalytic current density.

6. Recently, considerable attention has been drawn to the discovery of the ternary hybrid catalysts due to their unique structural property and excellent catalytic performance. In this chapter, we discuss a ternary hybrid catalysts based on transition metal oxides. A high active OER catalyst has been obtained by simply in situ growing ultrathin CoMn_2O_4 nanosheets with abundant oxygen vacancies vertically aligned on cobalt/nitrogen co-functionalized CNFs ($\text{CoMn}_2\text{O}_4\text{-CoNC}$) by a facile spontaneous redox reaction between CoNC and KMnO_4 solution. The resultant $\text{CoMn}_2\text{O}_4\text{-CoNC}$ composite manifests high catalytic activity and an excellent stability during the OER process in an alkaline medium.
7. The transition metal oxides have shown excellent OER catalytic performance, besides, transition metal carbides, *e.g.* Fe_3C , have been reported to have the ability for water oxidation. We developed a facile, scalable method to synthesize the catalyst composed of Fe_3C encapsulated in nitrogen-enriched CNTs aligned on nitrogen doped CNFs ($\text{Fe}_3\text{C@NCNTs-NCNFs}$) by the electrospinning technique. The as-prepared $\text{Fe}_3\text{C@NCNTs-NCNFs}$ composite exhibits outstanding electrocatalytic activity and excellent stability.

8. In chapter 8, we have developed a bifunctional catalyst that is able to catalyze hydrogen and oxygen evolution simultaneously. We design a facile, scalable method to synthesize cobalt nanoparticles embedded in porous nitrogen doped CNFs (Co-PNCNFs) by electrospinning technique. The unique encapsulated structure could efficiently avoid the metal nanoparticles directly contact with the harsh environmental, protecting the metal nanoparticles from corrosion and aggregation during the catalytic process. Benefiting from its high exposed effective surface area, improved electronic conductivity, intimate interaction and synergetic effect, Co-PNCNFs can serve as active electrocatalyst for both OER and HER with an outstanding performance and excellent stability.

Chapter 1: Literature review

1.1 Introduction

With the rapid development of modern society, the increasing demand of fossil fuels (coal, oil, natural gas, etc) has caused serious energy issues worldwide.^{1, 2} Meanwhile, the unavoidable release of toxic gases and the generation of solid wastes along with the combustion of fossil fuels have been also major severe environmental problems. Therefore, the strong dependence on fossil fuels and the corresponding increasing detrimental effects on environment have stimulated extensive efforts to develop clean, renewable alternatives. Hydrogen has been identified as one of the most promising energy carriers due to its environmental friendliness and recyclability. To this end, effective production of hydrogen is key element of the hydrogen economy.^{3,4}

Hydrogen is supposed to be a major energy carrier, which could provide high combustion heat. Hydrogen is not only an environmentally benign fuel for power generation, but also a versatile reagent for chemical synthesis. Today, the industrial production of hydrogen is achieved by steam reforming of methane and water, in which the accompanying product is carbon dioxide.⁵ However, methane is not a renewable energy source and the CO₂ released may cause new problems. Reduction of water for H₂ production offers an alternative strategy, which is a potential replacement of methane reforming.⁶⁻⁸ Importantly, the abundant water on earth provides an ideal resource for hydrogen production in a cheap and reliable way. The possible energy strategy, water splitting, has attracted much attention in the past few decades.

Although electrolysis of water to produce H₂ is a facile method, the high cost of the consumed electrical power prevents its wide application. Therefore, producing H₂ in an economic and green way is highly desirable and becomes a scientific challenge. In the many studies reported so far, Pt-based materials were found to be well-performing

catalysts, and they are used not only for electrochemical water reduction, but also for photoelectrochemical water splitting. The high activity of Pt-based catalysts toward water reduction indicates that the surface of Pt-based catalysts provides efficient active sites for catalytic H₂ evolution. However, the large-scale application of Pt-based catalysts has been limited by their low natural abundance and high cost. In recent years, extensive efforts have been devoted to looking for alternative catalysts containing only non-precious elements.

Water splitting can be divided into two reactions: hydrogen evolution reaction (HER) and oxygen evolution reaction (OER), which is mainly hindered by the sluggish kinetics of OER (four-electron transfer).^{9, 10} The major challenge for OER is also to develop catalysts with high efficiency, low overpotential, as well as long-term stability. At present, precious metal oxides or complexes of ruthenium (Ru) and iridium (Ir) are the most active catalysts towards OER, achieving high electrochemical performance.^{11, 12} However, the scarcity and prohibitive cost of these noble metals impede them to be used on a large scale. Therefore, it is important to develop new highly active catalysts for oxygen evolution, especially those composed of earth-abundant and inexpensive materials.

1.2 Electrochemistry of water splitting

1.2.1 The mechanism of electrochemical water splitting

As shown in Figure 1-1, an electrolyzer has three component parts: an electrolyte, a cathode, and an anode. To accelerate the water splitting reaction process, the hydrogen evolution catalyst and oxygen evolution catalyst are coated on the cathode and anode, respectively. When given an external voltage to the electrodes, water molecules are decomposed into hydrogen and oxygen. The hydrogen can be stored for fuel and the

oxygen is released into the atmosphere. Therefore, the water splitting process can be divided into two half-reaction: hydrogen evolution reaction (HER) and oxygen evolution reaction (OER).

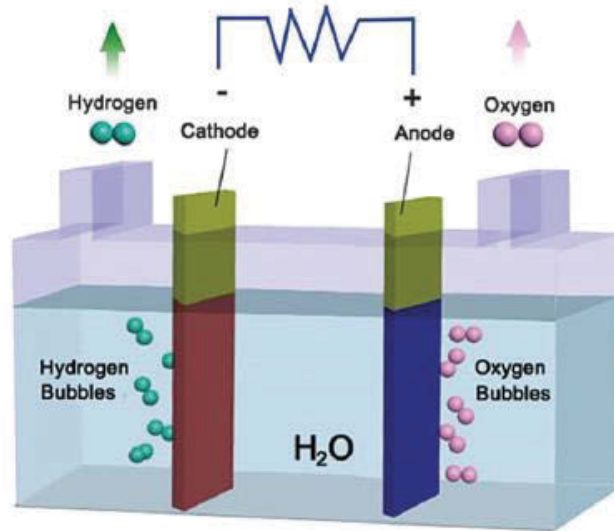
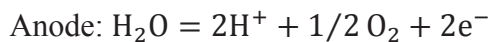
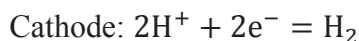


Figure 1-1 Schematic diagram of an electrolyzer.

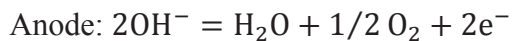
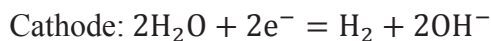
According to different media in which water splitting occurs, the water splitting can be expressed chemically in different ways.



In acidic solution :



In neutral and alkaline solution:



Regardless of the media in which water splitting takes place, the thermodynamic voltage of water splitting is 1.23 V at 25 °C and 1 atm. However, we generally must apply a higher potential to expedite the electrochemical water splitting, thus resulting in the consumption of excess energy and decreasing the conversion efficiency. The excess

potential (overpotential, η) is mainly caused by intrinsic reaction activation barriers and some other resistances, such as solution resistance and contact resistance.⁷ Therefore, much research has been devoted to developing efficient electrocatalysts for water splitting with lower overpotential.

1.2.2 Electrochemical parameters for the evaluation of HER and OER catalytic activity

1.2.2.1 Onset potential and overpotential

The overpotential is an important criteria to drive a reaction at a certain rate, denoted as η . The electrode activity and overpotential is generally estimated by cyclic voltammetry (CV) or linear sweep voltammetry (LSV). In order to determine the catalytic activity of the material, we usually compare two representative overpotentials: onset potential and overpotential. The onset potential is the applied potential with apparent currents (cathodic or anodic). However, the onset potential is actually a poorly-defined value. Usually, the onset overpotential is defined as the suitable current density of 0.5-2 mA cm⁻². The other relevant overpotential is that the overpotential to reach a current density of 10 mA cm⁻², which is the current density expected for a 12.3% efficient solar water splitting device. Generally, an ideal material could generate high current density with lower overpotential.

1.2.2.2 Tafel slope and exchange current density

The reaction kinetics of water reduction and oxidation can be revealed by Tafel slopes.¹³ Tafel plots can be derived from the Linear sweep voltammetry (LSV) by fitting the linear regions to the Tafel equation ($\eta = b \log(j/j_0)$, where η is the overpotential, b is the Tafel slope, j is the current density, and j_0 is the exchange current density), which is usually used to evaluate the efficiency of the catalytic reaction. Tafel slope varies in a

complex manner depending on many factors (reaction pathway, catalyst preparation, catalyst categories, adsorption conditions of the active site, electrode modification procedure, etc.) In principle, a lower Tafel slope means a catalyst requires a lower applied overpotential to generate a required current. Exchange current density (j_0) is obtained when η is assumed to be zero, indicating the intrinsic catalytic activity of the material under equilibrium conditions. The exchange current density is a measure of the electron transfer rate of the catalyst, which is related to the electrode materials, electrode surface state, electrolyte composition and experimental temperature. The Tafel slope and exchange current density are two important parameters to indicate the catalytic activity. A good catalyst should have a high exchange current density and low Tafel slope.

1.2.2.3 Stability

Good structure and long-term stability of the catalysts towards water splitting is one of the most important parameters for the potential application of a material. Generally, there are two methods to assess the stability of a catalyst, namely, CV and chronoamperometry (potential-time) or chronopotentiometry (current-time). For the CV test, the stability is usually evaluated by comparing the polarization curves before and after the cycling test, normally more than 5000 cycles. If the polarization curve is identical to the initial one, which suggests the catalyst have good endurance in the electrolyte. Moreover, chronoamperometry or chronopotentiometry test is to measure the potential or current varies with time. For this measurement, normally, 10 hours is regard as a benchmark for comparison and the potential is usually related to 10 mA cm^{-2} . The structure stability could be further investigated by the SEM images of the catalyst after the electrochemical stability test, which could signify the catalyst have a good tolerance for the water splitting process.

1.2.2.4 Electrochemical impedance (EIS) analysis

The EIS analysis conducted at the open-circuit or various overpotentials is used to gain insight into the interface reaction and electrode kinetics of the catalysts for the HER or OER process. The charge transfer resistance (R_{ct}) is related to the interface charge-transfer process of the electrode, which could be obtained from the diameter of the semicircles in the high frequency zone, whereas the adsorption resistance (R_{ad}) associated to the adsorption of oxidized species on the electrode surface obtained from the low frequency zone. The EIS usually conducts under the open circuit voltage, therefore, the open circuit should be tested. Moreover, the EIS could be also measured under various overpotential. Generally, similar trend of EIS indicates the similar mass transport properties and reaction mechanism, and lower impedance contributes to better catalytic activity.

1.2.2.5 Electrochemical active surface area (ECSA)

The ECSA of the catalysts towards HER or OER could be estimated from the electrochemical double-layer capacitance of the catalytic surface. The electrochemical capacitance was determined by measuring the non-Faradaic capacitive current associated with the double-layer charging. To measure double-layer charging via CV, a potential range with no apparent Faradaic process occur was determined from static CV.¹⁴ The potential range is usually a 0.1 V potential window centered at the open circuit potential of the system and all measured current in this potential range is assumed to be due to double-layer charging. The charging current is then measured from CVs at multiple scan rates. The large double-layer charging demonstrates more exposed surface reactive sites and much higher current density.

1.2.2.6 Turnover Frequency (TOF)

TOF is another crucial detector to evaluate the catalytic activity. TOF is defined as the number of reactant that a catalyst convert to a desired product per catalytic site in unit time. Generally, TOF could be calculated by two steps: (1) calculation of active sites, (2) calculation of TOF values. However, the active sites are very difficult to identify. Therefore, assuming that all deposited materials were involved in the electrochemical reaction, the lower limits for turnover frequency (TOF) can be derived from the catalytic current. The high TOF value shows the outstanding catalytic activity of the catalysts towards HER or OER.

1.2.3 Evaluation criteria of HER and OER catalysts

Nowadays, the evaluation criteria of HER and OER mainly includes: (1) the specific surface area and pore size distribution of the catalysts, which is related to the mass transportation and the contact between electrolyte and catalysts; (2) conductivity, higher conductivity could efficiently accelerate the electron transfer; (3) active sites, the hydrogen and oxygen evolution mainly occur on the active sites of the catalysts, therefore more exposed active sites could generate enhanced catalytic activity; (4) chemical and structural stability, stability is an important factor of the catalyst in the practical application; (5) cost, one of the major challenge of the HER and OER catalysts for the practical production is the development and utilization of the materials with low price and abundant distribution.

1.3 Electrochemical hydrogen evolution reaction

1.3.1 Mechanism of electrochemical hydrogen evolution reaction

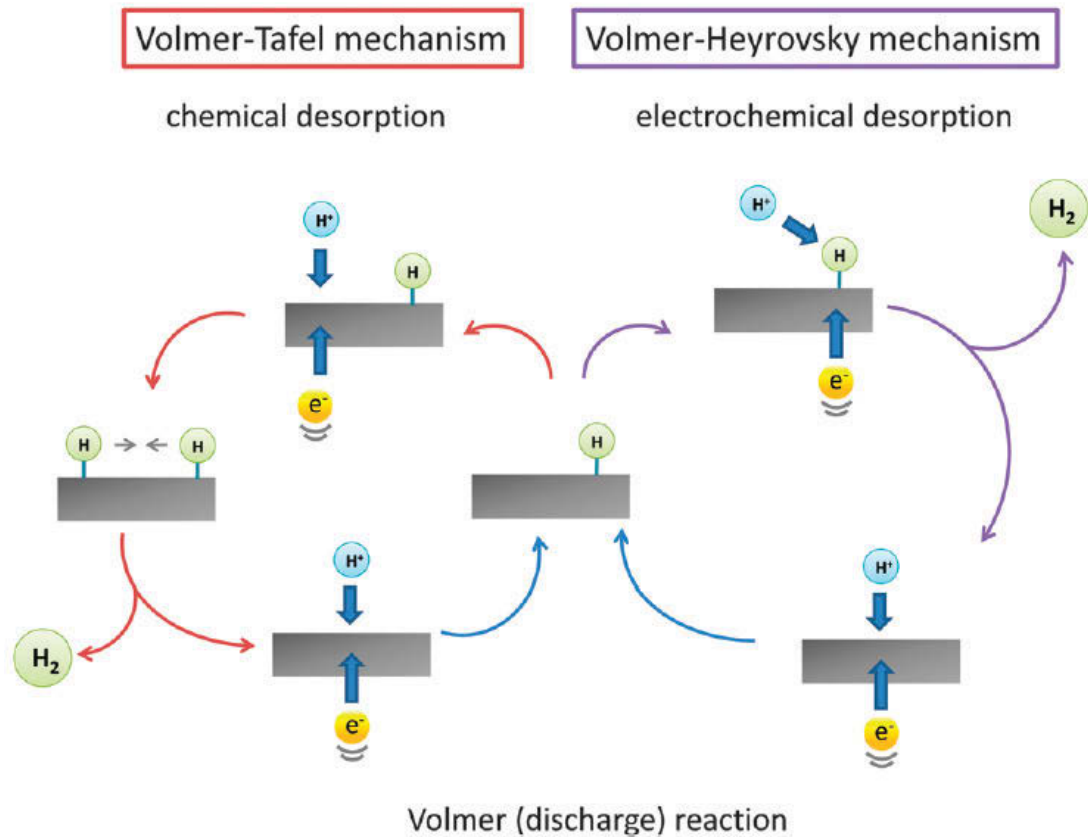


Figure 1-2 The mechanism of hydrogen evolution on the surface of an electrode in acidic solutions.

HER is a multi-step process taking place on the surface of an electrode. Typically, three elementary reactions were involved in the HER process, as shown in Figure 1-2. In first step, an electron and a proton adsorbed on active sites of the catalyst, forming the adsorbed H, namely Volmer or discharge reaction. In acidic electrolytes the proton source is the hydronium cation (H_3O^+) whereas water molecule (H_2O) in alkaline solutions. After that, the adsorbed H tends to form H_2 via the Heyrovsky or Tafel route, and sequentially releases to air. In Heyrovsky route, the generated absorbed H combined with another proton from the solution and then receives an electron to evolve H_2 . In contrast, two absorbed H directly combine on the surface of the electrode to generate H_2 (Tafel route).

As mentioned in 1.2.2.2, Tafel slope are commonly used to discern the predominant HER mechanism.¹⁵ For HER process, if the discharge step is slow, then Tafel slope should be $4.6RT/F$, that is, 116 mV dec^{-1} at 25°C . Generally, the initial discharge step to form adsorbed hydrogen is considered to be fast, while the following hydrogen desorption step is typically rate-limiting. Therefore, if H_2 is evolved via Heyrovsky route, the Tafel slope is $4.6RT/3F$ (38 mV dec^{-1} at 25°C). In contrast, if H_2 is evolved via Tafel route, the Tafel slope should be $2.3RT/2F$ (29 mV dec^{-1} at 25°C).

1.3.2 Catalysts for HER

1	2	3	4	5	6	7	8	9	10	11	12	13	14	15	16	17	18
H	Periodic Table of Elements																He
Li	Be											B	C	N	O	F	Ne
Na	Mg											Al	Si	P	S	Cl	Ar
K	Ca	Sc	Ti	V	Cr	Mn	Fe	Co	Ni	Cu	Zn	Ga	Ge	As	Se	Br	Kr
Rb	Sr	Y	Zr	Nb	Mo	Tc	Ru	Rh	Pd	Ag	Cd	In	Sn	Sb	Te	I	Xe
Cs	Ba	La	Hf	Ta	W	Re	Os	Ir	Pt	Au	Hg	Tl	Pb	Bi	Po	At	Rn




	Pt-containing noble metal HER catalysts
	Metals that are used for constructing noble metal-free HER catalysts
	Nonmetals that are used for constructing noble metal-free HER catalysts

Figure 1-3 Elements that are used for constructing HER electrocatalysts.

Figure 1-3 shows the main elements that are used for constructing HER catalysts. According to their general physical and chemical properties, these elements can be divided into three groups: 1) noble metal, for example platinum; 2) transition metals, such as iron (Fe), cobalt (Co), nickel (Ni), copper (Cu), molybdenum (Mo), and tungsten (W); 3) non-metals, including boron (B), carbon (C), nitrogen (N), phosphorus

(P), sulfur (S), and selenium (Se). Generally, the catalysts used for the hydrogen evolution are all fabricated based on the above elements.

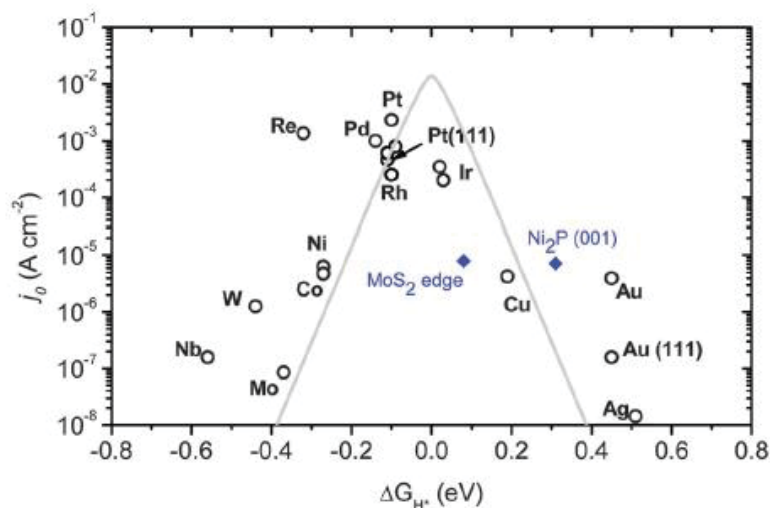


Figure 1-4 A volcano plot of experimentally measured exchange current density as a function of the DFT-calculated Gibbs free energy of adsorbed atomic hydrogen.

HER catalysts exhibit different catalytic efficiency during the hydrogen evolution process, which could be explained by the Gibbs free energy for hydrogen adsorption (ΔG_{H^*}) on a metal.¹⁶⁻¹⁸ Figure 1-4 shows the exchange current densities vs ΔG_{H^*} has a volcano shape. Among all the metals, noble metals, such as Pt, are at the summit of the volcano, possessing close to zero hydrogen absorption energy, thus show the highest catalytic activity towards HER. The other metals distribute to both side of the noble metal. Ni, Mo, W, Co etc. on the left side, bind to hydrogen atoms too strongly, while Cu, Ag, Au etc. on the right side, binds hydrogen too weakly. Therefore, it is desirable to synthesize suitable catalysts for HER.

1.3.2.1 Noble metal (Pt) catalyst

The most well-known efficient electrocatalysts for HER are Pt and Pt-group metals with nearly zero overpotential. The state of art HER catalyst, Pt, has an exchange current density in the order of $10^{-3} \text{ A cm}^{-2}$ and a Tafel slope of 30 mV dec^{-1} . Moreover,

Pt shows outstanding catalytic activity and stability towards HER in both of the acidic and alkaline solution.¹⁹ However, these noble metal catalysts are unfortunately limited by their scarcity and accompanying expensive price. Nowadays, the researchers make efforts to develop of non-noble, abundance metal electrocatalysts for HER. There are enormous efforts being carried out in the exploration of non-noble metal sulfides, phosphides, selenides, nitrides, and carbides in virtue of their excellent electroconductivity and corrosion resistance.

1.3.2.2 Metal sulfides

Metal sulfides, such as MoS₂, WS₂, FeS₂, NiS₂ and CoS₂, show excellent catalytic activity towards HER.

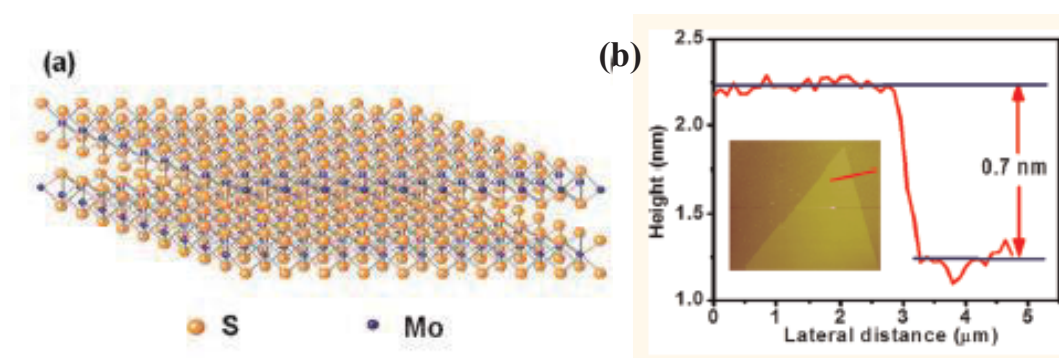


Figure 1-5 Structure and characterization of atomically thin MoS₂. (a) Three-dimensional schematic of the atomic structure of MoS₂. (b) AFM height profile of monolayer MoS₂; inset is the corresponding AFM image.

MoS₂ is a promising catalyst for the electrocatalytic HER. The structural unit of a MoS₂ crystal is composed of a Mo-layer sandwiched between two S-layers through covalent S-Mo-S bonding, and van der Waals forces then hold the repeating units together with a layer-to-layer distance of about 0.62 nm (Figure 1-5).²⁰⁻²² Recently, both density functional theory (DFT) calculations and experimental results have demonstrated that the electrocatalytic HER activity of crystalline MoS₂ catalysts

originates from the unsaturated Mo-S sites along the edges.²²⁻²⁴ Inspired by this fundamental understanding, extensive efforts have been dedicated to increasing the number of exposed active sites on MoS₂ catalysts by engineering the nanostructures, vertically aligned MoS₂ films, defect-rich MoS₂ nanosheets, MoS₂ nanowire, MoS₂ nanorods and so on.^{23, 25-31} For example, Jaramillo et.al reported that vertically oriented core-shell nanowires (NWs) produced by low-temperature sulfidization of MoO₃ nanowires have high activity for HER. A current density of 10 mA cm⁻² requires an overpotential of 250 mV and a low Tafel slope (50-60 mV dec⁻¹) has been achieved.²⁸ Another example is the defect-rich MoS₂ ultrathin nanosheet displays a density of active sites that is 13 times higher than that of bulk MoS₂.²⁵ Current densities as high as 13 mA cm⁻² are obtained at overpotential of 200 mV and a Tafel slope of 50 mV dec⁻¹. Moreover, chemical exfoliation of the bulk MoS₂ by the lithium intercalation method is widely used to obtain single- or few-layered MoS₂. Interestingly, chemically-exfoliated MoS₂ nanosheets exhibit an unexpected phase transformation from the thermodynamically favored 2H phase to the metastable 1T polymorph partially.³² The metallic 1T polymorph is described by a single S-Mo-S layer composed of edge-sharing MoS₆ octahedra, and it is not naturally found in bulk. Jin's group and Chhowalla's group demonstrate that 1T polymorph of MoS₂ had higher metallic character and more competitive HER activities than the 2H phase, ascribing to both the increase of active sites and the improvement of conductivity.^{23, 24}

WS₂ has the similar structure and electronic properties to MoS₂, therefore, researchers pay substantial attention to WS₂ in recent years.³³⁻³⁷ One of the most interesting researches for WS₂ is in which the electrical properties can vary from metallic and semiconducting via adjusting the crystal structure and the number of layers.^{33, 38} As shown in Figure 1-6, Chhowalla's group reported the synthesis of mono-

layered nanosheets of chemically exfoliated WS₂ by the lithium intercalation method in 2013.³⁸ The as-exfoliated nanosheets had a high concentration of the strained metallic 1T phase, which was proven to be an important factor in enhancing the catalytic activity of WS₂ nanosheets. In addition, the strain induced local lattice distortion was also believed to facilitate HER.

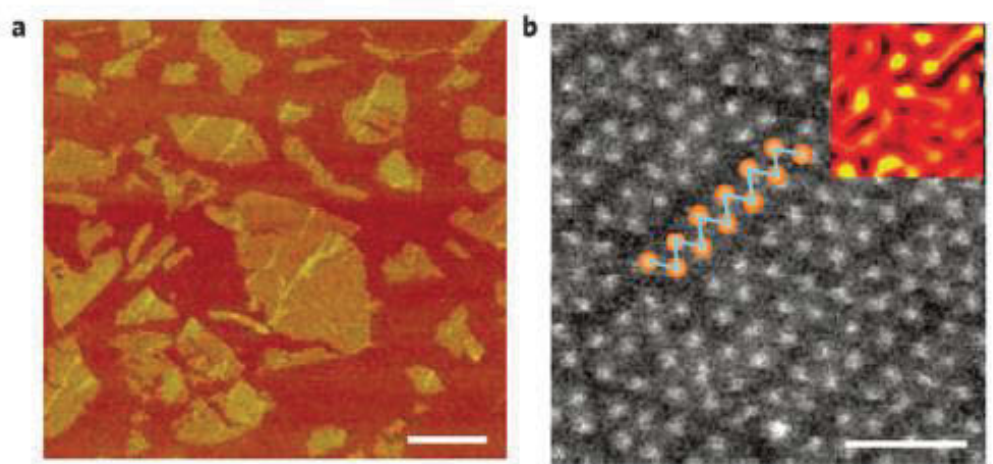


Figure 1-6 Typical AFM image of exfoliated nanosheets of WS₂. Scale bar, 500 nm. (b) High-resolution STEM images of an as-exfoliated WS₂ monolayer showing regions exhibiting the 1T superlattice. Scale bar, 1 nm.

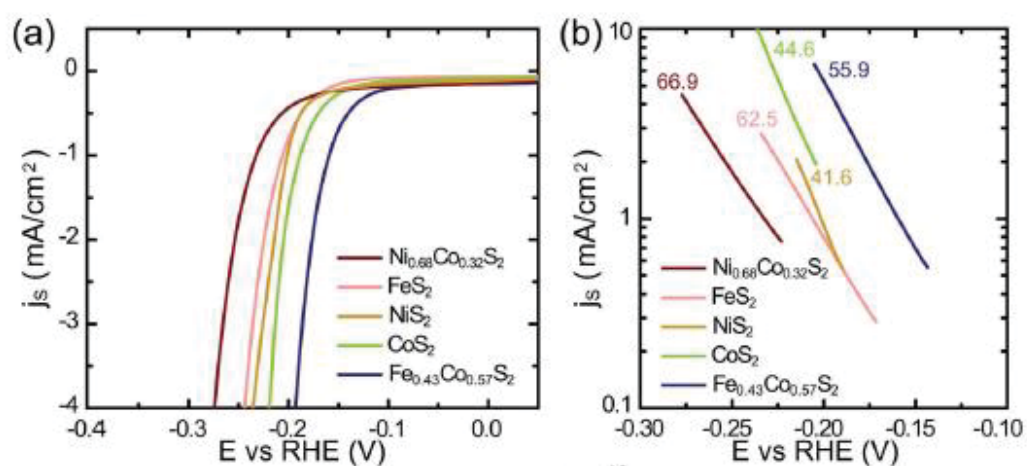


Figure 1-7 Electrochemical measurements of transition metal dichalcogenide films grown on glassy carbon electrodes. (a) Polarization curves of transition metal disulfides, (b) the corresponding Tafel plots.

Within the family of metal sulfide, first-row transition metal dichalcogenides, FeS₂, CoS₂ and NiS₂ are common and well-studied HER catalysts.³⁹ FeS₂, CoS₂ and NiS₂ share the pyrite or related marcasite structure, in which the metal atoms are octahedrally bonded to adjacent sulfur atoms. As a common structural feature, metal cations on the low-index surfaces of these dichalcogenides tend to exhibit a reduced coordination number.⁴⁰ Previous research demonstrated that both FeS₂ and NiS₂ had a comparable catalytic activity towards HER, and FeS₂ had a higher stability than NiS₂ in acidic solution.^{39, 41} Yi Cui's group (Figure 1-7) developed a facile process to grow polycrystalline dichalcogenide films on diverse substrates, such as FeS₂, CoS₂ and NiS₂, and they all showed excellent activity towards HER, achieving a cathodic current density of 4 mA cm⁻² that ranges from 190 mV to 270 mV.⁴¹ In their study, the best activity among the metal dichalcogenides is achieved using using CoSe₂ and Fe_{0.43}Co_{0.57}S₂ as catalysts, and their superior catalytic activity is likely linked with their unique electronic structure.

1.3.2.3 Metal carbide

Metal carbides have been under investigation for decades in the fields of catalysis in view of their high analogy to platinum group metals with their d-band electronic structures and catalytic properties, possessing high electrical conductivity and optimal hydrogen-adsorption properties.⁴² Among the metal carbide, Mo₂C and WC, had long been expected to be effective non-Pt electrocatalysts for HER.⁴³⁻⁴⁹ Additionally, they have been used as stable supports for precious metals over different ranges of pH. In 2012, Hu's group made the first observation of the commercial Mo₂C showing high activity towards HER in both acidic and alkaline solution.⁵⁰ Since then, fine structural optimization of molybdenum carbide catalysts at the nanoscale has been actively pursued, and recent efforts have begun to bear more fruits. Liao et al. developed a

highly active and stable electrochemical catalyst of nanoporous molybdenum carbide nanowires (np-Mo₂C NWs) for HER.⁴³ The np-Mo₂C NWs were synthesized simply by pyrolysis of a MoO_x/amine hybrid precursor with sub-nanosized periodic structure under an inert atmosphere. The Mo₂C nanowires were composed of nanocrystallites of about 10-15 nm in size, and had a large surface area of 63.9 m² g⁻¹. The excellent catalytic activity of this nanowire material was attributed to its large surface areas, nanosized crystallites and porous structure. Asefa group synthesized a novel Mo-based composite (Mo₂C@NC) by one-step facile thermal treatment of ammonium molybdate and DCDA.⁵¹ Mo₂C@NC is composed of ultrasmall molybdenum carbide (Mo₂C) nanoparticles embedded within nitrogen rich carbon (NC) nanolayers. The Mo₂C@NC hybrid nanoelectrocatalyst shows remarkable catalytic activity, has great durability, and gives about 100% Faradaic yield toward the hydrogen-evolution reaction (HER) over a wide pH range (pH 0-14). Combined with the DFT results, Mo₂C@NC gave a small ΔG (≈ 0 eV) because of the doped N atoms, creating super active non-metallic catalytic sites.

WC was the first found to have Pt-like catalytic activity by R. B. Levy and M. Boudart in 1973.⁴² WC exhibits high corrosion resistance and superior electronic conductivity, which makes it a suitable candidate to replace Pt group metals. There are several methods to prepare WC, including heating the fully mixed WO₃ (or W metal) and carbon powder at a high temperature (1400-1600 °C), ball milling, microwave heating, and plasma processing technique.⁵²⁻⁵⁶ All of these methods could obtain nanoscale WC. Burstein and co-workers compared the HER activity of WC particles prepared by microwave carburisation and by furnace heating.⁵⁷ The microwave synthesis produced particles with a finer grain size which were better catalysts. As shown in Figure 1-8, Xia Guo group WC fabricated nanocrystals grown on vertically aligned carbon nanotubes with a hot filament chemical vapor deposition (HF-CVD) method through the directly

reaction of tungsten metal with carbon source.⁵⁸ WC-CNTs material exhibited an excellent catalytic activity for HER with the overpotential for 10 mA cm⁻² of 145 mV, attributing to the high crystallinity, small size, and uniform distribution of WC particles on the carbon support.

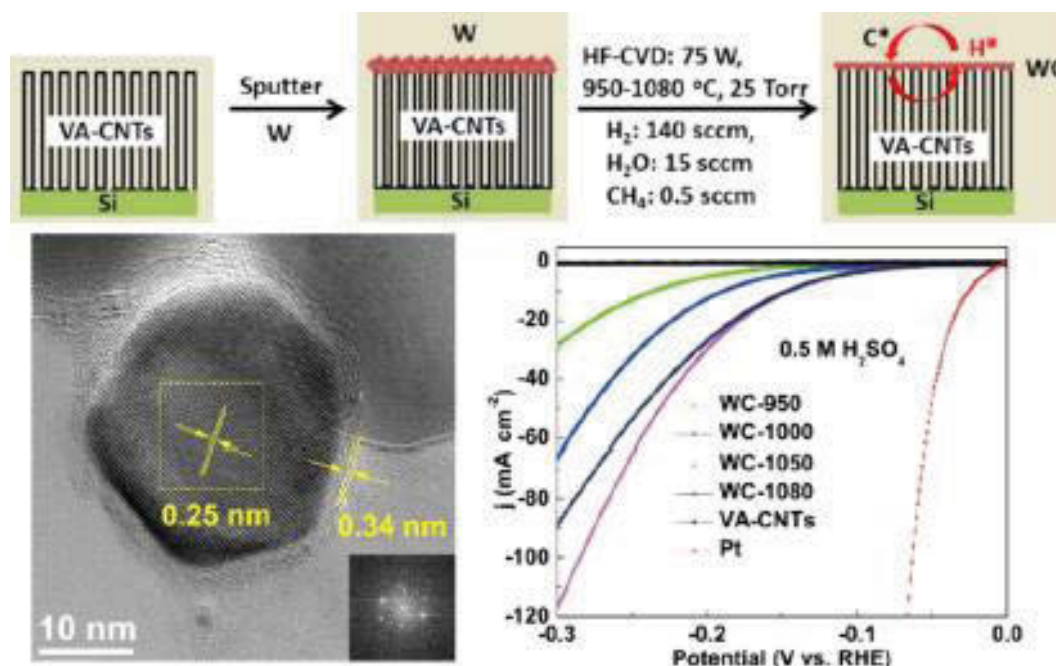


Figure 1-8 (a) Scheme of the process of WCNCs grown on the tips of VA-CNTs. (b) TEM images of an individual NCs, (c) HER voltammograms of WC-CNTs synthesized at different temperatures in 0.5 M H₂SO₄ (pH = 0).

1.3.2.4 Metal nitride

Transition-metal nitrides, referred as interstitial alloys, have attracted much attention in electrocatalysis due to their unique physical and chemical properties, including their superior corrosion stability, low electrical resistance and high stability.^{59, 60} The introduction of nitrogen atoms modifies the nature of the d-band of the parent metals, which makes the electronic structure of transition-metal nitrides similar to group VIII noble metals.⁶¹ The catalytic and electronic properties of transition-metal nitrides are highly dependent on their morphology and surface structure.⁶²⁻⁶⁵ Xie et.al prepared atomically-thin MoN nanosheets by liquid exfoliation of the bulk material in N-methyl-

2-pyrrolidone (NMP).⁶³ The metallic behavior of the novel catalyst guarantees fast electron transport during the electrocatalytic process, thus enriching the electrically connected active sites. The atomically-thin MoN nanosheets exhibited a remarkably low onset overpotential of 100 mV and the cathodic current density reaches 38.5 mA cm⁻² at the overpotential of 300 mV. Even though it has been proven that MoN exhibits HER activity in acidic solution, it is far lower than those of ternary metal nitride, such as Ni-Mo-N or Co-Mo-N, by introducing in Ni or Co into Mo-N. Hong Jin Fan group synthesized 3D porous hierarchical nickel-molybdenum nitrides by RF Plasma treatment at a relatively low reaction temperature (450 °C) and shorter duration (15 min). The obtained bimetallic nitrides exhibit outstanding HER performance with a small overpotential of around 109 mV to acquire the current density of 10 mA cm⁻² with an outstanding durability at different current densities.⁶⁶

1.3.2.5 Metal phosphide

Transition metal phosphides have been widely explored as hydrodesulfurization (HDS) catalysts due to their high catalytic ability, and can also be considered as HER catalysts.⁶⁷ The previous theoretical and experimental studies have demonstrated that the catalytic activity of the transition metal phosphide for HER arises from metal sites located on the surface.⁶⁸⁻⁷¹ Transition metal phosphide can be viewed as doping P atoms into crystal lattices of transition metal. Until now, only six different transition metals (Fe, Co, Ni, Cu, Mo and W) are found to form TMPs as efficient HER catalysts. Metal phosphides tend to form a more isotropic crystal structure instead of a layered structure that is observed in metal sulfides.⁷² There are a few synthetic strategies for fabricating the transition metal phosphide, including solution-phase reaction, gas-solid reaction, cathodic electrodeposition, hydrothermal reaction.⁷³⁻⁷⁷ Popczun et al. reported Ni₂P and CoP nanoparticles (10-20 nm) for the first time as highly efficient HER catalysts,

showing small Tafel slopes of 46 and 50 mV dec^{-1} , respectively.⁷⁸ Xin Wang group prepared molybdenum phosphide (MoP) as a highly efficient catalyst for HER. MoP is synthesized through a facile method by sintering of molybdenum and phosphorus precursors assisted by citric acid.⁶⁸ MoP shows a low onset potential for HER at around 50 mV vs. RHE and the current density reaches 30 mA cm^{-2} at a potential of 0.18 V vs. RHE in acid solution.

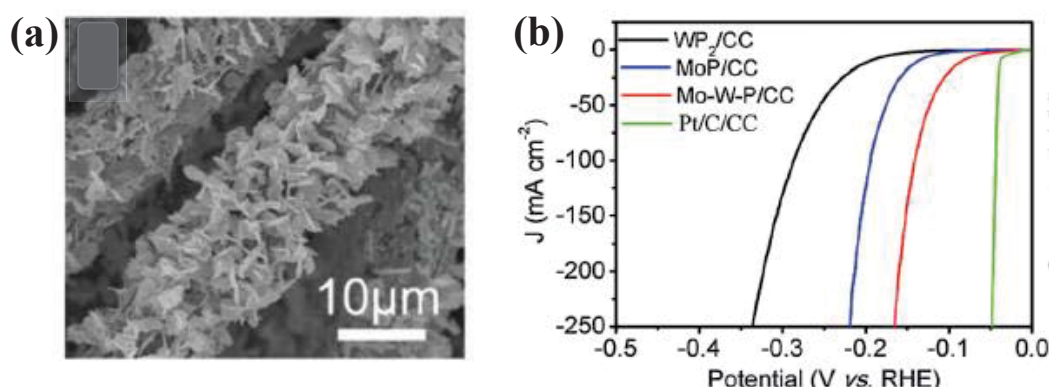


Figure 1-9 (a) SEM image of Mo-W-P/CC, (b) Polarization data for Mo-W-P/CC in 0.50 M H_2SO_4 electrolyte, along with plots of MoP/CC, WP_2 /CC and Pt/C/CC for comparison.

Metal transition phosphides have similar properties to ordinary metallic compounds, such as carbides and nitrides. The incorporation of foreign metal atoms with similar electron configuration into the crystal lattice can dramatically enhance the electrocatalytic activities of transition metal phosphide.⁷⁹⁻⁸² Dai-Bin Kuang group reported a novel excellent porous molybdenum tungsten phosphide (Mo-W-P) hybrid nanosheet catalyst for hydrogen evolution (Figure 1-9).⁸³ The obtained Mo-W-P hybrid nanosheets exhibit impressively high catalytic activity with a low overpotential of 138 mV to reach 100 mA cm^{-2} and a small Tafel slope of 52 mV dec^{-1} in 0.5 M H_2SO_4 , which are significantly higher than those of single MoP nanosheets and WP_2 nanorods.

1.3.2.6 Heteroatom-doped carbon materials

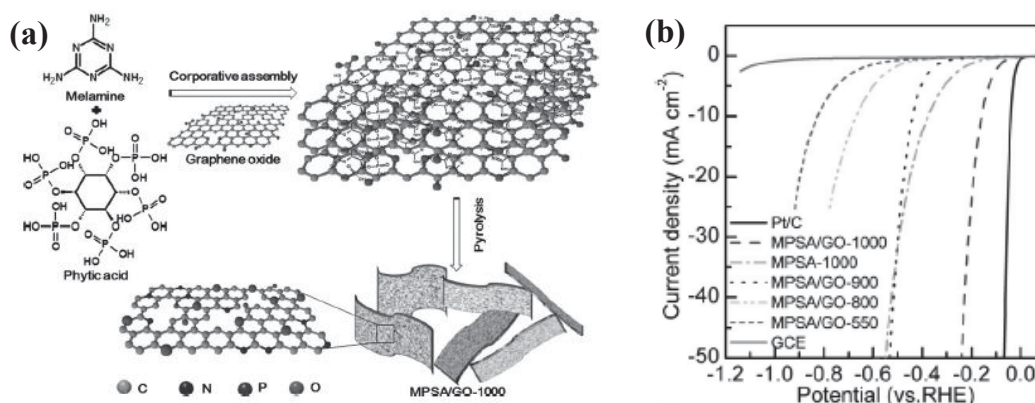


Figure 1-10 (a) Preparation process of MPSA/GO-1000 via cooperative assembly and pyrolysis, (b) Polarization curves of various samples for hydrogen evolution in 0.5 M H₂SO₄.

Metal-free catalysts, such as graphene, carbon nanotube, are often as supports for these poorly-conducting catalysts to provide good electron transfer, leading to synergic effects to enhance the HER performance. Generally, carbons could provide either favorable structural supports (e.g., large surface area), cooperative electrical effects (e.g., enhanced electron transfer and transport) or strong tolerance to acid/alkaline environments. Therefore, it is desirable to understand the intrinsic roles of carbons in these carbon-supported metal-based HER catalysts and their carbon-based metal-free counterparts. The pure carbon materials are HER inert intrinsically, but the heteroatom-doped carbons (N, B, P, S, Co, Ni, Fe) could turn the inert carbon into active sites for HER. The introduction of heteroatom might lead to the creation of defect sites that can modulate the physical and chemical properties of carbon materials.⁸⁴⁻⁹⁰ The fundamental difference between heteroatom-doped carbon catalysts and conventional metal-based catalysts (metal sulfide, metal carbide, metal nitride, metal phosphide) is that the active sites of the carbons do not involve metal ions.^{87, 89} Even though the metal heteroatoms, such as Co, Ni, Fe, the metals are well encapsulated by the carbon, thus the active sites

come from carbon materials. Liming Dai group developed a simple template-free approach to fabricate 3D porous carbon networks co-doped with nitrogen and phosphorus by pyrolysis of a supermolecular aggregate of self-assembled melamine, phytic acid, and graphene oxide.⁹¹ The generated catalysts exhibited high catalytic activity towards HER with a low overpotential of 0.06 V and achieving the current density of 30 mA cm⁻² at the overpotential around 210 mV. As shown in Figure 1-10, Qiao's group explore the effects of various dopants (N, B, O, S, P, F) in graphene toward HER activity by using DFT calculations and experimental method.⁸⁵ The results proved that N and O acted as electron acceptors for the adjacent C, while F, S, B, and P served as electron donors and N and P co-doped graphene showed the most favorable H^{*} adsorption-desorption property among several doped graphene models, indicating the best HER catalytic activity. Moreover, the metal encapsulated catalysts also displayed outstanding HER catalytic activity. Tewodros Asefa group reported the synthesis of cobalt-embedded nitrogen-rich CNTs (Co-NRCNTs) that can serve as highly active electrocatalyst for HER under acidic, neutral or basic media alike.⁸⁷ Junhong Chen et. al. prepared a novel hybrid electrocatalyst consisting of nitrogen-doped graphene/cobaltembedded porous carbon polyhedron (N/Co-doped PCP//NRGO) through simple pyrolysis of graphene oxide-supported cobalt-based zeolitic imidazolate-frameworks.⁹² The obtained hybrid exhibited superior performance towards HER, offering a low onset overpotential of 58 mV and a stable current density of 10 mA cm⁻² at 229 mV in acid media.

1.4 Electrochemical oxygen evolution reaction

1.4.1 Mechanism of electrochemical oxygen evolution reaction

Table 1-1 Overall reaction pathway for OER in acidic and alkaline solutions

Overall reaction (condition)	Reaction pathway
$2\text{H}_2\text{O} \rightarrow \text{O}_2 + 4\text{H}^+ + 4\text{e}^-$ (Acidic solution)	$\ast + \text{H}_2\text{O} \rightarrow \ast\text{OH} + \text{H}^+ + \text{e}^-$ $\ast\text{OH} \rightarrow \ast\text{O} + \text{H}^+ + \text{e}^-$ $\ast\text{O} + \text{H}_2\text{O} \rightarrow \text{OOH}\ast + \text{H}^+ + \text{e}^-$ $\ast\text{OOH} \rightarrow \ast\text{O}_2 + \text{H}^+ + \text{e}^-$ $\ast\text{O}_2 \rightarrow \ast + \text{O}_2$
$4\text{OH}^- \rightarrow \text{O}_2 + 2\text{H}_2\text{O} + 4\text{e}^-$ (Alkaline solution)	$\ast + \text{OH}^- \rightarrow \ast\text{OH} + \text{e}^-$ $\ast\text{OH} + \text{OH}^- \rightarrow \text{H}_2\text{O} + \ast\text{O} + \text{e}^-$ $\ast\text{O} + \text{OH}^- \rightarrow \ast\text{OOH} + \text{e}^-$ $\ast\text{OOH} + \text{OH}^- \rightarrow \ast\text{O}_2 + \text{e}^-$ $\ast\text{O}_2 \rightarrow \ast + \text{O}_2$

As we aforementioned, the water splitting reaction can be classified into two half reactions: HER and OER, both of which are vital for the overall efficiency of water splitting. We have discussed HER catalysts in part of 1.3, and in this section, we will introduce the OER catalysts. Compared to HER, the OER is inherently more complex and has sluggish oxygen evolution kinetics, since it involves a four-electron transfer process with the removal of four protons from water molecules to generate one oxygen molecule, thus leading to a large overpotential to facilitate the reaction efficiently.^{93, 94} In acid solution, water is oxidized into oxygen and hydrogen ions, whereas in neutral and alkaline solutions, the hydroxyl ion is oxidized into water and oxygen. The mechanism of OER is very sensitive to the structure of electrode surface; different materials or one material with different facets can exhibit various reaction mechanisms. Therefore, appropriate catalysts are in need of settling OER kinetically slow process, thus enhancing the overall water splitting process.

1.4.2 Catalysts for OER

1.4.2.1 Precious metals based catalysts

To date, the precious metals and their oxides, such as Ru, Ir, RuO₂, and IrO₂, are recognized to be the best OER electrocatalysts in aqueous acidic and alkaline solutions

because of their lowest overpotential for the OER at practical current densities.^{11, 12} Additionally, Ru–Ir alloys and oxides have been studied as OER electrocatalysts with enhanced electrochemical activity and thermodynamic stability.⁹⁵ However, the scarcity and high cost of the precious metals are the major barriers for the global-scale applications. For this reason, effective low-cost electrocatalysts are urgently needed to expedite the OER reaction, reduce the overpotential, and thus enhance the energy conversion efficiency.

1.4.2.2 Transition metals oxides

Generally, transition metal oxides, such as Ni, Co, Mn and Fe, are popular OER catalysts in alkaline electrolytes owing to their environmental friendliness, abundant reserves, thermal stability, and low cost. Hence, synthesis and fine structural optimization of transition metal oxide-based catalysts and a deep understanding of their structure-property relationships in the OER have been actively pursued.

a Atomic-scale phase transformation for synthesis of γ -CoOOH nanosheets

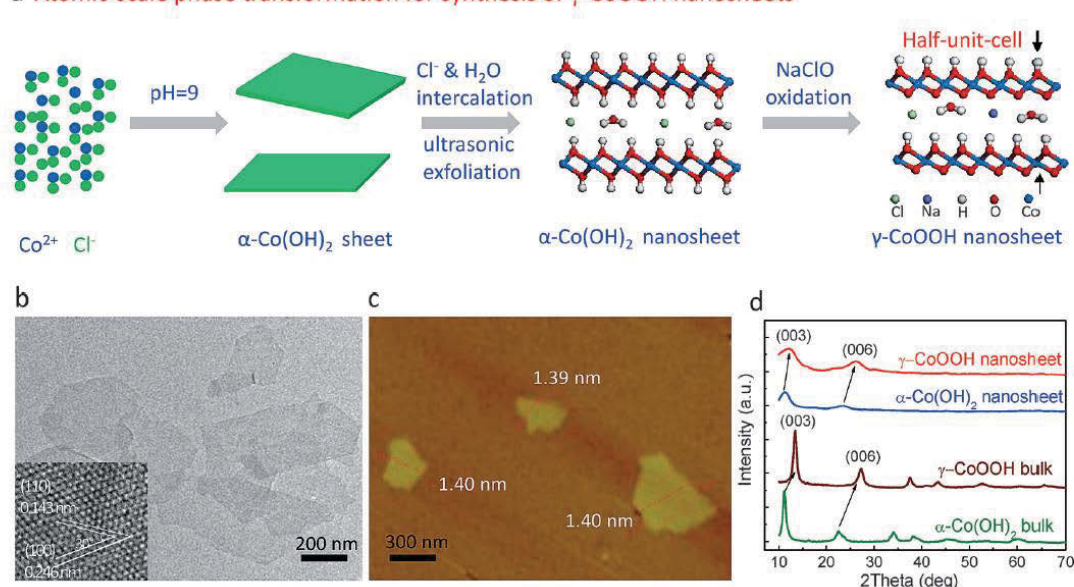


Figure 1-11 (a) Synthetic route for the γ -CoOOH nanosheets. (b) TEM image and (c) AFM image for the γ -CoOOH nanosheets. The inset in (b) shows the HRTEM image for

the γ -CoOOH nanosheets. (d) XRD pattern for the γ -CoOOH nanosheets. The patterns of bulk γ -CoOOH and bulk and nanosheet α -Co(OH)₂ are also displayed for comparison.

Co₃O₄ is a typical electrocatalyst with many applications, which has been used as a catalyst for electrochemical water splitting since the 1970s.⁹⁶ Almost all kinds of cobalt oxide (Co₃O₄, CoO, CoOOH), regardless of their preparation methods and the nature of the supports, give approximately the similar Tafel slope of around 60 mV dec⁻¹, illustrating the catalytic mechanism is similar for the cobalt oxides.⁹⁶⁻¹⁰⁰ Increasing the surface area and engineering the surface active sites are the important strategies to lower the overpotential and further enhance the catalytic activity. Many efforts have been devoted to synthesizing nanostructures or mesoporous frameworks of cobalt oxide. As shown in Figure 1-11, Gengfeng Zheng group developed a facile solution reduction method to synthesize the mesoporous Co₃O₄ nanowires with the treatment of NaBH₄.¹⁰¹ Compared to the pristine Co₃O₄ NWs, the reduced mesoporous Co₃O₄ NWs show a seven-fold enhancement of water oxidation catalytic activity with a lower onset potential of 1.52 V vs. RHE and a large current density of 13.1 mA cm⁻² at 1.65 V vs. RHE. The atomically thin cobalt oxyhydroxide (*r*-CoOOH) nanosheet as an efficient electrocatalyst for water oxidation has been reported by Shiqiang Wei.⁹⁹ They design a two-step chemistry route of “atomic-scale phase transformation process” to synthesize the 1.4 nm *r*-CoOOH nanosheets, including the liquid exfoliation and NaClO oxidation process. The obtained ultrathin *r*-CoOOH nanosheets can effectively oxidize water with an extremely large mass activity of 66.6 A g⁻¹ at a quite small overpotential of 300 mV, 20 times higher than that of γ -CoOOH bulk and 2.4 times higher than that of the benchmarking IrO₂ electrocatalyst. In addition, enhanced performance can be obtained by the incorporation of additional metal ions (including Fe, Ni, Cu, Li and Zn) into cobalt oxide. For example, Yu-Zhi Su group developed ZnCo₂O₄ quantum dots on

nitrogen doped carbon nanotubes ($\text{ZnCo}_2\text{O}_4/\text{N-CNT}$) as catalyst towards OER.¹⁰² The replacement of Co^{2+} by Zn^{2+} at the tetrahedral sites provided an enhanced utilization rate for the highly active Co^{3+} species that occupy the octahedral sites, thus $\text{ZnCo}_2\text{O}_4/\text{N-CNT}$ delivered high catalytic activity and outstanding stability during the OER test compare to the Co_3O_4 . Also, Maiyalagan et al. reported that lithiated spinel-type LiCoO_2 , prepared at 400 °C, exhibited superior OER performance over Co_3O_4 .¹⁰³

Nickel oxides were discovered to exhibit electro-catalytic activity towards OER in alkaline solution in the early last century. Many researchers have paid much attention on the fabrication of nanostructure of NiO . For example, Xile Hu group prepared small nanoparticles of nickel as catalyst for OER in alkaline solutions.¹⁰² These nanoparticles showed excellent catalytic activity, giving a current density of 10 mA cm^{-2} at overpotential of 330 mV for NiO_x .

One of the most interesting discoveries was that as nickel was always found in combination with iron (Fe) on earth and Fe impurities in the nickel hydroxide (Ni(OH)_2) electrodes can cause detrimental effects on Ni-based alkaline batteries by greatly lowering the OER overpotential.¹⁰⁴⁻¹⁰⁷ The discovery had inspired many scientists to study the phenomenon, optimizing Fe content and synthesizing various NiFe mixed compounds for obtaining better OER electrocatalysts. The first investigation of the effect of Fe on nickel oxide electrodes towards OER was found by Corrigan.¹⁰⁷ By adjusting Fe content, a composite NiFe hydrous oxide with >10% Fe showed intriguing activities toward OER electrocatalysis with ~200-250 mV overpotential at a current density of 10 mA cm^{-2} and a low Tafel slope of 20-25 mV decade^{-1} . The NiFe alloy, NiFe oxide and NiFe layered double hydroxide have been fabricated since then as high efficient electrocatalysts towards OER.¹⁰⁸⁻¹¹⁷ For example, Louie et al. studied NiFe thin films obtained by electrodeposition technique, by optimizing Ni/Fe ratio and the NiFe catalyst

containing 40% Fe exhibited the highest activity among the catalyst.¹¹⁷ Qiang Zhang et.al designed a novel composite based on NiFe LDHs and graphene, which was synthesized by means of defect-anchored nucleation and spatially confined growth of nanometer-sized NiFe LDHs into a three-dimensional graphene framework (Figure 1-12).¹¹⁸ The obtained NiFe LDH/graphene hybrid shows high OER performance, with a remarkably low Tafel slope (45 mV dec⁻¹), a substantially decreased overpotential (337 mV required for 10 mA cm⁻²), and enhanced durability.

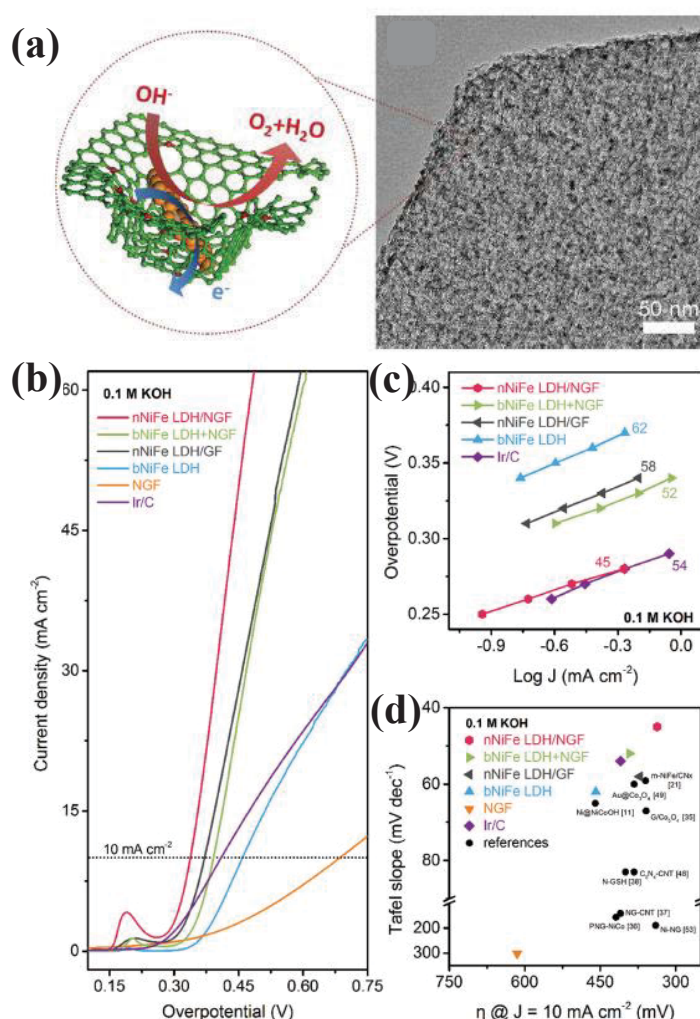


Figure 1-12 (a) Schematic of the spatially confined hybrids and crosssectional TEM image of a sheet of nNiFe LDH/NGF electrocatalyst. (b, c) polarization curves and Tafel slope of nNiFe LDH/NGF and other samples for comparison. (d) Figures of merit with respect to both kinetics (Tafel slope) and activity (the overpotential required to achieve 10 mA cm⁻²), with references all measured in 0.1 M KOH electrolyte.

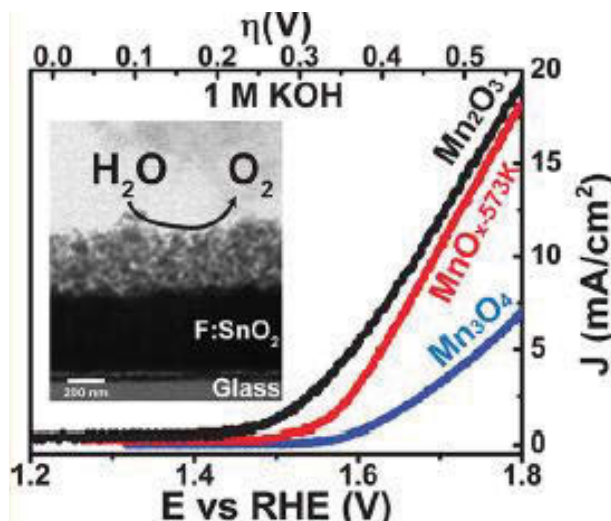


Figure 1-13 polarization curves of Mn-based catalysts towards OER.

Oxygenic photosystem II (PS-II) with $\text{Mn}_4\text{O}_4\text{Ca}$ as the core of its catalytic center surrounded by ample proteins inspired the investigation of manganese oxides (Mn_2O_3 and rutile MnO_2) as the electrocatalysts towards OER.¹¹⁹⁻¹²² Manganese oxides have more than 20 polymorphs, which make them more complicated than simple oxides. The catalytic activities of manganese oxides rely heavily on their chemical compositions and crystallographic structures, as well as morphologies and pore structures.¹²³⁻¹²⁸ Alejandra Ramírez evaluated the electrochemical catalytic performance of MnO_x , Mn_2O_3 and Mn_3O_4 electrodeposited films towards OER.¹²⁹ Compared to Mn_3O_4 , crystalline α - Mn_2O_3 and MnO_x -573 K are the most efficient catalyst for water oxidation in the manganese-oxygen system (Figure 1-13). Their results show that structural changes, oxidation of Mn II and Mn III toward Mn IV under oxygen evolving conditions, played an important role in the catalytic activity of the manganese oxides.

1.4.2.3 Perovskite oxides

Perovskites with structure of ABO_3 is another class of OER catalysts that has been intensively investigated.¹³⁰⁻¹³⁵ Compared to other type of oxides, a major advantage of perovskite oxides is the flexibility of tuning their physical-chemical and catalytic

properties of the ABO_3 formulation (Figure 1-14 (a)), where A sites are rare earth or alkali metal ions and B sites are transition metal ions. The physico-chemical and catalytic properties of perovskites oxide can be modified by substituting ions of the same or different oxidation states in the A and/or B sites.^{136, 137}

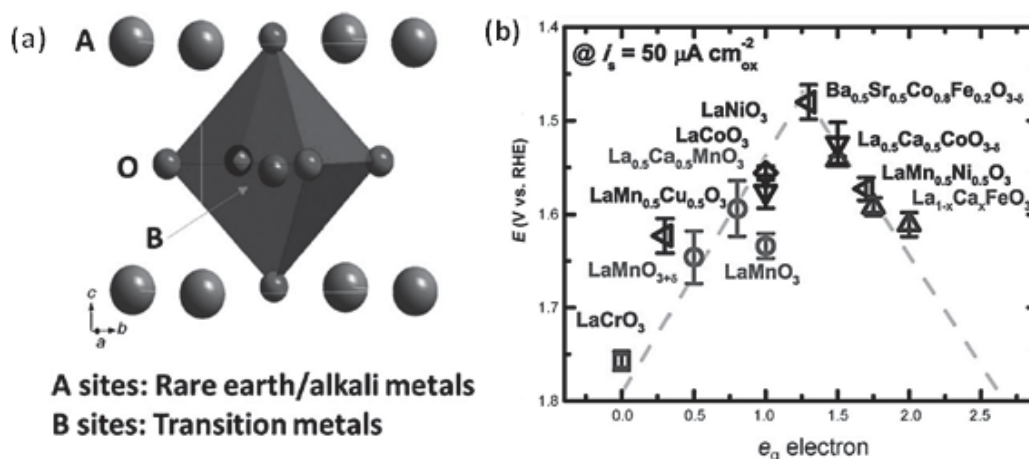


Figure 1-14 (a) A unit cell in perovskite showing relative positions of different ions, (b) The relation between the OER catalytic activity, defined by the overpotentials at $50 \text{ mA cm}^{-2}_{\text{ox}}$ of the OER current, and the occupancy of the e_g -symmetry electron of the transition metal (B in ABO_3).

There are varieties of synthesis routes for perovskites oxide, including solid-state route, co-precipitation method, reverse micelle synthesis, sol-gel method, hydrothermal process.¹³⁸⁻¹⁴⁴ Currently, the most popular perovskites oxides are $LaCoO_3$, $LaNiO_3$, $SrCoO_3$ and $LaMnO_3$. Due to their high versatility in the electronic structure and choice of metal cations, advanced perovskites have been progressively developed and modified to yield a typical structure in order to achieve desired properties. The substitution of the A-site and B-site metal cations and generation of oxygen deficiency/vacancy have large characteristic effects on their OER performance.^{130, 136, 137, 145} Suntivich et al. proposed that the e_g filling of surface transition metal cations can significantly influence the binding between the OER intermediates and perovskites surface, which results in different OER activity.¹⁴⁶ The highest OER activity among all oxides studied as

predicted by the e_g activity descriptor is $\text{Ba}_{0.5}\text{Sr}_{0.5}\text{Co}_{0.8}\text{Fe}_{0.2}\text{O}_{3-x}$ (BSCF), and as shown in Figure 1-14 (b) the intrinsic OER activities of perovskites exhibit a volcano-shaped dependence on the occupancy of the 3d electron with an e_g symmetry of surface transition metal cations in an oxide.

1.4.2.4 Metal complexes

In recent years, molecular catalysts for water oxidation, mainly composed of transition-metal complexes, have gained considerable attention.¹⁴⁷⁻¹⁴⁹ Metal complexes supported with organic ligands might act as homogeneous catalysts or serve only as precursors of more active heterogeneous catalysts towards OER. Molecular metal complexes as catalysts are either homogeneous or heterogeneous during water oxidation depending on the sort of metals, pH, oxidants, and supporting ligands.¹⁵⁰⁻¹⁵⁶ Therefore, it is very important to carefully characterize the active species before, during, and after water oxidation catalysis. There are some efficient OER catalysts based on earth-abundant metals, such as cobalt, nickel, iron, copper and manganese, and all of them could be used as homogeneous or heterogeneous catalysts towards OER.

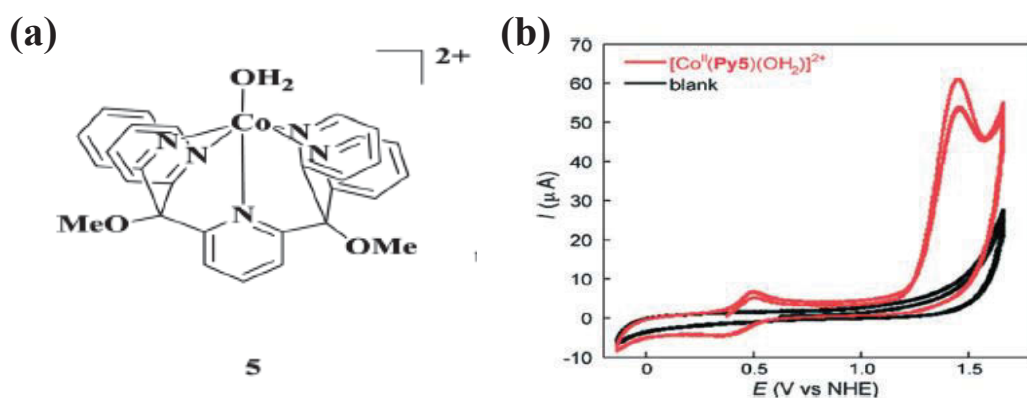


Figure 1-15 (a) Molecular cobalt complexes, (b) CV of 5 recorded in phosphate buffer solution (0.1 mM, pH 9.2) with a scan rate of 50 mV s⁻¹ (red), and a blank scan without 5 under the same conditions (black).

A mono-cobalt aqua complex, **5** (Figure 1-15), with an oxidative stable pentadentate Py5 ligand, $[\text{Co}(\text{Py}_5)\text{OH}_2](\text{ClO}_4)_2$ [$\text{Py}_5 = 2,6\text{-(bis(bis-2-pyridyl)methoxy-methane)-pyridine}$], acted as an efficient homogeneous OER catalysts in alkaline media.¹⁵⁷ The water oxidation catalysis started at the potential $>+1.2$ V vs. RHE, which is attributed to the Co(III)/Co(II) proton-coupled electron transfer step within the pH range of 7.6-10.3 .

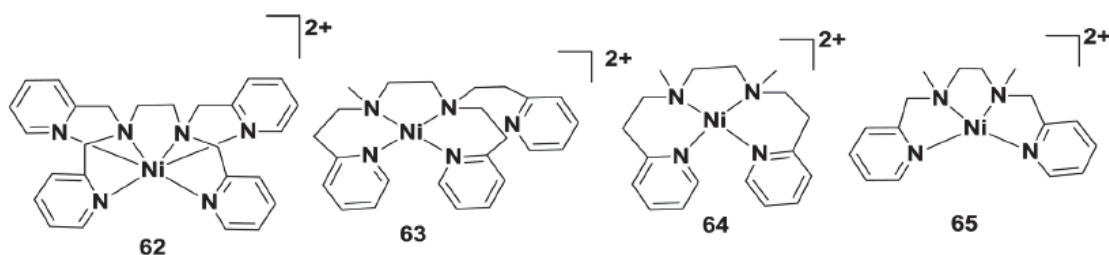


Figure 1-16 Structures of nickel(II) complexes used as precatalysts.

Tai-Chu Lau and coworkers developed a series of NiII complexes **62-65** as shown in Figure 16.¹⁵⁸ These NiII complexes bear multidentate N-donor ligands that serve as precatalysts and convert into Ni oxide nanoparticles during the electrochemical test. These nanoparticles serve as the true catalyst towards OER. Complexes **63-65** yielded a greater amount of O_2 in borate buffer at pH 8.0, with turnover numbers (TONs) and turnover frequencies (TOFs) that ranged from 31-54 and $0.19\text{-}0.42\text{ s}^{-1}$, respectively.

1.4.2.5 Heteroatom-doped carbon materials

Nowadays, the electrocatalysts towards OER so far are mainly based on transition-metal based materials, or the transition-metal based materials supported by carbon materials to facilitate fast electron transfer. Although there are some reports of metal-free catalysts towards HER, however, only a few reports discussed direct use of carbon materials as catalysts towards OER. Very recently, N(5)-ethyl-flavinium ions were found to work as organic metal-free catalysts towards OER N(5)-ethyl-flavinium ions

were found.¹⁵⁹ Even though the catalytic activity is lower than those of existing transition metal-based catalysts (0.73 V vs. RHE, pH 2), it has opened up a new strategy for designing OER catalysts.

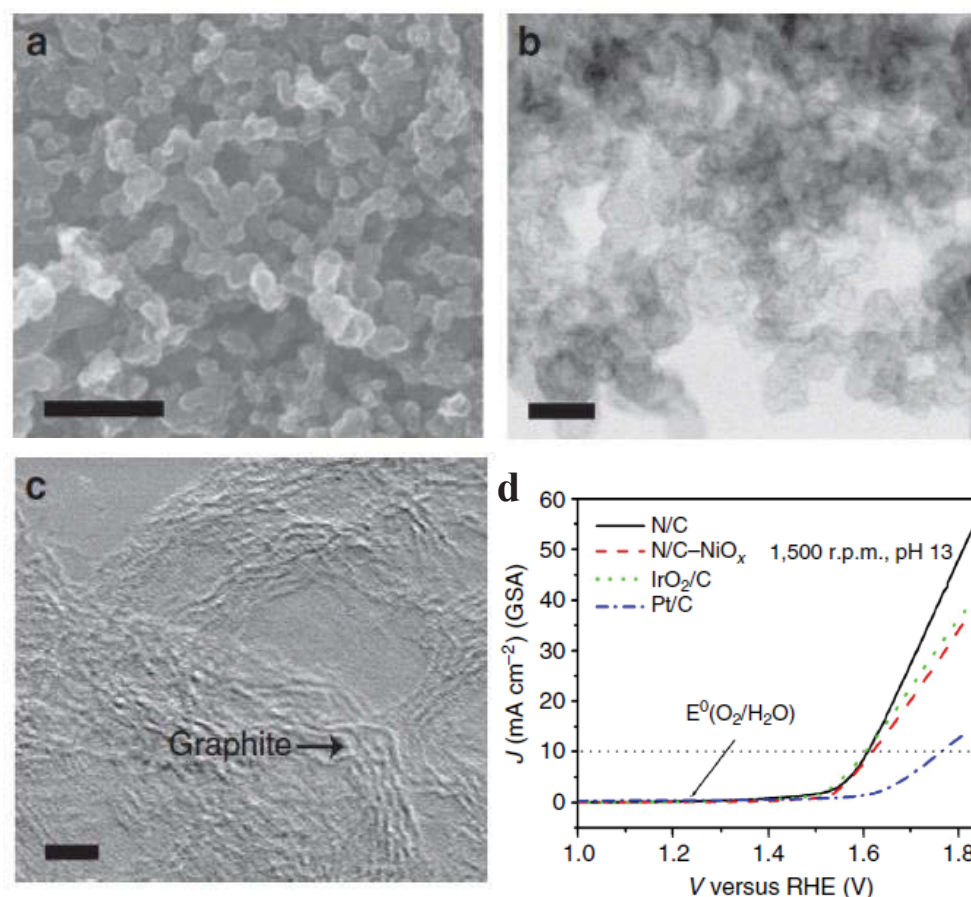


Figure 1-17 (a-c) SEM and TEM images of the N/C, (d) Oxygen evolution activities of the N/C, N/C-NiO_x, IrO₂/C (20 wt%) and Pt/C (20 wt%) electrodes with KOH electrolyte (pH 13).

Nowadays, metal-free carbonaceous materials doped with heteroatoms (e.g., N, P, B, S, or I) have been the focus of oxygen electrocatalysis. The electronic and catalytic property modulation are mostly achieved by extrinsic doping of heteroatoms.¹⁶⁰⁻¹⁶⁴ As shown in Figure 1-17 Zhao *et. al* report that the nitrogen-doped carbon materials act as the efficient OER electrocatalysts.¹⁶⁵ The catalyst achieved a current density of 10 mA cm⁻² at the overpotential of 0.38 V in alkaline solution, values that are comparable to those of iridium and cobalt oxide catalysts. Shizhang Qiao's group design the metal-free

OER catalyst composed of graphitic carbon nitride nanosheets and carbon nanotubes (g-C₃N₄ NS-CNT), which was fabricated by self-assembly strategy with π - π stacking and electrostatic interactions.¹⁶⁶ The g-C₃N₄ NS-CNT composite displayed higher current density than that of IrO₂-CNT at potentials higher than 1.62 V.

1.5 Bifunctional catalysts for HER and OER

Nowadays, the electrochemical catalytic activity of HER in acidic media and OER in alkaline media has achieved great progress, such as MoS₂, Co/Ni-WS_x, FeS, Ni₃S₂, MoC, MoP, CoP and Ni₂P for HER and oxides/hydroxides of cobalt, nickel, manganese, iron, and copper for OER. However, there are very few catalysts that are able to catalyze both HER and OER in the same electrolyte. Generally, the catalysts show good catalytic performance in acidic media often tend to be inactive or even unstable in basic media, and the same phenomenon could be found for the catalysts which work better in basic media.^{167, 168} If we only integrate two types of catalysts that are specially suitable for the HER and OER, respectively, it is usually incompatible and thus results in a poor overall performance. Moreover, the theoretical minimum value of water splitting is 1.23 V, however, the commercial water electrolyzers generally operate at a larger voltage of 1.8-2.0 V, which is related to the energy consumption and electrical efficiency. Therefore, designing a new type of bifunctional materials that work as both HER and OER catalysts in the same electrolyte is of prime importance for overall water splitting, which remains a significant challenge.^{92, 169-171}

As shown in Figure 1-18 Lifeng Liu group prepared carbon fiber paper (CP) integrated with bifunctional nickel phosphide (Ni-P) electrocatalysts (CP@Ni-P) by electrodeposition of Ni on functionalized CP, followed by a convenient one-step phosphorization treatment in phosphorus vapor at 500 °C.¹⁷² The obtained CP@Ni-P

exhibited excellent electrocatalytic performance towards HER and OER, achieving 100 mA cm^{-2} at the overpotential of 250 mV for HER and 50.4 mA cm^{-2} at an overpotential of 300 mV for OER in alkaline solution, respectively. As CP@Ni-P show well-defined bifunctionality, a full alkaline electrolyzer is constructed using two identical CP@Ni-P electrodes as cathode and anode, respectively, which can realize overall water splitting with efficiency as high as 91.0% at 10 mA cm^{-2} for 100 h.

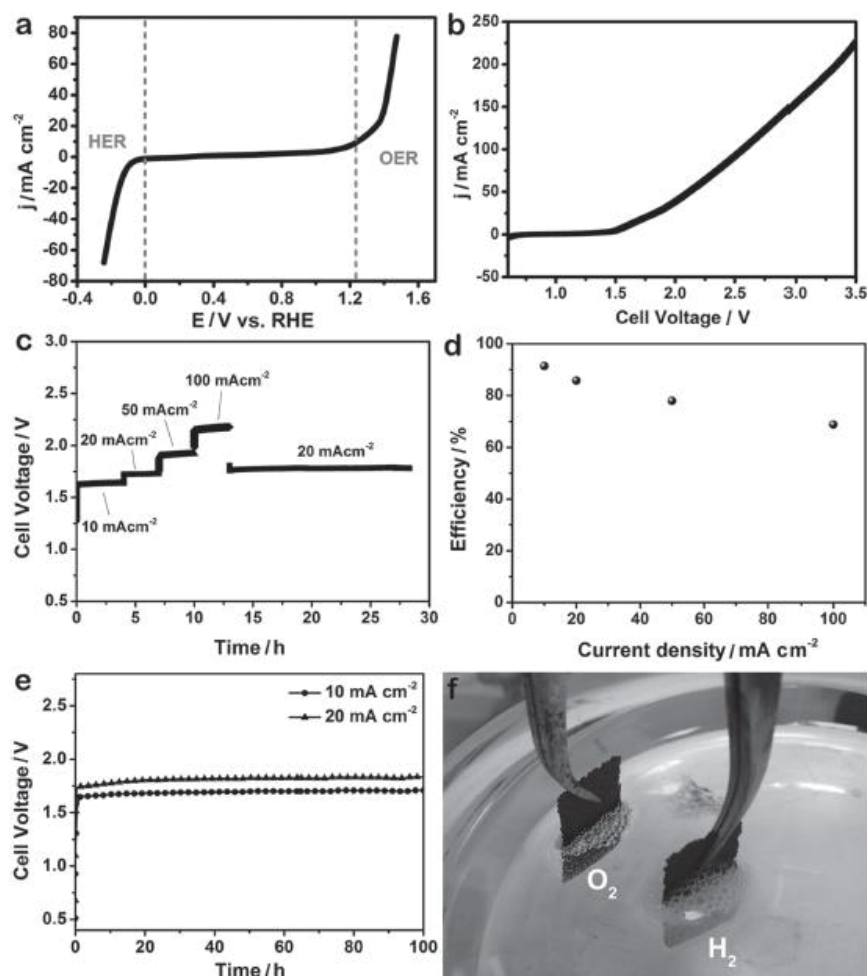


Figure 1-18 (a) Polarization curve showing the bifunctionality of CP@Ni-P toward both HER and OER. (b) Polarization curve in a two-electrode configuration. (c) Chronopotentiometric curve of water electrolysis at several different current densities. (d) Energy efficiency of the CP@Ni-P electrolyzer as a function of current density. (e) Long-term durability tests made at 10 and 20 mA cm⁻². (f) A digital photograph showing the evolution of H₂ and O₂ gas from the electrodes at 20 mA cm⁻².

Xinliang Feng group constructed the catalyst composed of cobalt selenide ($\text{Co}_{0.85}\text{Se}$) nanosheets vertically oriented on electrochemically exfoliated graphene foil, with subsequent deposition of NiFe layered double-hydroxide by a hydrothermal treatment ($\text{EG}/\text{Co}_{0.85}\text{Se}/\text{NiFe-LDH}$).¹⁷³ $\text{EG}/\text{Co}_{0.85}\text{Se}/\text{NiFe-LDH}$ nanosheets show bifunctional property towards HER and OER, which only requires overpotentials of 0.26 V to attain current density of 10 mA cm^{-2} towards HER and 1.50 V to reach current densities of 150 mA cm^{-2} towards OER. It is remarkable that an efficient water electrolyzer constructed by using $\text{EG}/\text{Co}_{0.85}\text{Se}/\text{NiFe-LDH}$ nanosheets as both anode and cathode, achieving 20 mA cm^{-2} at 1.71 V.

Chapter 2 experimental method and characterization

2.1 Overview

The overall research procedures for designing different nanostructure materials and their following applications are shown in Figure 2-1. The research work mainly includes three parts: the preparation of materials; characterization of the obtained materials; the application of the materials as catalysts towards water splitting.

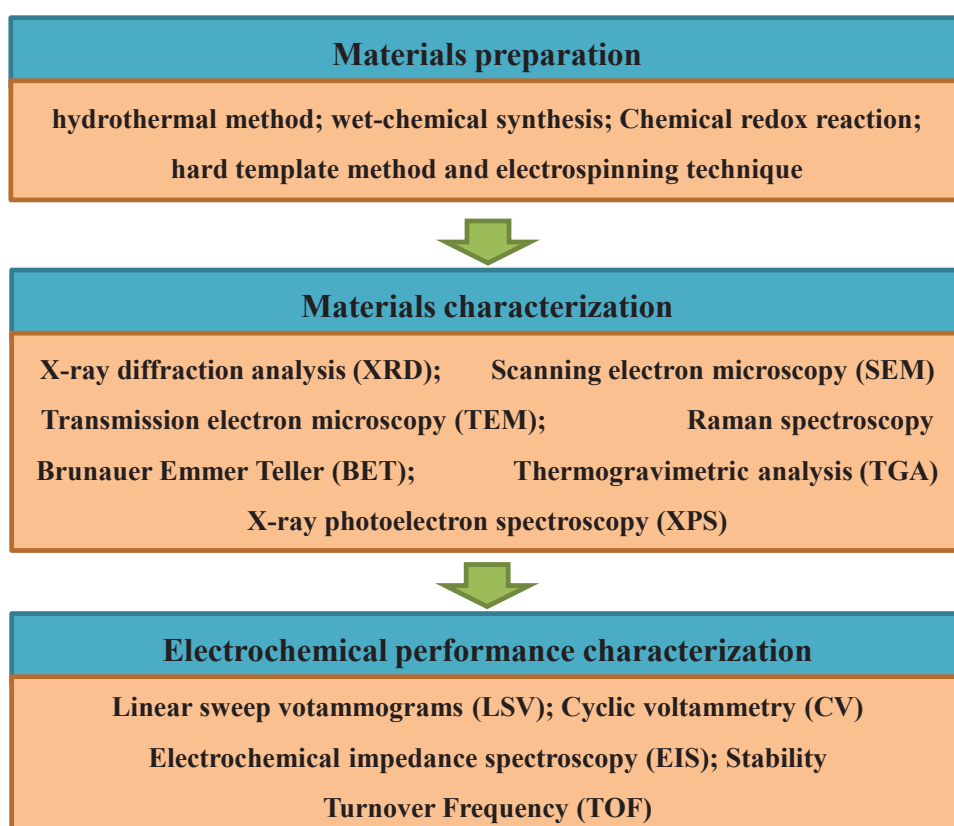


Figure 2-1 Schematic illustration for materials preparations, characterizations and applications.

A list of the names of materials and chemicals involved in the thesis, along with their formula, purity and supplier, is shown below in **Table 2-1**.

Materials and chemicals	Formula	Purity	Supplier
Carbon black	C	99%	Lexel

Cobalt(II) nitrate hexahydrate	$\text{Co}(\text{NO}_3)_2 \cdot 6\text{H}_2\text{O}$	98%	Sigma-Aldrich
Nickel(II) nitrate hexahydrate	$\text{Ni}(\text{NO}_3)_2 \cdot 6\text{H}_2\text{O}$	98%	Sigma-Aldrich
Ethanol	$\text{CH}_3\text{CH}_2\text{OH}$	99.5%	Sigma-Aldrich
Iron(II) acetate	$\text{Fe}(\text{NO}_3)_3$	99.99%	Sigma-Aldrich
Graphite (natural flakes)	C	75%	Sigma-Aldrich
Hydrazine hydrate	$\text{NH}_2\text{NH}_2 \cdot x\text{H}_2\text{O}$	50–60%	Sigma-Aldrich
Hydrochloric acid	HCl	37%	Sigma-Aldrich
Hydrogen peroxide solution	H_2O_2	30–32%	Sigma-Aldrich
Potassium hydroxide	KOH	90%	Sigma-Aldrich
Potassium permanganate	KMnO_4	99%	Sigma-Aldrich
Sodium borohydride	NaBH_4	99.99%	Sigma-Aldrich
Sulfuric acid	H_2SO_4	95–98%	Sigma-Aldrich
polyacrylonitrile	$(\text{C}_3\text{H}_3\text{N})_n$	95%	Sigma-Aldrich
N,N-dimethylformamide	$\text{C}_3\text{H}_7\text{NO}$	99%	Chem-supply
Ammonium Heptamolybdate	$(\text{NH}_4)_6\text{Mo}_7\text{O}_{24}$	99%	Sigma-Aldrich
Oleic acid	$\text{C}_{18}\text{H}_{34}\text{O}_2$	99%	Sigma-Aldrich
Nafion	Nafion	5%	Sigma-Aldrich
Hexadecyltrimethylammonium bromide	$\text{C}_{19}\text{H}_{42}\text{BrN}$	99%	Sigma-Aldrich

2.2 Material preparation

In this thesis, several approaches are used to fabricate the materials for water splitting (HER and OER), including hydrothermal method; wet-chemical synthesis; Chemical redox reaction; hard template method and electrospinning technique.

2.2.1 Hydrothermal method

The hydrothermal method is a synthetic method with an accurate control of temperature and pressure by using the autoclave, preparing the graphene hydrogel and MoS₂ nanosheets. The hydrothermal method is widely used method to synthesize the nanostructure materials. The synthesis conditions can highly affect the final properties (composition, morphology, and crystal structure) of the obtained materials, including temperature, kinds of the solvent, the volume of the solvent and concentration of the precursors. The disadvantage of this technique is that the *in-situ* monitoring of crystal growth is impossible. The details for synthesizing each material will be specifically described in the particular chapters (Chapter 3).



Figure 2-2 Autoclaves for hydrothermal synthesis.

2.2.2 Wet-chemical synthesis

Wet-chemical synthesis is a method for preparing nanostructure materials in solvent, and the morphologies are controlled by adding different hydrophobic/hydrophilic solvent agents, such as CTAB. After the reaction, the materials further treated in a Muffle furnace.

2.2.3 Chemical redox reaction

A chemical redox reaction was used to synthesize of graphene nanosheets. Graphene oxide (GO) was synthesized by a modified Hummers method.¹⁷⁴ In a typical synthetic process, graphite flakes (0.5 g, Sigma-Aldrich), NaNO_3 (0.5 g), and H_2SO_4 (23 mL) were stirred together in an ice bath. KMnO_4 (3 g) was added slowly to the above solution. After stirring for 30 min, the suspension was transferred to a 35 °C water bath and stirred for about 1 h. H_2O (40 mL) was added and the mixture was stirred for another 30 min, while the temperature was raised to 90 °C. Finally, H_2O (100 mL) was added, followed by the slow addition of H_2O_2 (3 ml, 30%). The final suspension was then filtered and washed with water to obtain graphite oxide. The as-synthesized graphite oxide was dispersed into distilled water and sonicated for 2 h to form a homogeneous suspension of GO/ H_2O (2.0 mg ml^{-1}).

2.2.4 Hard template method

The hard template method is an effective method to obtain the three-dimensional (3D) porous graphene. The materials which could be used as the hard templates usually possess well-defined void in the form of channels, pores or connected hollow spaces. The porous graphene could be prepared by hard template methods by assembling graphene oxide (GO) with pre-formed solid templates, such as metal oxides particles (SiO_2), polymer spheres (PS, PMMA), Nickel foam and coagulated aqueous solutions (hydrogel and freeze-drying). The final porous graphene can be obtained after the removal of the hard template by etching with HF or NaOH. The details for synthesizing porous graphene are described in the particular chapters (Chapter 5).

2.2.5 Electrospinning technique

Electrospinning technique is unique method to obtain the ultra-fine fibers with diameters in the micrometre to nanometre range, starting from molten polymers or polymers in solution. The conventional electrospinning facility consists of three major parts: a high voltage (kV) power supply, a spinneret (a syringe or pipette tip) and a grounded collector (typically a metal plate or a rotating mandrel). The obtained electrospun nanofibres usually show specific properties, including high surface/volume, porous structure, flexible. The advantages of electrospinning technique are simplicity, efficiency, low cost, high yield and high degree of reproducibility of the obtained materials.

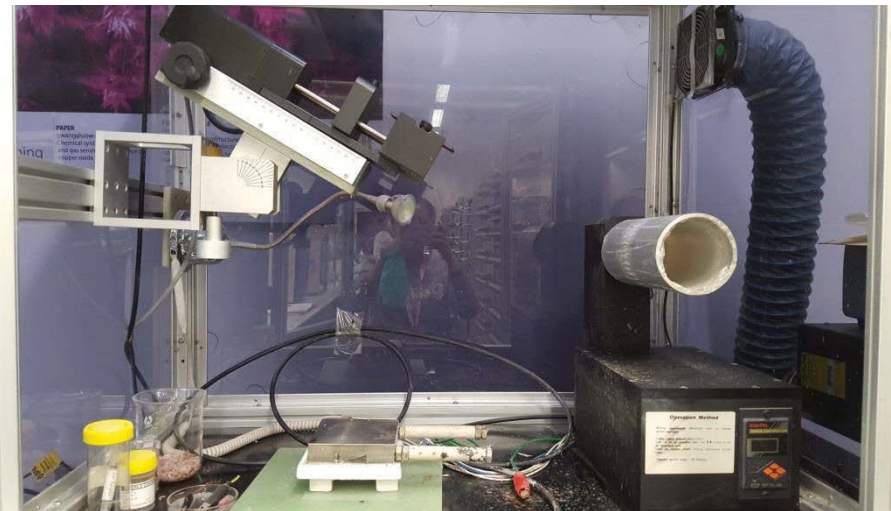


Figure 2-3 The electrospinning instrument for the experiment.

2.3 Materials characterization

2.3.1 X-ray diffraction analysis (XRD)

X-ray diffraction (XRD) is a characterization method to obtain the crystallographic structure of a wide range of materials, including atomic arrangement, crystal size, and imperfections, which is non-destructive and versatile. The samples can be collected for other test after the XRD measurement.



Figure 2-4 The Bruker D8 Discover XRD instrument.

The X-ray diffractometer generates an X-ray beam hitting a sample as a function of incident and scattered angle, polarization, and wavelength or energy. Each crystal has its unique characteristic X-ray diffraction pattern based on Bragg's law (Equation -1).

$$2d\sin \theta = n\lambda \quad \text{Equation 2-1}$$

In the above equation, d is the interplanar spacing, θ represents the incident angle, n is any integer, and λ is the wavelength of the X-ray beam. The collected XRD data of particular samples can be identified by using the standard database (JCPDS cards).

In this work, a Bruker D8 Discover XRD (Figure 2-1) was used to obtain the X-ray powder diffraction pattern of the as-synthesized materials. X-ray diffraction (XRD) measurements were carried out by employing a scanning step of 0.04° per second in the 2θ range from 10 to 80° .

2.3.2 Scanning electron microscopy (SEM)

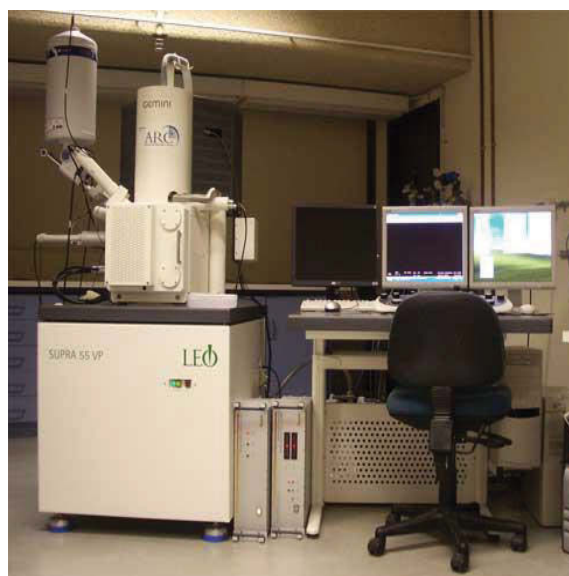


Figure 2-5 The field emission scanning electron microscopy in a mode of Supera 55 VP produced by Zeiss and equipped with EDS detector.

SEM is an important technique to characterize the morphology and size of the prepared materials by scanning it with a beam of electrons. The electron beam emitted by the electron gun at the accelerating voltage interacts with the sample, producing signals that form the images. At present, SEM can not only characterize the morphology of the sample, but also can be combined with X-ray energy scatterometer (EDX) to analyze the composition of the sample and the distribution of elements.

In this work, field-emission electron microscopy (FESEM, Zeiss Supra 55VP) and element mapping and electron energy dispersive spectroscopy (Zeiss Evo SEM) were conducted to characterize the morphology and surface structure of as-prepared

materials.

2.3.3 Transmission electron microscopy (TEM)

TEM is a microscopy technique to observe the morphology, crystal structure and electronic structure of as-prepared samples. The beam of electrons is transmitted through an ultra-thin specimen, interacting with the samples as it passes through, and then the image is formed. The resolution of TEM images is much higher compared to that of SEM images. The lattice shown in the TEM images was indexed by matching the calculated d , the inter-planer spacing, which is consistent with the XRD results.

In this work, the morphology and chemical composition of the as-prepared samples were observed by transmission electron microscopy (TEM, Model JEM-2010, JEOL) with a normal operation accelerating voltage of 200 kV. The TEM Samples were prepared by depositing the as-prepared materials onto a holey carbon support film on a copper grid.



Figure 2-6 Transmission electron microscopy (TEM, Model JEM-2011, JEOL).

2.3.4 Raman spectroscopy

Raman spectroscopy is a spectroscopic technique used to study the molecular vibrations at the atomic scale in inorganic and organic compounds, which provides sufficient information to identify a specific molecular. Raman experiments usually perform without sample preparation, directly loading the powder on the surface of a silicon wafer or mica and this technique is non-destructive, providing an option of continued examination of the samples. In my thesis, Raman spectroscopy is mainly used to analyse the graphitic and defected carbon in graphene.

In this work, Raman spectra were collected on an inVia Renishaw Raman spectrometer system (HR Micro Raman spectrometer, Horiba JOBIN YVON US/HR800 UV) using a 632.8 nm wavelength laser.



Figure 2-7 The Renishaw inVia Raman microscope equipped with a Leica DMLB microscope (Wetzlar, Germany) and a 17 mW at 633 nm Renishaw helium neon laser.

2.3.5 Brunauer Emmer Teller (BET)

Brunauer Emmer Teller (BET) is a useful technique served to analyze the surface area, pore size distribution and pore volume of the as-prepared materials. The theory of

BET is using the nitrogen adsorption and desorption techniques at ultra-low temperature conditions (liquid nitrogen) before the materials are completely dried with heat and vacuum to measure the properties of the materials.

The instrument used in this doctoral work, shown in Figure 2-8, is a 3 Flex surface characterization analyser produced by Micromeritics with three available ports, using a Quadrasorb SI analyser at 77 K. Brunauer–Emmett–Teller (BET) surface area of the obtained materials was achieved by using experimental points at a relative pressure of $P/P_0 = 0.05\text{--}0.25$.



Figure 2-8 The 3 Flex surface characterization analyser instrument produced by Micromeritics.

2.3.6 Thermogravimetric analysis (TGA)

Thermogravimetric analysis is a type of testing for continuous recording of the mass changes of the materials with the increase of temperature, which is useful technique to determine the physical and chemical properties of certain material based on the temperature. The gas we usually used in TGA test is air or high purity Argon.

In this work, the TGA was used to determine the carbon content in the carbon-

based materials. TGA was carried out by simultaneous TG-DTA (SDT 2960) with a heating rate of 5 °C min⁻¹ from room temperature to 800 °C in air.

2.3.7 X-ray photoelectron spectroscopy (XPS)

X-ray photoelectron spectroscopy (XPS) is a surface-sensitive quantitative spectroscopic technique that measures the surface elemental composition and the electronic environment. XPS spectra are obtained by irradiating a material with a beam of X-rays while simultaneously measuring the kinetic energy and number of electrons that escape from the top 0 to 10 nm of the material being analyzed.

In this work, X-ray photoelectron spectroscopy (XPS) measurement was performed on an ESCALAB250Xi (Thermo Scientific, UK) equipped with monochromated Al K alpha (energy 1486.68 eV).

2.4 Electrode preparation

2.4.1 Glassy carbon electrode



Figure 2-9 The three-electrode system.

The HER and OER performance of the catalysts was measured on an electrochemical workstation (CHI 660E, CH Instrument) by using a three-electrode configuration with platinum wire and Ag/AgCl as the counter and reference electrodes, respectively. The reference electrode, Ag/AgCl (saturated KCl solution), was calibrated with the respect to the reversible hydrogen electrode (RHE), $E_{\text{RHE}} = E_{\text{Ag/AgCl}} + 0.059 \times \text{pH} + 0.1971$. The working electrode was glassy carbon (GC) electrode with a diameter of 3 mm. To prepared the electrode slurry, 4 mg of catalyst, 80 μl of Nafion (5 wt %) and 1 ml solvent (1:1 v/v water/isopropanol) mixed together and then sonicated for 30 min to form a dispersion. 10 μl of the dispersion was dropped onto the GC electrode (loading amount 0.56 mg cm^{-2}), followed by drying at room temperature.

2.4.2 Rotating ring-disk electrode



Figure 2-10 The Pine rotating ring-disk electrode (RRDE) instrument.

For the rotating ring-disk electrode (RRDE) measurement, a rotating ring disk electrode with a glassy carbon disk (5 mm in diameter) and a Pt ring were used (Pine Research Instrumentation, USA). The as-prepared catalyst was loaded onto the disk electrode by using the above mentioned method. A rotating speed of the RRDE was

held at 1600 rpm for the test. To ensure the oxidation current originated from the oxygen evolution, the ring potential was held constantly at 0.45 V *vs.* RHE to reduce the formed O₂ from the catalyst on the disk (disk potential fixed at 1.48 V *vs.* RHE) in N₂-saturated 1 M KOH solution. A continuous OER (disk electrode) → ORR (ring electrode) process occurred on the RRDE. The Faradaic efficiency was calculated as follows: $\varepsilon = I_r/(I_d N)$, where I_d is the disk current, I_r is the ring current, and N represents the current collection efficiency of the RRDE ($N = 0.2$). on the other hand, to detect the content of the formed hydrogen peroxide (HO₂⁻) intermediates, the ring potential was held constantly at 1.50 V *vs.* RHE in O₂-saturated 1 M KOH solution and recorded the data at a scan rate of 5 mV s⁻¹.

2.5 Electrochemical performance characterization

The electrochemical performances of water splitting (HER and OER) with different kinds of nanostructured materials are mainly evaluated by using five types of measurement approaches: linear sweep votammograms (LSV), cyclic voltammetry (CV), electrochemical impedance spectra (EIS), stability and turnover frequency (TOF).

2.5.1 Linear sweep votammograms (LSV)

Two important factors to evaluate the performances of the catalysts for HER or OER are overpotential and current density, which can be measured by the linear sweep votammograms (LSV). The working electrode is the one at which the water oxidation/reduction reactions occur, and after the water molecules on the surface of the working electrode are reacted, the new molecules comes into contact with the surface of working electrode. LSV is a voltammetric method to measure the current density at a working electrode based on the overpotential.

The polarization curves were obtained in 1 M KOH solution with a scan rate of 5 mV s⁻¹, which were all corrected for the *i*R contribution within the cell.

2.5.2 Cyclic voltammetry (CV)

Cyclic voltammetry (CV) is used to measure double-layer charging in this work. There is a linear property between double-layer charging and electrochemical active surface areas, which mean electrochemical active surface areas of the as prepared materials could be estimated from the electrochemical double-layer capacitance of the catalytic surface. The potential of CV should be in the range with no apparent Faradaic processes occur. This range is typically a 0.1 V potential window centered at the open-circuit potential (OCP) of the system. All measured current in this non-Faradaic potential region is assumed to be due to double-layer charging. The charging current, is then measured from CVs at multiple scan rates.

In this work, CV was conducted centered at open circuit potential at scan rates ranging from 10 to 100 mV s⁻¹.

2.5.3 Electrochemical impedance spectroscopy (EIS)

Electrochemical impedance spectroscopy (EIS), is an effective experimental method to characterize electrochemical behaviors, especially for the conductivity. The impedance of a system measured using this technique usually reveals the presence of two time constants: high-frequency time constant and low-frequency time constant, which is often expressed graphically as a Nyquist and Bode plots. The EIS result provides the information of the interface reaction and electrode kinetics towards HER or OER.

In this work, the EIS were recorded with a frequency ranging from 10⁶ to 0.01 Hz and an amplitude of 5 mV at the open circuit potential or a certain constant

overpotential.

2.5.4 Stability

Stability of the as prepared materials towards HER or OER is also important for energy conversion system. The cycling performance of catalysts based electrode was operated by repeating linear sweep voltammograms (LSV) running for more than 1000 cycles or the current–time plots were obtained at a static overpotential.

2.5.5 Turnover Frequency (TOF)

TOF is another crucial detector to evaluate the catalytic activity, which could be derived from the mass content of the active catalysts in the composite calculated from the TGA test and assuming that all deposited materials were involved in the electrochemical reaction, the lower limits for turnover frequency (TOF) can be derived from the catalytic current.

Chapter 3 MoS₂ nanosheets supported on 3D graphene aerogel as a highly efficient catalyst for hydrogen evolution

3.1 Introduction

The advent of graphene has intrigued tremendous studies in two-dimensional materials, which could be applied in electrocatalysis, photocatalysis, sensors, supercapacitors and lithium/sodium ion batteries due to their unique physical and chemical properties.^{33, 62, 175-179} These two-dimensional materials, including transition-metal dichalcogenides, have a layered structure, and consist of covalently bonded monolayers brought together via weak van der Waals interactions. Among them, MoS₂ with vertically stacked S–Mo–S interlayer, has garnered intensive interest as a potential catalyst for the electrochemical and photocatalytic hydrogen evolution.^{20, 180-184} The study of MoS₂ towards hydrogen evolution reaction (HER) can be traced to 1970s, which demonstrated that the bulk MoS₂ has no catalytic activity for HER.¹⁸⁵ MoS₂ has not been considered as a promising HER catalysts before Hinnemann found (1010) Mo-edge structure had a close resemblance to the active site of nitrogenase in 2005.¹⁷ In addition, they claimed the free energy of atomic hydrogen bonding to MoS₂ was close to that of Pt by using the theoretical calculation, which confirmed the possibility by using MoS₂ as a promising catalyst towards HER. In their study, they also synthesized the composite of MoS₂ and graphite, further verifying the catalytic activity of MoS₂ for HER experimentally. Since then, much more efforts have been devoted to the investigation of MoS₂ towards HER. In order to further improve the catalytic activity, the researchers identify the active sites of MoS₂ in the HER process by using the theoretical and experimental studies, indicating that the edges of MoS₂ are catalytically active while the basal plane remains inert.

The catalytic activity of MoS₂ towards HER are related to the density and reactivity of the active sites and the electrical transport. However, the intrinsic stacking and aggregation properties among the MoS₂ catalyst seriously reduce the number of exposed active sites. Moreover, the inherent semiconductor properties with an observable anisotropic behaviour in conductivity of MoS₂ further hinders its application as an efficient HER catalyst. Maximizing the exposed edge sites and enhancing the electrical transport of MoS₂ are the key issues for improving its catalytic performance.^{23, 32, 186} Fabricating nanostructured dichalcogenides or hybridizing MoS₂ with gold, graphene or other materials are considered as high performance catalysts towards HER compared with the bulk one.^{26, 187-189} Cao's group demonstrated that the layer-dependent electrocatalysis of MoS₂ materials towards HER decreased by a factor of ~ 4.47 for every additional layer, which suggests that the exposed edge sites are catalytically active.²² Liu and co-workers developed MoS₂ nanoparticles grown on mesoporous graphene, exhibiting excellent electrocatalytic activity and rapid charge transfer kinetics.¹⁸⁸

Graphene aerogel (GA) represents a new class of porous carbon materials with macroscopic pores and high specific surface areas.¹⁹⁰⁻¹⁹² GA has received enormous interest towards energy storage and conversion applications, adsorption, and catalysis. More importantly, GA consists of three-dimensional (3D) porous networks that not only could efficiently improve the electrolyte diffusion, facilitating catalyst utilization, but also supply multidimensional electron transport pathways for enhancing the electronic conductivity.^{193, 194} These properties strongly suggest that GA is an ideal scaffold for improving the catalytic activity of supported materials.

Herein, we demonstrate an active catalyst composed of MoS₂ nanosheets and 3D architectural GA. The flexible graphene sheets partially overlap in 3D space to form an

interconnected porous microstructure, which greatly prevents serious restacking of graphene, and further provides large surface area for growing MoS₂ nanosheets. The resultant MoS₂ supported on 3D GA (GA-MoS₂) composite possesses uniform deposition of MoS₂ nanosheets and fast electronic properties, exhibiting high catalytic performance and strong stability for electrocatalytic HER application.

3.2 Experimental

3.2.1 Synthesis of graphene hydrogel

Graphene oxide (GO) was synthesized by natural graphite flakes *via* the modified Hummers method. Then, aqueous suspension of GO at a concentration of 2 mg mL⁻¹ was prepared by ultrasonication (~ 30 min). Graphene hydrogel was obtained by hydrothermal assembly of GO. Typically, graphene oxide (20 ml) was sealed in a Teflon-lined stainless steel autoclave and heated at 150 °C for 12 h. After cooling naturally, graphene hydrogel was obtained and dialyzed in water for 24 h.

3.2.2 Synthesis of graphene hydrogel-MoS₂

Graphene hydrogel-MoS₂ nanocomposite was prepared by a hydrothermal method. Ammonium heptamolybdate ((NH₄)₆Mo₇O₂₄, 100 mg) and thiourea (CH₄N₂S, 1g) were dispersed in 20 ml deionized water containing graphene hydrogel obtained in the previous procedure. Then the mixture was transferred into a 25 ml autoclave and heated in an oven at 180 °C for 24 h. After the autoclave cooled to room temperature, product was dialyzed in water for another 24 h to remove impurities. The resultant material (GA-MoS₂) was obtained after freeze-drying.

3.2.3 Synthesis of the comparison materials

MoS₂ formed on graphene was synthesized by the same process as GA-MoS₂ by simply replacing graphene hydrogel with graphene oxide. The pure MoS₂ was prepared without graphene oxide or graphene hydrogel.

3.2.4 Structural Characterization

The morphology analysis was conducted using field emission scanning electron microscopy (FESEM, Zeiss Supra 55VP) and transmission electron microscopy (TEM, JEOL 2010). Element mapping was performed with Zeiss Evo SEM. X-ray diffraction (XRD) of the samples was characterized by Siemens D5000 using Cu K α radiation with a scanning step of 0.02° per second. Raman spectra were recorded on an inVia Renishaw Raman spectrometer system (HR Micro Raman spectrometer, Horiba JOBIN YVON US/ HR800 UV) equipped with a 632.8 nm wavelength laser. Surface oxidation state of GA-MoS₂ was investigated by X-Ray Photoelectron Spectroscopy (XPS, ESCALAB250Xi (Thermo Scientific, UK) equipped with mono-chromated Al K alpha (energy 1486.68 eV)). Brunauer–Emmett–Teller (BET) surface area of GA was calculated by experimental points at a relative pressure of $P/P_0 = 0.05\text{--}0.25$. The percentage of MoS₂ in the composite was determined by a TGA/differential thermal analysis (DTA) analyzer (TA Instruments, SDT 2960 module, New Castle, DE, USA) at a heating rate of 3 °C min⁻¹ from room temperature to 650 °C in air atmosphere.

3.2.5 Electrochemical Measurements

Electrochemical measurements were performed in 0.5 M H₂SO₄ solution using a three electrode system on an electrochemical workstation (CHI 660E). The platinum wire and Ag/AgCl (1 M KCl) work as the counter and reference electrodes ($E_{\text{SHE}} = E_{\text{Ag/AgCl}} + 0.059 \times \text{pH} + 0.2224$), respectively. The working electrode was prepared by depositing

the target materials on the glassy carbon (GC) electrode with a diameter of 3 mm. First, 4 mg of catalyst and 80 μl of Nafion (5 wt %) were mixed in 1 ml solvent (1:1 v/v water/isopropanol) by sonication for more than 30 min to obtain a homogeneous ink. Then, catalyst ink (10 μl) was drop-cast onto the GC electrode and followed by drying at room temperature. Linear sweep voltammetry (LSV) was conducted at a scan rate of 5 mV s^{-1} . Electrical impedance spectroscopy (EIS) was carried out at selected overpotential from 10^6 to 0.01 Hz with ac voltage amplitude 5 mV. Cyclic voltammetry measurements were conducted without faradaic processes at different scan rates (10, 30, 50, 70 and 100 mV s^{-1}).

3.3 Results and Discussion

3.3.1 The characterization of the catalysts

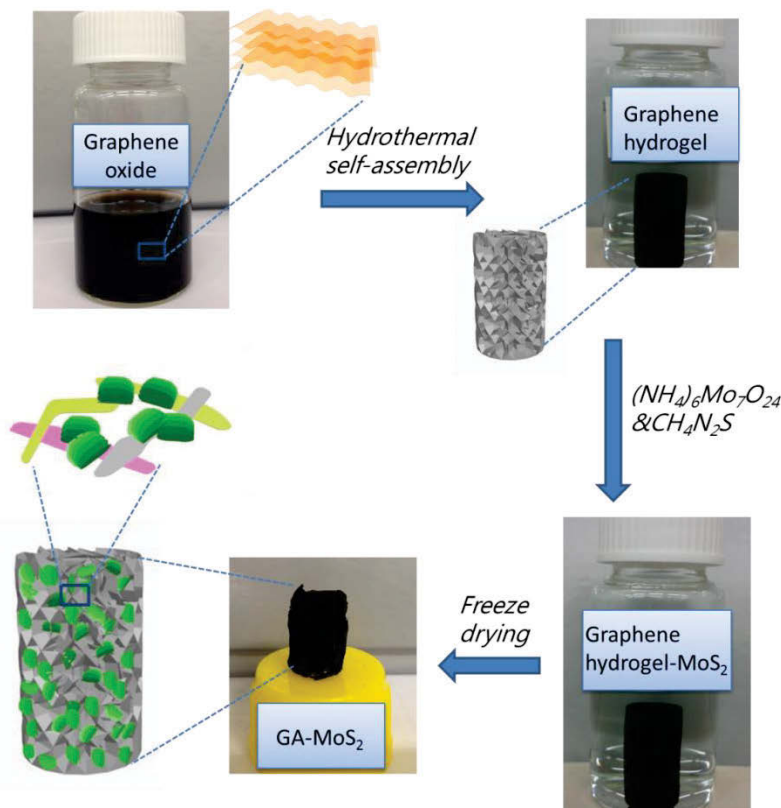


Figure 3-1 Schematic illustration for the synthesis procedure of GA-MoS₂ composite.

GA-MoS₂ was prepared in solution by two steps. Figure 3-1 displays the schematic illustration for the synthesis route of GA-MoS₂ hybrid. Graphene hydrogel could be easily prepared by one-step chemical reduction of graphene oxide dispersion.¹⁹⁵ The final product, GA-MoS₂, was obtained by hydrothermal route of ammonium heptamolybdate ((NH₃)₄Mo₇O₂₄) with thiourea (CH₄N₂S) in water solution containing graphene hydrogel as the matrix at 180 °C followed by freeze drying. The optical image displayed in Figure 3-1 shows that GA-MoS₂ is a self-supported macroscopic cylinder.

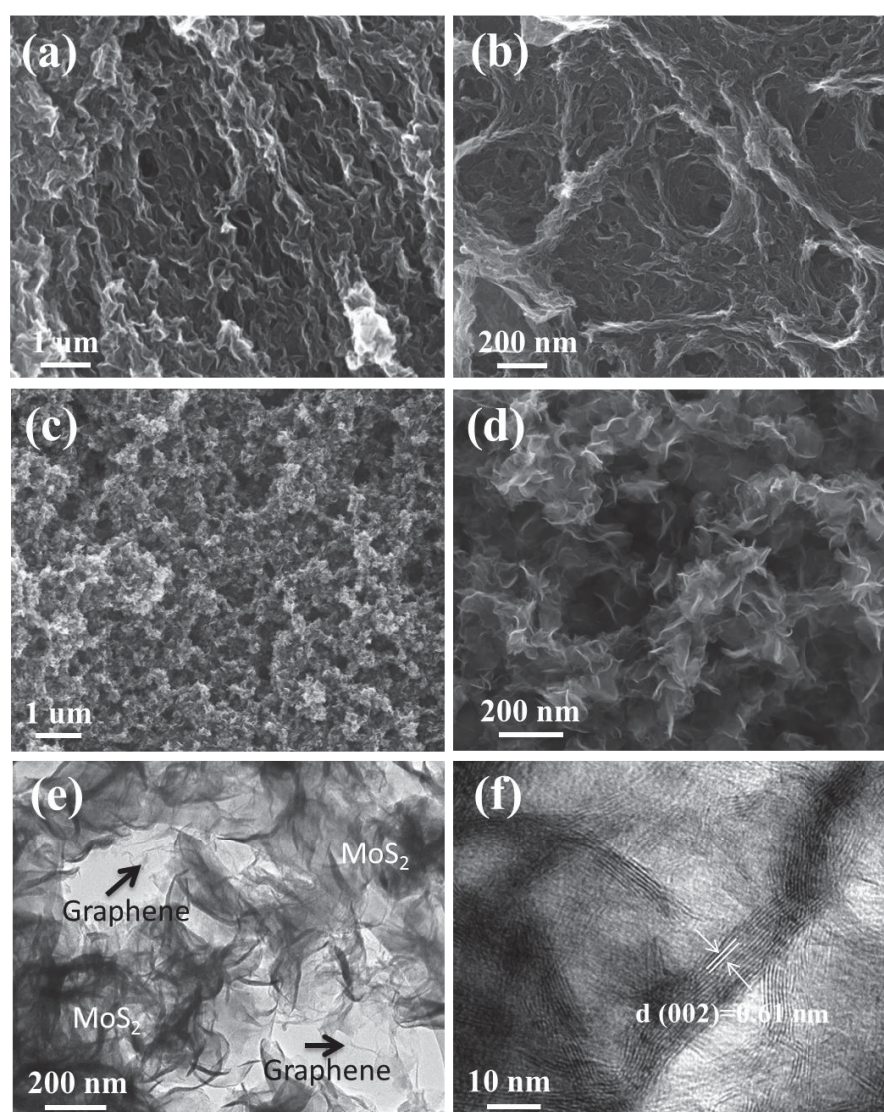


Figure 3-2 Electron microscope characterization of GA and GA-MoS₂: a, b) low and high magnification SEM images of GA, c, d) low and high magnification SEM images of GA-MoS₂, e, f) low and high magnification TEM images of GA-MoS₂.

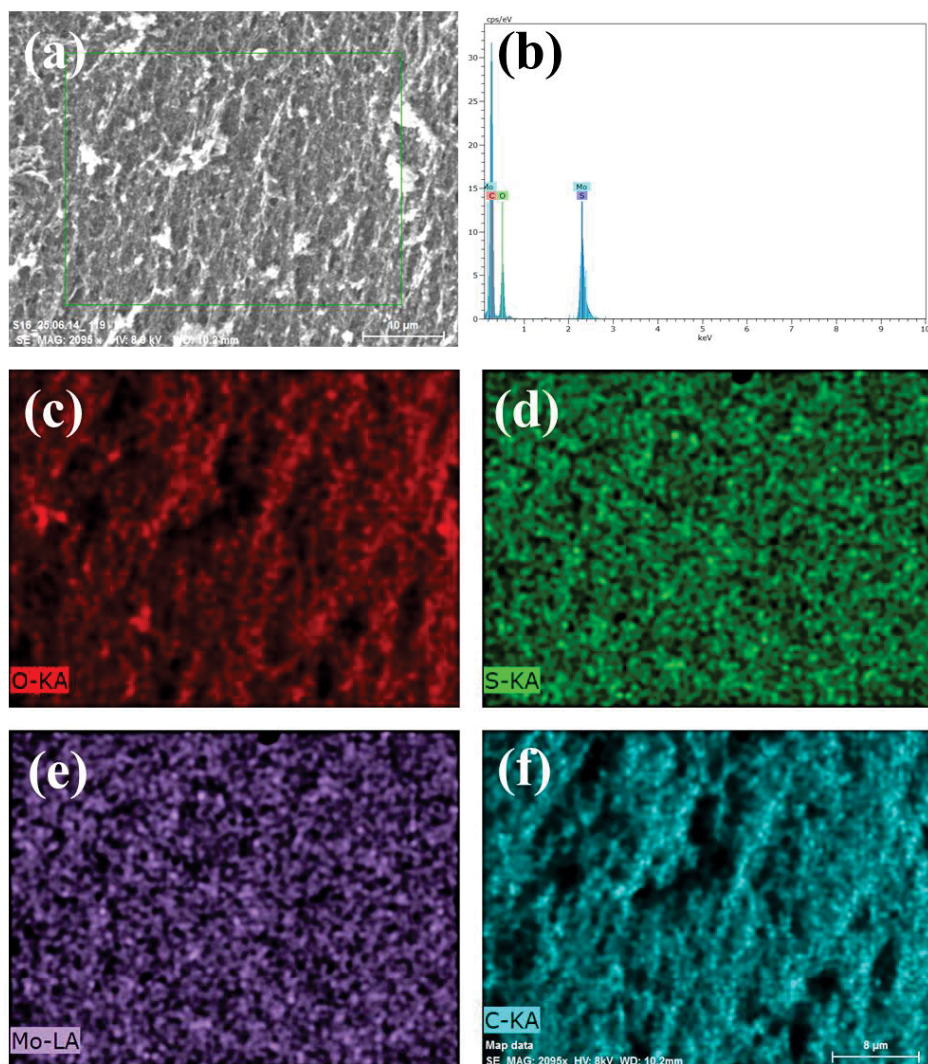


Figure 3-3 SEM image and EDS elemental mappings of GA-MoS₂, (a) SEM image of GA-MoS₂, (b) EDS profile, (c) element of O, (d) element of S, (e) element of Mo, (f) element of C.

The morphology of the as-prepared GA and GA-MoS₂ was investigated by SEM and TEM. SEM images in Figure 3-2 (a and b) show an interconnected, porous 3D graphene framework with continuous pores. The highly porous property of GA contributes to large specific surface area. Similar morphology and network structure could be found for GA-MoS₂ hybrid as shown in Figure 3-2 (c). GA-MoS₂ maintained an excellent porous structure and assembled with MoS₂ nanosheets around the edge of the pores (Figure 3-2 (d)), providing relatively large amounts of exposed edge sites for

hydrogen evolution. The morphology and composition of GA-MoS₂ hybrid were further examined by TEM and high-resolution TEM (HRTEM). TEM characterization (Figure 3-2 (e and f)) validated the ultrathin MoS₂ nanosheets supported by GA with highly porous network. HRTEM revealed typical lamellar MoS₂ nanosheets property with interlayer spacing of 0.61 nm.

The uniform distribution of MoS₂ nanosheets supported by GA could be further confirmed by element mapping (Figure 3-3), which shows homogeneous distribution of C, Mo, S and O elements inside GA-MoS₂ composite.

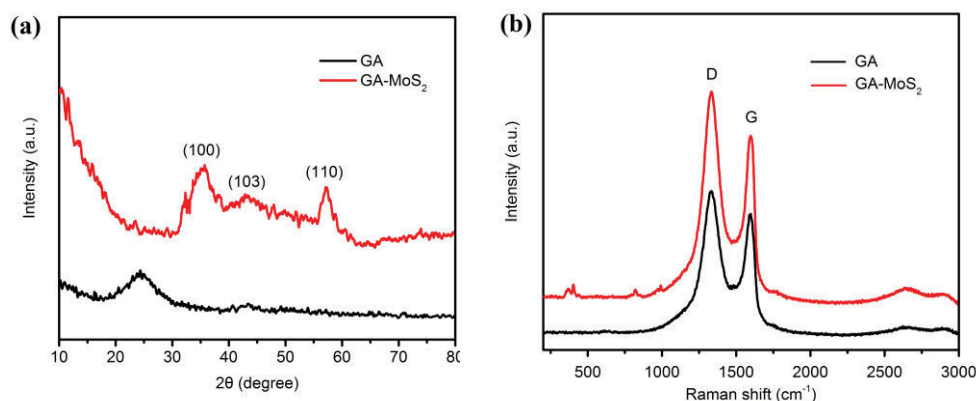


Figure 3-4 (a) XRD patterns and (b) Raman spectra of GA and GA-MoS₂.

Additional structural characterizations are acquired by X-ray diffraction (XRD) and Raman spectroscopy. As shown in Figure 3-4 (a), an obvious evolution of XRD patterns can be revealed. The diffraction peak around 24° could be assigned to graphene (002) for GA. XRD pattern of GA-MoS₂ reveals the prominent peaks match well with the hexagonal structure of MoS₂ (JCPDS 37-1492). The broad peaks of the XRD pattern indicate low crystallinity of the material.¹⁹⁶ Figure 3-4 (b) displays Raman spectra of GA and GA-MoS₂, and the characteristic peaks of graphene are revealed. Both GA and GA-MoS₂ show two dominant Raman peaks at 1328 and 1598 cm⁻¹, which can be assigned to D and G bands of graphene, respectively. D band occurs because of the A_{1g}

mode (owing to defects); therefore, the increased D band to G band intensity ratio (I_D/I_G) is an indication of more defects in the carbon lattice. The I_D/I_G value for GA-MoS₂ hybrid (1.22) is higher than pure GA (1.16), demonstrating that the introduction of MoS₂ nanosheets has made a contribution to the carbon defects.¹⁹⁷ Furthermore, the emergence of new Raman peaks for GA-MoS₂ at 371 and 400 cm⁻¹ associated with the in-plane E_{2g}^1 and out-of-plane A_{1g} vibrational modes of hexagonal MoS₂, respectively, which is consistent with the results of XRD and TEM. However, GA-MoS₂ also shows the characteristic Raman bands of MoO₃. The Raman bands at 994 and 820 cm⁻¹ match with the stretching vibration of the terminal Mo=O bonds along the *a*- and *b*-axes.¹⁹⁸ The existence of MoO₃ may be ascribed to the partial oxidation of the MoS₂ surface in air or exposure to the laser.

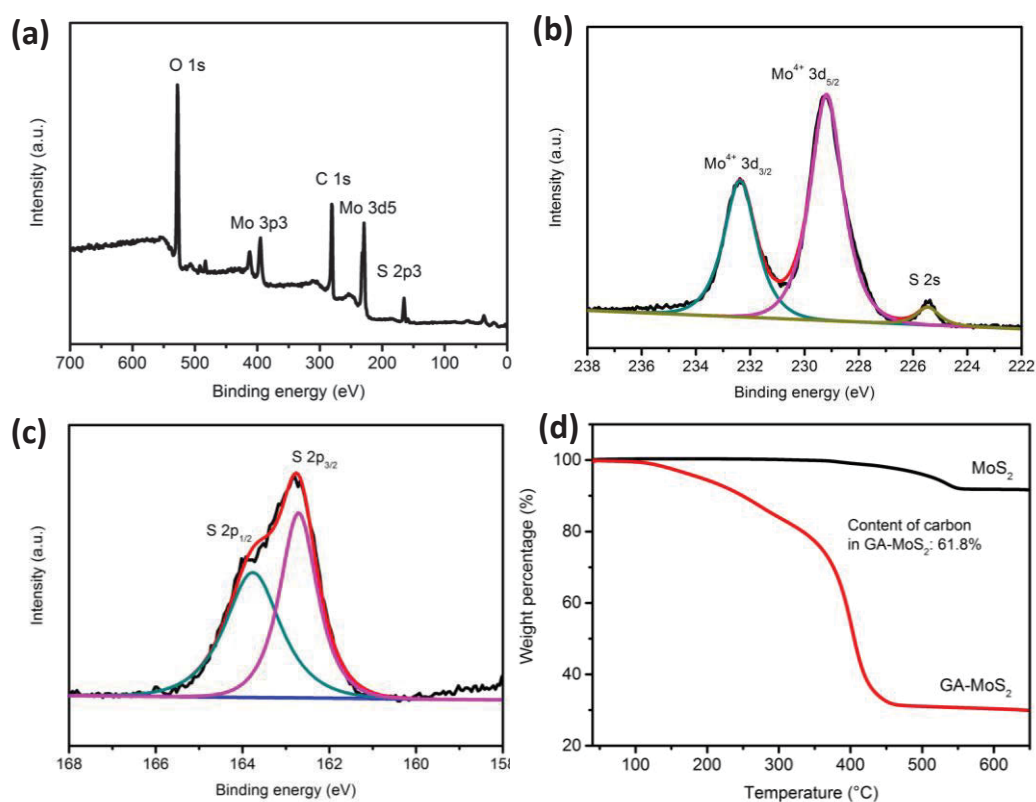


Figure 3-5 (a) XPS survey spectrum of GA-MoS₂ composite, high-resolution XPS spectra of GA-MoS₂ c) Mo 3d, d) S 2p. (d) thermogravimetric analysis in air of GA-MoS₂ and MoS₂ in air, used for calculating the content of MoS₂ in GA-MoS₂ composite.

X-Ray Photoelectron Spectroscopy (XPS) survey scans were used to further confirm the surface electronic state and composition of GA-MoS₂. The survey spectrum suggests that GA-MoS₂ is composed of C, Mo, S and O elements (Figure 3-5 (a)). The high resolution XPS of the composite in Figure 3-5 (b) shows two characteristic peaks located at 229.2 and 232.4 eV, attributing to Mo 3d_{5/2} and Mo 3d_{3/2} orbitals, whereas the peaks at 162.7 and 163.8 eV are corresponding to S 2p_{3/2} and S 2p_{1/2} (Figure 3-5 (c)) , which further signifies the formation of MoS₂ in the composite. The thermogravimetric analysis (TGA) curve of GA-MoS₂ is presented in Figure 3-5 (d), from which the content of MoS₂ can be determined to be 38.2 wt %.

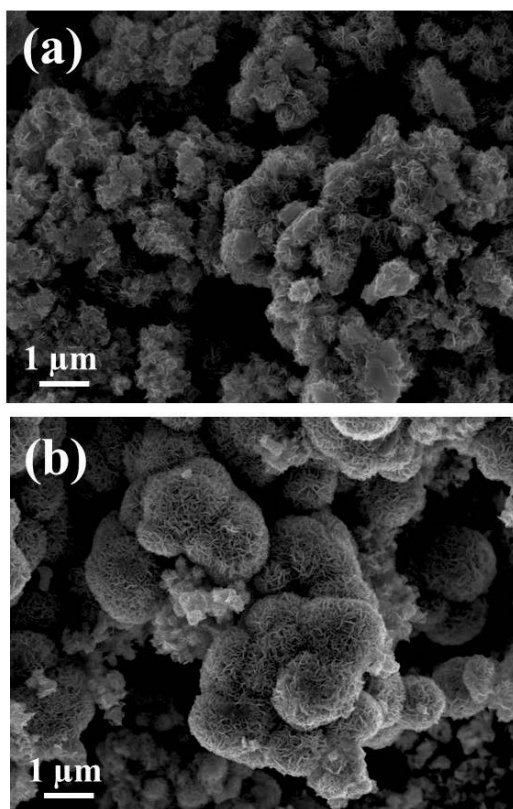


Figure 3-6 SEM images of (a) G-MoS₂ and (b) pure MoS₂.

In order to further investigate the importance by using GA as the substrate, the comparison materials, graphene-MoS₂ (G-MoS₂) and pure MoS₂, were also synthesized

by a similar procedure. The SEM images in Figure 3-6 displayed the highly aggregated morphology of G-MoS₂ and MoS₂ without the 3D graphene framework as the scaffold.

The results of nitrogen sorption isotherm of GA, GA-MoS₂, G-MoS₂ and MoS₂ are shown in Figure 3-7, which reveals that GA has a surface area of 294 m² g⁻¹ and GA-MoS₂ hybrid shows a little lower surface area of 62 m² g⁻¹, whereas G-MoS₂ and MoS₂ shows even lower surface area, 49 m² g⁻¹ and 17 m² g⁻¹, respectively. Therefore, GA-MoS₂ shows a slightly larger surface area, which is benefited to the interaction of the electrolyte/catalyst.

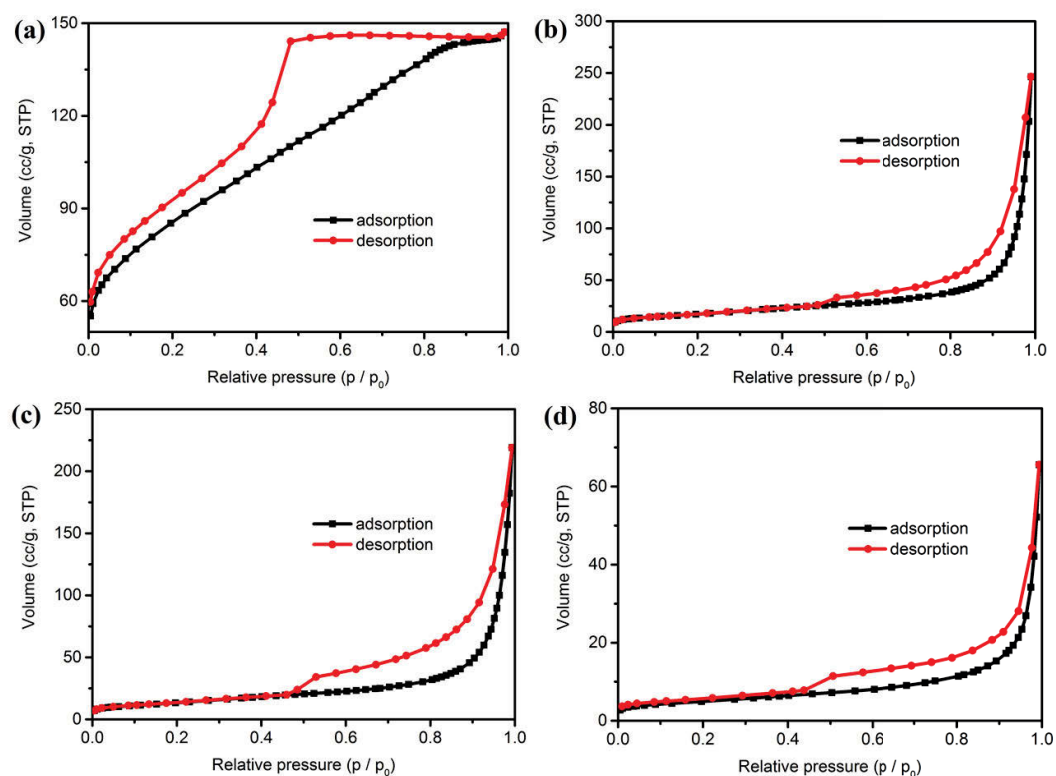


Figure 3-7 Nitrogen adsorption/desorption isotherm of (a) GA, (b) GA-MoS₂, (c) G-MoS₂, (d) pure MoS₂.

3.3.2 The electrochemical performance test of the catalysts

Electrochemical results were acquired in a standard three-electrode glass cell with platinum wire as counter electrode and Ag/AgCl as reference electrode in 0.5 M H₂SO₄

solution. Comparative studies were performed on G-MoS₂, MoS₂ and GA with the same loading.

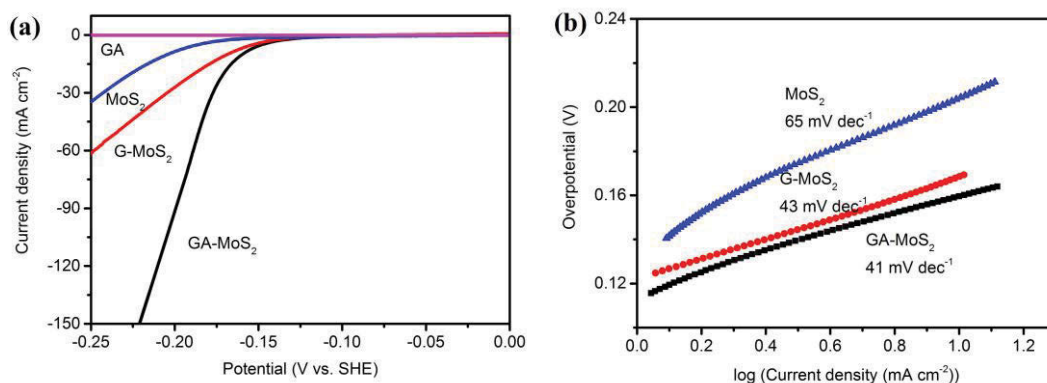


Figure 3-8 Electrochemical performance of the HER catalysts in 0.5 M H₂SO₄: a) polarization curves for GA-MoS₂, G-MoS₂, MoS₂ and GA loaded onto GC electrodes; b) Tafel curves of GA-MoS₂, G-MoS₂ and MoS₂.

As shown in Figure 3-8 (a), GA-MoS₂ showed highest catalytic activity towards HER compared with the other samples, benefiting from its unique 3D network structure. GA-MoS₂ exhibited the onset potential near 100 mV (vs. SHE), which is lower than the comparison materials. More importantly, the cathodic current of GA-MoS₂ increased rapidly at more negative potentials, exhibiting a current density of 95 mA cm⁻² at the overpotential of 200 mV. In contrast, G-MoS₂ and MoS₂ displayed much less HER activity with current densities of 27 and 8 mA cm⁻² at the same overpotential, respectively. GA displays negligible activity towards HER, confirming that the high performance of GA-MoS₂ composite is mainly attributed to the ultrathin MoS₂ nanosheets with large exposed active sites. The electrochemical activity of GA-MoS₂ is even better than that of the oxygen-incorporated MoS₂ nanosheets, spaced confined MoS₂ nanosheets with graphite, and is even comparable with the performance of metallic MoS₂ nanosheets.^{24, 189, 199} To further demonstrate the high performance of the catalysts, Tafel plots were derived from the Linear sweep voltammetry (LSV) by fitting

the linear regions to the Tafel equation ($\eta = b \log(j/j_0)$, where η is the overpotential, b is the Tafel slope, j is the current density, and j_0 is the exchange current density), which is usually used to evaluate the efficiency of the catalytic reaction. The Tafel slope of 41 mV dec⁻¹ for GA-MoS₂ (Figure 3-8 (b)) is smaller than that of pure MoS₂, but similar to those of G-MoS₂ and other MoS₂-based on carbon materials, suggesting a similar surface chemistry towards HER for MoS₂ supported on carbon materials.

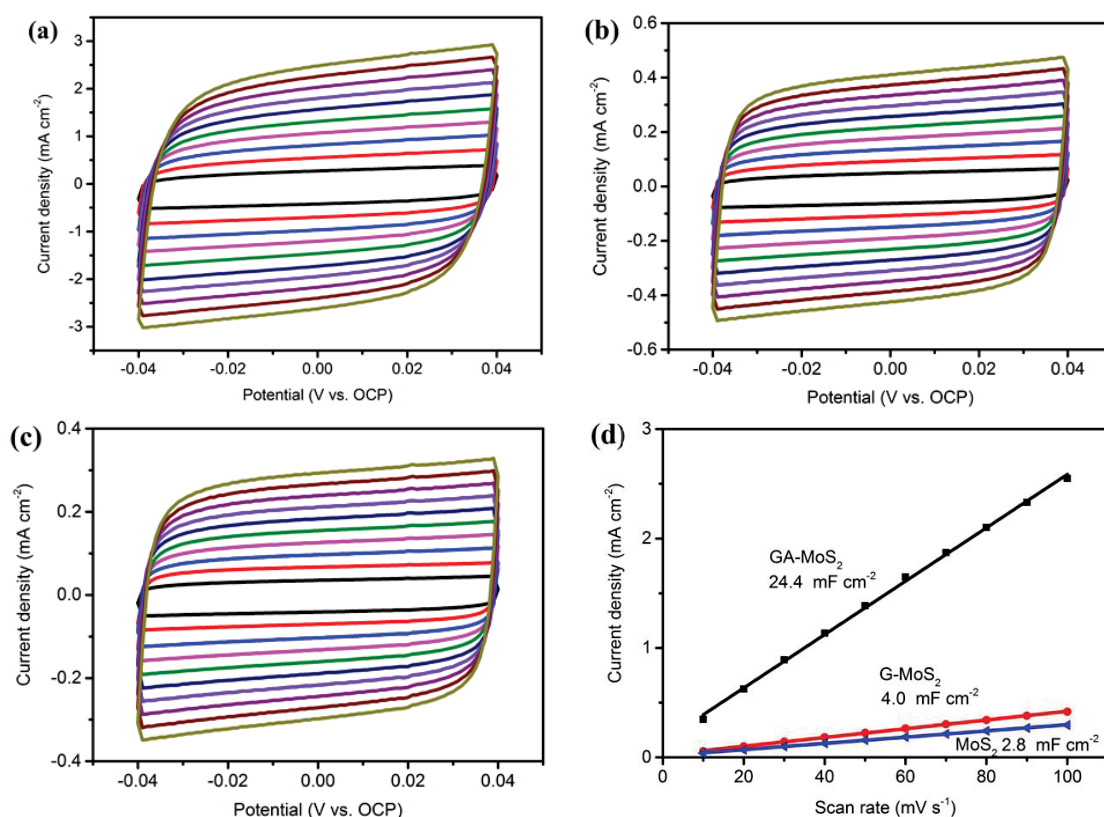


Figure 3-9 Electrochemical capacitance measurements: Cyclic voltammograms are performed in 0.5 M H₂SO₄ solution in a potential window without faradaic processes and the scan rate from 10 to 100 mV s⁻¹, (a) GA-MoS₂, (b) G-MoS₂, (c) MoS₂. (d) scan rate dependence of the average capacitive current densities at open circuit potential for GA-MoS₂, G-MoS₂ and MoS₂.

The high performance of GA-MoS₂ demonstrates the advantage of the 3D framework of GA and thin MoS₂ nanosheets, which results in much more active edge sites for hydrogen evolution. This speculation is further confirmed by the measurement

of electrochemical double-layer capacitance, an alternative approach to estimate the electrochemically active surface areas.^{200, 201} Cyclic voltammetry (CV) measurements were conducted in a potential range with no apparent faradaic processes occurrence, where the currents are mainly attributed to the charging of double layer. Representative plots for the determination of GA-MoS₂, G-MoS₂ and MoS₂ active surface areas are shown in Figure 3-9. The capacitance of GA-MoS₂ is 24.4 mF cm⁻², while G-MoS₂, MoS₂ are 4.0 and 2.8 mF cm⁻², respectively. The electrochemical active surface area was increased by 6~8 times by introducing GA as the matrix, further resulting in high catalytic performance.

Electrical impedance spectroscopy (EIS) at various overpotentials was employed to further gain more insight into the interface reaction and electrode kinetics of GA-MoS₂ hybrid towards HER. The representative Nyquist and Bode plots are presented in Figure 3-10 (a-d), which fit well with the typical two time constants model (high-frequency time constant and low-frequency time constant).^{43, 202} The charge transfer resistance (R_{ct}), related to kinetics of electrocatalysis, was determined from the semicircle in the low-frequency range (Figure 3-10 (e, f)). In the reaction process, R_{ct} of GA-MoS₂ decreased from 211.6 Ω at overpotential of 100 mV to 15.6 Ω at 180 mV, which is lower than those of G-MoS₂ in the same region (797.5 Ω to 27.0 Ω). The lower charge transfer resistance of GA-MoS₂ during the test is mainly attributed to the multidimensional electron transport pathways of the 3D network structure, and the fast charge transfer between the electrode and active sites of MoS₂ nanosheets, which further leads to the high electrocatalytic performance towards HER.

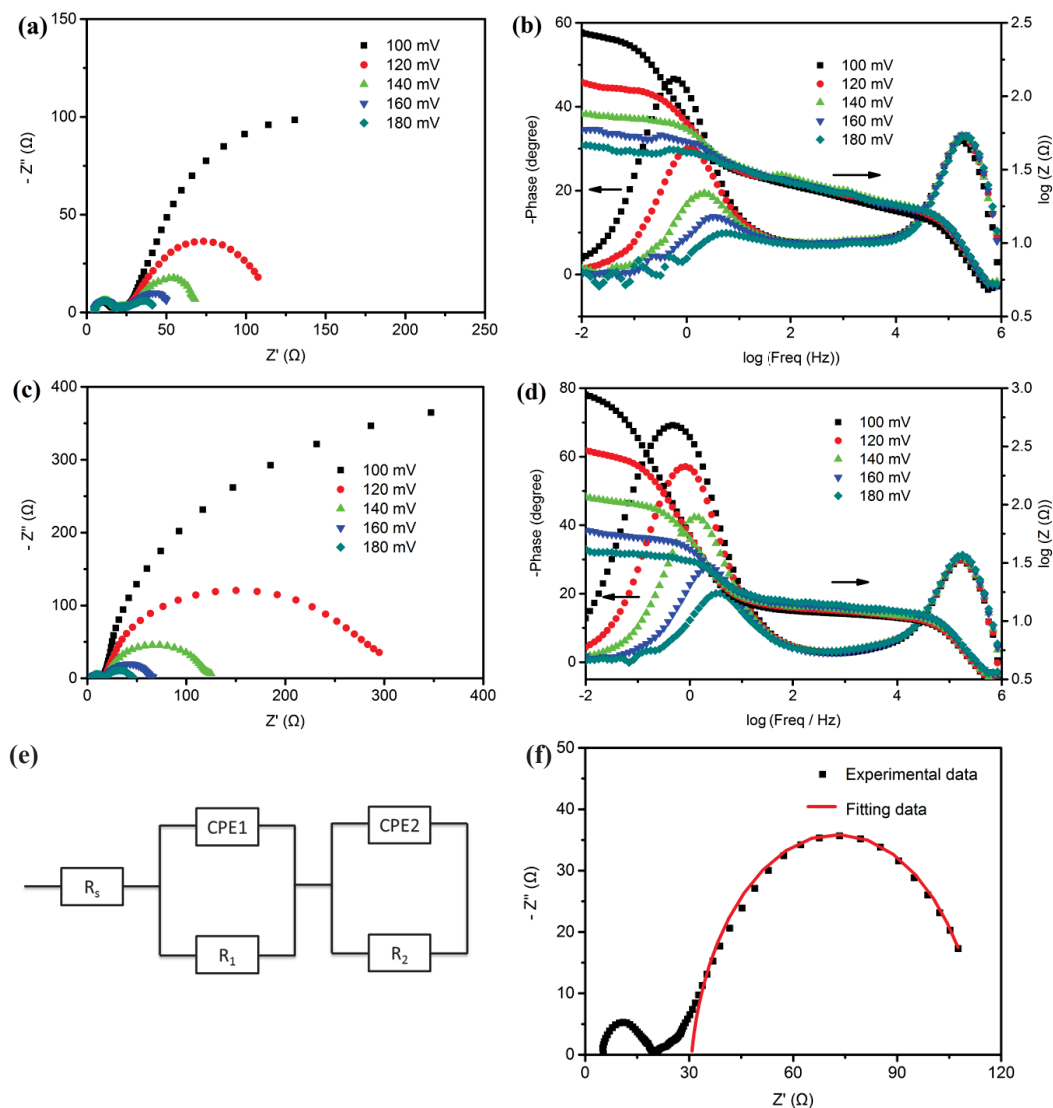


Figure 3-10 (a) Nyquist and (b) Bode plots for GA-MoS₂ hybrid modified GC electrode recorded at various HER overpotentials in 0.5 M H₂SO₄; (c) Nyquist and (d) Bode plots for G-MoS₂ hybrid. (e) Equivalent electrical circuit used to model the HER process on GA-MoS₂ and G-MoS₂ modified GC electrodes at various overpotentials, (f) the square symbols are experimental data and the red solid line are modelled by (e).

Besides high catalytic activities, good stability towards HER is also a critical aspect for an energy conversion system. To investigate the durability in an acidic environment, long-term potential cycling of GA-MoS₂ modified GC electrode was performed by taking continuous LSV at an accelerated scanning rate of 100 mV s⁻¹ for 2000 cycles. As shown in Figure 3-11 (a), GA-MoS₂ composite shows excellent

stability in 0.5 M acid solution. Even after the cycles, the GA-MoS₂ electrocatalyst still remained in a similar polarization curve to the initial one, which demonstrates the highly stable property even in an accelerated degradation. It is consistent with the results obtained under different scan rates (Figure 3-11 (b)). The catalytic currents of GA-MoS₂ are much less affected by scan rates, with similar polarization curves at the scan rate from 10 to 100 mV s⁻¹. These properties highly illustrate the importance of the 3D network structure for the efficient mass and charge transport in the HER process.

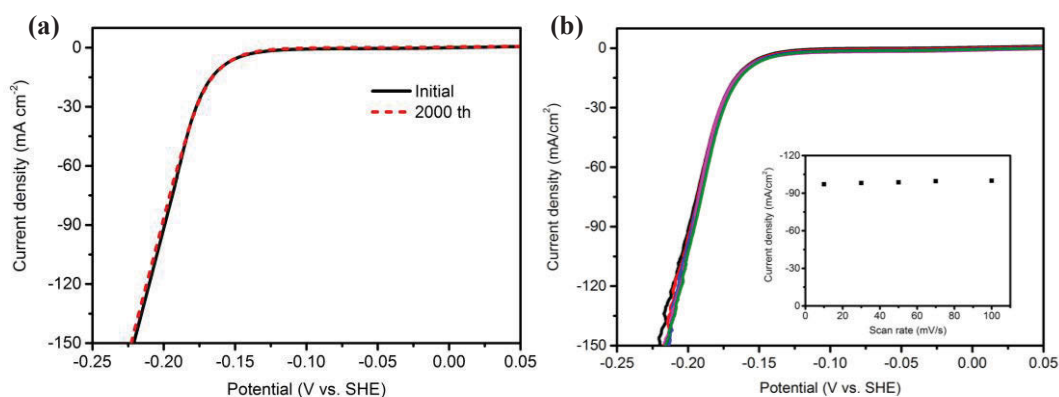


Figure 3-11 (a) stability test of GA-MoS₂ through potential cycling, polarization curves before and after 2000 potential cycles, (b) polarization curves of GA-MoS₂ at different scan rates, and the inset of d) shows the corresponding data of the current density (at -0.2 V vs SHE) vs scan rate.

The high catalytic activity and durability indicate that GA-MoS₂ is an efficient HER catalyst. GA with 3D network, highly porous structure provides a stable skeleton and large specific surface area for loading layer MoS₂ nanosheets around the edge of the pores. 3D structure of the catalyst could also supply efficient conducting network for rapid electronic transport during the electrocatalytic process, offsetting the poor intrinsic conductivity of MoS₂ because of a large bandgap. Furthermore, low crystallinity of MoS₂ and more defects in the carbon lattice also proved to be advantage for contributing to the high performance. Layer MoS₂ nanosheets further provide large

electrocatalytic surface areas for hydrogen evolution. Finally, the macropores provide easy access to the electrolyte for the catalysts based on the electrode, enhancing the communication between the electrolyte and the catalysts and further accelerating the reaction.

3.4 Conclusion

In summary, 3D network GA supported MoS₂ nanosheets have been successfully synthesized and demonstrated as a highly active and stable catalyst towards HER. The resultant material displays a well-organized structure with layer MoS₂ nanosheets uniformly distributed around the pores of GA. The unique 3D architecture and large active surface areas lead to superior HER activity with low overpotential and high catalytic current density. Moreover, GA-MoS₂ also exhibited good stability in acid solution, indicating the importance of the stable framework provided by 3D GA. The excellent electrochemical performance of GA-MoS₂ makes it a promising material for hydrogen evolution.

Chapter 4 Graphene-Co₃O₄ nanocomposite as electrocatalyst with high performance for oxygen evolution reaction

4.1 Introduction

Transition metal oxides, such as cobalt oxide, nickel oxide and manganese oxide, are promising electrochemical water oxidation catalysts.^{98, 101, 107, 119, 120, 129, 203} Among these catalysts, cobalt oxide, has attracted extensive attentions owing to their high activity and superior stability. F. W. Skirrow synthesized CoO_x by electrochemical deposition method in a buffered solution over a century ago. CoO_x has commonly been used as a cathode for electrochemical water splitting since the 1970s.²⁰⁴ The preparation technique of CoO_x has a great influence on the morphology and electrochemical performance, therefore, the researchers focused on developing new method to synthesize different morphology of CoO_x, such as nanowire, nanotube, nanocages, nanosphere et.al.²⁰⁵⁻²⁰⁷ CoO_x shows better catalytic performance in the alkaline solution, whereas the performance decreases in the neutral solution. Consequently, it is very urgent for the researchers to fabricate multi-functional CoO_x catalyst for electrocatalytic oxygen evolution reaction.

Co₃O₄, a typical spinel oxide, is an attractive oxygen evolution catalyst. The unique structure of Co₃O₄ leads to the high catalytic activity and stability in the oxygen evolution reaction.²⁰⁸⁻²¹⁰ Increasing surface area and engineering surface active sites of Co₃O₄ are effective way to enhance the catalytic performance.²¹¹⁻²¹³ Many efforts have been devoted to synthesizing porous frameworks or small size of Co₃O₄ by various preparation methods. For example, mesoporous Co₃O₄ has been reported as the OER catalyst with current densities of 27.2 mA cm⁻² at 1 V (vs. Ag/AgCl) and the crystalline Co₃O₄ showed a relatively small Tafel slope (49 mV dec⁻¹).^{211, 214} In addition, Co₃O₄

could also be utilized in photocatalytic system. Jiao *et al.* reported the photocatalytic properties of the mesoporous Co_3O_4 combined with the $[\text{Ru}(\text{bpy})_3]^{2+}$ with a high turnover frequency (TOF) of $\sim 2.2 \times 10^{-3} \text{ s}^{-1}$ per Co atom.²¹³ However, the strong causticity of alkaline solution and the intrinsically low conductivity of Co_3O_4 have impeded the further development of Co_3O_4 as OER catalyst.

Combining Co_3O_4 nanoparticles with conductive substrates can efficiently enhance the conductivity of the catalyst and significantly affect its catalytic activity and stability. Carbon materials, such as carbon nanotube (CNT), graphene (G) and mesoporous carbon, have been widely employed as the supporting substrates owing to their high conductivity and large specific surface area.²¹⁵⁻²¹⁷ Recently, Dai's group synthesized Co_3O_4 nanocrystals supported on graphene by hydrothermal reaction and demonstrated high electrocatalytic performance.²¹⁸ Zhao and coworkers reported OER catalysts of Co_3O_4 nanoparticle/graphene composites, fabricated by the layer-by-layer assembly.²¹⁹ $\text{Co}_3\text{O}_4/\text{CNT}$ (single-walled or multi-walled) materials were also prepared as high performance catalysts towards oxygen evolution.^{220, 221}

Herein, we report a simple method to prepare a unique sandwich-architected catalyst composed of graphene and Co_3O_4 (G- Co_3O_4). Ultrafine Co_3O_4 particles uniformly anchor onto both sides of graphene sheets. The unique sandwich-architecture leads to large amount loading of the active Co_3O_4 nanocrystals and enhances electron transfer kinetics between the materials. Therefore, the catalytic activity and stability of the catalyst have been substantially promoted. G- Co_3O_4 composite catalyst shows low overpotentials of 313 mV and 498 mV to achieve the current density of 10 mA/cm^2 in the alkaline and neutral conditions, respectively. Furthermore, there is no obvious current density decay after the stability test.

4.2 Experimental

4.2.1 The preparation of G-Co₃O₄

Graphene oxide (GO) was prepared by the oxidation and exfoliation of the graphite according to the previously reported procedure. Sandwich-like G-Co₃O₄ was synthesized *via* an oleic acid assisted method followed by thermal treatment.²²² In a typical synthesis process, 0.68 g oleic acid was mixed with 40 ml dry xylene under vigorous magnetic stirring. Then, 0.5 g cobalt acetate tetrahydrate (Co(AC)₂, Aldrich) was introduced into the mixture and sonicated for 1 min. After that, the mixture was mixed with 40 ml GO solution (2 mg ml⁻¹) by vigorous stirring and reacted in a pre-heated oil bath under refluxing for 4 h at 105 °C. Then, 10 ml (5 mg/ml) NaBH₄ was added to the reaction mixture and kept stirring for another 10 min. The precipitation was collected by filtration and annealed at 300 °C for 3 h in argon atmosphere. The final product was obtained after annealing at 400 °C for another 2 h in air.

4.2.2 The preparation of Co₃O₄

The pristine Co₃O₄ was synthesized by similar method without the addition of GO solution.

4.2.3 The preparation of Ru/C

The comparison sample of ruthenium nanocrystals supported on carbon black (Ru/C) was synthesized by using hydrophilic and hydrophobic tri-block copolymer F127 as a soft template, followed by low temperature heat treatment.²²³

4.2.4 Structural Characterization

The morphology of the obtained materials was characterized by field emission scanning electron microscopy (FESEM, Zeiss Supra 55VP) and transmission electron microscopy

(TEM, Model JEM-2011, JEOL). X-ray diffraction (XRD) patterns were collected on Siemens D5000 diffractometer using Cu K α radiation with a scanning step of 0.02° per second. Raman spectra were recorded with an inVia Renishaw Raman spectrometer system (HR Micro Raman spectrometer, Horiba JOBIN YVON US/ HR800 UV) equipped with a 632.8 nm wavelength laser. Thermal gravimetric analysis (TGA) of G-Co₃O₄ composite were performed using a TGA/differential thermal analysis (DTA) analyzer (TA Instruments, SDT 2960 module, New Castle, DE, USA) at a heating rate of 10 °C min⁻¹ in air from room temperature to 700 °C.

4.2.5 Electrochemical Measurements

Electrocatalytic activity measurements were carried out on an electrochemical workstation (CHI 660E) in a three-electrode glass cell system. A glass carbon (GC) electrode coated with as-prepared materials was used as the working electrode. A platinum wire was used as the counter electrode (CE). The potential was recorded using an Ag/AgCl (1 M KCl) reference electrode, which was converted to the reversible hydrogen electrode (RHE) according to Nernst equation $E_{\text{RHE}} = E_{\text{Ag/AgCl}} + 0.059 \times \text{pH} + 0.2224$. The working electrode was prepared as follows: 4 mg sample was dispersed in 1 ml of 1:1 v/v water/isopropanol by ultrasonification. Then 80 μl Nafion (5 wt %) was added to the solution to obtain a homogeneous ink. The catalyst ink (10 μl) was loaded onto the GC electrode with a diameter of 5 mm. Linear sweep voltammetry (LSV) was conducted in KOH solution (0.1 M, 1 M) and phosphate buffer solution (PBS, 0.1 M) at a scan rate of 2 mV s⁻¹. The polarization curves were all corrected by 95% iR compensation and our typical electrochemical cell had $R_u = \sim 8 \Omega$ in 1 M KOH, $R_u = \sim 20 \Omega$ in 0.1 M KOH and $R_u = \sim 26 \Omega$ in 0.1 M PBS. TOFs were calculated according to the equation of $\text{TOF} = n_{\text{O}_2}/n_{\text{Co}} = (Q/4F)/n_{\text{Co}}$ (F is the faraday constant, 96485 C/mol).

Stability was carried out for 10 h at 0.50 V (vs. Ag/AgCl) in 1 M KOH and 0.60 V (vs. Ag/AgCl) in 0.1 M KOH solution. Electrical impedance spectroscopy (EIS) was recorded under the following condition: ac voltage amplitude 5 mV, frequency ranges from 10^6 to 0.1 Hz, and open circuit. Cyclic voltammograms (CV) of G- Co_3O_4 and G+ Co_3O_4 measured in 1 M KOH solution in a potential window (-0.16 V to -0.08 V (vs. Ag/AgCl)) without faradaic processes with scan rates of 10, 30, 50, 70, 90 mV/s.

4.3 Results and discussion

4.3.1 The characterization of the catalysts

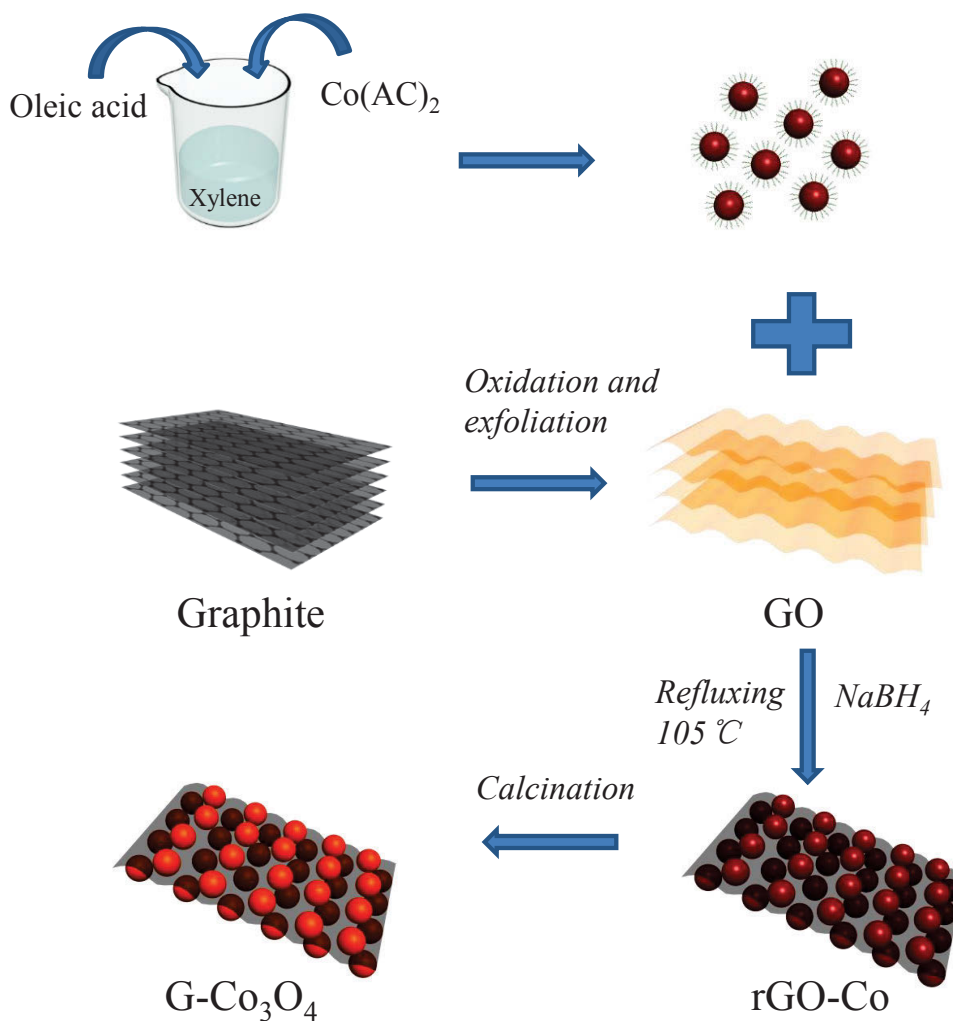


Figure 4-1 A schematic illustration for preparing G- Co_3O_4 nanocomposite with a sandwich-architecture.

The synthesis of the sandwich-architected composite is illustrated in Figure 4-1. Cobalt (II) acetate was added into the xylene and oleic acid mixed solution. The oleic acid in the mixture acted as a capping agent in order to control the particle growth and prevent colloidal particles from aggregation. Then, the as-prepared GO solution was introduced into the above solution under vigorous stirring. Co^{II} cations attached on both sides of the GO nanosheets by electrostatic interaction.²²⁴ During the following refluxing process and the reducing process by adding NaBH_4 , Co nanoparticles were loaded on the surface of rGO nanosheets. The final product of G- Co_3O_4 with unique sandwich-architecture was obtained after calcination.

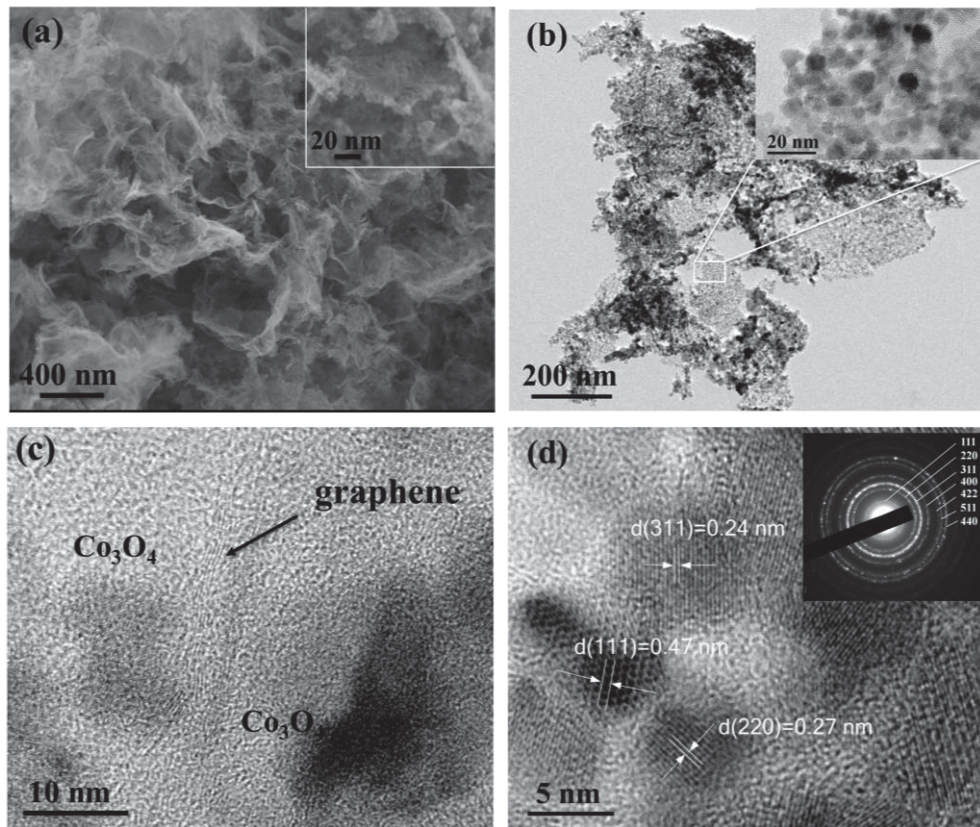


Figure 4-2 Microscope observation of the G- Co_3O_4 composite. (a) Low and high magnification SEM images of G- Co_3O_4 . (b) Low magnification TEM image of G- Co_3O_4 . (c) High resolution TEM (HRTEM) image of G- Co_3O_4 , showing a sandwich-like microstructure. (d) HRTEM image of Co_3O_4 nanocrystals and SAED pattern of G- Co_3O_4 .

The morphology of the synthesized G-Co₃O₄ composite was investigated by SEM. The low magnification image in Figure 4-2 (a) clearly shows that the obtained G-Co₃O₄ composite displayed layer structure. The high magnification in the inset of Figure 4-2 (a) shows two layers of Co₃O₄ particles homogeneously distributed. From the layer structure and the homogeneous distribution of the Co₃O₄ particles, we infer that the Co₃O₄ particles attached on both sides of the graphene nanosheets, which could form a unique sandwich-architecture. The TEM image in Figure 4-2 (b) further demonstrates the homogeneous distribution of Co₃O₄ nanoparticles on graphene substrate. High resolution TEM (HRTEM) in Figure 4-2 (c) clearly confirmed the sandwich-architecture. The graphene was definitely imbedded between the parallel layers of Co₃O₄ particles even after a strong sonication, suggesting a relatively strong interaction between graphene and Co₃O₄ particles. The graphene nanosheets acted as a binder to link neighboring Co₃O₄ particles together and also increased the conductivity of the composite. They can further prevent the aggregation of the Co₃O₄ nanoparticles during thermal treatment. Furthermore, as shown in Figure 4-2 (d), the lattice fringes in HRTEM image and the selected area electron diffraction (SAED) pattern further confirmed the formation of crystalline Co₃O₄.

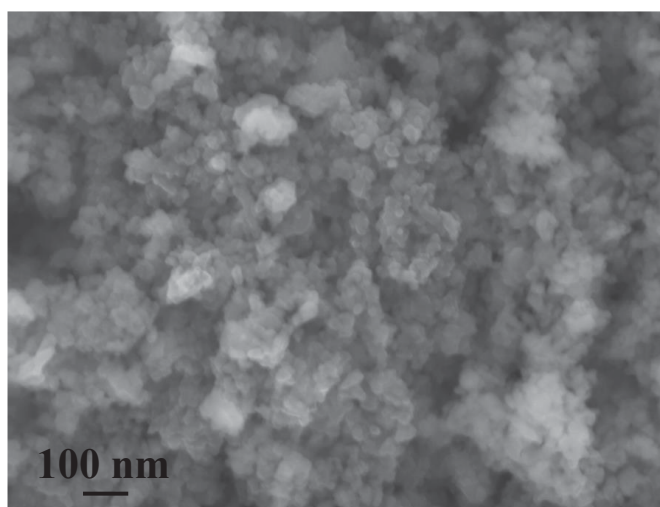


Figure 4-3 The SEM image of pristine Co₃O₄.

We also synthesized pristine Co_3O_4 through similar process without adding graphene oxide. The SEM image in Figure 4-3 shows that the Co_3O_4 nanoparticles seriously aggregated together with larger particle size of 30-40 nm. The larger particle size and aggregated phenomenon of bare Co_3O_4 nanoparticles reduced the surface area and active sites, which will result in decreased catalytic performance. By comparing the morphology of Co_3O_4 and G- Co_3O_4 composite, we notice that the introduction of graphene in G- Co_3O_4 composite leads to the formation of small particle, homogenous distribution and unique sandwich-structure.

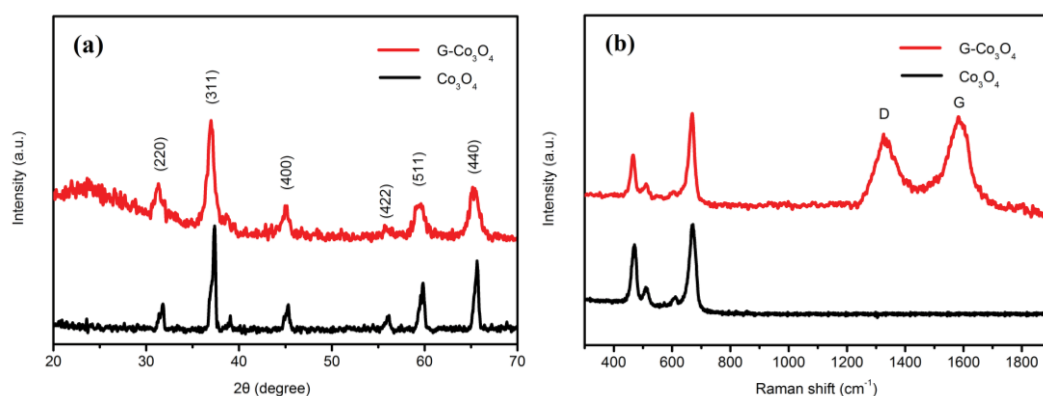


Figure 4-4 The characterization of the G- Co_3O_4 composite: (a) XRD patterns of Co_3O_4 and G- Co_3O_4 composite. (b) Raman spectra of Co_3O_4 and G- Co_3O_4 composite catalyst.

The crystal structure of the obtained G- Co_3O_4 composite and pristine Co_3O_4 nanoparticles was determined by X-ray diffraction (XRD) method as shown in Figure 4-4 (a). The prominent peaks at 31.2° , 37.1° , 45.1° , 59.7° , 65.6° of G- Co_3O_4 and pristine Co_3O_4 can be indexed to face-centered cubic phase (Fd3m, JCPDS card No. 76-1802). The broad diffraction peak appeared at around 24.8° in the G- Co_3O_4 composite is attributed to the (002) direction of graphene. Raman spectra of the G- Co_3O_4 composite and pristine Co_3O_4 are shown in Figure 4-4 (b). Two peaks at ca. 470 and 671 cm^{-1} can be assigned to Co_3O_4 . Moreover, G- Co_3O_4 also displays another two obvious peaks at 1327 and 1584 cm^{-1} , which can be indexed to the peaks of graphene.^{225, 226} The XRD

and Raman spectra further confirm the successful synthesis of G-Co₃O₄ composite catalyst.

4.3.2 The electrochemical performance test of the catalysts

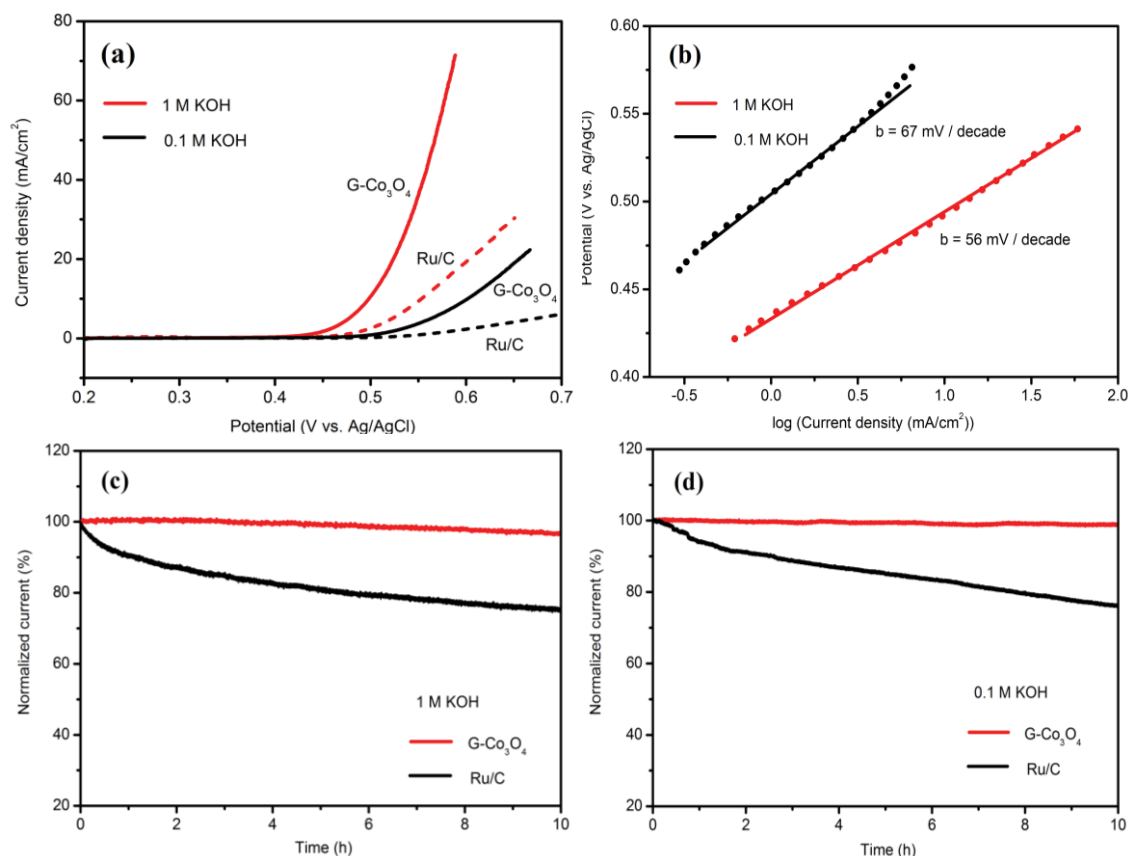


Figure 4-5 Electrochemical performance: (a) Polarization curves of G-Co₃O₄ and Ru/C catalysts on GC electrodes in 0.1 and 1 M KOH. (b) The Tafel curves of G-Co₃O₄ in 0.1 and 1 M KOH. (c, d) Chronoamperometric responses (percentage of current retained versus operation time) of G-Co₃O₄ and Ru/C catalysts in 1 M and 0.1 M KOH electrolytes.

Based on the mass content of the Co₃O₄ in the composite calculated from the TGA test and assuming that all deposited materials were involved in the electrochemical reaction, the lower limits for turnover frequency (TOF) can be derived from the catalytic current. We calculated a high TOF of 0.45 s⁻¹ referring to per Co atom for G-Co₃O₄ catalyst at the overpotential of 350 mV in 1 M KOH and 0.194 s⁻¹ at the

overpotential of 400 mV in 0.1 M KOH, which are higher than those of previous reports about Co based materials (Co_3O_4 , 0.08 s^{-1} at overpotential of 507 mV in 1 M KOH and mesoporous Co_3O_4 , $3.16 \times 10^{-3} \text{ s}^{-1}$ at 400 mV in 0.1M KOH).^{211, 227}

Tafel plot is applied to evaluate the efficiency of the catalytic reaction in alkaline solutions (0.1 and 1 M KOH), which is derived from the polarization curves using the Tafel equation $\eta = b \log(j/j_0)$, where η is the overpotential, b is the Tafel slope, j is the current density, and j_0 is the exchange current density. The G- Co_3O_4 catalyst exhibits Tafel slopes of $b = 56 \text{ mV/decade}$ in 1 M KOH and $b = 67 \text{ mV/decade}$ in 0.1 M KOH (Figure 4-5 (b)), which are lower than previously reported $\text{Co}_3\text{O}_4/\text{Graphene}$ (67 mV/decade in 1 M KOH) and graphene/ NiCo_2O_4 hybrid paper (156 mV/decade in 0.1 M KOH). The observed Tafel slope value suggests the favorable OER kinetics over G- Co_3O_4 catalyst and also the good chemical and electronic coupling between the Co_3O_4 nanoparticles and graphene nanosheets.

The G- Co_3O_4 catalyst also exhibits good stability in the alkaline solutions, which is another important factor for energy conversion systems. In 1 M KOH solution, the G- Co_3O_4 electrode shows excellent durability with no obvious activity decay compared with the initial value, while the Ru/C catalyst electrode degrades by 25.8 % of the initial value (Figure 4-5 (c)). A similar trend is also observed in 0.1 M KOH (Figure 4-5 (d)). The result of repeating potential cycling for 1000 cycles also confirmed the good stability of the material. Furthermore, no obvious morphology change is observed in the SEM image of G- Co_3O_4 after long-term stability testing, suggesting that G- Co_3O_4 catalyst can tolerate long-term corrosion and possess robust mechanical properties.

The G- Co_3O_4 composite has shown high catalytic activity and good stability towards OER in alkaline solution. On the other hand, the enhanced catalytic activities in

neutral solution are more desirable owing to the benign nature and weak causticity. The catalytic activity of Co_3O_4 towards OER is sensitive to a low pH value, especially for the neutral solution according to the previous investigation.²²⁸ Therefore, it is necessary to evaluate the electrochemical performance of G- Co_3O_4 catalyst in neutral solution.

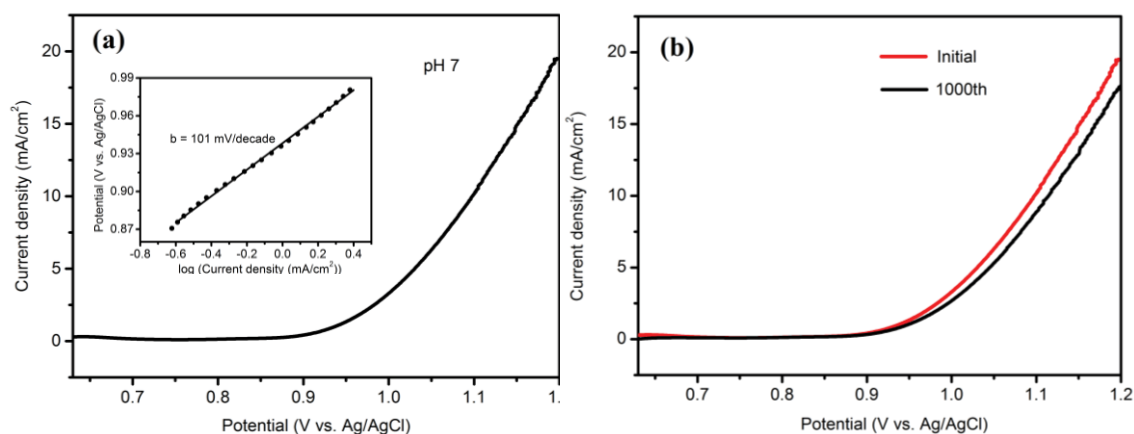


Figure 4-6 Electrochemical performance of G- Co_3O_4 composite OER catalyst: (a) LSV and Tafel slope of G- Co_3O_4 in neutral solution, (b) OER stability test of G- Co_3O_4 , the initial and 1000th polarization curves in neutral solution.

The G- Co_3O_4 electrode with the same mass loading was tested in 0.1 M phosphate buffer solution (PBS) at pH 7. The LSV curve of G- Co_3O_4 catalyst and the corresponding Tafel plot obtained in the neutral solution are presented in Figure 4-6 (a). In the neutral condition, G- Co_3O_4 catalyst shows an onset potential at 0.858 V (vs. Ag/AgCl) and achieves a current density of $j=10 \text{ mA/cm}^2$ at the overpotential of 498 mV, which exhibit better performance than those of the previous report (810 mV).²²⁰ Moreover, G- Co_3O_4 catalyst exhibits a little smaller Tafel plot of 98 mV/decade compared to others (104 mV/decade or 110 mV/decade).^{220, 229} The decreased Tafel slope value can be ascribed to the synergistic coupling and the fast charge transport of the materials. Furthermore, the stability of G- Co_3O_4 is assessed by repeated potential cycling for 1000 cycles, as shown in Figure 4-6 (b). Only a slight decay of the activity (< 10%) was observed referred to the polarization curves after the long-term test.

The excellent electrochemical performance of G-Co₃O₄ catalyst suggests its promising application towards OER both in alkaline and neutral solution. The high activity and excellent durability of G-Co₃O₄ towards OER are mainly attributed to the unique sandwich-architecture of the materials. A series of controlled experiments, shown in Figure 4-7, have demonstrated that the obtained G-Co₃O₄ catalyst displayed better OER activity than those of the simple physical mixture of Co₃O₄ and graphene (G+Co₃O₄), pure Co₃O₄ and graphene in 1 M and 0.1 M KOH conditions. The activity order is G-Co₃O₄ > G+Co₃O₄ > pure Co₃O₄ > graphene. The strong interaction of Co₃O₄ nanoparticles with graphene nanosheets and the unique sandwich-architecture have strong effect on the catalytic property of the composite. Simple physical mixing cannot create effective interfacial contacts between the Co₃O₄ nanoparticles and graphene nanosheets, resulting in lower catalytic performance.

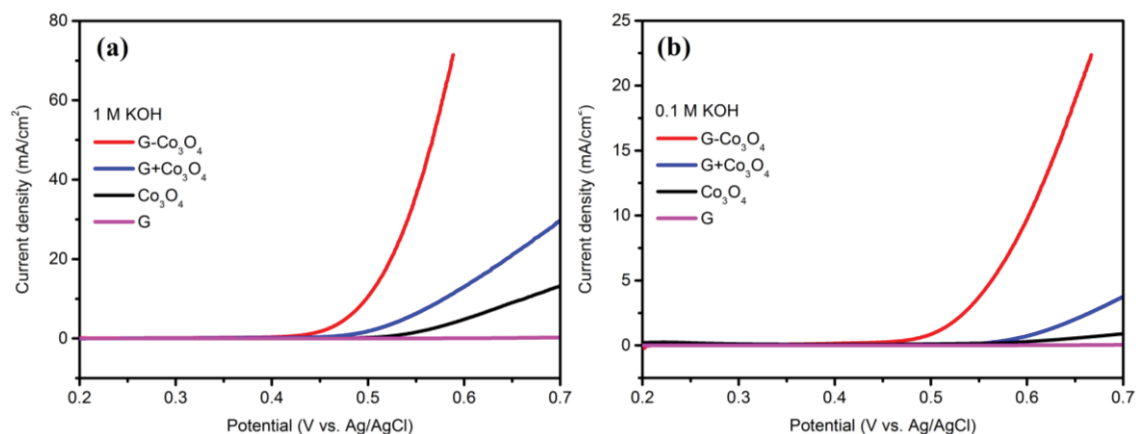


Figure 4-7 Electrochemical performance: Polarization curves of G-Co₃O₄, G+Co₃O₄, the pristine Co₃O₄ and graphene in (a) 1 M and (b) 0.1 M KOH solutions.

The Nyquist plots of G-Co₃O₄, G+Co₃O₄ and Co₃O₄ are shown in Figure 4-8, which show that the OER charge resistance of the G-Co₃O₄ catalyst is the smallest among the other samples (G+Co₃O₄, Co₃O₄). This further illustrates that the strong chemical coupling and good interaction between the Co₃O₄ and graphene can significantly improve the electron transport and reaction kinetics during the OER.

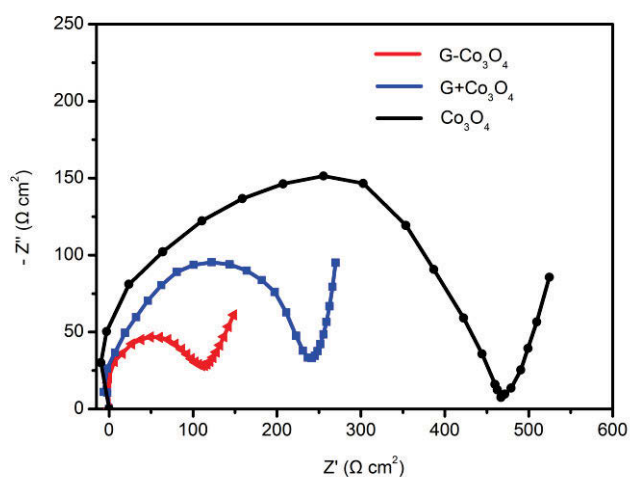


Figure 4-8 Nyquist plots of the G- Co_3O_4 , the G+ Co_3O_4 and the pristine Co_3O_4 modified electrodes in 1 M KOH solution.

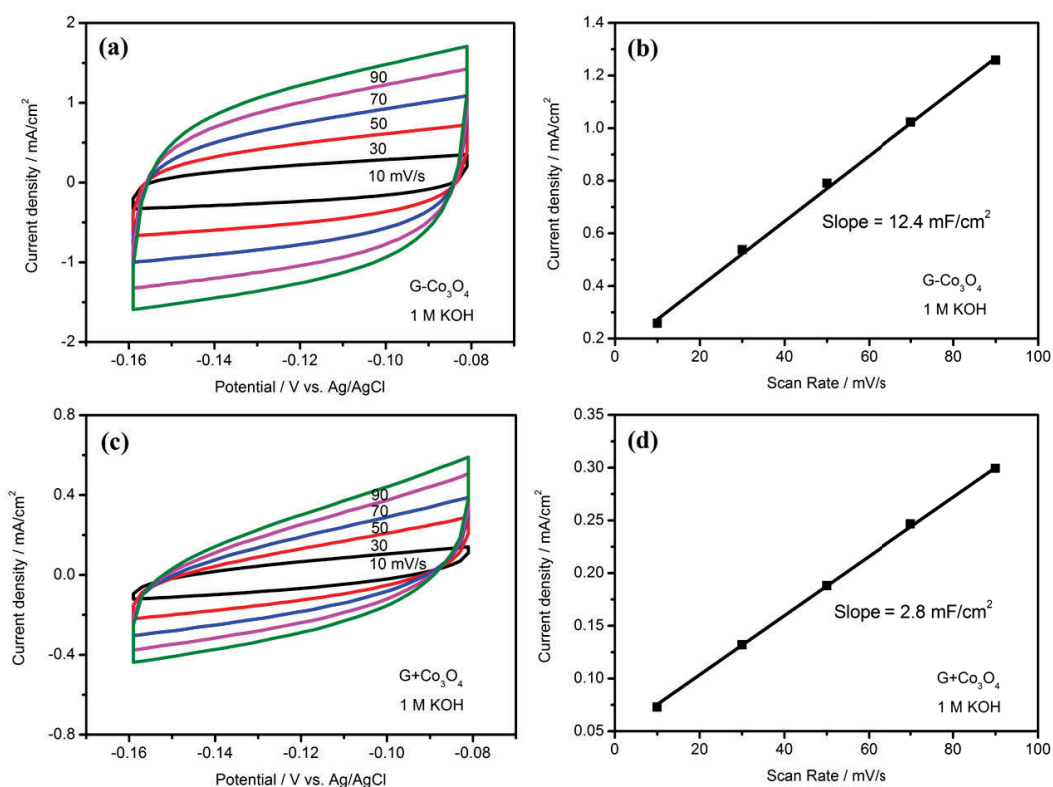


Figure 4-9 (a, c) Electrochemical capacitance measurements: typical Cyclic voltammograms (CV) of G- Co_3O_4 and G+ Co_3O_4 measured in 1 M KOH solution in a potential window without faradaic processes (scan rate: 10, 30, 50, 70, 90 mV/s); (b, d) Average capacitive current obtained from center of potential window (-0.12 V vs Ag/AgCl) as a function of scan rate for G- Co_3O_4 and G+ Co_3O_4 electrodes.

In order to further investigate the high performance of G-Co₃O₄, the effective surface areas were estimated, which was determined by electrochemical capacitance measurements from static cyclic voltammetry (Figure 4-9).^{200, 201} The capacitance for G-Co₃O₄ composite is 12.4 mF cm⁻², which is much higher than G+Co₃O₄ (2.8 mF cm⁻²). Therefore, the high performance could be also associated with the high electroactive surface area.

The observed enhanced activity of the G-Co₃O₄ catalyst indicates that the sandwich-architecture is favorable for the oxygen evolution, in which the graphene nanosheets provide large specific surface area and good conductivity. This specific structure also leads to large amount loading and much small particle size of the Co₃O₄ anchored on both sides of the graphene sheets, which provides much more electroactive surface area for the oxygen evolution. In addition, the unique and intimate contact between the graphene and Co₃O₄ afforded by one-step facile mechanism contributes to the superior catalytic activity.

4.4 Conclusion

In conclusion, sandwich-architected G-Co₃O₄ composite was successfully synthesized exhibiting good interaction between Co₃O₄ nanoparticles and graphene nanosheets. G-Co₃O₄ catalyst exhibits enhanced catalytic performances with high catalytic activities, good stability and favorable reaction kinetics in both the alkaline and neutral solutions, as catalyst for water oxidation. The enhanced catalytic performance demonstrates large electroactive surface area, fast electron transfer rate and superior electrical and chemical coupling of the composite. The unique morphology and excellent electrochemical performance of G-Co₃O₄ catalyst render this material a promising noble metal free catalyst towards the oxygen evolution reaction.

Chapter 5 Porous graphene wrapped CoO nanoparticles for highly efficient oxygen evolution

5.1 Introduction

In Chapter 4, we have studied the composite of metal cobalt oxide (Co_3O_4) and graphene with improved electron transport and strong interaction, resulting in enhanced catalytic performance towards OER. Porous graphene with controlled porous textures have garnered more interests compared to the nonporous graphene because of their attractive properties such as ordered pores, large pore volume and good conductivity.^{2, 230-232} Templates play pivotal roles in the pore generating process. Based on their physical properties, templates can be generally classified into two groups: rigid nanostructure solids (hard templates) and supramolecular aggregates (soft templates). Hard templates, such as Ni foam, silica spheres, polymer particles and coagulated solvents (freeze-drying), are usually employed to synthesize porous graphene with different pore sizes and morphologies.^{190, 233-242} For example, Wang's group report the synthesis of porous graphene with different pore size architectures by using different size and morphology of silica as hard templates.²⁴³ Porous graphene materials exhibited significantly higher discharge capacities than that of nonporous graphene. Furthermore, porous graphene with pore diameter around 250 nm showed the highest discharge capacity among the porous graphene with the small pores (about 60 nm) and large pores (about 400 nm). Soft template, usually take emulsions and micelles as the templates.²⁴⁴⁻²⁴⁶ Soft template method has some advantages, such as easy processing, high efficiency and low-cost, however, the pore size control capability of that soft template method is not satisfactory. Huang et.al developed F127 micelles and n-hexadecane as soft templates to synthesize porous graphene, respectively, which exhibited better performance in lithium- O_2 battery and hydrogen evolution reaction.^{247, 248}

Herein, we developed an active catalyst, CoO nanoparticles wrapped by porous graphene sheets. The porous graphene was prepared by using 1D silica nanorods as the template. The results indicate that ultrafine CoO nanoparticles were uniformly dispersed and wrapped by porous graphene, which could efficiently avoid the corrosion during electrochemical test. The homogenous distribution of particles and porous structure of graphene enable the efficient utilization of catalysts, which could be used as an active non-precious metal material for oxygen evolution.

5.2 Experimental

5.2.1 Synthesis of porous graphene catalysts (PGE)

1D silica nanorods were used as the template to synthesize PGE. The 1D silica nanorods were prepared according to a previous literature, using F127 and CTAB (hexadecyl trimethyl ammonium bromide) as binary templates in alkaline aqueous solutions at room temperature.³⁸ Typically, a solution formed by F127 (0.123 g), H₂O (3.5 ml), CTAB (12.5 ml, 0.04 M), and aqueous ammonia solution (15 ml, 2.5 wt %) and then TEOS (tetraethyl orthosilicate, 0.6 ml) was added under stirring. After stirring for 2 mins, the mixture was kept for 3 h at room temperature, resulting in the formation of a white suspension. After that, the resultant suspension (~ 20 ml) was dialyzed for 48 h and then diluted to 40 ml with deionized water. Concentrated HCl (10 ml, 10 M), DMDMS (dimethoxydimethylsilane, 0.5 ml) and Pluronic F108 (0.50 g) were added into the diluted suspension. The reaction was allowed to continue for another 48 h and then neutralized by the ammonium hydroxide solution (25 wt %). Graphene oxide (GO, obtained by oxidation and exfoliation of the natural graphite) suspension (120 ml, 1.0 mg ml⁻¹) was mixed with the neutralized solution and the mixture was left to stir for 12 h at room temperature. Then, the solid precipitate was obtained by centrifugation at

4500 r min⁻¹ and dried at 50 °C in vacuum oven. The dried precipitate was calcined at 900 °C for 5 h under the inert atmosphere. The final product (PGE) was achieved by washing with NaOH solution (2 M) twice to remove the template.

5.2.2 Synthesis of PGE-CoO catalyst

An ethanolic solution (20 mL) of cobalt nitrate (Co(NO₃)₂·6H₂O, 40 mg) was constantly stirred for 24 h at room temperature with 30 mg of PGE.³⁹ The resultant product was separated by filtration and dried at room temperature. The dried sample was then heat treated at 600 °C for 2 h in inert atmosphere to obtain the final product, PGE-CoO.

5.2.3 Synthesis of the comparison catalysts

Non-porous graphene-CoO (GE-CoO) was synthesized by the same method by replacing PGE with GE and the pure CoO was prepared without PGE.

5.2.4 Structural Characterization

The morphology of the as prepared materials was characterized by field emission scanning electron microscopy (FESEM, Zeiss Supra 55VP) and transmission electron microscopy (TEM, Model JEM-2011, JEOL). Element mapping was performed with Zeiss Evo SEM. X-ray diffraction (XRD) patterns were recorded by Siemens D5000 using Cu K α radiation with a scanning step of 0.02° per second. X-Ray Photoelectron Spectroscopy (XPS) was performed on ESCALAB250Xi (Thermo Scientific, UK) equipped with mono-chromated Al K alpha (energy 1486.68 eV). The Brunauer–Emmett–Teller (BET) surface area of the obtained materials was calculated by experimental points at a relative pressure of $P/P_0 = 0.05–0.25$. The percentage of CoO nanoparticles in PGE-CoO composite was analyzed using a TGA/differential thermal

analysis (DTA) analyzer (TA Instruments, SDT 2960 module, New Castle, DE, USA) at a heating rate of 10 °C min⁻¹ from room temperature to 800 °C in air atmosphere.

5.2.5 Electrochemical Measurements

All electrochemical measurements were performed in a standard three electrode glass cell on an electrochemical workstation (CHI 660E) with platinum wire as the counter electrode and Ag/AgCl (1 M KCl) as the reference electrode. The potentials reported here were quoted against the reversible hydrogen electrode (RHE) according to Nernst equation $E_{RHE} = E_{Ag/AgCl} + 0.059 \times pH + 0.2224$. The working electrode was prepared by depositing the target materials on the glassy carbon (GC) electrode with a diameter of 3 mm. 4 mg of the material was dispersed in 1 ml solvent (1:1 v/v water/isopropanol) by ultrasonication, followed by 80 μ l Nafion (5 wt %) was added to obtain a homogeneous ink. The catalyst ink (10 μ l) was loaded onto the GC electrode and then dried at room temperature. Linear sweep voltammetry (LSV) was conducted in KOH solution (selected concentration) at a scan rate of 10 mV s⁻¹. The polarization curves were all corrected by 95% iR compensation and turnover frequency (TOF) was calculated by the equation of $TOF = n_{O_2}/n_{Co} = (Q/4F)/n_{Co}$ (F is the faraday constant, 96485 C mol⁻¹). Electrical impedance spectroscopy (EIS) was recorded under the following condition: ac voltage amplitude 5 mV, frequency ranges from 10⁶ to 0.01 Hz, and open circuit or selected overpotential. Cyclic voltammetry measurements were conducted from -0.12 to -0.04 V (vs. Ag/AgCl) without faradaic processes at different scan rates (1 to 20 mV s⁻¹).

5.3 Results and discussion

5.3.1 The characterization of the catalysts

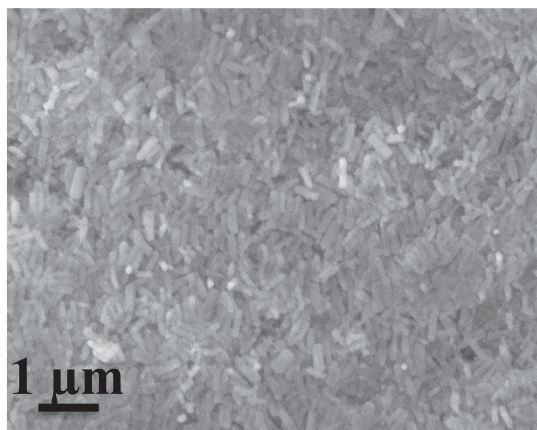


Figure 5-1 SEM image of silica nanorod templates for the synthesis of PGE.

The silica nanorods were first prepared by the well-known Stöber method. The SEM image in Figure 5-1 shows that the 1D silica nanorods with a size about 200 nm wide and 400 nm long.

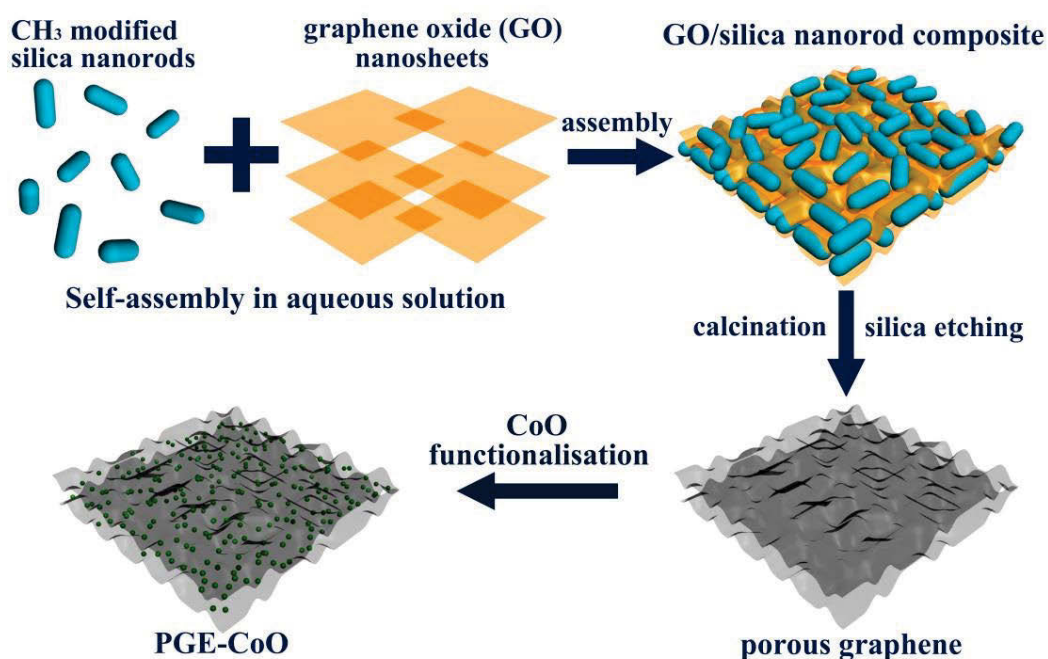


Figure 5-2 Schematic illustration for the synthesis procedure of PGE-CoO materials.

Graphene with highly porous structure was synthesized by a hard template method, which is effective for achieving porous graphene with controlled pore size. Figure 5-2

displays the schematic illustration for the synthesis route of the PGE-CoO hybrid. The 1D silica nanorods functionalized with surface methyl groups as the hard template. Subsequently, GO/silica composites were formed by mixing silica nanorods and GO nanosheet suspension together. The as-prepared composites were then calcinated in the inert atmosphere to reduce GO into PGE. The final products PGE-CoO were obtained by heating the mixture of PGE and cobalt precursor.

The SEM image of PGE in Figure 5-3(b) depicts the highly porous architecture with nanorod-shape pores. The structure and size of the pore are consistent with the particle shape of the silica nanorod templates. The BET results in Figure 5-3(a) reveal that PGE has a surface area of $417 \text{ m}^2 \text{ g}^{-1}$ and a large pore volume of $1.69 \text{ cm}^3 \text{ g}^{-1}$.

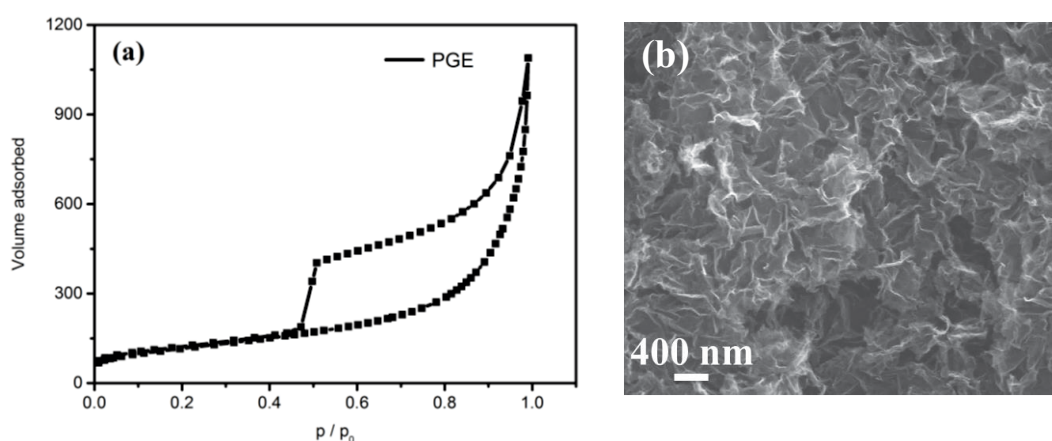


Figure 5-3 (a) Nitrogen adsorption/desorption isotherm of PGE, (b) SEM image of PGE.

The low magnification SEM image of PGE-CoO composite in Figure 5-4(a) shows that the material maintains the structure of porous graphene, which is beneficial to the effective contact of electrolyte/catalysts. Moreover, particles could not be observed in the low magnification SEM image. Figure 5-4(b) shows the high magnification SEM image of PGE-CoO composite. PGE and CoO particles are co-assembled into a well-organized hybrid. Moreover, highly distributed and ultrafine CoO nanoparticles were wrapped by porous graphene, which could efficiently avoid aggregation and corrosion

of CoO particles. TEM images in Figure 5-4(c, d) not only show the uniform distribution and good crystalline structure of CoO nanoparticles with the particle size less than 20 nm, but also confirm the wrapped structure, which is in consistent with the SEM result.

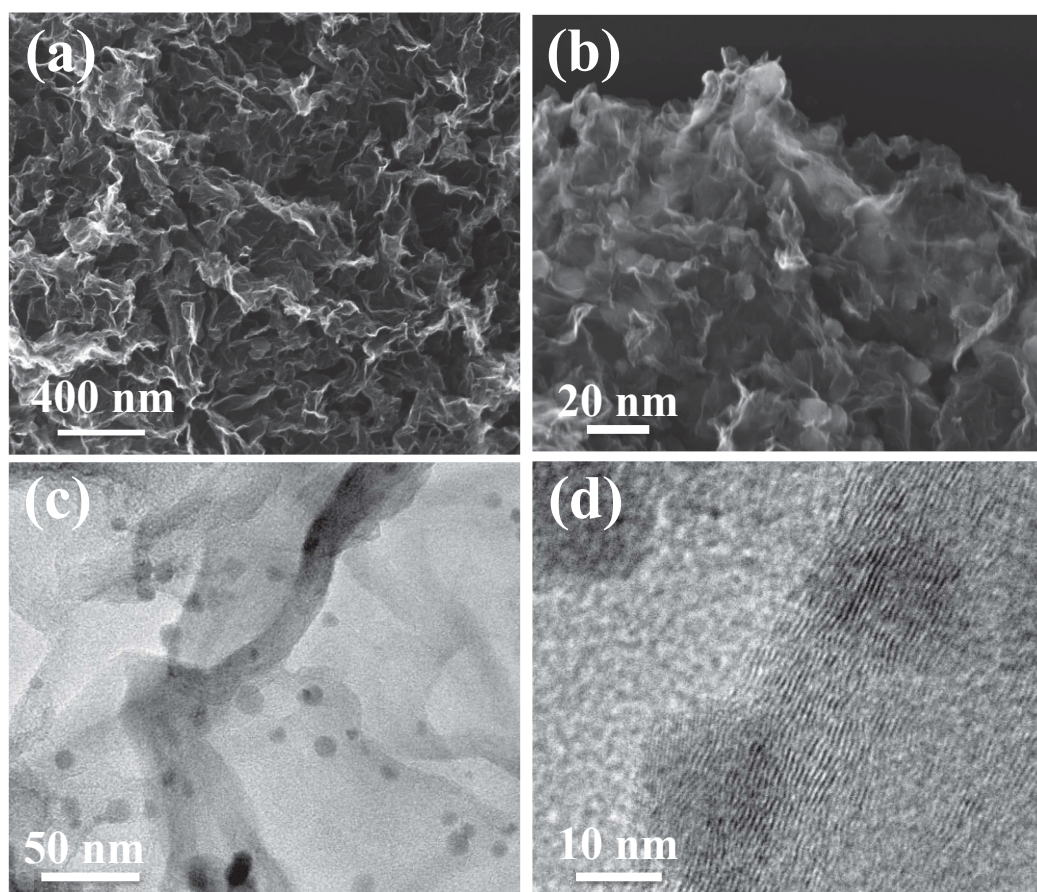


Figure 5-4 The characterization of PGE-CoO hybrid: (a, b) low and high magnification SEM images of PGE-CoO, (c, d) TEM images of PGE-CoO.

The pure CoO and GE-CoO are synthesized by using the similar method to PGE-CoO as the comparison materials. The SEM images of pure CoO and GE-CoO are shown in Figure 5-5(a, b). The pure CoO particles highly aggregated together, while GE-CoO displayed a relatively uniform distribution of CoO particles on graphene surface. However, no porous and wrapped structure could be found for CoO and GE-CoO, which illustrates that PGE as the substrate could not only provide large surface

area for the CoO growth, but also effectively prevent the aggregation and corrosion phenomenon. The nitrogen sorption isotherm of PGE-CoO hybrid shows a surface area of $254 \text{ m}^2 \text{ g}^{-1}$ and a pore volume of $1.35 \text{ cm}^3 \text{ g}^{-1}$, which are much higher than those of GE-CoO ($32 \text{ m}^2 \text{ g}^{-1}$, $0.14 \text{ cm}^3 \text{ g}^{-1}$) (Figure 5-5(c, d)).

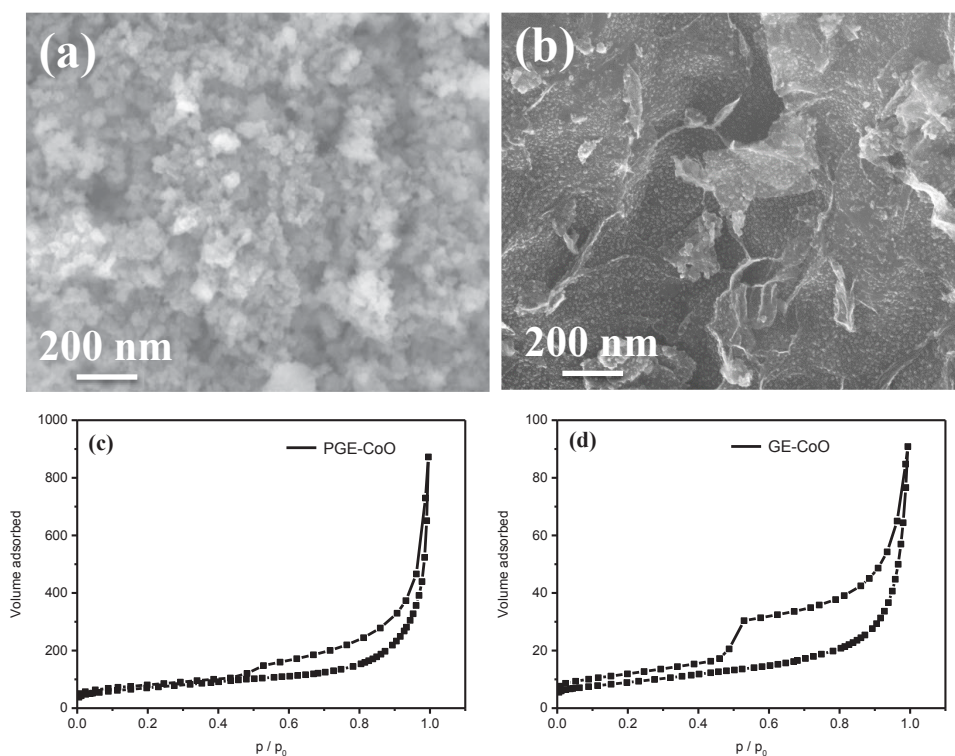


Figure 5-5 (a, b) SEM images of pure CoO and GE-CoO, (c, d) Nitrogen adsorption/desorption isotherm of PGE-CoO and GE-CoO.

Figure 5-6(a) shows the wide-angle XRD patterns of the PGE and PGE-CoO composite. The diffraction peak around 25° could be assigned to graphene (002) for both PGE and PGE-CoO. After loading CoO nanoparticles into PGE, two broad weak diffraction peaks appeared in the XRD pattern, which can be indexed to the (111) and (200) crystal planes of the cubic CoO (PDF No. 43-1004). XPS measurements were carried out on PGE-CoO to further investigate the composition and determine the surface electronic state. The high-resolution Co 2p spectrum exhibits two prominent peaks at 797.6 and 781.4 eV, corresponding to the Co $2p_{1/2}$ and Co $2p_{3/2}$ spin-orbit

peaks of CoO (Figure 5-6(b)). The peak O at 531.5 eV corresponds to the dominant O 1s feature in CoO (Figure 5-6(c)).^{203, 249} The TGA curve of PGE-CoO is presented in Figure 5-6(d), from which the content of CoO can be determined to be 16.8 wt %.

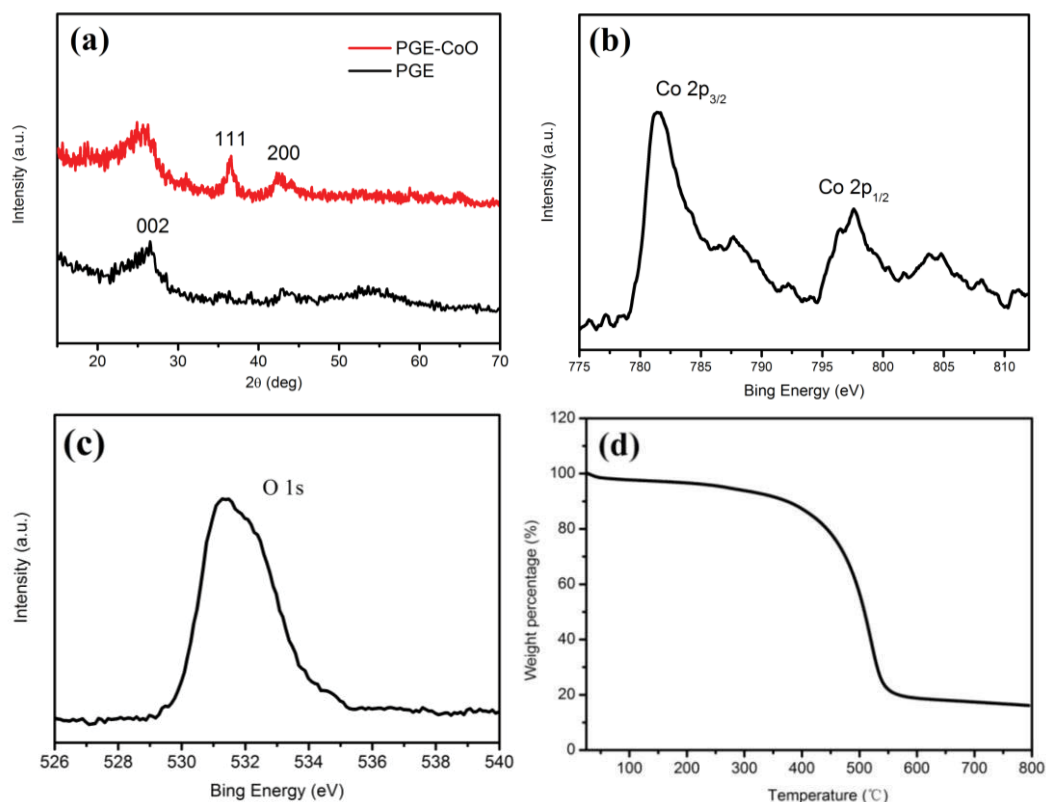


Figure 5-6 (a) XRD patterns of PGE-CoO and PGE, high-resolution spectra XPS (b) Co 2p, (c) O 1s, (d) thermogravimetric analysis in air of PGE-CoO.

5.3.2 The electrochemical performance test of the catalysts

The OER catalytic properties were investigated in a three-electrode system in 0.1 M KOH solution by LSVs. Comparative studies were performed on GE-CoO, CoO and PGE with the same loading. The PGE-CoO hybrid shows a high activity with a small onset potential of 504 mV (vs. Ag/AgCl, determined by Chen's method, Figure 5-7(a)), which is more negative than that of other samples, GE-CoO (560 mV) and CoO (570 mV). Moreover, the high activities can also be derived by the comparison of current density of the samples, especially for the current density of 10 mA cm⁻². The PGE-CoO

composite achieved a current density of $j=10 \text{ mA cm}^{-2}$ at the overpotential of 348 mV, which is even comparable to that of previously reported noble metal catalysts, and higher than many other Co-based materials (366 mV for NG-CoSe₂ and 390 mV for Co₃O₄/CNT) at the same conditions.^{221, 225} On the contrary, both CoO (510 mV) and GE-CoO (438 mV) exhibit much lower OER activities in terms of the same current density.

TOF could be calculated by the proportion of the CoO in the hybrid obtained from the TGA result and the current density. We achieved a high TOF of 1.37 s⁻¹ referring to per Co atom for PGE-CoO hybrid at the overpotential of 400 mV (GE-CoO 0.38 s⁻¹ and CoO 0.045 s⁻¹) in 0.1 M KOH. This value is the lower limits for turnover frequency, assuming that deposited materials were all involved in the electrochemical reaction. The TOF of PGE-CoO is also much higher than that of other previously reported Co based materials.^{211, 212}

The Tafel plots were derived from the LSVs, which are usually used to evaluate the efficiency of the catalytic reaction. The linear regions were fitted to the Tafel equation ($\eta = b \log(j/j_0)$, where η is the overpotential, b is the Tafel slope, j is the current density, and j_0 is the exchange current density). The PGE-CoO composite exhibits a Tafel slope of 79 mV dec⁻¹ (Figure 5-7(b)), which is much smaller than that of GE-CoO (192 mV dec⁻¹) and CoO (354 mV dec⁻¹). The small Tafel slope and high current density of PGE-CoO catalyst could be ascribed to the fast charge transport kinetics of the porous graphene and the strong interaction between PGE and CoO particles. This theory can also be confirmed by the EIS results under the condition of open circuit (Figure 5-7(c)). The samples displayed the similar trend with both of the semi-circles and the slopes. This indicated the similar mass transport properties and the reaction mechanism.

However, PGE-CoO hybrid shows much lower impedance compared to GE-CoO and CoO, which contributes to the high catalytic activities.

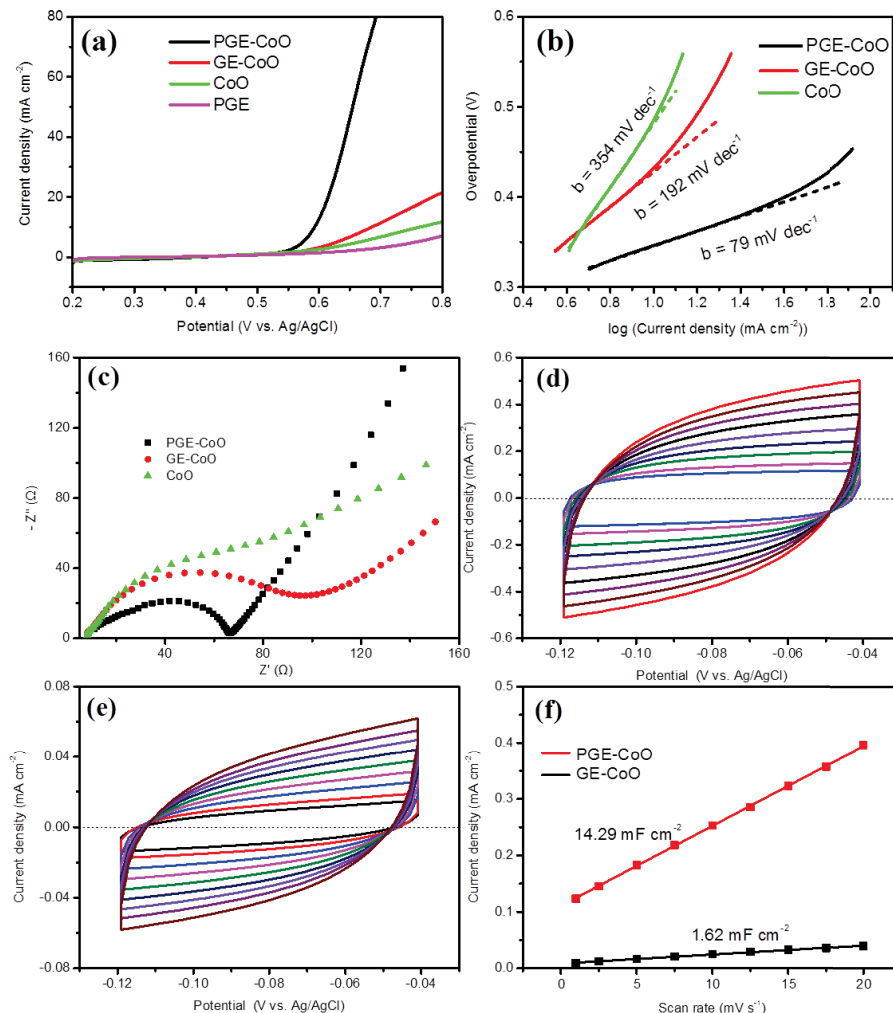


Figure 5-7 Electrochemical performance of the OER catalysts: (a) polarization curves for PGE-CoO, GE-CoO, CoO and PGE on GC electrodes in 0.1 M KOH. (b) Tafel curves of PGE-CoO, GE-CoO and CoO in 0.1 M KOH. (c) Nyquist plots of the PGE-CoO, GE-CoO and CoO modified electrodes in 0.1 M KOH solution. (d, e) electrochemical capacitance measurements: cyclic voltammograms (CV) were performed in 0.1 M KOH solution in a potential window without faradaic processes. (f) scan rate dependence of the average capacitive currents at -0.08 V vs Ag/AgCl for PGE-CoO and GE-CoO.

The electrochemically active surface areas for PGE-CoO and GE-CoO were estimated from the electrochemical double-layer capacitance of the catalytic surface.²⁰⁰,

201 Representative plots for the determination of PGE-CoO and GE-CoO surface areas are shown in Figure 5-7(d-f), respectively. Cyclic voltammetry measurements were conducted in a region of -0.12 ~ -0.04 V (vs. Ag/AgCl), where the currents are mainly attributed to the charging of the double layer. The capacitance of PGE-CoO is 14.29 mF cm⁻², while the capacitance of GE-CoO is only 1.62 mF cm⁻². The measured active surface areas is not an absolute value, however, it could serve as a guide for the comparison of surface roughness for the similar materials. The results are in good agreement with that of the BET results (PGE-CoO, 254 m² g⁻¹ and GE-CoO, 32 m² g⁻¹). The larger specific surface areas and active surface areas play an important role on the high performance of PGE-CoO towards OER.

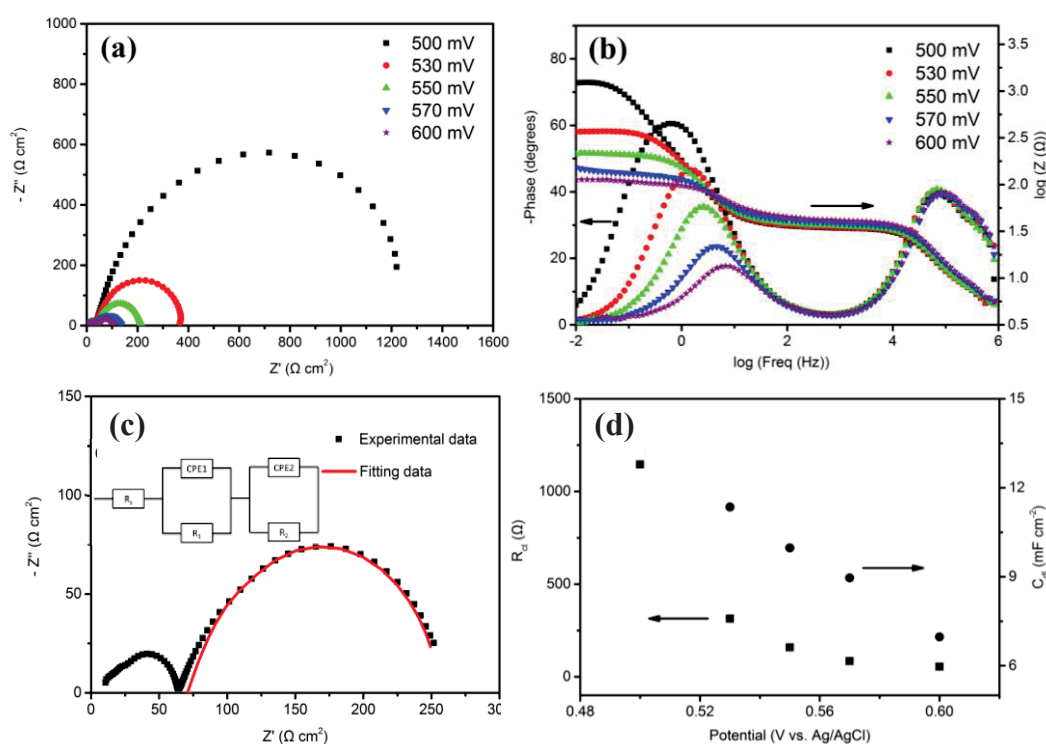


Figure 5-8 (a) Nyquist and (b) Bode plots for the PGE-CoO hybrid modified GC electrode recorded at various OER overpotentials in 0.1 M KOH, (c) the square symbols are experimental data and the red solid line are modelled by the Equivalent electrical circuit shown in the inset, (d) the low-frequency charge transfer resistance (R_{ct}) and

constant phase element (C_{dl}) as a function of the OER overpotentials for PGE-CoO-modified GC electrode in 0.1 M KOH.

EIS at various overpotentials was measured to further investigate the interface reaction and electrode kinetics of PGE-CoO hybrid towards OER in 0.1 M KOH solution. The representative Nyquist and Bode plots are presented in Figure 5-8(a, b). The analogous plot profiles at different overpotentials suggest the similar electrochemical mechanism towards OER. The PGE-CoO hybrid electrode displays two semicircles in the Nyquist plots at the selected overpotentials, which reveals the presence of two time constants: high-frequency time constant and low-frequency time constant.^{43, 202} The semicircle at high-frequency is attributed to the porous structure of the modified electrode and it displays constant properties over the different overpotentials; while the other one at low-frequency is related to process of electrochemical reaction at the interface. The Bode plots also display the same trend of two time constants. The superior electrocatalytic performance of PGE-CoO hybrid could be explained by the observation of the lower charge transfer resistance (R_{ct}) and higher interfacial capacitances during the reaction process (derived from the fitted data of low frequency) (Figure 5-8(c)). R_{ct} is related to the kinetics of electrocatalysis, and a lower value represents a fast reaction rate, which is strongly reliant on the overpotential. In this system, R_{ct} decreased from 1145 Ω at 500 mV (vs. Ag/AgCl) to 54.7 Ω at 600 mV. Furthermore, PGE-CoO displayed high constant phase element (CPE) during the test, varying from 13.25 mF cm⁻² to 6.97 mF cm⁻² and the decreased value of CPE may be ascribed to the bubbles blocking the active sites of the electrode materials during the test. The low charge transfer resistance and high interfacial capacitances during the test are mainly attributed to the superior conductivity of porous graphene and large specific

surface area, which further illustrated the high electrocatalytic performance of PGE-CoO hybrid towards OER.

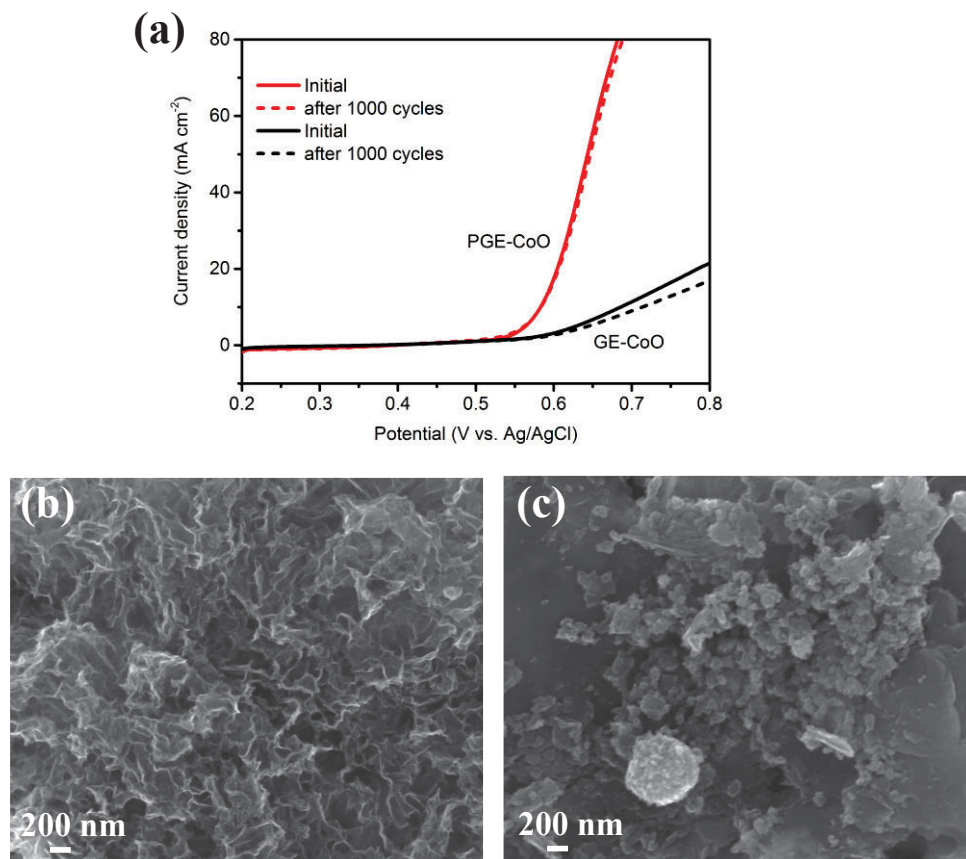


Figure 5-9 (a) The stability of PGE-CoO and GE-CoO modified electrodes before and after LSV testing for 1000 cycles, (b, c) SEM images of PGE-CoO and GE-CoO after stability test.

Besides the high catalytic activities, the good stability towards OER is also important for energy conversion system. The stability of the materials was measured for 1000 cycles. The PGE-CoO hybrid showed excellent durability in 0.1 M alkaline solution. Even after long time cycles, PGE-CoO electrocatalyst still remained a similar polarization curve to that in the initial cycle (Figure 5-9(a)), which should be ascribed to the unique wrapped structure and synergistic effects between CoO and flexible porous graphene. However, the stability of GE-CoO modified GC electrode was not as good as that of the PGE-CoO. After 1000 cycles, the anodic current density of the GE-CoO

electrode was reduced by about 20% (from 21.3 mA cm⁻² to 16.9 mA cm⁻² at 0.8 V, vs. Ag/AgCl). In addition, the *ex-situ* SEM also confirmed that the morphology of PGE-CoO is well maintained, however, the particles of GE-CoO all aggregated together after the stability test (Figure 5-9(b, c)). This further demonstrates the advantage of the wrapped structure of PGE-CoO composite, in which CoO particles are well confined by the porous graphene, which could not only prevent aggregation, but also protect CoO particles from corrosion, and therefore enhance the stability.

The excellent catalytic activity and durability indicate that PGE-CoO is an efficient OER catalyst, which could be attributed to the porous, wrapped structure and the strong chemical and electronic coupling between graphene and CoO. Normally, there are three intermediate steps in the oxygen evolution process. These include the adsorption of water onto electrode surface, splitting water into molecular oxygen and oxygen evolution. The porous structure of graphene can provide large specific surface areas for water adsorption and also play an important role for cobalt precursor to form the deposition of the active center (CoO particles). The porous structure could efficiently suppress the agglomeration of CoO particles and further expose much more active sites to oxidise OH⁻ to oxygen, which could accelerate the reaction process.

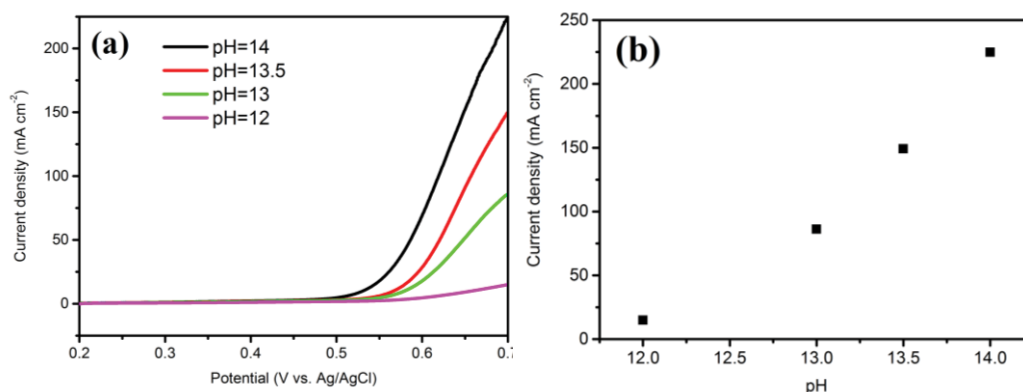


Figure 5-10 (a) Polarization curves for PGE-CoO in various KOH concentrations. (b) current densities at 0.7 V *vs.* Ag/AgCl for PGE-CoO in solutions with various KOH concentrations.

This study also illustrates that electrolyte concentration (OH^-) is also an important parameter for electrochemical reactions. Electrochemical catalysis using PGE-CoO catalyst was conducted in a series of KOH solutions with different pH. The results are presented in Figure 5-10. It was found that the oxidative catalytic activity gradually decreases with the lowering of alkaline concentration (from pH = 14, 224.89 mA cm⁻² to pH = 12, 14.89 mA cm⁻² at 0.7 V, *vs.* Ag/AgCl). Moreover, the high conductivity of graphene can offer fast charge transport between the material and the electrode. The porous structure plays an important role of access by water to “inner” catalytic layers in electrocatalytic reaction. The fast diffusional mass transport to the particles further confirms the efficient utilization of the catalyst. The wrapped structure is also attractive because it could not only enhance their interface contact, but also efficiently avoid the corrosion of CoO particles during the test and further enhance the stability. Finally, the synergetic effect between PGE and CoO is also an important factor for the enhanced catalytic activity and high durability.

5.4 Conclusions

In conclusion, we devised a noble-metal free electrocatalytic material for efficient oxygen evolution. The material consists of a well-organized structure, in which the CoO nanoparticles are well wrapped by porous graphene. The highly porous structure and the excellent chemical and electronic coupling between the composite material lead to the superior OER activity with a low overpotential and high catalytic current density. Furthermore, PGE-CoO also exhibited good stability in alkaline solution, indicating the wrapped structure could efficiently prevent the corrosion of CoO nanoparticles. PGE-CoO could be a promising electrocatalyst for oxygen evolution reaction.

Chapter 6: Ultrathin CoMn₂O₄ nanosheets with abundant Oxygen Vacancies vertically aligned on Functionalized Carbon Nanofibers as High-Performance Catalyst for Oxygen Evolution

6.1 Introduction

In chapter 4 and 5, we have investigated that transition metal oxide, cobalt oxide, as catalysts towards water oxidation, displaying excellent catalytic activity and stability. Recently, considerable attention has been drawn to the discovery of the ternary hybrid catalysts due to their unique structural property and excellent catalytic performance.^{250, 251} Several hybrid catalysts have been developed, such as Mo-W-P, Co-Mo-N, Ni-Co-O, Mn-Ru-O, exhibiting higher catalytic performance compared to the single ones.^{83, 252-254} Motivated by this strategy, the ternary compounds, by incorporating other cations, *e.g.* Mn, into the material of Co₃O₄, possess the mixed valence state and isostructural nature, thus their electrocatalytic activities towards OER suppose to be enhanced. Cobalt based ternary structure have a range of versatile properties, including abundance distribution, multiple valence and prominent Jahn-Teller effect.¹²⁵ These properties are highly sensitive to their chemical composition, crystallographic structures, and oxidation state of the cations, which depend strongly on the synthesis conditions. Therefore, it is urgently desirable to develop a simple, novel strategy to fabricate the efficient, high performance catalysts based on ternary composite for OER.

Apart from the compositions, the active sites also play an important role in the OER process, therefore, increasing their corresponding number and reactivity is an effective way to further enhance the catalytic performance. Ultrathin nanosheets, as a promising structural motif, possess the maximum number of active sites, which effectively enhances the activity of various kinds of metal oxides.^{122, 255, 256} Furthermore, oxygen vacancies in metal oxide have been reported to increase the catalytic

performance, as oxygen vacancies could not only directly serve as the active sites, but also change the geometric and electronic structures as well as the chemical properties of metal oxides.²⁵⁷⁻²⁶⁰ Consequently, the design of ultrathin nanosheets containing abundant oxygen vacancies seems to be an effective strategy to provide sufficient active sites for the electrochemical process.

As desired, a high active OER catalyst has been obtained by simply in situ growing ultrathin CoMn_2O_4 nanosheets with abundant oxygen vacancies vertically aligned on cobalt/nitrogen co-functionalized CNFs ($\text{CoMn}_2\text{O}_4\text{-CoNC}$) by a facile spontaneous redox reaction between CoNC and KMnO_4 solution. Different from the previous study (carbon and KMnO_4),²⁶¹⁻²⁶³ this is the first time we introduce in metallic cobalt as the co-reducing agent in the redox reaction and the ternary structure formed by the substitution of Mn with Co. The well aligned architecture, coexistence of Mn and Co cations, abundant oxygen vacancies, and strong synergetic interaction are responsible for the outstanding electrochemical catalytic performance. The resultant $\text{CoMn}_2\text{O}_4\text{-CoNC}$ composite manifests high catalytic activity (307 mV for 10 mA cm^{-2}) and an excellent stability during the OER process in an alkaline medium. This work paves the path for easy preparation of ternary structure catalysts to replace the benchmarking precious Ir/Ru OER catalysts.

6.2 Experimental

6.2.1 Synthesis of Nitrogen-doped CNFs (NC)

NC was prepared by using an electrospinning method with a subsequent heat treatment. Briefly, 600 mg of polyacrylonitrile (PAN, $M_w = 150,000 \text{ g mol}^{-1}$) were dissolved in 6 ml N,N-dimethylformamide (DMF). The above solution was left at 50 °C under vigorous stirring overnight and then transferred to a 10 ml plastic syringe with a 20-

gauge blunt tip needle. A high voltage of 18 kV was applied in the electrospinning process with a flow rate of $14.8 \mu\text{l min}^{-1}$. The distance between the needle and rotating grounded collector was around 15 cm. The as-collected electrospun fibers carbonized in an Ar flow at 800 °C for 6 h to obtain NC. The heating rate was kept at $1 \text{ }^{\circ}\text{C min}^{-1}$.

6.2.2 Synthesis of Cobalt/Nitrogen doped CNFs (CoNC)

CoNC was also fabricated by electrospinning method followed by high temperature treatment. Briefly, 320 mg of cobalt nitrate ($\text{Co}(\text{NO}_3)_2 \cdot 6\text{H}_2\text{O}$) and 600 mg of PAN were dissolved in 6 ml DMF. The above solution was left at 50 °C under vigorous stirring overnight and then transferred to a 10 ml plastic syringe with a 20-gauge blunt tip needle. The electrospinning process was same to that of NC. The as-collected electrospun fibers underwent the calcination process by heat treatment at 700 °C for 6 h in an H_2 ($\text{H}_2 : \text{Ar} = 5 : 95 \text{ vol\%}$) atmosphere. The heating rate was kept at $1 \text{ }^{\circ}\text{C min}^{-1}$.

6.2.3 Synthesis of CoMn_2O_4 nanosheets on CoNC ($\text{CoMn}_2\text{O}_4\text{-CoNC}$)

$\text{CoMn}_2\text{O}_4\text{-CoNC}$ was prepared by a facile spontaneous redox reaction between CoNC and KMnO_4 solution. Typically, 2 mg of KMnO_4 dissolved in 10 ml deionized water in a sealed glass bottle, followed by heating to 100 °C. The as prepared CoNC (3 mg) was added into the solution and maintained for different time (20 min, 1 h, 4 h, 8 h and 15 h). After the reaction, the samples were taken out and cleaned with water by filtration before being fully dried at 80 °C overnight under vacuum.

6.2.4 Synthesis of MnO_2 nanosheets on NCNFs ($\text{MnO}_2\text{-NC}$)

$\text{MnO}_2\text{-NC}$ was fabricated by the similar procedure to that of $\text{CoMn}_2\text{O}_4\text{-CoNC}$. Briefly, 2 mg of KMnO_4 dissolved in 10 ml deionized water in a sealed glass bottle, followed by heating to 100 °C. The as prepared NC (3 mg) was added into the solution and

maintained for 8 h. After the reaction, the samples were taken out and cleaned with water by filtration before being fully dried at 80 °C overnight under vacuum.

6.2.5 Synthesis of Co₃O₄ nanoparticles on CoNC (Co₃O₄-CoNC)

Co₃O₄-CoNC was synthesized by simply sintering CoNC in air at 450 °C for 2 h with a heating rate of 2 °C min⁻¹.

6.2.6 Characterization

The morphology and chemical composition of the as-prepared samples were observed by field emission scanning electron microscopy (FESEM, Zeiss Supra 55VP), element mapping and electron energy dispersive spectroscopy (Zeiss Evo SEM), transmission electron microscopy (TEM, Model JEM-2010, JEOL) and scanning transmission electron microscopy (STEM, JEOL JEM-ARM200F). X-ray diffraction (XRD) measurements were carried out by employing a scanning step of 0.04° per second in the 2 θ range from 10 to 80° (Bruker D8 Discover XRD). Raman spectra were collected on an inVia Renishaw Raman spectrometer system (HR Micro Raman spectrometer, Horiba JOBIN YVON US/ HR800 UV) using a 632.8 nm wavelength laser. X-ray photoelectron spectroscopy (XPS) measurement was performed on an ESCALAB250Xi (Thermo Scientific, UK) equipped with mono-chromated Al K alpha (energy 1486.68 eV). Brunauer–Emmett–Teller (BET) surface area of the obtained materials was achieved by using experimental points at a relative pressure of $P/P_0 = 0.05\text{--}0.25$. Thermogravimetric analysis (TGA) was carried out by simultaneous TG-DTA (SDT 2960) with a heating rate of 5 °C min⁻¹ from room temperature to 800 °C in air.

6.2.7 Electrochemical Measurements

The OER performance of the catalysts was measured on an electrochemical workstation (CHI 660E, CH Instrument) by using a three-electrode configuration with platinum wire and Ag/AgCl as the counter and reference electrodes, respectively. The reference electrode, Ag/AgCl (saturated KCl solution), was calibrated with the respect to the reversible hydrogen electrode (RHE), $E_{\text{RHE}} = E_{\text{Ag/AgCl}} + 0.059 \times \text{pH} + 0.1971$. The working electrode was glassy carbon (GC) electrode with a diameter of 3 mm. To prepared the electrode slurry, 4 mg of catalyst, 80 μl of Nafion (5 wt %) and 1 ml solvent (1:1 v/v water/isopropanol) mixed together and then sonicated for 30 min to form a dispersion. 10 μl of the dispersion was dropped onto the GC electrode (loading amount 0.56 mg cm^{-2}), followed by drying at room temperature. The polarization curves were obtained in 1 M KOH solution with a scan rate of 5 mV s^{-1} , which were all corrected for the iR contribution within the cell. The cycling performance of CoMn_2O_4 -CoNC based electrode was operated by repeating linear sweep votammograms (LSV) running for 5000 cycles and the current–time plots were obtained at a static overpotential. The electrochemical impedance spectra (EIS) were recorded with a frequency ranging from 10^6 to 0.01 Hz and an amplitude of 5 mV at a constant overpotential of 250 mV. To measure the electrochemical capacitance of the catalysts, cyclic voltammetry (CV) was conducted centered at open circuit potential at scan rates ranging from 10 to 100 mV s^{-1} .

For the rotating ring-disk electrode (RRDE) measurement, a rotating ring disk electrode with a glassy carbon disk (5 mm in diameter) and a Pt ring were used (Pine Research Instrumentation, USA). The as-prepared CoMn_2O_4 -CoNC catalyst was loaded onto the disk electrode by using the above mentioned method. A rotating speed of the RRDE was held at 1600 rpm for the test. To ensure the oxidation current originated from the

oxygen evolution, the ring potential was held constantly at 0.45 V *vs.* RHE to reduce the formed O₂ from the catalyst on the disk (disk potential fixed at 1.48 V *vs.* RHE) in N₂-saturated 1 M KOH solution. A continuous OER (disk electrode) → ORR (ring electrode) process occurred on the RRDE. The Faradaic efficiency was calculated as follows: $\varepsilon = I_r/(I_dN)$, where I_d is the disk current, I_r is the ring current, and N represents the current collection efficiency of the RRDE ($N = 0.2$). on the other hand, to detect the content of the formed hydrogen peroxide (HO₂⁻) intermediates, the ring potential was held constantly at 1.50 V *vs.* RHE in O₂-saturated 1 M KOH solution and recorded the data at a scan rate of 5 mV s⁻¹.

6.3 Results and discussion

6.3.1 The characterization of the catalysts

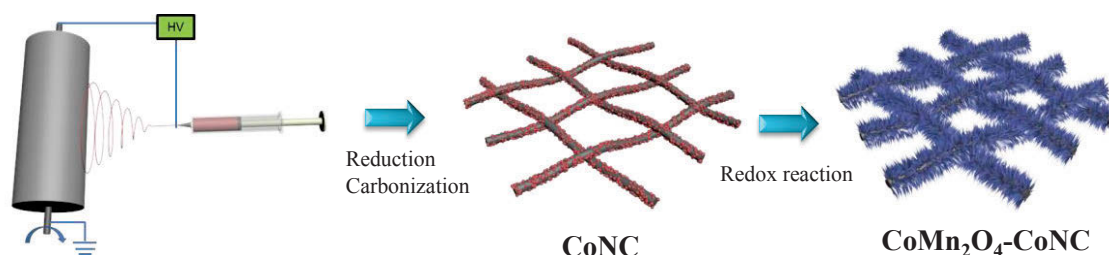


Figure 6-1 schematic illustration for the fabrication process of CoMn₂O₄-CoNC.

CoMn₂O₄-CoNC is facilely fabricated by two steps as shown in Figure 6-1. In the first step, the as-electrospun cobalt nitrate/PAN composite was obtained, followed by reduction and carbonization to achieve cobalt nanoparticles and nitrogen co-functionalized carbon nanofibers (CoNC). CoMn₂O₄-CoNC catalyst was produced through a spontaneous redox reaction by using metallic cobalt and carbon as the co-reducing agents and KMnO₄ as the oxidizing agent.

The morphology of CoNC precursor is first investigated by SEM. The representative SEM image in Figure 6-2(a) reveals CoNC possesses a well-organized 1-

D cylindrical morphology and form continuous carbon fiber networks. The average diameter of the electrospun nanofibers is around 500 nm and cobalt nanoparticles uniformly distribute on the surface of CNFs. The embedded cobalt nanoparticles of CoNC are elucidated by the TEM image (Figure 6-2(b)). The XRD spectrum of CoNC precursor in Figure 6-2(c) shows the typical peaks of metallic cobalt and graphitic carbon.

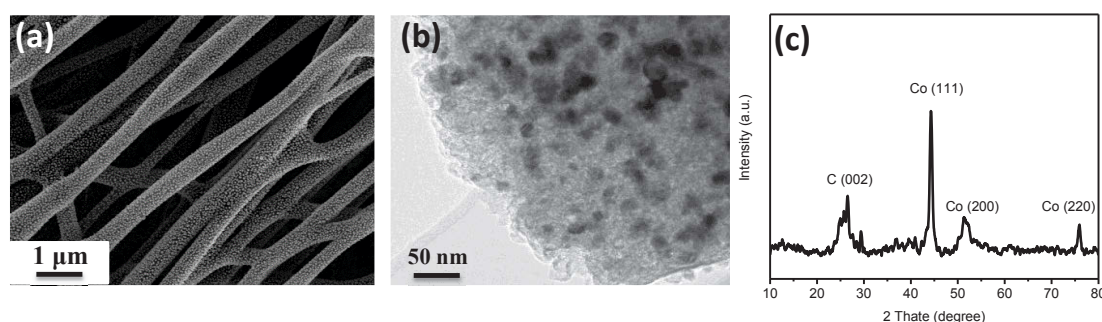


Figure 6-2 (a, b) SEM and TEM images of CoNC; (c) XRD pattern of CoNC.

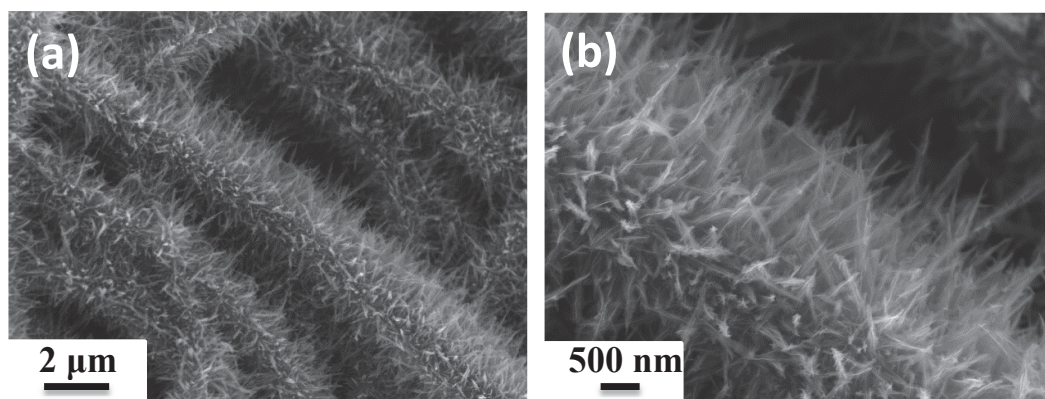


Figure 6-3 (a, b) the low and high magnification SEM images of CoMn₂O₄-CoNC.

After redox reaction between CoNC and KMnO₄, the hybrid catalyst well preserves the 1D structure of these carbon fibers, while the average diameter of the fibers increases to more than 2 μm (Figure 6-3). The entire surface of CoNC is uniformly covered with CoMn₂O₄ nanosheets. The densely packed nanosheets are vertically aligned on each individual nanofiber. Moreover, the hierarchical CoMn₂O₄

arrays possess abundant empty space among adjacent nanosheets, providing large area and easy way for electrode/reactant interaction.

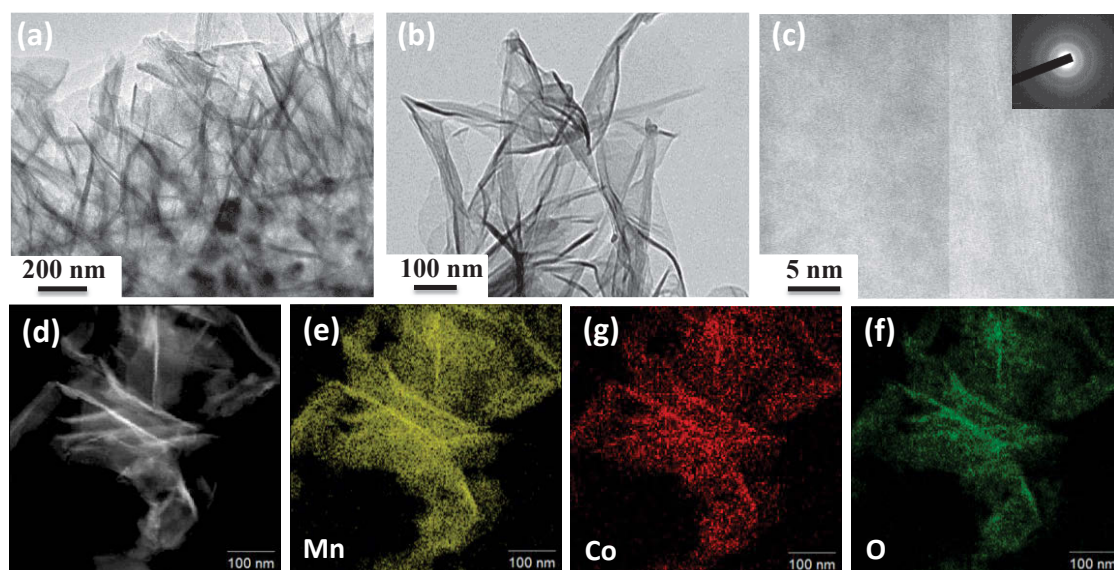


Figure 6-4 (a-c) low and high magnification TEM images of CoMn₂O₄-CoNC; STEM element mapping of CoMn₂O₄-CoNC: (d) high angle annular dark field (HAADF) image showing the area of mapping, (e-g) element mapping in STEM mode for Mn, Co and O elements.

The TEM image in Figure 6-4(a) further confirms the formation of the nanosheets on CoNC surface, where nanosheets with length of about 800 nm can be clearly observed. The interfacial profiles between CoMn₂O₄ nanosheets and CoNC could be well distinguished, showing their strong bond and intimate connection, which is in favour of electron transfer and structure stability. The remained embedded cobalt nanoparticles are inaccessible with the electrolyte and also beneficial to the electron transfer in the electrochemical process. The high transparency of CoMn₂O₄ nanosheets under the electron beam demonstrates their ultrathin nature (Figure 6-4(b)). The HRTEM image of a selected area of the CoMn₂O₄ nanosheets does not show any clear lattice fringe spacing, indicating their poor crystallinity (Figure 6-4(c)). STEM technology was used to investigate the microstructure of CoMn₂O₄ nanosheets. The

elemental mapping results prove the existence of cobalt, manganese and oxygen elements (Figure 6-4(d-f)), demonstrating the homogeneous distribution of the above mentioned three elements in the nanosheets.

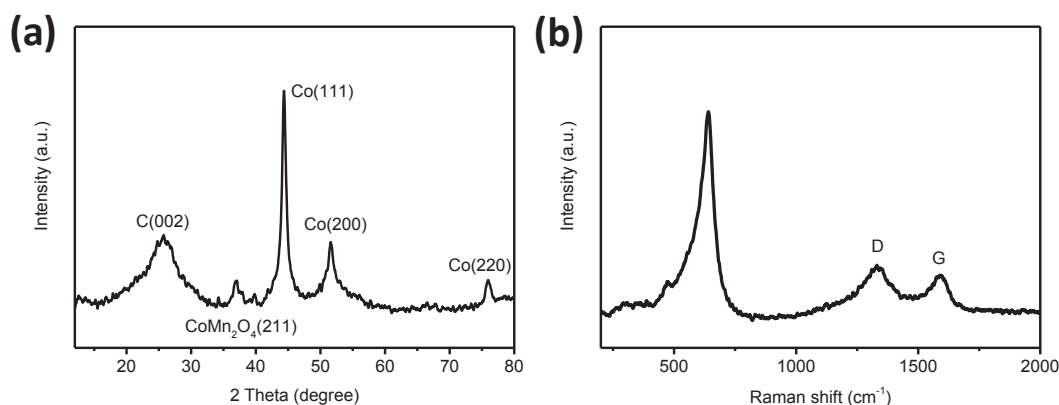


Figure 6-5 (a, b) XRD and Raman spectra of CoMn₂O₄-CoNC.

The structure information of CoMn₂O₄-CoNC is investigated by XRD. As shown in Figure 6-5(a), the diffraction peak of carbon in CoMn₂O₄-CoNC composite appears at around 25.9°, referring to the partially graphitized carbon species, which formed with the assistance of cobalt nanoparticles as catalyst during high temperature process. The predominated peaks at around 44.4, 51.7 and 76.1° are attributed to the encapsulated metallic cobalt, indexing to the (111), (200) and (220) crystal planes of the cobalt (PDF No. 15-0806). The rest low intensity peaks located between 34 and 42°, such as 34.3, 37.0, 37.9, 39.8, 41.9° can be indexed to CoMn₂O₄, indicating the successful formation of CoMn₂O₄ during the redox reaction. The low intensity XRD peaks of CoMn₂O₄ are ascribed to low crystallinity property, in accordance with the HRTEM result. The Raman spectrum of CoMn₂O₄-CoNC composite reveals the existence of D-band (1335.6 cm⁻¹) and G-band (1589.8 cm⁻¹) for CNFs (Figure 6-5(b)). Apart from the peaks of carbon in Raman spectrum, there are two more peaks could be observed at 473 and

639 cm^{-1} , associated with M–O stretching vibrations (M = Mn, Co), further suggesting the successful preparation of CoMn_2O_4 .²⁶⁴

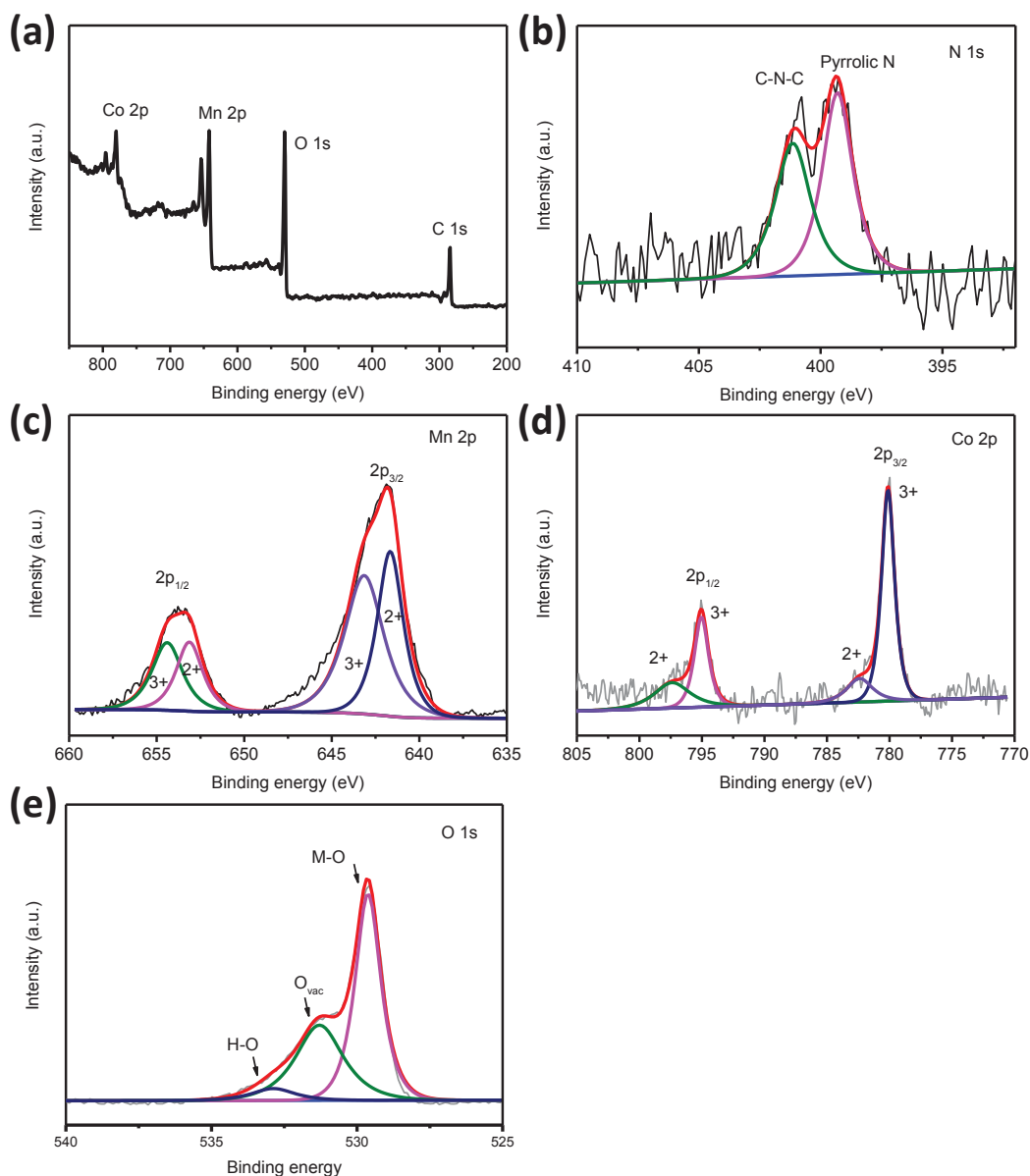


Figure 6-6 (a) XPS survey spectra of $\text{CoMn}_2\text{O}_4\text{-CoNC}$, high resolution XPS spectra of $\text{CoMn}_2\text{O}_4\text{-CoNC}$, (b) N 1s, (c) Mn 2p, (d) Co 2p, (e) O 1s.

The chemical composition of $\text{CoMn}_2\text{O}_4\text{-CoNC}$ is further investigated by XPS. Figure 6-6(a) shows the XPS survey spectrum of $\text{CoMn}_2\text{O}_4\text{-CoNC}$ composite, and only C, O, Mn, Co elements could be observed. No distinguishable signal for N in the survey spectrum because of the core-shell structure with long CoMn_2O_4 nanosheets aligned on

CoNC. The high-resolution N 1s spectrum in Figure 6-6(b) reveals the presence of pyrrolic N and C-N-C. The high resolution spectra of Mn and Co display the co-existence of +2 and +3 in manganese and cobalt species with the atomic ratio of 2.4/1 (Mn/Co) (Figure 6-6(c, d)). Three peaks can be identified from the O 1s spectrum centred at 529.6, 531.3, 532.9 eV to reflect three different oxygen environments (Figure 6-6(e)). The band at 529.6 eV corresponds to lattice oxygen atoms bound to metals in a fully coordinated environment, whereas 532.9 eV is attributed to the surface adsorbed species (M-OH). Moreover, the band at 531.3 is deemed as the oxygen atoms in the vicinity of an oxygen vacancy.

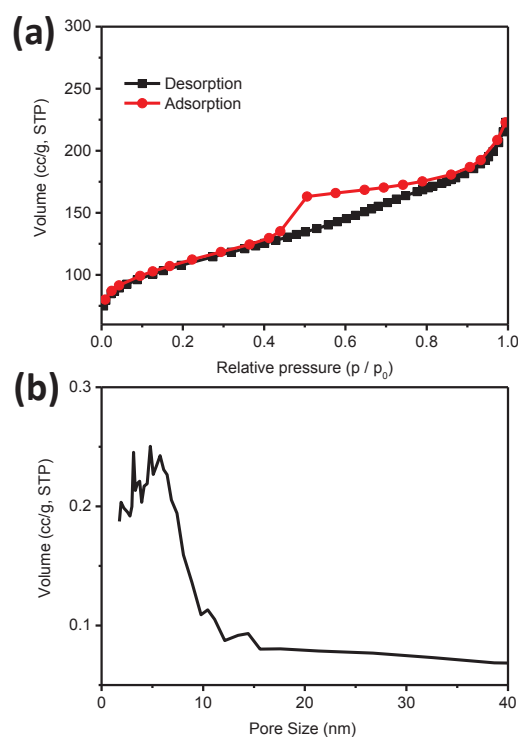


Figure 6-7 (a) Nitrogen adsorption/desorption isotherm and (b) pore size distribution of CoMn₂O₄-CoNC.

The surface area and pore size distribution are investigated by N₂ sorption measurements. The N₂ sorption isotherms of CoMn₂O₄-CoNC can be identified as type-IV isotherms, with a pronounced hysteresis loop (uptakes at a relative pressure ranging

from 0.4 to 0.9), suggesting the existence of a mesoporous structure. $\text{CoMn}_2\text{O}_4\text{-CoNC}$ shows a relatively broad pore size distribution (mainly centered at 3-9 nm) and large specific surface area of $360.7 \text{ m}^2 \text{ g}^{-1}$ (Figure 6-7).

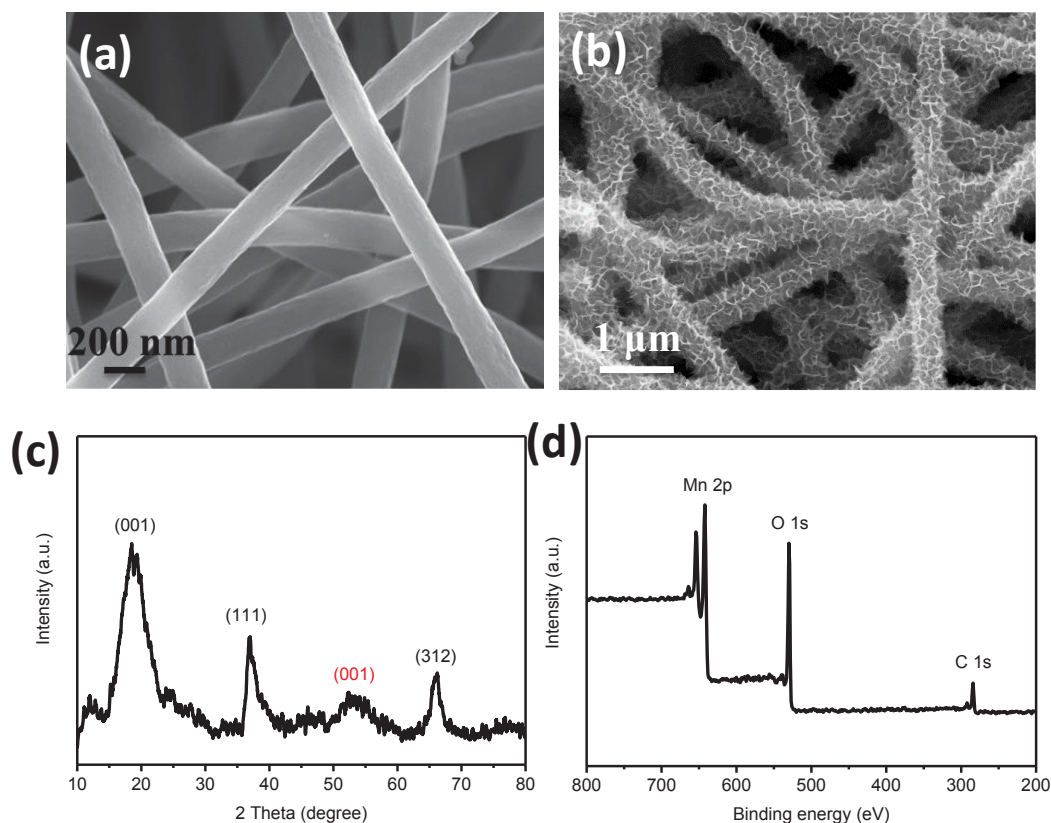


Figure 6-8 (a) SEM image of pure NCNFs, (b) SEM image, (c) XRD spectrum, (d) XPS survey spectrum of $\text{MnO}_2\text{-NC}$.

It is noteworthy that the presence of metallic cobalt plays a critical role in the formation of long, ultrathin CoMn_2O_4 nanosheets during the redox reaction. The metallic cobalt can work as cobalt source and reducing agent (together with carbon), while KMnO_4 acts as manganese source and oxidizing agent, and both of them contribute to the eventual formation of CoMn_2O_4 nanosheets. In contrast, only interconnected MnO_2 nanosheets could be observed in the absence of cobalt nanoparticles in CNFs, which is similar to the previous reports of MnO_2 nanosheets

derived from the redox reaction between carbon and KMnO_4 (SEM, XRD and XPS shown in Figure 6-8).²⁶¹⁻²⁶³

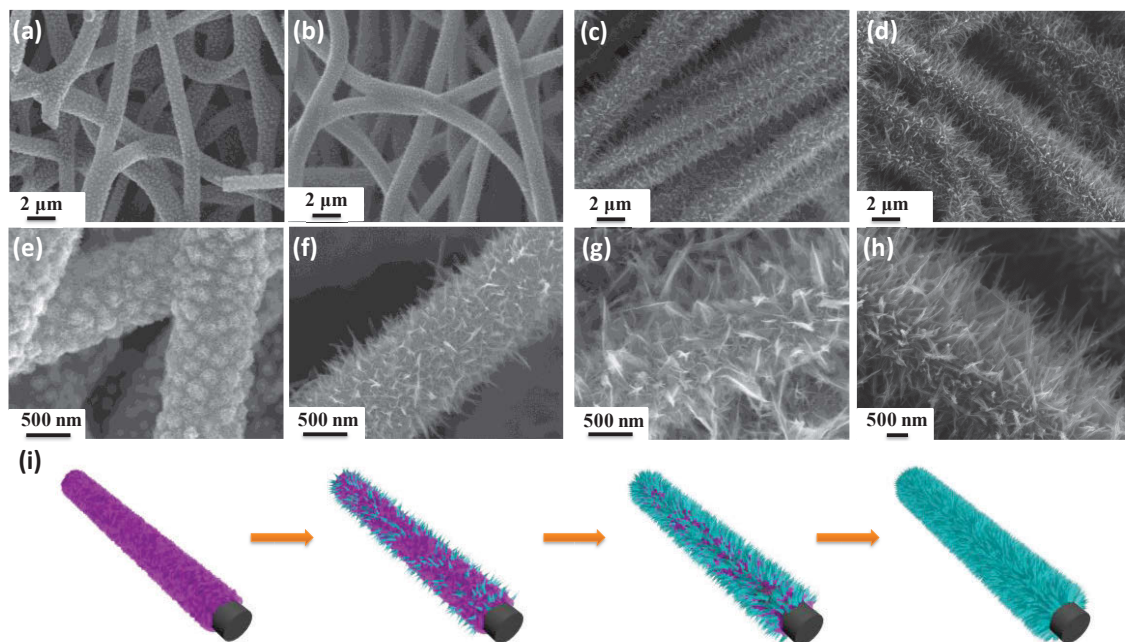


Figure 6-9 Typical SEM images of the products after reaction for (a, e) 20 min, (b, f) 1 h, (c, g) 4 h and (d, h) 8 h. (i) Schematic illustration of the formation procedure of CoMn_2O_4 -CoNC composite.

To better understand the function of cobalt in the synthesis process, time course study was carried out on CoMn_2O_4 -CoNC. As shown in Figure 6-9, after 20 min reaction, particles on the surface of CoNC still could be observed, besides, decorated by many tiny nanosheets, attributing to the redox reaction between Co/C and KMnO_4 . The lateral dimension of the nanosheets increases after 1 h reaction, accompanied by the gradual disappearance of the nanoparticles. With the reaction proceeding, obviously, the nanosheets (CoMn_2O_4) achieved based on cobalt nanoparticles are much longer and thinner than the products derived from carbon, which suggests that metallic cobalt nanoparticles possess better catalytic ability during the redox reaction. After 4 h reaction, long CoMn_2O_4 nanosheets surrounding little amount MnO_2 are observed on

CoNC. It is worth noting that long and ultrathin CoMn_2O_4 nanosheets vertically aligned on CoNC are obtained after 8 h redox reaction.

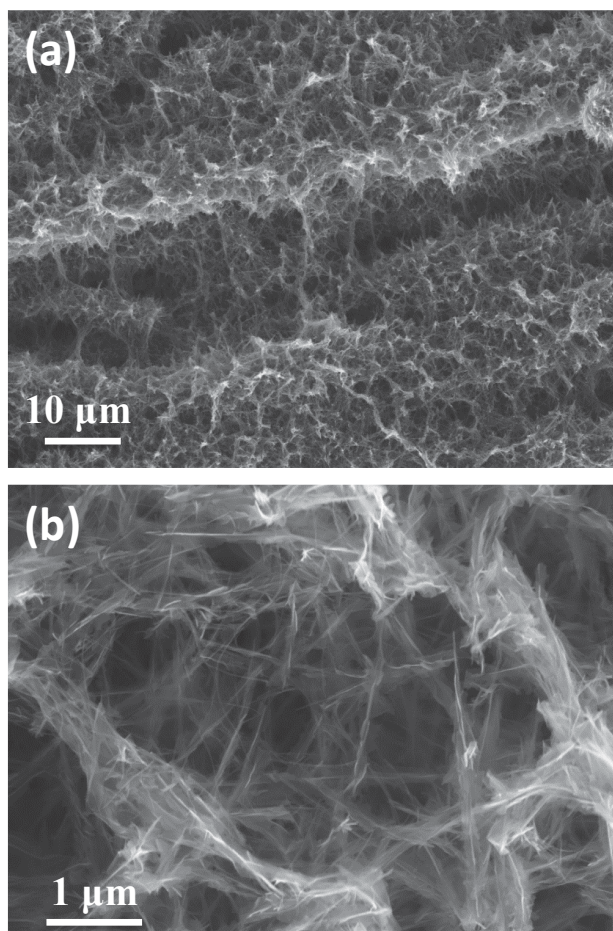


Figure 6-10 (a, b) SEM images of CoMn_2O_4 -CoNC obtained after 15 h reaction.

We try to further prolong time, the framework of CoNC is destroyed (Figure 6-10, 15 h reaction), maybe ascribed to the complete consume of Co/C or the involvement of long nanosheets, therefore, we mainly focus on the first four stages in the following characterizations.

The XRD of the products during the redox reaction process are presented in Figure 6-11(a). The XRD result in Figure S8a suggests the co-existence of CoMn_2O_4 (37.0, 39.8°) and MnO_2 (42.5, 61.4°) in the products after 20 min and 1 h reactions. The corresponding peaks for MnO_2 disappear after 4 h reaction, and more XRD peaks for CoMn_2O_4 (between 34 and 42°) emerge (after 8 h reaction), reversely. The Raman

spectra show the enhanced vibration of M-O (M=Mn, Co) and reduced peaks for carbon with the reaction proceeding Figure 6-11(b).

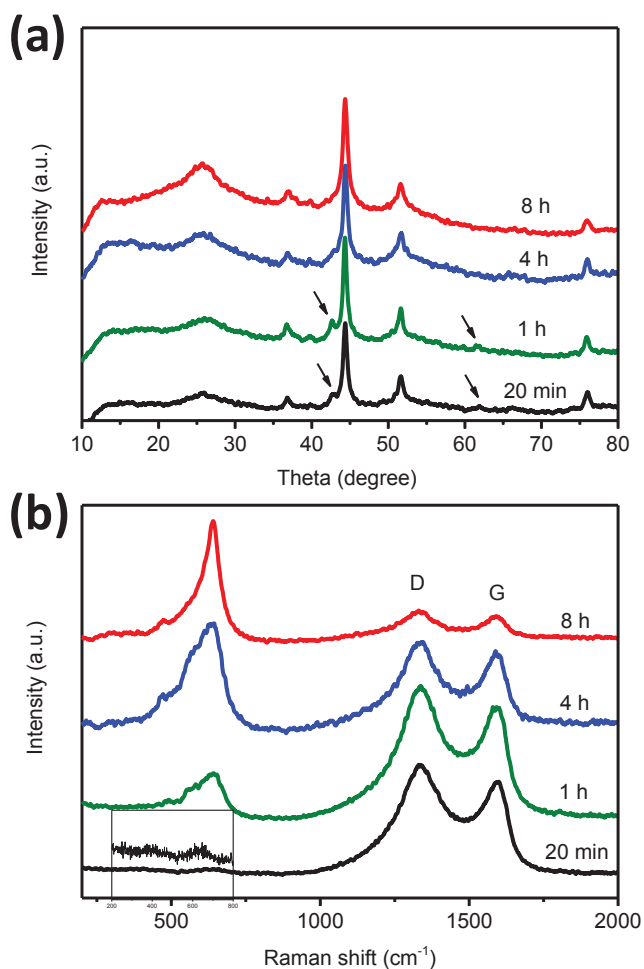


Figure 6-11 (a) XRD and (b) Raman spectra of CoMn₂O₄-CoNC obtained at different time.

The XPS analysis (survey spectra, Figure 6-12(a)) reveals that the products we obtained at different stage show similar elemental composition (C, O, Mn, Co). The high resolution spectrum of Co 2p shows similar peak position (Figure 6-12(b)), while the position of Mn 2p slightly shifts to the lower binding energy (Figure 6-12(c)), which signifies the decrease of Mn valent state along with the reaction time. The ratio between manganese and cobalt (Mn/Co) decreases during the redox reaction process from 12.89 to 2.47, further reconfirming the embedded cobalt nanoparticles participated in the

redox reaction. In the O 1s core level spectra, three peaks can be clearly identified for the samples obtained at different time. The major O 1s peak for the samples shifts to a lower level with the reaction process (Figure 6-12(d)), which indicates a change in the coordination configuration of M-O (M=Mn, Co). More importantly, the area of the peak at around 531.3 eV increases along with the reaction time and CoMn₂O₄-CoNC after 8 h reaction shows the largest area, suggesting more oxygen vacancies introducing into the CoMn₂O₄ nanosheets during the redox reaction.

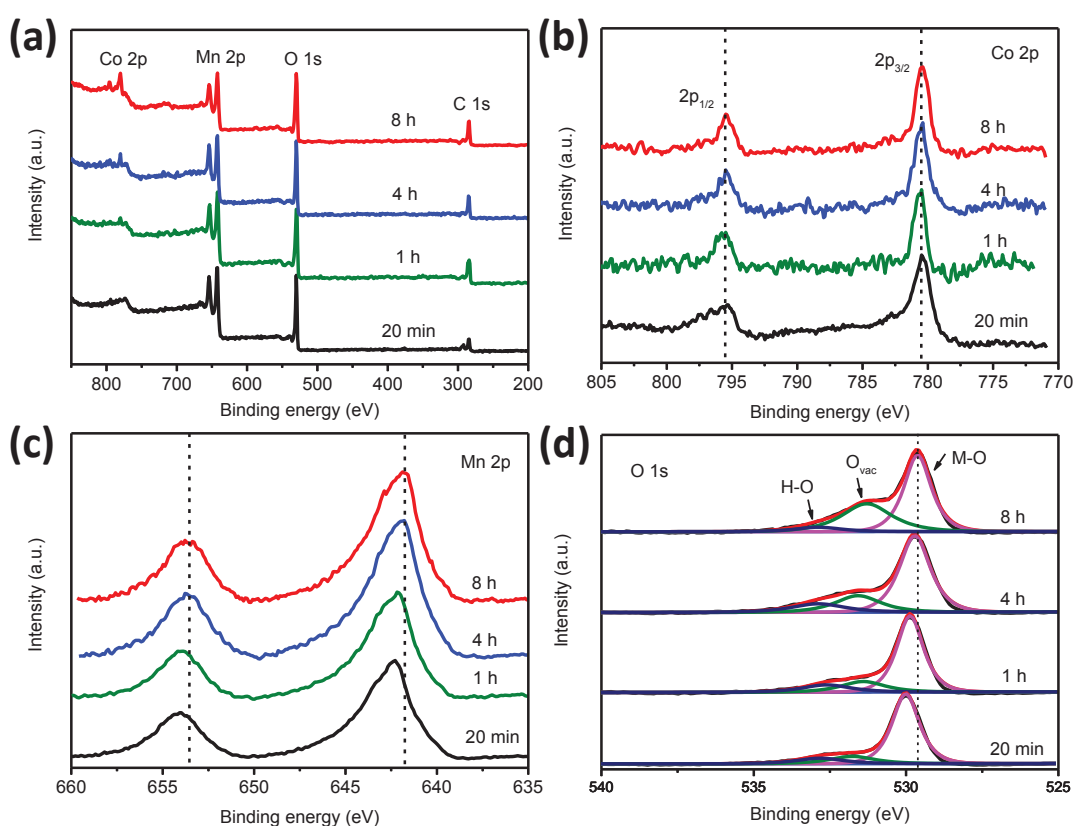
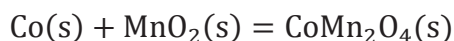
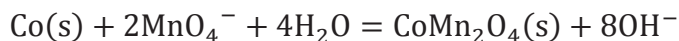


Figure 6-12 (a) XPS survey spectra, high resolution XPS spectra of (b) Co 2p, (c) Mn 2p, (d) O 1s of CoMn₂O₄-CoNC obtained at different time.

The results of SEM, XRD, Raman and XPS analysis of the products collected during the reaction process suggest that the metallic cobalt nanoparticles contribute to the formation of long, ultrathin nanosheets, rich in oxygen vacancies. During the redox reaction, the embedded cobalt nanoparticles are gradually released to participate in the

redox reaction as the co-reducing agents. Given the mechanistic insight into the transformation from CoNC to ultrathin CoMn_2O_4 nanosheets, we speculate that the actual process is dependent on the following three equations:



The transformation mechanism first involves the initially redox reaction between the reducing agents, including surface cobalt nanoparticles and carbon, and oxidizing agent, KMnO_4 . During the following reaction, more embedded cobalt nanoparticles are exposed, because of the continuously expending of carbon and cobalt in the redox reaction. At this stage, the as-formed MnO_2 nanosheets as well as KMnO_4 take part in the redox reaction reacting with the exposed cobalt nanoparticles. The metal and carbon act as co-reducing agents contributing to the unique morphology.

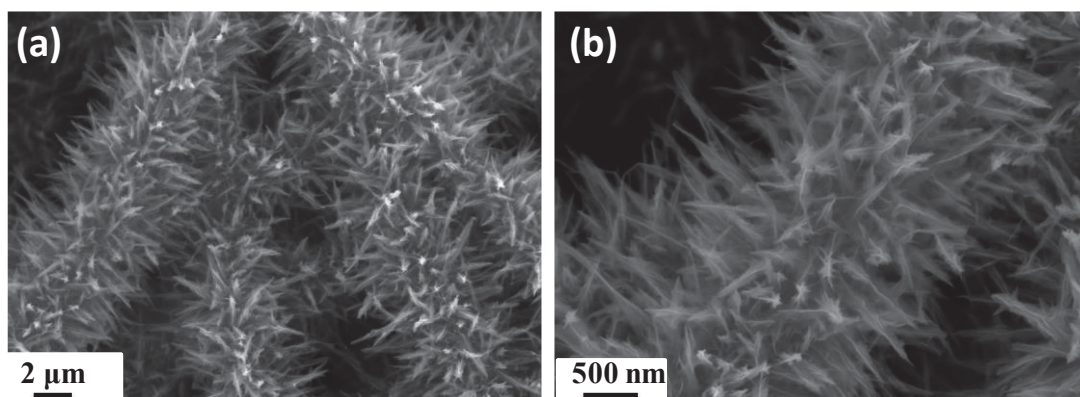


Figure 6-13 Low and high SEM images of NiMn_2O_4 -NiNC.

This strategy should be suitable for synthesizing other mixed transition metal oxide with the similar structure. When nickel/nitrogen bi-functionalized CNFs (NiNC) is adopted as the reducing agents, the spontaneous redox reaction between NiNC and KMnO_4 is able to produce ultrathin NiMn_2O_4 nanosheets vertically aligned on NiNC (Figure 6-13).

6.3.2 The electrochemical performance test of the catalysts

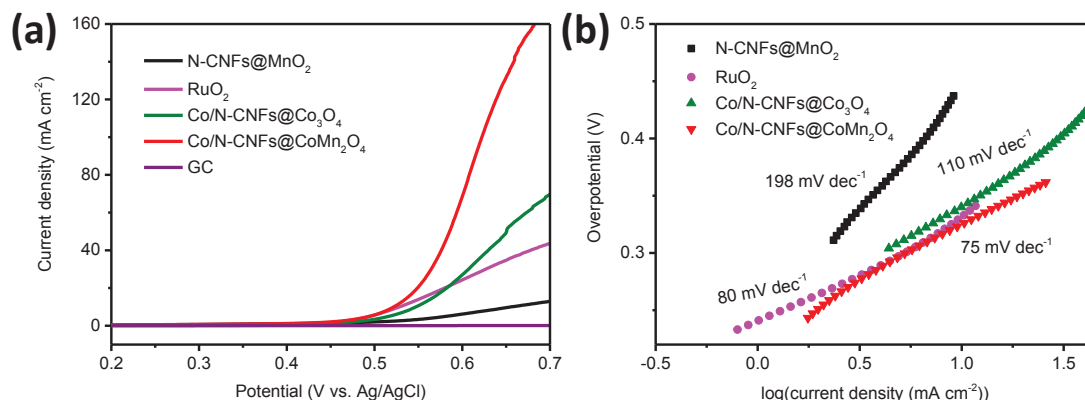


Figure 6-14 (a) polarization curves and (b) corresponding Tafel plots of CoMn₂O₄-CoNC, MnO₂-NC, Co₃O₄-CoNC, NC and RuO₂.

We then investigated the electrochemical performance of CoMn₂O₄-CoNC as catalyst towards OER using a three-electrode electrochemical configuration in 1 M KOH solution. For comparison, the corresponding single metal oxides, MnO₂-NC and Co₃O₄-CoNC, were also measured using the similar approach. The activity of a RuO₂ based electrode was tested as reference. The polarization curves after *i*R correction are shown in Figure 6-14(a). CoMn₂O₄-CoNC exhibits an earlier onset of catalytic current and superior current density with respect to the comparison materials. CoMn₂O₄-CoNC requires an overpotential of only 307 mV to reach 10 mA cm⁻², which is found to be 319, 337 and 432 mV for RuO₂, Co₃O₄-CoNC and MnO₂-NC, respectively. It is worth noting that the excellent OER activity of CoMn₂O₄-CoNC is comparable to the high performance catalysts, such as FeNi@NC, γ -CoOOH and superior to CP/CTs/Co-S, ultrathin NiCo₂O₄ nanosheets.^{9, 99, 265, 266} To gain additional insights into the OER process, Tafel slopes are acquired from the polarization curves by the equation ($\eta = b \log(j/j_0)$), where η is the overpotential, b is the Tafel slope, j is the current density, and j_0 is the exchange current density). As shown in Figure 6-14(b), the lower Tafel slope value for CoMn₂O₄-CoNC (75 mV dec⁻¹), indicates its more favourable kinetics relative

to those of $\text{Co}_3\text{O}_4\text{-CoNC}$ (110 mV dec^{-1}) and $\text{MnO}_2\text{-NC}$ (198 mV dec^{-1}), suggesting that more rapid OER rates can be achieved in practical applications by using $\text{CoMn}_2\text{O}_4\text{-CoNC}$ as electrocatalyst.

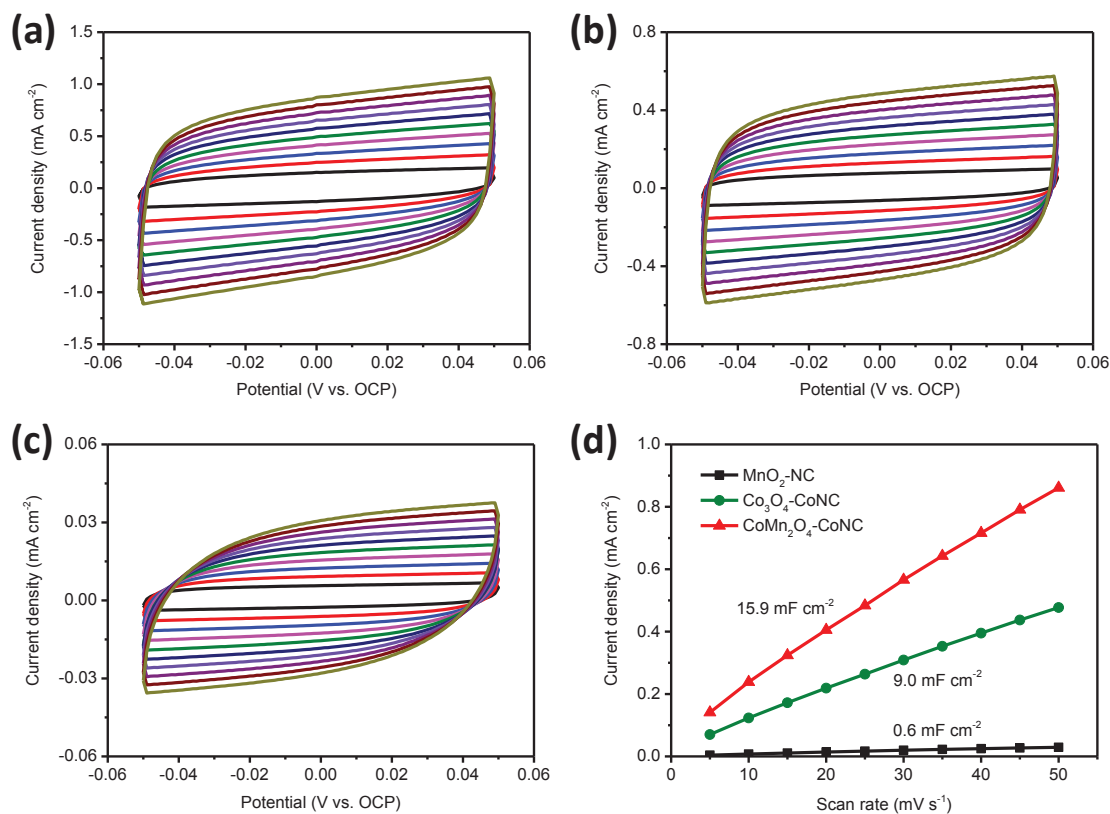


Figure 6-15 Cyclic voltammograms (CV) of (a) $\text{CoMn}_2\text{O}_4\text{-CoNC}$, (b) $\text{Co}_3\text{O}_4\text{-CoNC}$ and (c) $\text{MnO}_2\text{-NC}$, in 1 M KOH solution in a potential window without faradaic processes. (d) Scan rate dependence of the average capacitive current densities at open circuit potential for $\text{CoMn}_2\text{O}_4\text{-CoNC}$, $\text{Co}_3\text{O}_4\text{-CoNC}$ and $\text{MnO}_2\text{-NC}$.

Conclusively, these findings (low onset overpotential, high current density and low Tafel slope value), demonstrate the superior electrocatalytic activity of $\text{CoMn}_2\text{O}_4\text{-CoNC}$ towards OER compared to any single one, $\text{Co}_3\text{O}_4\text{-CoNC}$ or $\text{MnO}_2\text{-NC}$, which mainly originates from the unique architecture, ternary properties and abundant oxygen vacancies. First, the vertically aligned ultrathin nanosheets and abundant oxygen vacancies could provide more active sites, which can be evaluated approximately by using the electrochemical double-layer capacitance (C_{dl}).^{267, 268} $\text{CoMn}_2\text{O}_4\text{-CoNC}$ (15.9

mF cm⁻²) exhibits a 1.8 and 26.5-times C_{dl} than those of Co₃O₄-CoNC (9.0 mF cm⁻²) and MnO₂-NC (0.6 mF cm⁻²), respectively (Figure 6-15). Generally, the higher effective surface area contributes to higher electrochemical catalytic activity. As a result, CoMn₂O₄-CoNC exhibits improved catalytic performance compared to the single metal based materials.

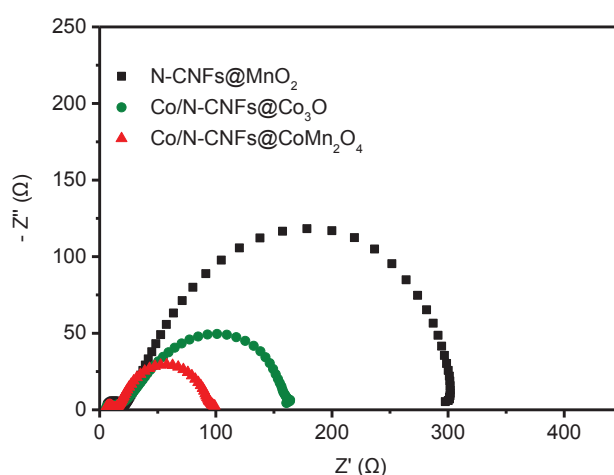


Figure 6-16 Nyquist plots of the as-prepared samples modified electrodes recorded at a constant overpotential of 250 mV.

Second, the unique 3D interconnected and vertically aligned structure provide efficient pathway for electron transport, and thus facilitates favourable reaction kinetics. This viewpoint is confirmed by the electrochemical impedance spectroscopy. As shown in Figure 6-16, the Nyquist plots reveal that the charge transfer resistance of CoMn₂O₄-CoNC is smaller than those of Co₃O₄-CoNC and MnO₂-NC. This result demonstrates the vertically aligned ultrathin ternary nanosheets with abundant oxygen vacancies formed with the assistance of metallic Co nanoparticles lead to fast charge transfer during the OER process, which affords markedly electrocatalytic performance.

Both of the long-term LSV cycling and time-dependent current density test were carried out in alkaline solution to evaluate the catalyst's stability. Figure 6-17 shows the

polarization curves recorded before and after 5000 potential cycles with negligible decrease of the current density. The current-time plots of CoMn₂O₄-CoNC based electrode was obtained by electrolysis at a static potential. The inset of Figure 5d shows the current density could stabilize at this potential during the following 12 h. These results provide sufficient evidence for the good stability of CoMn₂O₄-CoNC catalyst towards OER in alkaline solution.

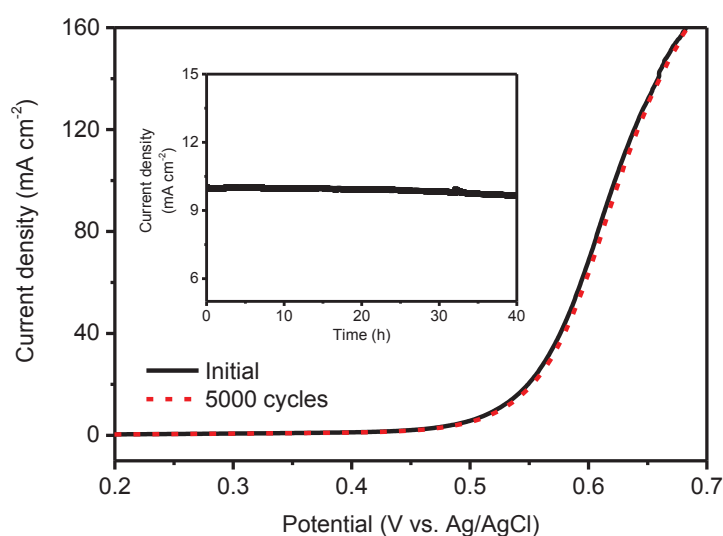


Figure 6-17 Stability test of CoMn₂O₄-CoNC through potential cycling, the inset shows the time dependence of catalytic current density during electrolysis at a static potential.

To verify the rapid increase of current density in Figure 6-14(a) originates from water oxidation rather than other side reactions and further calculate the Faradaic efficiency, RRDE apparatus was applied in N₂-saturated 1 M KOH solution, rendering a continuous OER (disk electrode)-ORR (ring electrode) process.^{146, 201} As shown in Figure 6-18(a), with the disk potential holds constant at 1.48 V *vs.* RHE (obtained current at around 164.5 μ A), O₂ molecules generates from CoMn₂O₄-CoNC surface on the disk electrode and then the formed O₂ molecules are further reduced by sweeping across the surrounding Pt ring electrode with an ORR potential of 0.45 V *vs.* RHE. A

ring current of approximately 32.3 μA is collected, corresponding to a Faradaic efficiency of 98.2% (see calculation details in the Experimental part). Furthermore, we also analyze the content of by-product (peroxide intermediates) that formed at the surface of $\text{CoMn}_2\text{O}_4\text{-CoNC}$ catalyst during the OER process to further understand the reaction mechanism. Figure 6-18(b) shows a relatively low ring current (peroxide intermediates) compared to the disk current. Additionally, with the increasing of disk current, the ring current gradually decreases, which means that the rapid increase of the current could suppress the formation of peroxide intermediates, leading to a desirable four-electron transfer pathway to form O_2 molecules.

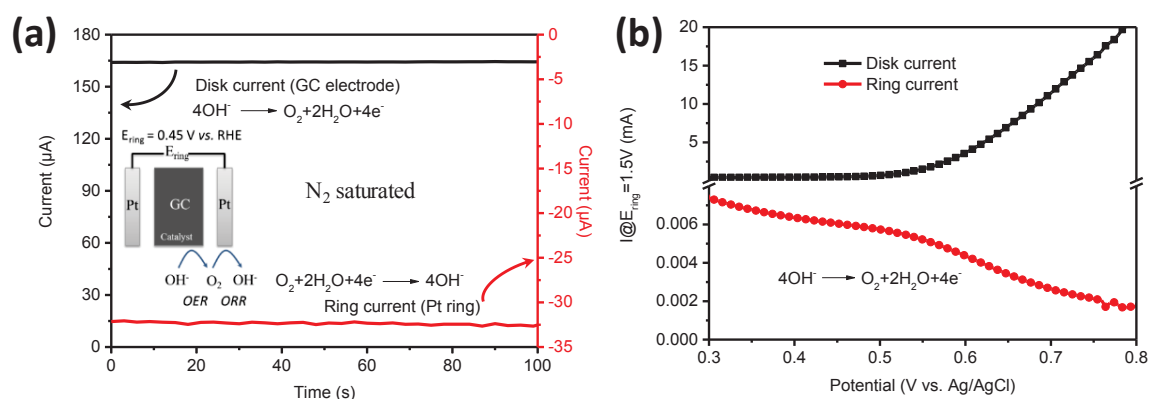


Figure 6-18 (a) Evidence of O_2 generated from $\text{CoMn}_2\text{O}_4\text{-CoNC}$ catalyst using RRDE measurements (1600 rpm) (disk potential: 1.48 V, ring potential: 0.45 V vs. RHE), with inset showing the continuous OER \rightarrow ORR process initiated on the RRDE. (b) Disk and ring current of $\text{CoMn}_2\text{O}_4\text{-CoNC}$ catalyst on an RRDE (1600 rpm) with a ring potential of 1.5 V (vs. RHE).

The above mentioned results demonstrate that $\text{CoMn}_2\text{O}_4\text{-CoNC}$ composite exhibits excellent electrocatalytic performance towards OER, which is associated with its remarkable structural properties and synergistic effect. First, the mixed-valence state of CoMn_2O_4 nanosheets is favourable to the water oxidation process, providing donor-acceptor chemisorption sites for the reversible adsorption of reactant. Moreover, the as-formed ultrathin nanosheets rich in oxygen vacancies provide a unique means for

enhancing the electrochemical oxygen evolution. Second, 1D CoNC acts as an interconnected conducting substrate associated with stable architecture and high electrical conductivity. Nitrogen doping and cobalt encapsulation further enhance the electron transfer, expediting the OER kinetics processes. Third, CoMn₂O₄-CoNC with 3D architecture achieved by vertically growing the ultrathin CoMn₂O₄ nanosheets on 1D CoNC, which could not only shorten the ion diffusion paths, further accelerating the charge transfer, but also generate the flexible structure, leading to a highly stable performance. Lastly, the intimate interaction between CoMn₂O₄ nanosheets and CoNC affords by a facile redox reaction between CoNC and KMnO₄, forming strong synergistic coupled effect, and thus leading to the enhanced OER catalytic activity. Therefore, these collaborative advantages enable CoMn₂O₄-CoNC as OER catalyst with superior performance.

6.4 Conclusion

In conclusion, we have successfully fabricated a novel structure composite, CoMn₂O₄-CoNC, with ultrathin nanosheets vertically aligned on 1D CoNC substrate by a facile spontaneous redox reaction. CoMn₂O₄-CoNC performs as a cost-effective OER catalyst, exhibiting superior performance with high current density, low transfer resistance and long-time durability. The attractive performance of CoMn₂O₄-CoNC are originated from its unique structure with ultrathin CoMn₂O₄ nanosheets (abundant oxygen vacancies) as the catalysts, 1D CoNC as conductive substrate as well as the strong synergistic effect and intimate contact between the nanosheets and substrate, which contributes to exposing more active sites, facilitating high charge transfer and therefore improving the OER kinetics. This simple strategy can be easily adapted to

prepare other ultrathin ternary metal oxide, which could not only apply for water splitting, but also for other key energy conversion and storage technologies.

Chapter 7: Facile Synthesis and Evaluation of Hierarchical Fe₃C based Catalyst for High Efficient Oxygen Evolution Reaction

7.1 Introduction

Transition metal oxide (Co₃O₄, CoO, CoMn₂O₄) based catalysts have been well developed and studied for OER in Chapter 4-6. Recently, the other kinds of catalysts based on transition metal carbides, chalcogenides and phosphides, featuring metals such as Fe, Co, Ni, Mn have garnered attention because of their abundance and capability for water oxidation.^{82, 103, 269-274} For example, Xie *et al.* investigated metallic Co₄N porous nanowire arrays, Nath *et al.* reported Ni₃Se₂ and Yan *et al.* developed Au@Co₃O₄ core-shell nanocrystals.^{98, 275, 276} These catalysts have exhibited good catalytic activity and long-term structural stability during OER test. However, these catalysts usually suffer from the complicated synthesis procedure, which is time consuming. Therefore, finding an effective technique, which is simple and can be scaled up, still remains a huge challenge.

Transition metal carbides, *e.g.* Fe₃C, are the robust candidates for wide use in hydrogen evolution reactions and oxygen reduction reactions (HER and ORR), exhibiting a catalytic activity similar to Pt-based electrochemical catalysts.²⁷⁷⁻²⁸⁰ Recently, Fe₃C has been also reported to have the ability for water oxidation.^{281, 282} Plenty of studies (HER, ORR, OER) have shown that the structure and morphology of materials greatly influence the activity of the catalysts. Fe₃C incorporated into microporous carbon can deliver an even higher electronic conductivity and catalytic performance. Specifically, well-aligned structures on conductive substrates are extremely interesting and represent a prime example of hybrid electrocatalysts. Recent researches, such as carbon paper/carbon nanotubes/Co-S, Sn@CNT-carbon paper and

FeOOH/CeO₂ with aligned structure, have been reported.^{9, 283, 284} Carbon nanofibers (CNFs), possess intrinsic properties, which include high surface area, fast electrical conductivity, and easy preparation procedure, making them as ideal supports for heterogeneous catalysts.^{285, 286} Meanwhile, nitrogen-doping can further improve the catalytic activity of Fe₃C based materials, attributed to the formation of nitrogen-containing active sites (C–N or Fe–N).²⁸⁷ Hence, at this point, there is a need for controllable synthesis of the material with uniquely aligned structures composed of Fe₃C and CNFs as a catalyst for water oxidation.

To achieve this important goal, we developed a facile, scalable method to synthesize the catalyst composed of Fe₃C encapsulated in nitrogen-enriched CNTs aligned on nitrogen doped CNFs (Fe₃C@NCNTs-NCNFs) by the electrospinning technique. The as-prepared Fe₃C@NCNTs-NCNFs composite displays uniquely aligned arrays and 3D hierarchical architecture, which exposes sufficient active sites and facilitates fast reaction kinetics towards OER. When tested as a catalyst for water oxidation, it exhibits outstanding electrocatalytic activity, including a low onset potential (1.39 V vs. RHE), a high current density (10 mA cm⁻² at the overpotential of 284 mV) and excellent stability, making Fe₃C@NCNTs-NCNFs an efficient nonprecious metal catalyst for water oxidation.

7.2 Experimental

7.2.1 Synthesis of Nitrogen-doped CNFs (NCNFs)

NCNFs were prepared by using an electrospinning method with a subsequent heat treatment. Briefly, 600 mg of polyacrylonitrile (PAN, M_w = 150,000 g mol⁻¹) was dissolved in 6 ml N,N-dimethylformamide (DMF) and the solution was kept at 50 °C under vigorous stirring overnight. Then the above solution was transferred to a 10 ml

plastic syringe with a 20-gauge blunt tip needle. For the electrospinning process, a voltage of 18 kV and a flow rate of 14.8 $\mu\text{l min}^{-1}$ were applied. The distance between the needle and rotating grounded collector was 15 cm. The as-collected electrospun fibers were firstly stabilized by heating to 280 °C for 6 h in air, and then the stabilized fibers were carbonized in an Ar flow at 800 °C for 6 h to obtain NCNFs. The ramping rate was kept at 1 °C min^{-1} .

7.2.2 Synthesis of $\text{Fe}_3\text{C}@\text{NCNTs-NCNFs}$

$\text{Fe}_3\text{C}@\text{NCNTs-NCNFs}$ composite was also fabricated by an electrospinning method followed by high temperature treatment. Briefly, 320 mg of Tris(acetylacetonate)iron(III) ($\text{Fe}(\text{acac})_3$) and 600 mg of polyacrylonitrile (PAN, $M_w = 150,000 \text{ g mol}^{-1}$) were dissolved in 6 ml N,N-dimethylformamide (DMF) and the solution was kept at 50 °C under vigorous stirring overnight. Then the above solution was transferred to a 10 ml plastic syringe with a 20-gauge blunt tip needle. The electrospinning and stabilizing processes were the same as those of NCNFs. Then the stabilized fibers underwent a calcination process by heat treatment at 800 °C for 6 h in the presence of melamine in the upper site (10 cm to the stabilized fibers, the weight ratio between melamine and stabilized fibers was 1:20) with an Ar flow. The ramping rate was kept at 1 °C min^{-1} . The comparison material, Fe_3C embedded in NCNFs ($\text{Fe}_3\text{C-NCNFs}$) was obtained by heat treatment of the stabilized fibers in the absence of melamine.

7.2.3 Characterization

Scanning electron microscopy (SEM) images and electron energy dispersive spectroscopy images were obtained on Zeiss Supra 55VP and Zeiss Evo SEM, respectively. Transmission electron microscopy (TEM) and high resolution TEM

images were recorded on a JEOL JEM-2010 and scanning transmission electron microscopy (STEM, JEOL JEM-ARM200F, at an accelerating voltage of 220 kV). X-ray diffraction (XRD) patterns were collected on a Bruker D8 Discover XRD with a scanning step of 0.02° per second in the 2θ range from 10 to 80°. Raman spectra were obtained on an inVia Renishaw Raman spectrometer system (HR Micro Raman spectrometer, Horiba JOBIN YVON US/ HR800 UV) using a 632.8 nm wavelength laser. X-ray photoelectron spectroscopy (XPS) was performed by a Thermo Scientific, UK ESCALAB250Xi system. Surface area was obtained by the Brunauer–Emmett–Teller (BET) technique at a relative pressure of $P/P_0 = 0.05\text{--}0.25$. TGA/differential thermal analysis (DTA) was employed by using a TA Instruments, SDT 2960 module, New Castle, DE, USA at a heating rate of 5 °C min⁻¹ from room temperature to 800 °C in an air atmosphere.

7.2.4 Electrochemical Measurements

Electrochemical tests were performed on an electrochemical workstation (CHI 660E, CH Instrument) by using a three-electrode configuration. Platinum wire, a Glassy carbon (GC) electrode (diameter of 3 mm) and Ag/AgCl were used as the counter, working and reference electrodes, respectively and the reference electrode, (Ag/AgCl with saturated KCl solution), was calibrated with the respect to the reversible hydrogen electrode (RHE), $E_{\text{RHE}} = E_{\text{Ag/AgCl}} + 0.059 \times \text{pH} + 0.1971$. The fabrication process for the working electrode was as follows: 4 mg of catalyst was dispersed in solvent containing 0.5 ml water, 0.5 ml isopropanol and 80 μl of Nafion (5 wt %). After thorough sonication, 10 μl of the formed catalyst dispersion was dropped onto the GC electrode to afford a mass loading of 0.04 mg cm⁻², followed by drying at room temperature. Linear sweep voltammetry (LSV) tests were conducted in 1 M KOH solution with a scan rate of 5 mV s⁻¹, and was all corrected for the *i*R contribution within the cell. The

electrochemical capacitance of the catalysts was measured by cyclic voltammetry (CV), which was conducted with amplitude 0.1 V with scan rates ranging from 10 to 100 mV s⁻¹. The electrochemical impedance spectra (EIS) were measured with a frequency range of 10⁶-0.01 Hz and an amplitude of 5 mV at a constant overpotential of 250 mV. The cycling performance of Fe₃C@NCNTs-NCNFs based electrode was measured by repeating linear sweep voltammograms (LSV) running for 5000 cycles and the current-time plots were obtained with a static overpotential of 284 mV.

For the rotating ring-disk electrode (RRDE) measurement, a GC disk electrode and a Pt ring electrode were used (Pine Research Instrumentation, USA). The as-prepared Fe₃C@NCNTs-NCNFs catalyst was loaded onto the disk electrode (diameter of 5 mm) by using the above mentioned method. The rotation speed of the RRDE was held at 1600 rpm for the test. To detect the content of the formed hydrogen peroxide (HO₂⁻) intermediates, the ring potential was held constantly at 1.50 V *vs.* RHE in N₂-saturated 1 M KOH solution. The scan rate was kept at 5 mV s⁻¹. On the other hand, the Faradaic efficiency was calculated as follows: $\varepsilon = I_r/(I_d N)$, where I_d is the disk current, I_r is the ring current, and N represents the current collection efficiency of the RRDE ($N = 0.2$). A continuous OER (disk electrode) → ORR (ring electrode) process occurred on the RRDE. The ring potential was held constantly at 0.45 V *vs.* RHE to reduce the formed O₂ from the catalyst on the disk (disk potential fixed at 1.48 V *vs.* RHE) in N₂-saturated 1 M KOH solution.

7.3 Result and discussion

7.3.1 The characterization of the catalysts

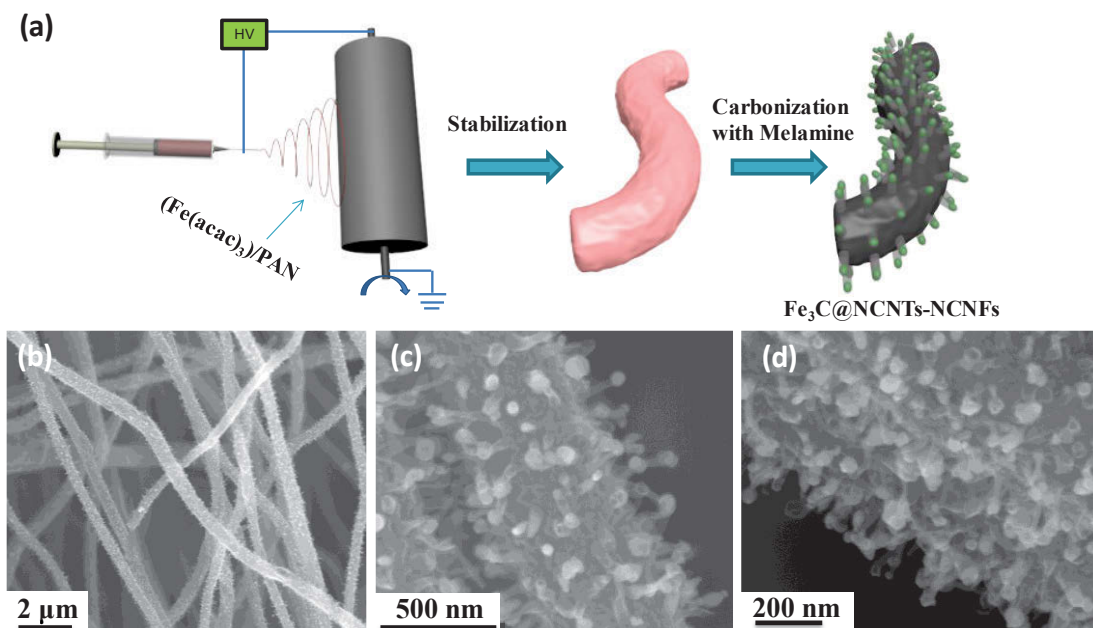


Figure 7-1 (a) Schematic illustration for the fabrication process of $\text{Fe}_3\text{C}@\text{NCNTs-NCNFs}$. (b) low and (c, d) high magnification SEM images of $\text{Fe}_3\text{C}@\text{NCNTs-NCNFs}$.

The fabrication process of $\text{Fe}_3\text{C}@\text{NCNTs-NCNFs}$ is shown in Figure 7-1(a). $(\text{Fe}(\text{acac})_3)/\text{PAN}$ composite was obtained by using a facile electrospinning technique, followed by stabilized process and carbonization in the presence of the melamine to achieve the aligned structure. The low magnification SEM image of $\text{Fe}_3\text{C}@\text{NCNTs-NCNFs}$ in Figure 7-1(b) shows the continuous and interconnected nanofibers forming a hierarchical 3D architecture. Many tiny nanotubes can be observed on the rough CNFs' surface, which is preferred for the interaction of the electrode/solution and the release of molecular oxygen. The average diameter of the electrospun fibers is around 500 nm. The enlarged SEM images in Figure 7-1(c, d) show that each individual CNF is covered by the nanotube structure of $\text{Fe}_3\text{C}@\text{NCNTs}$ arrays, which are nearly perpendicular to CNF with an average length around 150-200 nm. The $\text{Fe}_3\text{C}@\text{NCNTs}$ arrays are well dispersed on the CNF substrate, generating a loose porous structure with abundant open voids.

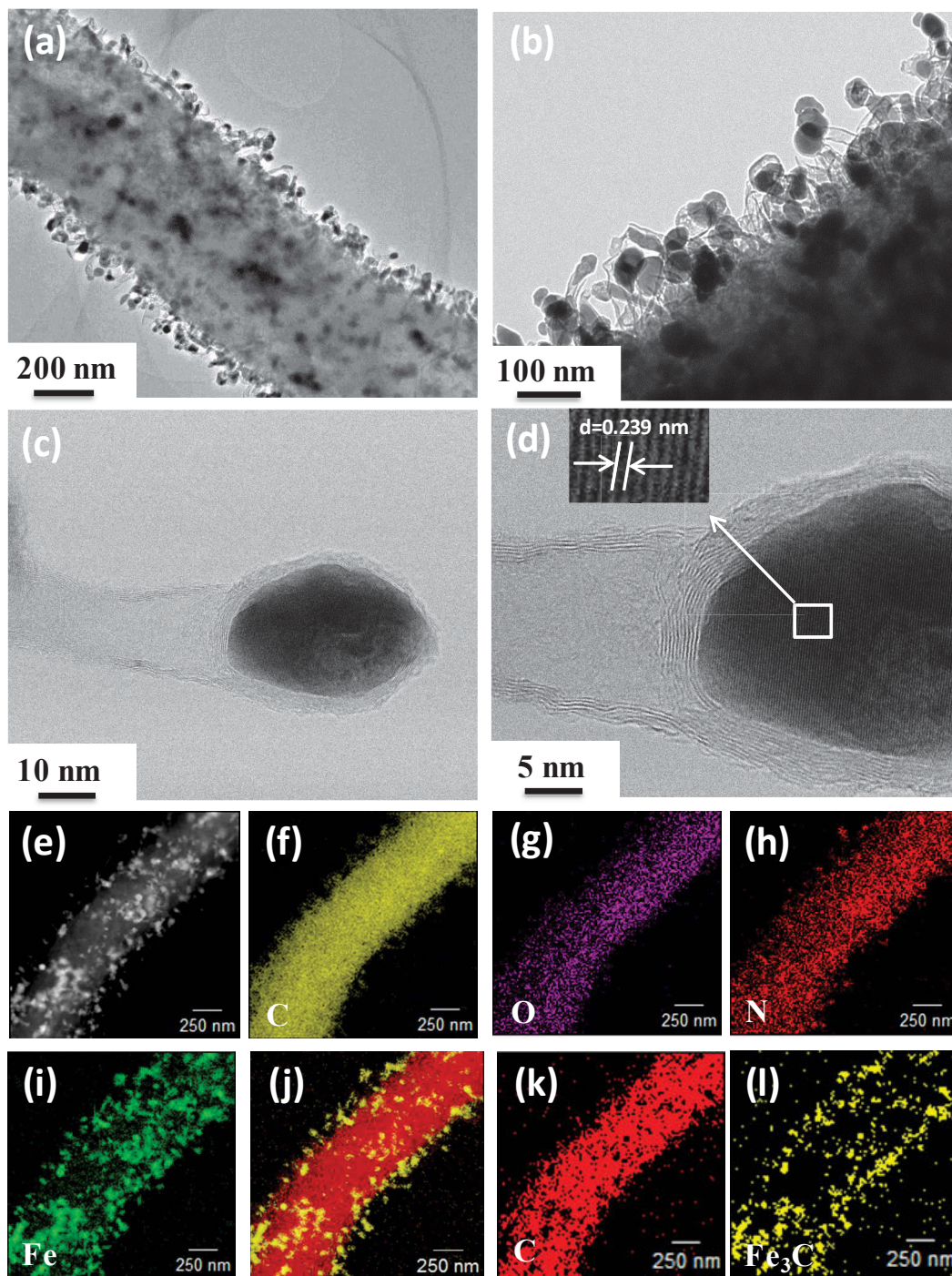


Figure 7-2 (a) TEM image of a single fibrous $\text{Fe}_3\text{C}@\text{NCNTs-NCNF}$. (b) HRTEM image of $\text{Fe}_3\text{C}@\text{NCNTs}$ aligned on NCNF. (c) high resolution TEM image of a single $\text{Fe}_3\text{C}@\text{NCNT}$. (d) a Fe_3C nanoparticle wrapped by multilayered graphitic carbon, the enlarged area as denoted in the white box, displaying an interplanar spacing of 0.239 nm. (e-i) STEM elemental mapping of $\text{Fe}_3\text{C}@\text{NCNTs-NCNFs}$. (j-l) two different phases of $\text{Fe}_3\text{C}@\text{NCNTs-NCNFs}$, (k) C, (l) Fe_3C .

Figure 7-2(a) shows a TEM image of a single fibrous $\text{Fe}_3\text{C}@\text{NCNTs-NCNF}$, verifying the uniformly aligned arrays on the surface of CNF. The TEM image also reveals some Fe_3C nanoparticles encapsulated in the CNF substrate, which could highly enhance the conductivity of the composite. The high resolution image in Figure 7-2(b) clearly shows the strong bond and intimate connection between CNT and CNF, and the CNT functions as an efficient conductor between the substrate (CNF) and Fe_3C nanoparticles, benefiting to the electron transfer and structure stability. The closer TEM images in Figure 7-2(c, d) reveal the graphitic structure of CNT and the presence of Fe_3C nanoparticles encapsulated in the multilayered carbon shell, especially at the tip of CNT. The encapsulated structure should efficiently prevent the corrosion of metal particles from a harsh environment and simultaneously promote the catalytic reaction on a carbon surface due to the electron transfer from encapsulated particles. The thickness of carbon layer is around 4 nm and these multiwalled CNTs are crystalline and display an interplanar spacing of 0.325 nm correspond to the C (002) plane. The inset of Figure 7-2(d) represents the enlarged area as denoted in white box and the lattice fringes with a d-spacing of 0.239 nm, which is well-matched with the interplanar plane of Fe_3C . STEM technology was used to investigate the microstructure of a single fibrous $\text{Fe}_3\text{C}@\text{NCNTs-NCNF}$. The elemental mapping results prove the existence of C, O, N and Fe elements (Figure 7-2(e-i)), indicating the homogeneous distribution of the above mentioned four elements. Nitrogen element distributes both on the substrate and nanotube structured arrays. Moreover, the STEM images in Figure 7-2(j-l) reveal the presence of two main phases in $\text{Fe}_3\text{C}@\text{NCNTs-NCNFs}$ composite, carbon and Fe_3C .

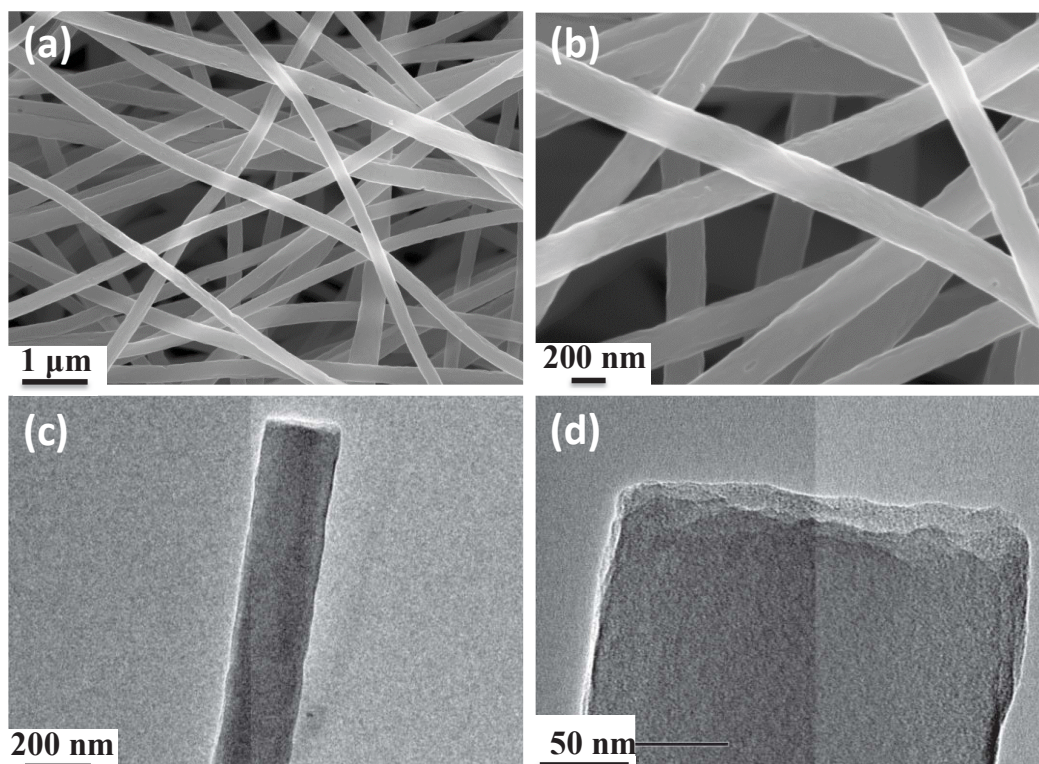


Figure 7-3 (a,b) SEM and (c,d) TEM images of NCNFs.

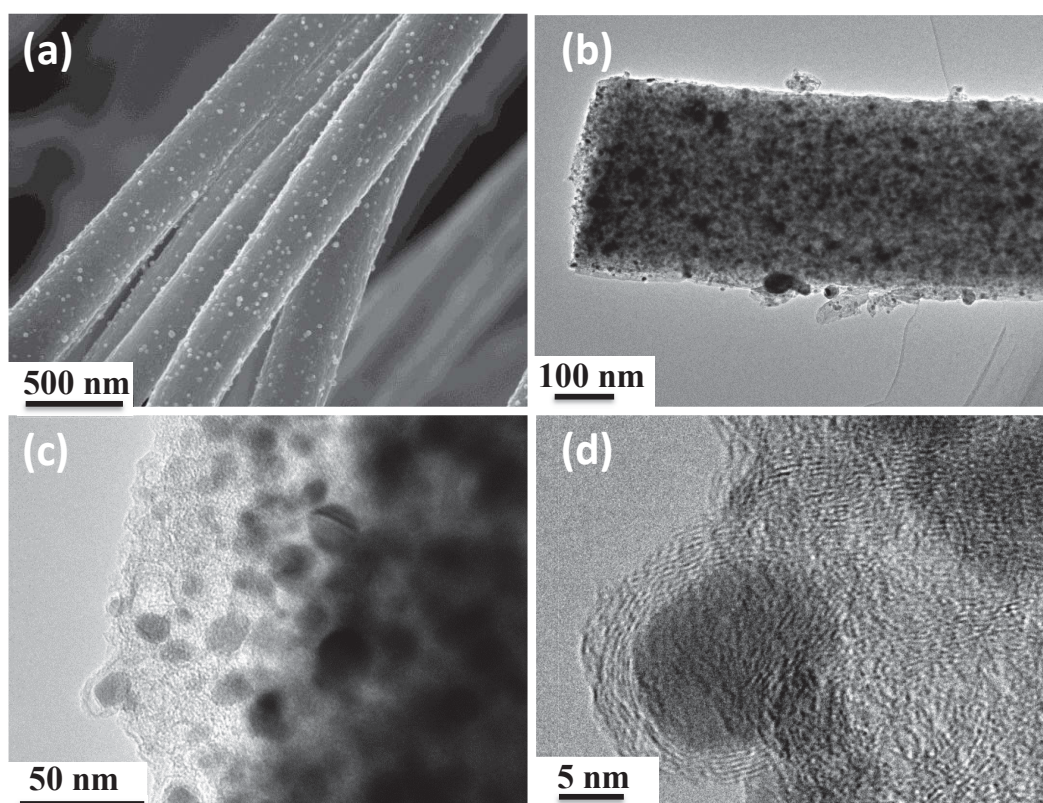


Figure 7-4 (a) SEM and (b-d) TEM images of Fe_3C -NCNFs.

NCNFs and Fe₃C-NCNFs are synthesized as the comparison materials. As shown in Figure 7-3, no nanoparticles and graphitic structure could be observed for pure NCNFs. Furthermore, without the additional carbon source, Fe₃C nanoparticles are randomly encapsulated by CNFs and no tube structure could be observed on the surface (Figure 7-4). Thus, it confirms that melamine is indispensable for forming the nanotube structured Fe₃C@NCNTs arrays upon pyrolysis. It is obviously observed that Fe nanoparticles catalyse CNT growth with the melamine serving as a carbon source during the carbonization process, ending with Fe₃C nanoparticles wrapped by graphitic carbon at the tip area of the nanotubes. This unique structure is beneficial to catalysis, providing sufficient active sites and better communication between the catalyst/electrolyte for the oxygen evolution.

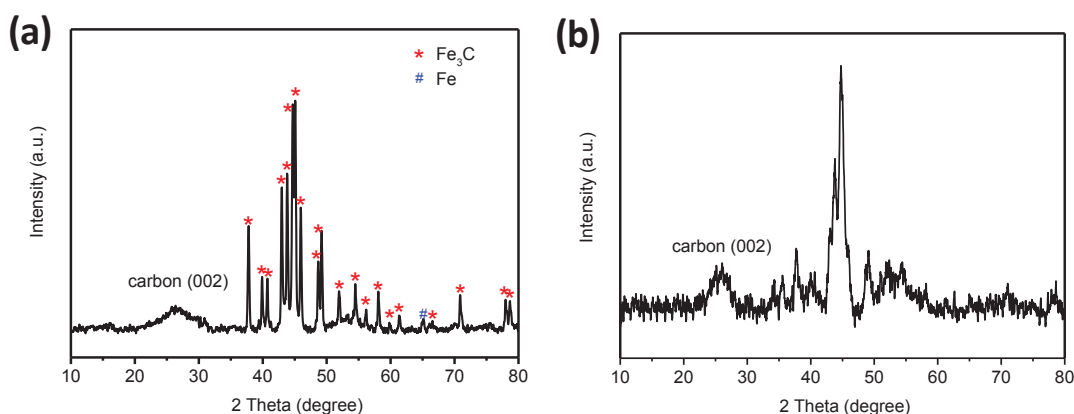


Figure 7-5 (a, b) XRD pattern of Fe₃C@NCNTs-NCNFs and Fe₃C-NCNFs.

The XRD pattern in Figure 7-5(a) indicates the existence of Fe₃C and graphitic carbon in Fe₃C@NCNTs-NCNFs composite. A peak at 26.5° is observed, corresponding to (002) plane of graphitic carbon, suggesting a partially graphitic structure. XRD analyse demonstrates the existence of Fe₃C, according to the diffraction data of Fe₃C (JCPDS, No. 89-2867) and small amount of metallic Fe (JCPDS No.87-0722). In contrast, Fe₃C-NCNFs shows more characterization peaks for metallic Fe and

much lower overall peak intensity (Figure 7-5(b)), suggesting the additional carbon source introduced in the carbonization process leads to the formation of Fe_3C and enhancement of the particles' crystallinity properties.

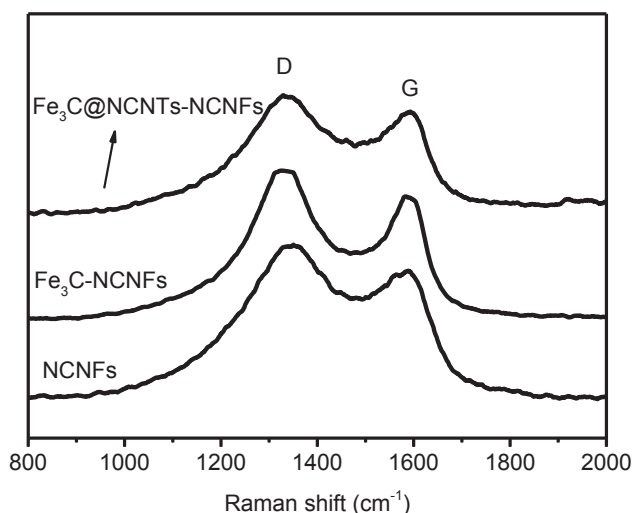


Figure 7-6 Raman spectra of $\text{Fe}_3\text{C}@\text{NCNTs-NCNFs}$, $\text{Fe}_3\text{C-NCNFs}$ and pure NCNFs.

The partial graphitic structure of $\text{Fe}_3\text{C}@\text{NCNTs-NCNFs}$ can be further confirmed by Raman spectra. $\text{Fe}_3\text{C}@\text{NCNTs-NCNFs}$, $\text{Fe}_3\text{C-NCNFs}$ and pure NCNFs display two typical peaks, corresponding to the defect induced D-band and graphitic G-band, respectively (Figure 7-6). The intensity ratio of D/G (I_D/I_G) value for $\text{Fe}_3\text{C}@\text{NCNTs-NCNFs}$ hybrid (1.04) is slightly lower than those of $\text{Fe}_3\text{C-NCNFs}$ (1.06) and NCNFs (1.08), indicating a higher graphitic degree of $\text{Fe}_3\text{C}@\text{NCNTs-NCNFs}$. These graphitic carbon structures formed during the carbonization process (graphitic carbon wrapped Fe_3C and the as-formed CNTs) can significantly enhance the electric conductivity and corrosion resistance, thus lead to high catalytic efficiency.

The surveyed XPS spectrum in Figure 7-7(a) reveals that $\text{Fe}_3\text{C}@\text{NCNTs-NCNFs}$ composite is composed of C, N, O, Fe and no other impurity is observed, which is consistent with the results of XRD and STEM mapping.

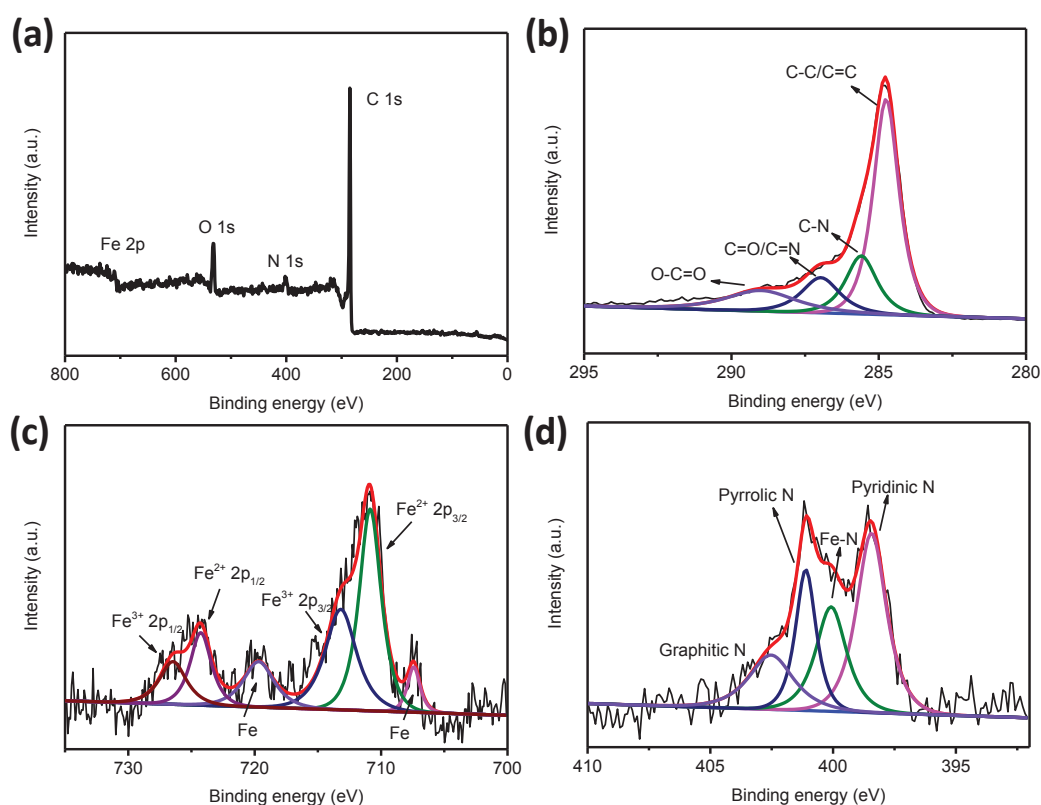


Figure 7-7 (a) XPS survey spectrum of $\text{Fe}_3\text{C}@\text{NCNTs-NCNFs}$. high resolution XPS spectra of (b) C 1s, (c) Fe 2p and (d) N 1s of $\text{Fe}_3\text{C}@\text{NCNTs-NCNFs}$ composite.

The high resolution C 1s spectrum (Figure 7-7(b)) is decomposed into four components, corresponding to sp^2 C at 284.5 eV, C-N at 285.6 eV, C=O/C=N at 286.9 eV and O-C=O at 289.1 eV. The high-resolution spectrum of Fe 2p in Figure 7-7(c) displays that Fe 2p signal can be deconvoluted into two pairs of peaks for Fe^{3+} (713.1 and 726.5 eV) and Fe^{2+} (710.8 and 724.3 eV). The signal of Fe^0 at 719.7 and 707.4 eV is far lower than that of Fe_3C , suggesting the main composition of the nanoparticles in the composite is Fe_3C after pyrolysis at 800 °C, whereas $\text{Fe}_3\text{C-NCNFs}$ show much higher peak intensity of Fe^0 (Figure S6b, consistent with the XRD result). The reduced amount of metallic Fe can be attributed to the relatively high carbonization degree for $\text{Fe}_3\text{C}@\text{NCNTs-NCNFs}$ composite with the additional carbon source. The high resolution N 1s spectrum is deconvoluted into four peaks, corresponding to graphitic N (402.5 eV), pyrrolic N (401.1 eV), Fe-N (400.1 eV) and pyridinic N (398.4 eV) (Figure

7-7(d)). The total N content is found to be 5.6 at% in Fe₃C@NCNTs-NCNFs composite, indicating the successful doping of nitrogen, which is induced by the N-rich precursor PAN and melamine. The existence of N dopant (C-N, C=N and Fe-N) in Fe₃C@NCNTs-NCNFs composite plays an important role in the OER process by inherently increasing the ability to interact with reactants (H₂O) and rendering asymmetrical charge distributions on the adjacent carbon atoms.^{102, 171}

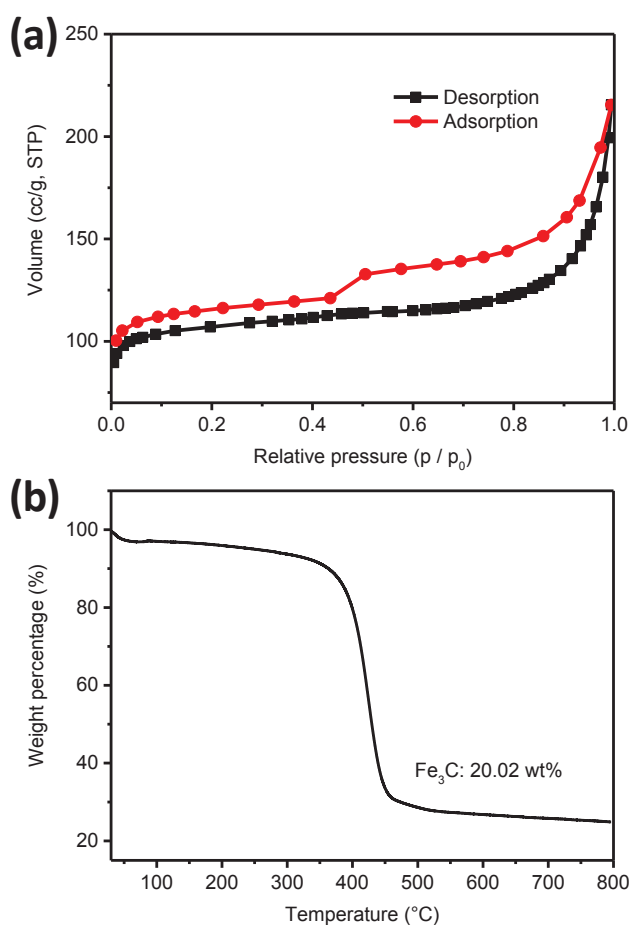


Figure 7-8 (a) Nitrogen sorption isotherm Fe₃C@NCNTs-NCNFs. (b) Thermogravimetric analysis of Fe₃C@NCNTs-NCNFs in air.

The BET surface area of Fe₃C@NCNTs-NCNFs is measured to be 356.6 m² g⁻¹ (Figure 7-8(a)) and this high surface area should be attributed to the unique 1D Fe₃C@NCNTs arrays aligned on 1D CNFs. The percentage of Fe₃C in Fe₃C@NCNTs-NCNFs composite is around 20.02 wt% based on the TGA result in Figure 7-8(b).

7.3.2 The electrochemical performance test of the catalysts

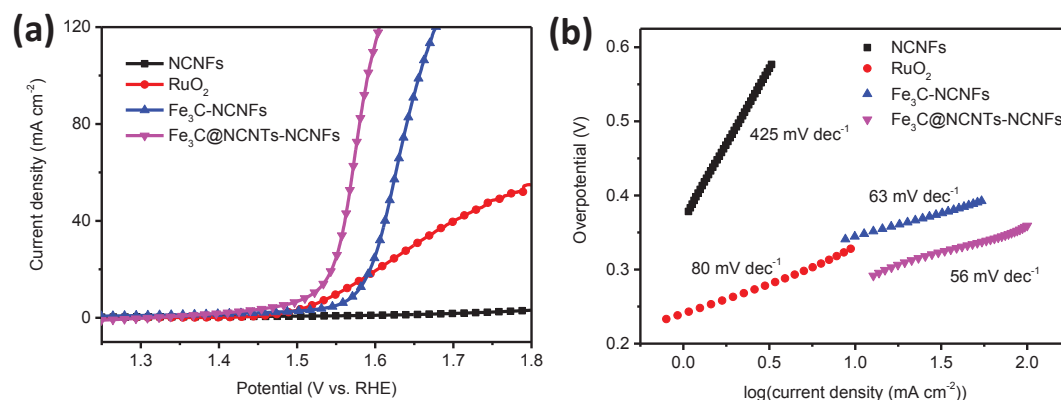


Figure 7-9 (a) polarization curves and (b) corresponding Tafel plots of Fe₃C@NCNTs-NCNFs, Fe₃C-NCNFs, NCNFs and RuO₂.

The catalytic performance of the as-prepared samples is investigated using a three-electrode system in 1 M KOH solution. The activity of a commercial RuO₂ catalyst based electrode is tested as reference to accurately evaluate their OER activities. The polarization curves after *i*R correction are shown in Figure 7-9(a). The pure NCNFs exhibit very poor OER activity. Fe₃C-NCNFs afford a low OER onset potential (1.46 V vs. RHE). Remarkably, Fe₃C@NCNTs-NCNFs show an improved performance with the onset potential shifting to as low as 1.39 V vs. RHE. To achieve a current density of 10 mA cm⁻², Fe₃C@NCNTs-NCNFs require a much lower overpotential (284 mV) towards water oxidation, whereas a higher overpotential of 314 mV and 341 mV is required for RuO₂ and Fe₃C-NCNFs catalysts, respectively. Compared with the other non-precious metal-based OER catalysts in the same condition (1 M KOH, overpotential towards 10 mA cm⁻²), such as Ni-P (300 mV), Fe₃O₄@Co₉S₈/rGO (320 mV), NiCo₂O₄ ultrathin nanosheets (320 mV), Co₃O₄/N-doped graphene (310 mV).^{218, 266, 271, 288} Fe₃C@NCNTs-NCNFs show much enhanced catalytic activity. The kinetic activities of the as-prepared materials are estimated by their corresponding Tafel slope. The Tafel slope of Fe₃C@NCNTs-NCNFs is measured to be 56 mV dec⁻¹, smaller than those of Fe₃C-

NCNFs sample (63 mV dec^{-1}), RuO_2 (80 mV dec^{-1}) and NCNFs (425 mV dec^{-1}), indicating that a more rapid OER rate can be achieved by using $\text{Fe}_3\text{C}@\text{NCNTs-NCNFs}$ as a catalyst in practical application (Figure 7-9(b)).

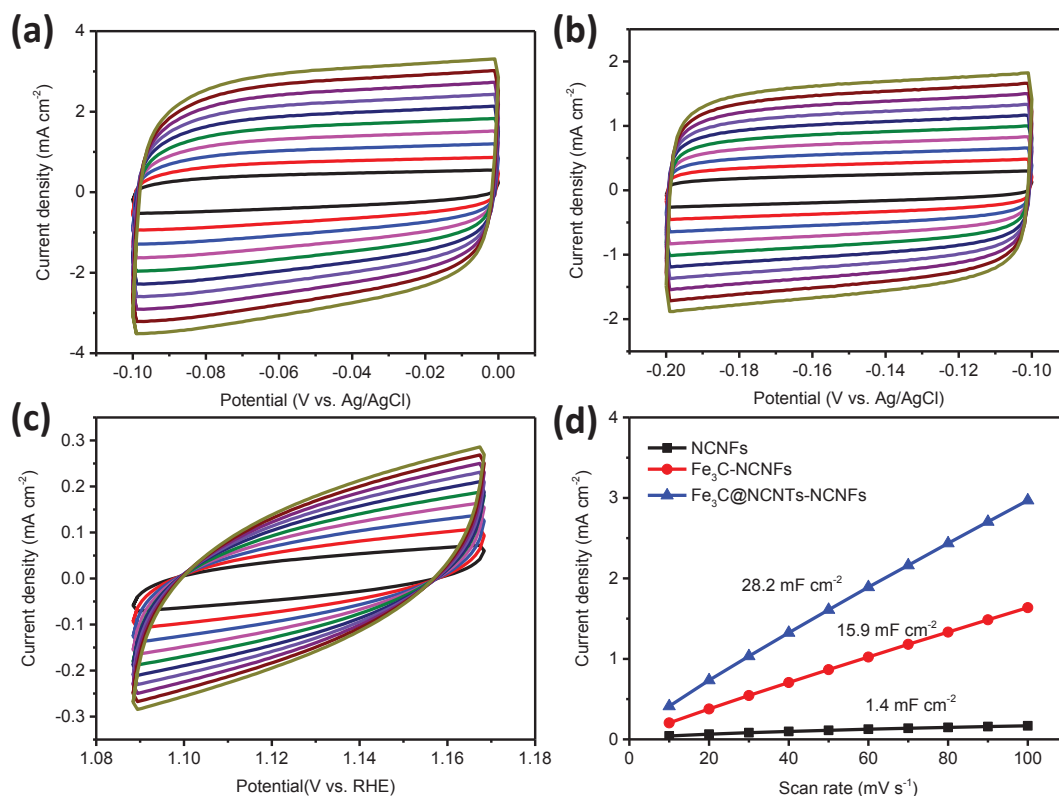


Figure 7-10 Cyclic voltammograms (CV) of (a) $\text{Fe}_3\text{C}@\text{NCNTs-NCNFs}$, (b) $\text{Fe}_3\text{C-NCNFs}$, (c) NCNFs, both in 1 M KOH solution in a potential window without faradaic processes. (d) Scan rate dependence of the average capacitive current densities at open circuit potential for $\text{Fe}_3\text{C}@\text{NCNTs-NCNFs}$, $\text{Fe}_3\text{C-NCNFs}$ and NCNFs.

To better understand the kinetics during the OER process, cyclic voltammetry (CV) and electrochemical impedance spectroscopy (EIS) were performed. CV was conducted in the potential region with no apparent Faradaic process occurrence. The electrochemical double-layer capacitance (C_{dl}) was measured to investigate the effective surface area.^{200, 268} The C_{dl} of $\text{Fe}_3\text{C}@\text{NCNTs-NCNFs}$ is 28.2 mF cm^{-2} , exhibiting a 1.8 and 20-times C_{dl} to those of $\text{Fe}_3\text{C-NCNFs}$ (15.9 mF cm^{-2}) and NCNFs (1.4 mF cm^{-2}), respectively (Figure 7-10).

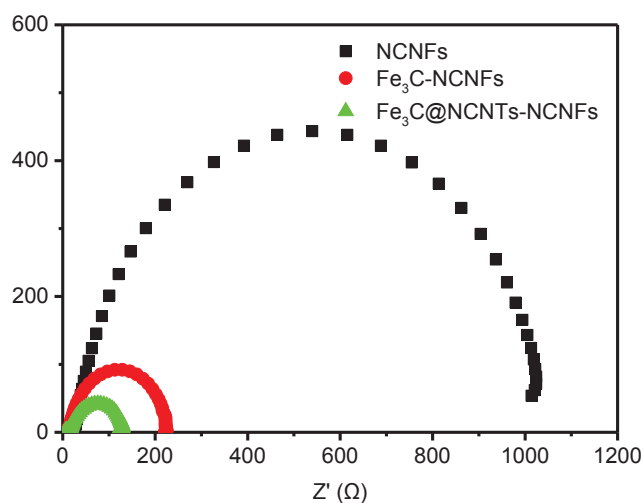


Figure 7-11 EIS spectra of $\text{Fe}_3\text{C}@NCNTs\text{-}NCNFs$, $\text{Fe}_3\text{C-NCNFs}$ and $NCNFs$ modified electrodes with an overpotential of 250 mV.

As shown in Figure 7-11, the charge transfer resistance of $\text{Fe}_3\text{C}@NCNTs\text{-}NCNFs$ is slightly lower than that of $\text{Fe}_3\text{C-NCNFs}$, which is obviously much lower than that of pure $NCNFs$. Therefore, the high effective surface area and low charge resistance suggest that $\text{Fe}_3\text{C}@NCNTs\text{-}NCNFs$ composite can provide more active sites and facilitate fast charge transfer during the OER process, leading to its superior catalytic performance.

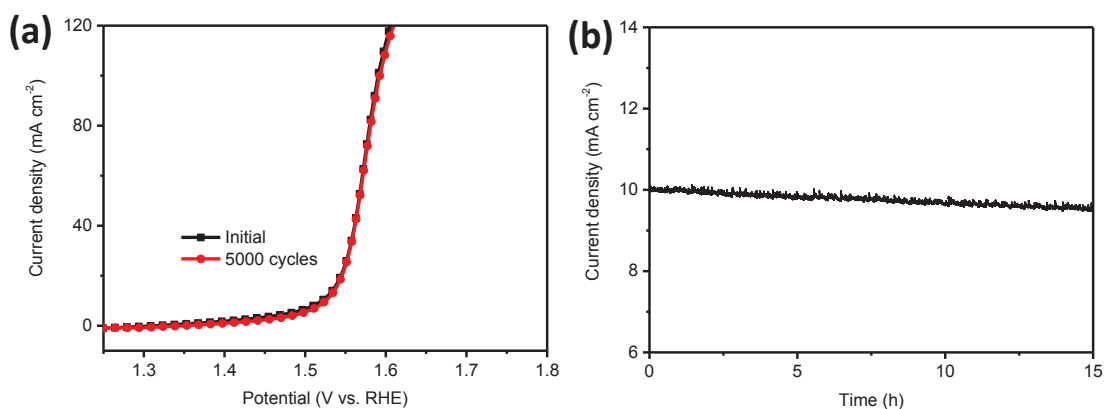


Figure 7-12 Stability test of $\text{Fe}_3\text{C}@NCNTs\text{-}NCNFs$ (a) through potential cycling. (b) time dependence of catalytic current density during electrolysis at a static overpotential.

Figure 7-12(a) presents the durability of Fe₃C@NCNTs-NCNFs composite by recording continuous LSVs for 5000 cycles at an accelerated scan rate of 100 mV s⁻¹. The polarization curve of Fe₃C@NCNTs-NCNFs after cycling is almost exactly the same as the initial test. Figure 7-12(b) demonstrates the stability of Fe₃C@NCNTs-NCNFs assessed by electrolysis at a static overpotential. Time dependence for the current density of Fe₃C@NCNTs-NCNFs shows only a little degradation after 15 h test (degradation of 4.4%). Such stable characteristic can be ascribed to the stable 1 D CNFs substrate, graphitic structure and the unique encapsulated structure.

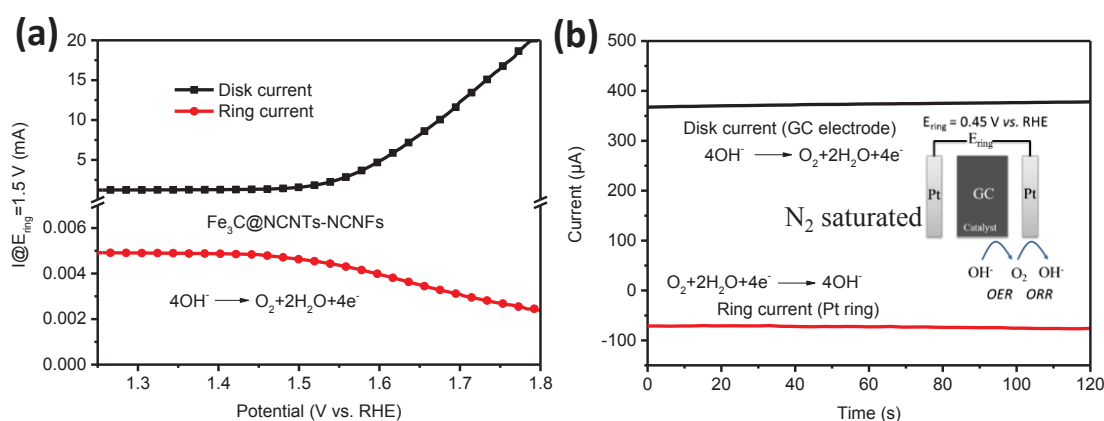


Figure 7-13 (a) Disk and ring current of Fe₃C@NCNTs-NCNFs catalyst on an RRDE (1600 rpm) with a ring potential of 1.50 V (vs. RHE). (b) Evidence of O₂ generated from Fe₃C@NCNTs-NCNFs catalyst using RRDE measurements (1600 rpm) (disk potential: 1.48 V, ring potential: 0.45 V vs. RHE), with inset showing the continuous OER → ORR process initiated on the RRDE.

Figure 7-13(a) reveals the reaction mechanism of Fe₃C@NCNTs-NCNFs during the OER process, applying the rotating ring-disk electrode (RRDE) apparatus in N₂-saturated 1 M KOH solution, to analyze the contents of by-products (peroxide intermediates) formed on the surface of the Fe₃C@NCNTs-NCNFs catalyst. A relatively low ring current (from peroxide intermediates) is observed (the ring potential was held at 1.50 V vs. RHE), which is far lower than that of the disk current, indicating negligible hydrogen peroxide formation and the existence of a desirable four-electron

transfer pathway during the OER process.¹⁴⁶ Furthermore, Faradaic efficiency was calculated during a continuous OER (disk electrode)-ORR (ring electrode) process. The disk potential holds constant at 1.48 V *vs.* RHE to generate O₂ molecules from Fe₃C@NCNTs-NCNFs, and then the as-formed O₂ molecules are further reduced by sweeping across the surrounding Pt ring electrode with an ORR potential of 0.45 V *vs.* RHE. A ring current of approximately 73 μ A was collected along with the obtained disk current of 373 μ A (Figure 7-13(b)), corresponding to a Faradaic efficiency of 97.8% (see calculation details in the Experimental section).¹⁰

The superior electrocatalytic activity of Fe₃C@NCNTs-NCNFs can mainly be attributed to the chemical composition and aligned structure with Fe₃C@NCNTs arrays on 1D CNFs as well as the multiple synergistic effects between Fe₃C, NCNTs and NCNFs. First, the aligned graphitic CNTs provide an open architecture for sufficient reactant/catalyst contact. The Fe₃C nanocrystals are encapsulated at the tips of CNTs, enabling the full utilization of active sites of the catalyst and resulting in greatly facilitated surface reactions. Second, the 1D nanostructure (CNFs) provides a stable, continuous and conductive network, expediting electron transfer during the electrochemical reaction process. Third, nitrogen doping (C-N, C=N, Fe-N) can induce asymmetrical charge distributions on the adjacent carbon atoms and decrease the energy required for the adsorption of the reactants on electrocatalyst, and thus lead to an improved catalytic performance. Last, the intimate interaction and strong coupling effects between Fe₃C, NCNTs and NCNFs, assist in providing additional active sites and facilitating fast charge transfer, further improving the OER kinetics. Therefore, these collaborative properties enable Fe₃C@NCNTs-NCNFs composite to be an excellent OER catalyst.

7.4 Conclusion

In conclusion, we have revealed a novel structure with Fe₃C@NCNTs aligned on CNFs through a facile, scalable electrospinning technique, followed by a carbonization route with the addition of melamine. The Fe₃C@NCNTs-NCNFs composite is demonstrated as a high performance OER catalyst, delivering a low onset potential (1.39 V *vs.* RHE), a high current density (10 mA cm⁻² at the overpotential of 284 mV), a low charge transfer resistance and excellent durability in 1 M KOH solution. The exceptional electrocatalytic performance of Fe₃C@NCNTs-NCNFs may be associated with synergistic effects from the chemical compositions and the robust 3D interconnected structure composed of Fe₃C@NCNTs arrays and CNFs substrate. This study should provide a guideline for the further design of favourable structures for water splitting and other energy applications.

Chapter 8 Electrospun Cobalt Embedded in Porous Nitrogen Doped Carbon Nanofibers as an Efficient Catalyst for Water Splitting

8.1 Introduction

In the previous Chapters, we have synthesized different kinds of catalysts and investigated their catalytic activity towards HER and OER. These catalysts, such as MoS₂-GA, G-Co₃O₄, PGE-CoO, CoMn₂O₄-CoNC, Fe₃C-NCNTs@NCNFs, displayed good catalytic activity and stability towards HER and OER, respectively. Notwithstanding significant progress, there are very few catalysts that are able to catalyze both HER and OER in the same electrolyte. The HER catalysts usually show good performance in acidic solution, whereas OER catalysts exhibit better performance in alkaline solution. Previously, Pt-free bifunctional electrocatalysts show the ability for the oxygen reduction reaction and OER, simultaneously. Therefore, developing a bifunctional catalyst that is able to catalyze both HER and OER, two half reactions occurring in the same electrochemical device (i.e., electrolyzer) will be very attractive, because this can potentially simplify the fabrication procedure of electrolyzers and substantially make the water splitting for large scale application.

Recently, a variety of cost-effective materials have been tested for catalyzing the electrochemical hydrogen evolution, including transition-metal chalcogenides, carbides, and complexes.^{22, 289-292} Furthermore, OER with more sluggish kinetics also requires efficient catalysts (cobalt oxides (CoO, Co₃O₄), substituted cobaltites M_xCo_yO₄ (M = Ni, Fe) to reduce the energy barrier and further accelerate the overall water splitting process.²⁹³⁻²⁹⁵ Nitrogen/transition metal (Co, Ni, Fe) functionalized carbon materials have been developed as the most promising candidates for HER and OER, due to their high catalytic performances.^{296, 297} The morphology, structure and electronic

conductivity are the key factors influencing their electrocatalytic efficiency.¹⁶² However, the corrosion property and poor stability of the transition metals may result in poor performances during the test. Recently, in order to further enhance the catalytic activity and stability, there are a few works reported based on the encapsulated structure, such as Co, Fe or FeCo, NiCo alloy nanoparticles embedded in nitrogen-doped carbon materials (carbon nanotubes or graphene), and these catalysts delivered high performance towards OER, HER or ORR.^{79, 87, 92, 298} The confinement of these composites not only provides an easy way to restrict the size of the encapsulated particles down to the nanometer scale, but also creates unique structural features with well-developed interactions between the encapsulated metal particles and the carbon materials. However, it is still a great challenge to create an effective way to disperse metal particles uniformly encapsulated by the carbon materials. Thus, developing a simple and scalable technique (e.g. electrospinning) to produce high performance electrocatalysts with the unique encapsulated structure is highly desirable, especially as catalysts towards overall water splitting.

Carbon nanofibers (CNFs), a popular one dimensional carbon material, have already garnered extensive interests due to their attractive properties of high electronic conductivity and good electrochemical stability, which can be synthesized by a facile electrospinning technique.^{197, 299-301} To date, only a few studies have been investigated by using electrospun materials as the catalysts.^{285, 302} Generally, CNFs merely work as matrix for providing large specific surface area and enhancing conductivity for the catalysts. The contribution for the catalytic performance directly from carbon is usually ignored. As above mentioned, functionalized carbon (CNTs or graphene) with transition metal or nitrogen element could efficiently convert the inert carbon into active sites as

electrocatalysts.^{303, 304} Therefore, it is significant to design novel functionalized CNF-based catalysts by electrospinning technique for water splitting.

Herein, we developed a facile, scalable method to synthesize cobalt nanoparticles embedded in porous nitrogen doped CNFs (Co-PNCNFs) by electrospinning technique. The Co-PNCNFs composite displays a well-defined 3D networks associated with encapsulated and porous structure. The unique encapsulated structure could efficiently avoid the metal nanoparticles directly contact with the harsh environmental, protecting the metal nanoparticles from corrosion and aggregation during the catalytic process. The porous structure could provide more active sites for oxygen evolution and facilitate fast and versatile transport pathways for the electrolyte diffusion. Benefiting from its high exposed effective surface area, improved electronic conductivity, intimate interaction and synergetic effect, Co-PNCNFs can serve as active electrocatalyst for both OER and HER with an outstanding performance and excellent stability.

8.2 Experimental

8.2.1 Synthesis of Co-PNCNFs

Co-PNCNFs were prepared using an electrospinning method with a subsequent heat treatment. 320 mg of cobalt nitrate ($\text{Co}(\text{NO}_3)_2 \cdot 6\text{H}_2\text{O}$, >98%, Sigma-Aldrich) and 600 mg of polyacrylonitrile (PAN, $M_w = 150000 \text{ g mol}^{-1}$, Sigma-Aldrich) were dissolved in 6 ml N,N-dimethylformamide (DMF, Chem-supply). The above solution was left at 50 °C under vigorous stirring overnight and then transferred to a 10 ml plastic syringe with a 20-gauge blunt tip needle. For the electrospinning, a high voltage of 18 kV and flow rate of $14.8 \mu\text{l min}^{-1}$ were applied, with a distance of 15 cm between the needle and rotating grounded collector. The as-collected electrospun fibers first underwent heat treatment at 450 °C for 2 h in an H_2 ($\text{H}_2 : \text{Ar} = 5 : 95 \text{ vol\%}$) atmosphere and then 800 °C

for 6 h in Ar atmosphere to obtain the composite (Co-NCNFs). The heating rate was kept at 1 °C min⁻¹. Cobalt nanoparticles loaded on the surface of CNFs were removed by washing in 0.5 M H₂SO₄ solution for 24 h to achieve the porous structure composite (Co-PNCNFs).

8.2.2 Synthesis of NCNFs

The preparation process of the pure N-doped CNFs (NCNFs) was the same as the method used for Co-PNCNFs, but without the addition of cobalt nitrate in the electrospinning solution.

8.2.3 Synthesis of the comparison materials

Nickel or iron embedded in porous nitrogen doped CNFs (Ni-PNCNFs, Fe-PNCNFs) were prepared by replacing cobalt nitrate with nickel nitrate or iron nitrate. Cobalt embedded in carbon nanofibers (Co-PCNFs) were fabricated by using polyvinylpyrrolidone (PVP M_w = 360000 g mol⁻¹) to replace PAN.

8.2.4 Characterization

The morphology and particle size of the samples were acquired with field emission scanning electron microscopy (FESEM, Zeiss Supra 55VP), element mapping and electron energy dispersive spectroscopy (Zeiss Evo SEM), and transmission electron microscopy (TEM, Model JEM-2011, JEOL). X-ray diffraction (XRD) of the samples was characterized by employing a scanning step of 0.02° per second in the 2 θ range from 10 to 80° (Siemens D5000 using Cu Kα radiation). Raman spectra were obtained on an inVia Renishaw Raman spectrometer system (HR Micro Raman spectrometer, Horiba JOBIN YVON US/ HR800 UV) using a 632.8 nm wavelength laser. X-ray photoelectron spectroscopy (XPS) was collected on an ESCALAB250Xi (Thermo

Scientific, UK) equipped with mono-chromated Al K alpha (energy 1486.68 eV). Brunauer–Emmett–Teller (BET) surface area of the obtained materials was achieved by using experimental points at a relative pressure of $P/P_0 = 0.05–0.25$. Thermogravimetric analysis (TGA) was performed by simultaneous TG-DTA (SDT 2960) at a heating rate of $5\text{ }^{\circ}\text{C min}^{-1}$ from room temperature to $800\text{ }^{\circ}\text{C}$ in air atmosphere.

8.2.5 Electrochemical Measurements

The electrocatalytic experiments were carried out on an electrochemical workstation (CHI 660E). Data were collected in a standard three-electrode glass cell, with platinum wire and Ag/AgCl (saturated KCl) working as the counter and reference electrodes ($E_{\text{RHE}} = E_{\text{Ag/AgCl}} + 0.059 \times \text{pH} + 0.1971$), respectively. OER and HER performance were tested by using materials on GC as working electrodes. The working electrode was fabricated as follows: the catalyst slurry was prepared by mixing 4 mg of catalyst, $80\text{ }\mu\text{l}$ of Nafion (5 wt %) and 1 ml solvent (1:1 v/v water/isopropanol) and then sonicated for 30 min to form a dispersion. $10\text{ }\mu\text{l}$ of the dispersion was dropped onto the glassy carbon (GC) electrode with the mass loading of 0.56 mg cm^{-2} (diameter of 3 mm), followed by drying at room temperature. Water electrolyzer tests were performed by using Co-PNCNFs on the Ni foam for water splitting. To prepare Co-PNCNFs on the Ni foam, 16 mg catalyst were dispersed in 2 ml solvent (1:1 v/v water/isopropanol, $200\text{ }\mu\text{l}$ of Nafion). After sonication, 1 ml of the suspension was dropped onto $1 \times 1\text{ cm}$ Ni foam (8 mg cm^{-2}) and then dried in the vacuum oven at $80\text{ }^{\circ}\text{C}$. OER or HER activities of the catalysts were evaluated by linear sweep voltammetry (LSV) in 1 M KOH solution at a scan rate of 5 mV s^{-1} . The polarization curves were all corrected for the iR contribution within the cell. The electrochemical impedance spectra were obtained by applying an amplitude of 5 mV within a frequency ranges from 10^6 to 0.01 Hz under open circuit. The effective surface area of Co-PNCNFs and NCNFs were evaluated by cyclic voltammetry (CV),

conducted in a potential range in which no apparent Faradaic processes occur at different scan rates (10 to 100 mV s⁻¹). The cycling performance of Co-PNCNFs based electrode was operated by repeating LSV running for 5000 cycles with the potential range from 1.20 to 1.70 V *vs.* RHE and the current–time plots were performed with the applied potentials at 1.52 or 1.54 V (*vs.* RHE).

The rotating ring-disk electrode (RRDE) voltammograms were carried out based on an RRDE configuration (Pine Research Instrumentation, USA) with a GC disk and Pt ring electrode. The as-prepared Co-PNCNFs catalyst was coated onto the disk electrode by using the above mentioned method. A rotating speed of the RRDE was held at 1600 rpm for the test. To ensure the oxidation current originated from oxygen evolution, the ring potential was held constantly at 0.45 V *vs.* RHE (disk current fixed at 250 μ A) to reduce the formed O₂ from the catalyst on the disk in N₂-saturated 1 M KOH solution. A continuous OER (disk electrode) \rightarrow ORR (ring electrode) process occurred on the RRDE. The Faradaic efficiency was calculated as follows: $\epsilon = I_r/(I_d N)$, where I_d is the disk current, I_r is the ring current, and N represents the current collection efficiency of the RRDE ($N = 0.2$). On the other hand, to detect the hydrogen peroxide (HO₂⁻) formation, the ring potential was held constantly at 1.50 V *vs.* RHE for oxidizing HO₂⁻ intermediate in O₂-saturated 1 M KOH (the disk potential was held constantly at 1.55 V *vs.* RHE).

8.3 Results and discussion

8.3.1 The characterization of the catalysts

Figure 8-1 illustrates the preparation of Co-PNCNFs nanofibers by electrospinning. The electrospun nanofibers were collected on the substrate, followed by the reduction in H₂/Ar and carbonization in Ar atmosphere. The nitrogen-rich PAN provides a good

strategy to form N-doped carbon materials, which is an efficient approach to improve the catalytic activity of carbon-based materials. The final material of Co-PNCNFs was obtained by acid treatment to remove the cobalt nanoparticles on the surface of CNFs.

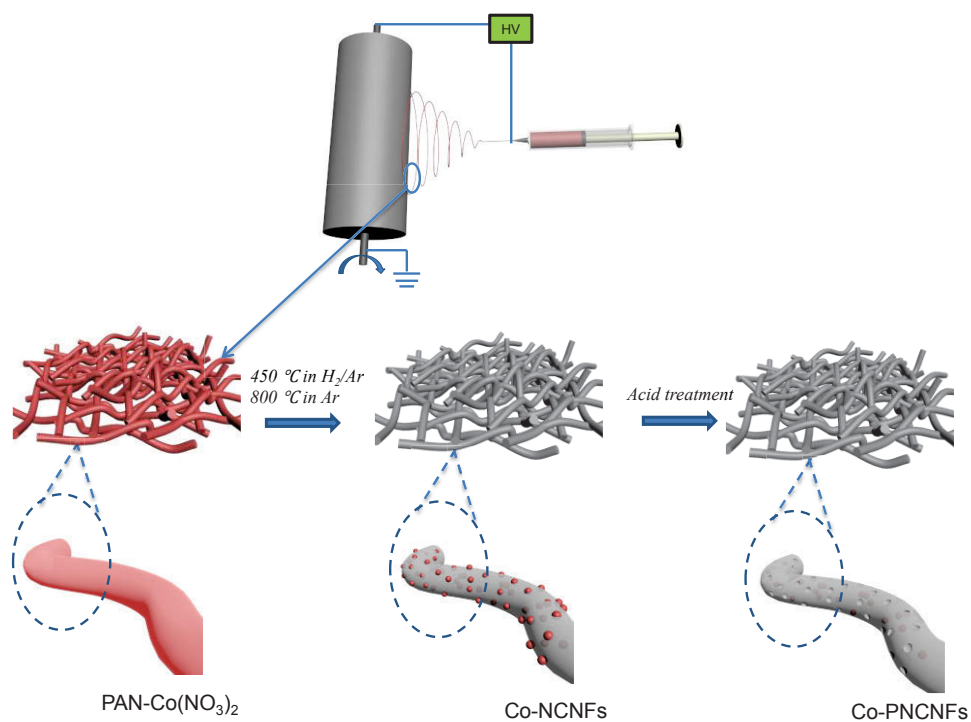


Figure 8-1 Schematic illustration for the preparation of Co-PNCNFs nanofibers by electrospinning.

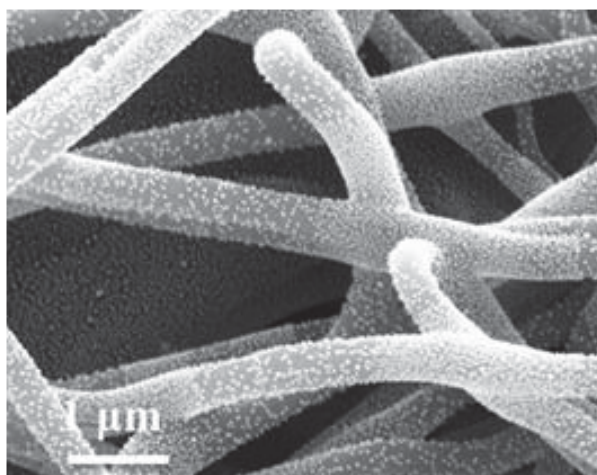


Figure 8-2 SEM image of Co-NCNFs (before acid treatment), showing the cobalt nanoparticles on the surface of CNFs.

The precursor we collected after high temperature carbonization is denoted as Co-NCNFs. The SEM image of Co-NCNFs in Figure 8-2 shows that Co-NCNFs display a well-organized 1-D cylindrical morphology, forming continuous carbon fiber networks. The average diameter of Co-NCNFs is around 400-500 nm. The cobalt nanoparticles uniformly distributed on the surface of CNFs.

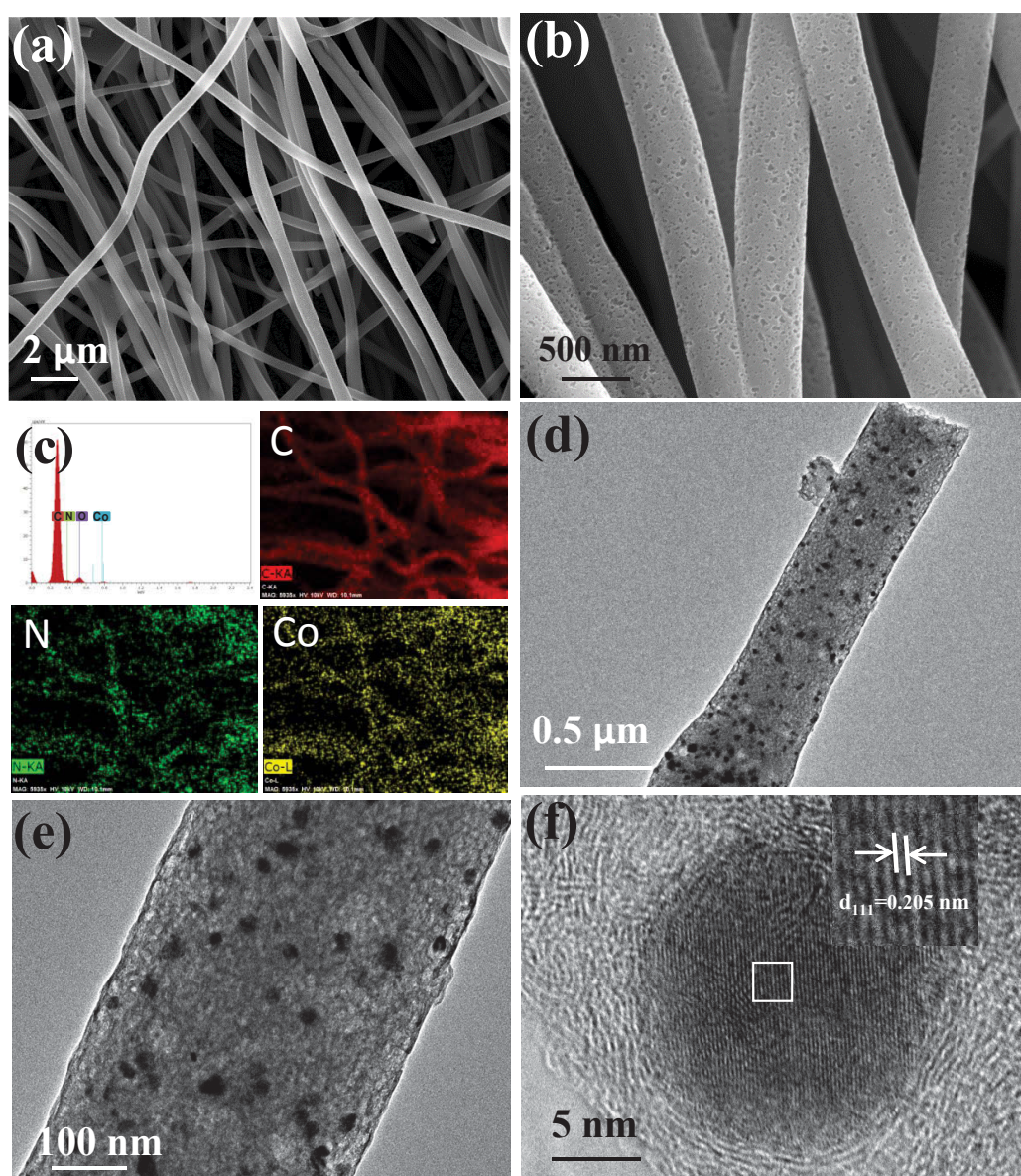


Figure 8-3 Electron microscopy characterization of Co-PNCNFs. (a) low magnification and (b) high magnification SEM images of Co-PNCNFs. (c) EDS analysis of Co-PNCNFs, showing homogenous distribution of C, N, Co elements in fibrous structure. (d) TEM image of a single fibrous Co-PNCNF. (e) Enlarged TEM image of a single Co-

PNCNF, demonstrating the structure of dispersed nanoparticles embedded in porous carbon fiber. (f) HRTEM image of a Co nanoparticle wrapped in carbon. The inset is the enlarged area as denoted in the white box, displaying an interplanar spacing of 0.205 nm.

Figure 8-3(a, b) show the SEM images of Co-PNCNFs. Co-PNCNFs highly maintain the 1-D cylindrical morphology of Co-NCNFs, suggesting the structural stability in the acidic solution. The high magnification SEM image of Co-PNCNFs (Figure 8-3(b)) reveals that no cobalt nanoparticles could be observed on the surface of CNFs. More importantly, the high magnification image indicates that the surface of Co-PNCNFs is rougher and more porous, owing to the removal of cobalt particles with acid treatment. Energy dispersive spectroscopy (EDS) and element mapping confirm that Co-PNCNFs are composed of C, N, Co, O elements, with homogenous distribution (Figure 8-3(c)). TEM characterization in Figure 8-3(d) further verifies that the particles on the surface of CNFs are all removed and only small cobalt nanoparticles (10-20 nm) encapsulated in CNFs can be observed. These carbon-encased cobalt nanoparticles are not exposed, as they remain embedded in CNFs even after being treated with acidic solution. In Figure 8-3(e), the high magnification TEM image clearly shows the porous structure formed on the surface of Co-PNCNFs. Figure 8-3(f) displays a single cobalt nanoparticle with size of 15 nm embedded in carbon fiber. The formation of a few layers onion-like graphitic carbon wrapped around the encapsulated Co nanoparticle can be ascribed to the catalytic effect of Co nano-catalyst during the carbonization process. The inset of Fig. 2f represents the enlarged area as denoted in white box, showing a d-spacing of 0.205 nm for the nanoparticles, which can be indexed to the (111) interplanar plane of cobalt.

The SEM images of NCNFs are shown in Figure 8-4(a, b), which shows that the surface of NCNFs is smooth and no obvious porous structure could be observed on the surface. The TEM images in Figure 8-4(c, d) are in consistent with the SEM result, moreover, there is no graphitic carbon for NCNFs. The SEM and TEM results suggest that the metallic cobalt nanoparticles play important role in the formation of the graphitic carbon and porous structure.

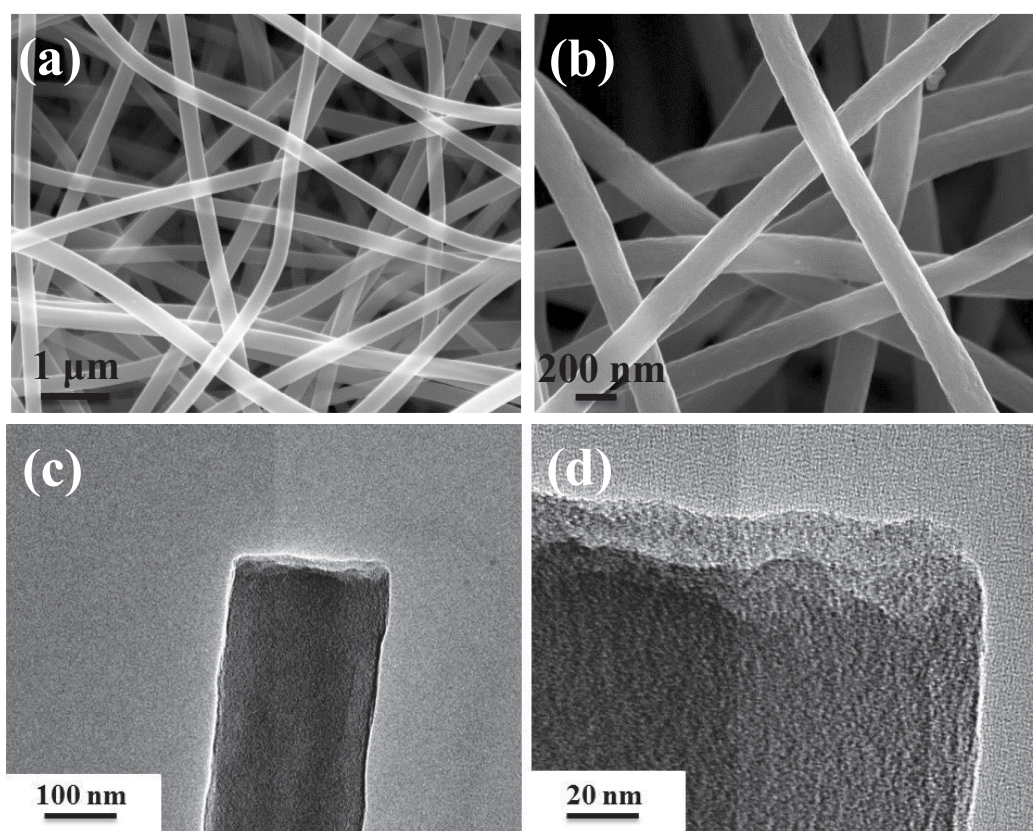


Figure 8-4 (a, b) Low and high magnification SEM images of NCNFs, (c, d) Low and high magnification TEM images of NCNFs.

Figure 8-5(a) shows the XRD patterns of the final materials of NCNFs and Co-PNCNFs. The diffraction peaks around 25.2° for NCNFs and Co-PNCNFs are attributed to the (002) crystallographic plane of graphite, indicating that the graphitic structure has been obtained after carbonization (corresponding to the HRTEM result). The presence of metallic cobalt in Co-PNCNFs is manifested by the two peaks around 43.8° and 51.9° ,

which can be indexed to the (111) and (200) crystal planes of the cobalt (PDF No. 15-0806), suggesting the successful reduction of cobalt ions to a metallic state during carbonization. And the d-spacing of cobalt (111) calculated from XRD peak by Bragg equation ($2d \sin \theta = n\lambda$ ($n=1$, $\lambda=0.154056$ nm)) is 0.2065 nm, which is quite close to the HR-TEM observation ($d=0.205$ nm). The low diffraction peaks of Co can be ascribed to the small amount of metallic cobalt in the composite (11.4 wt %, TGA).

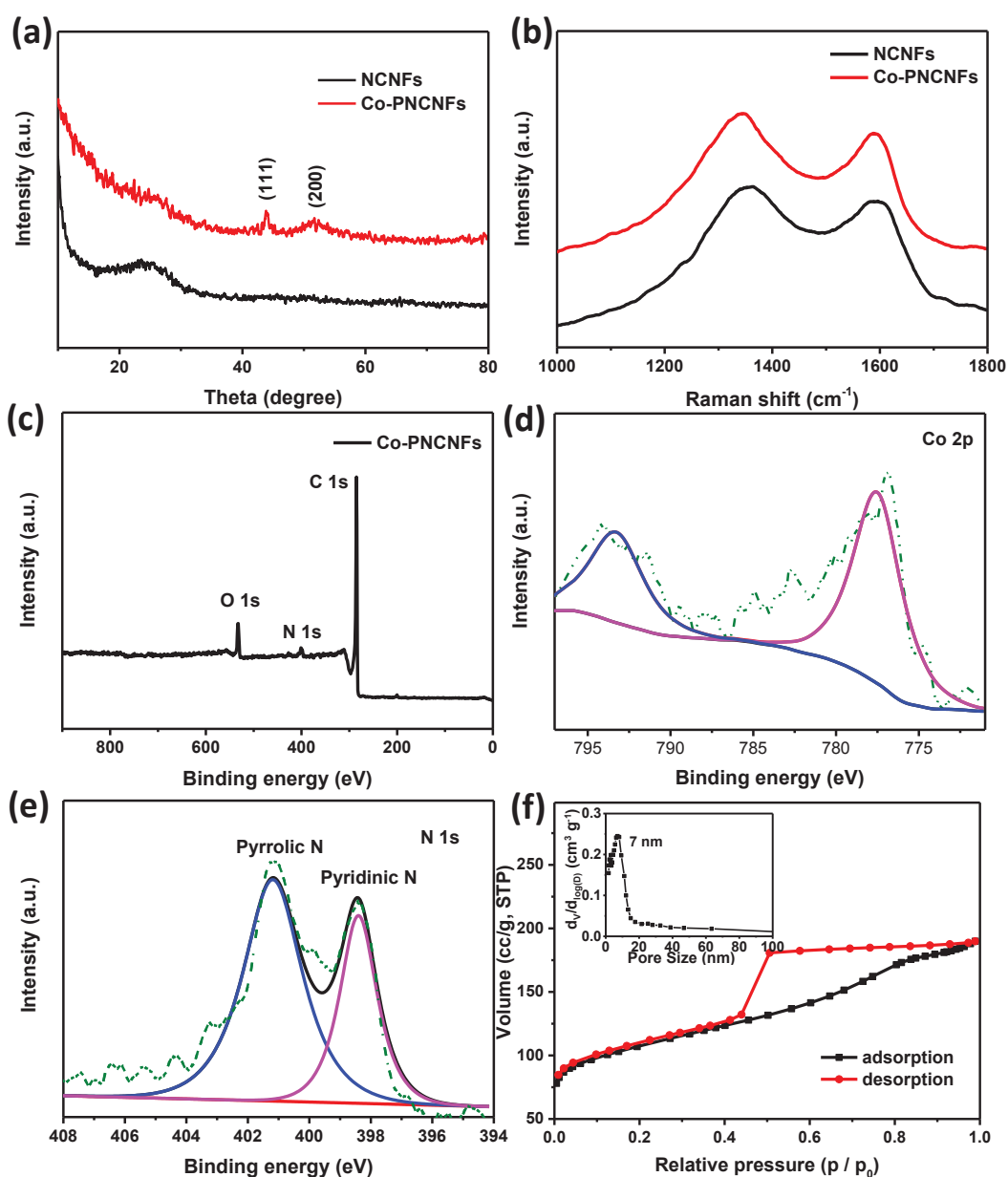


Figure 8-5 (a) XRD patterns of NCNFs and Co-PNCNFs. (b) Raman spectra of NCNFs and Co-PNCNFs. (c) XPS spectrum of Co-PNCNFs composite. High resolution XPS

spectra of (d) Co 2p and (e) N 1s. (f) Nitrogen sorption isotherm of Co-PNCNFs, inset shows the pore size distribution of Co-PNCNFs.

Figure 8-5(b) represents the typical Raman spectra of NCNFs and Co-PNCNFs that display two typical peaks, corresponding to the defect induced D-band and graphitic G-band, respectively.^{189, 197} The intensity ratio of D/G (I_D/I_G) value for Co-PNCNFs hybrid (1.17) is higher than that of pure NCNFs (1.08). The increased I_D/I_G indicates more defects in the carbon lattice of Co-PNCNFs, which may be as a result of the removal of cobalt nanoparticles (porous structure) and the defects in the graphitic structures. From the XPS survey spectrum of Co-PNCNFs in Figure 8-5(c), only C, N and O elements can be clearly observed, and there is no distinguishable signal for Co, because of its encapsulation in carbon matrix. The high resolution XPS spectrum in Figure 8-5(d) shows the characteristic peak located at 777.6 and 793.3 eV, attributing to the property of Co 2p. The high resolution N 1s spectrum (Figure 8-5(e)) could be deconvoluted into two peaks, corresponding to the pyridinic (398.4 eV) and pyrrolic N (401.2 eV), both of which have been proven to have efficient catalytic activity towards OER and HER. Based on the XPS result, the percentage of N in Co-PNCNFs is ~5.44 wt%. The BET surface area of Co-PNCNFs is 356.6 m² g⁻¹ (Figure 8-5(f)). This should be attributed to the unique porous structure of Co-PNCNFs (Pore size distribution of Co-PNCNFs is shown in the inset of Figure 8-5(f), displaying the presence of mesopores at 7 nm). The Co-PNCNFs with larger surface area are expected to provide more active sites for the water splitting reaction.

8.3.2 The electrochemical performance test of the catalysts

The electrocatalytic activities of the catalysts (Co-PNCNFs, NCNFs, RuO₂, Pt/C) were investigated for OER in 1 M KOH solution by LSV. As shown in Figure 8-6(a), Co-PNCNFs exhibit the highest catalytic activity with a low onset potential of 1.45 V

(vs. RHE), above which the anodic current rises rapidly. The current density of 10 mA cm^{-2} could be achieved at a low overpotential of 285 mV for Co-PNCNFs. This catalytic activity of Co-PNCNFs is superior to the behaviour of non-noble electrocatalysts at the same condition for OER, such as the exfoliated NiCo layered double hydroxide nanosheets, (367 mV for 10 mA cm^{-2}), Ni-Co double hydroxides nanocages (350 mV for 10 mA cm^{-2}) and $(\text{Co}_y\text{Fe}_{10-y}\text{O}_x/\text{NPC})$ nanosheets (328 mV for 10 mA cm^{-2}).^{10, 305, 306} Moreover, the catalytic activities of the deposited materials (including the commercial standard catalysts) were compared by recording their current densities at an overpotential of 400 mV. Co-PNCNFs exhibits the highest catalytic current density of 86 mA cm^{-2} (20 mA cm^{-2} for RuO_2 , 2.5 mA cm^{-2} for Pt/C, 1.3 mA cm^{-2} for NCNFs) and no OER catalytic activity for the bare GC electrode.

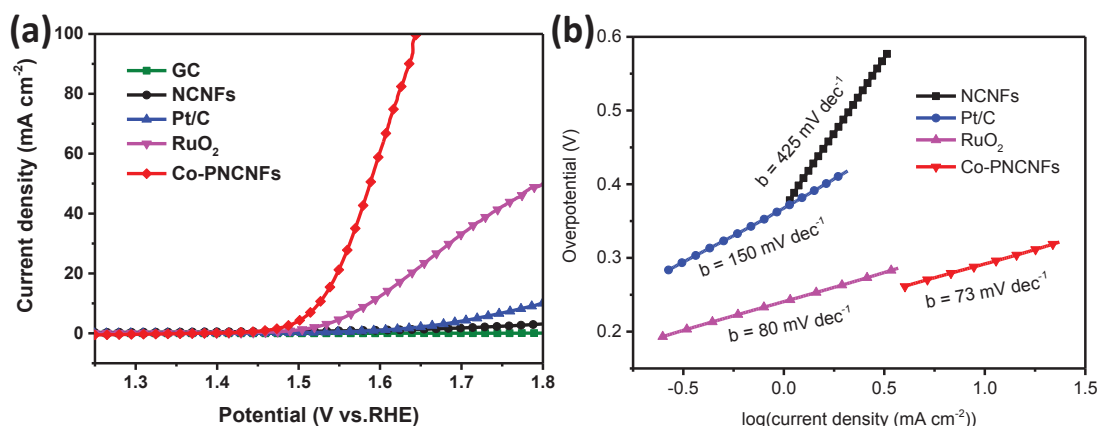


Figure 8-6 Electrochemical performance of the catalysts towards OER in 1 M KOH solution: (a) Polarization curves for Co-PNCNFs, NCNFs, RuO_2 , Pt/C and pure GC. (b) The corresponding Tafel plots of catalysts.

Tafel slopes are derived from the polarization curves in Figure 8-6(a) to gain insight into the OER process. The corresponding Tafel slope of Co-PNCNFs based electrode, 73 mV dec^{-1} , is much lower than that of pure NCNFs (425 mV dec^{-1}), indicating that the introduction of cobalt can deliver a much more favourable reaction kinetics and provide a remarkably increased OER rate with the increase of

overpotentials (drive a large catalytic current density at low overpotential). Co-PNCNFs deliver outstanding electrocatalytic performance as an efficient OER catalyst, including low overpotential, high catalytic current density and small Tafel slope. This enhancement can be ascribed to the unique porous 3D network architecture, and bi-functionalization with cobalt encapsulation and nitrogen doping.

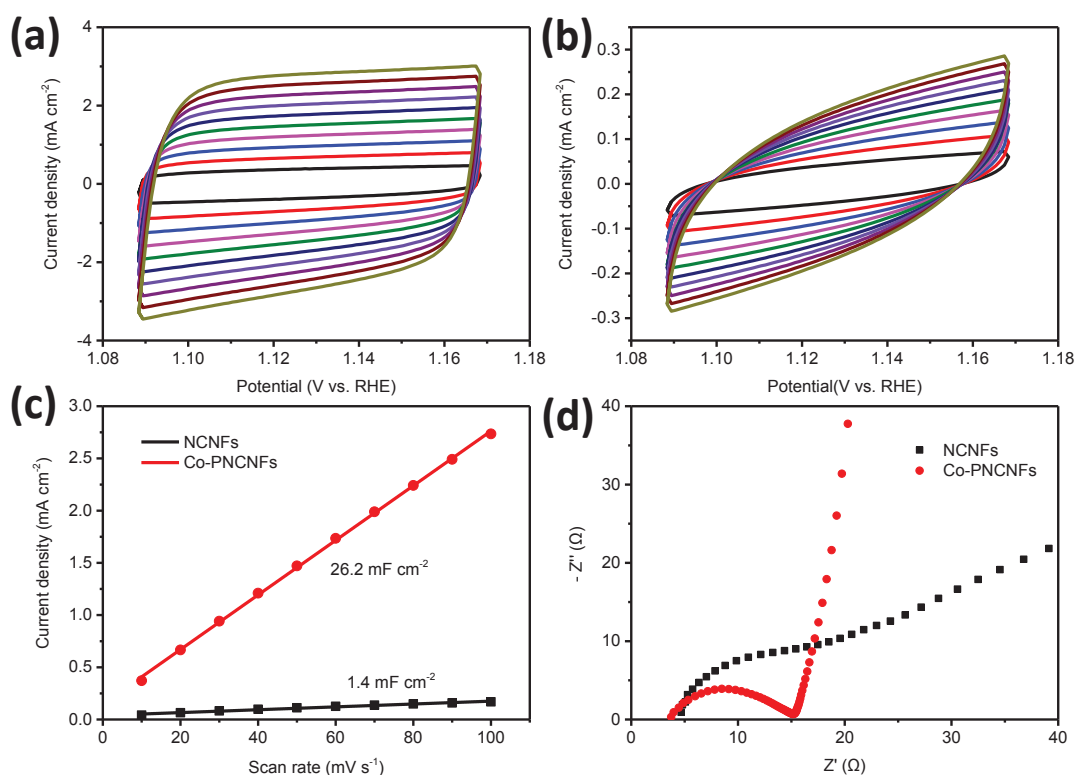


Figure 8-7 Cyclic voltammograms (CV) of (a) Co-PNCNFs, and (b) NCNFs, both in 1 M KOH solution in a potential window without faradaic processes. (c) Scan rate dependence of the average capacitive current densities at open circuit potential for Co-PNCNFs and NCNFs. (d) Nyquist plots of Co-PNCNFs and NCNFs modified electrodes.

To probe the effect of the structure and component of the catalysts on the OER process, effective surface area and electrochemical impedance spectra (EIS) were measured for Co-PNCNFs and NCNFs catalysts. Co-PNCNFs can provide a larger effective surface area, which can be evaluated approximately by using electrochemical

double-layer capacitance (C_{dl}).^{201, 307} Co-PNCNFs exhibit an 18.7-times C_{dl} (26.2 mF cm^{-2}) than that of pure NCNFs (1.4 mF cm^{-2}) (Figure 8-7(a-c)). Generally, the higher effective surface area is contributed to the higher electrocatalytic activity of the Co-PNCNFs composite. Figure 8-7(d) shows the EIS results, in which both Co-PNCNFs and NCNFs display a semicircle in the high frequency region and a straight-line in low frequency region, indicating the similar mass transport properties and reaction kinetics for OER process. It should be noted that Co-PNCNFs exhibit much lower impedance than that of NCNFs.

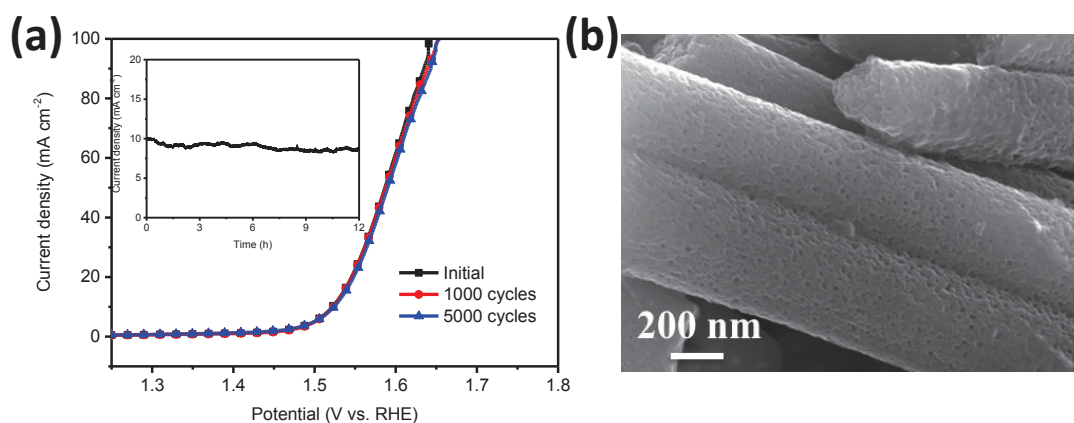


Figure 8-8 (a) Stability test of Co-PNCNFs through potential cycling, displaying polarization curves of initial one, after 1000 and 5000 potential cycles. Inset shows the chronoamperometric stability test over 12 h. (b) SEM image of Co-PNCNFs after stability test (60 h), displaying the carbon matrix and porous structure were maintained.

Besides high catalytic activities, good stability towards water splitting is also a critical aspect for an energy conversion system. To assess the stability of the catalyst, long-term potential cycling of Co-PNCNFs modified GC electrode was carried out in an alkaline solution by recording continuous LSVs for 5000 cycles. As shown in Figure 8-8(a), the polarization curves of Co-PNCNFs towards OER for the initial, 1000th and even 5000th cycles are identical, with negligible decrease of the current density. Furthermore, the practical operation of the catalyst is usually examined by electrolysis

at the fixed potentials. The current–time plots of the Co-PNCNFs based electrode with the applied potentials at 1.54 V (vs. RHE) are presented in the inset of Figure 8-8(a). The stable current density for 12 h and 60 h continuous operation suggests that the Co-PNCNFs electrode has a good durability for water splitting. The *ex-situ* SEM image (Figure 8-8(b)) implies the excellent stability of fibrous Co-PNCNFs towards long term testing. Such stable characteristic should originate from the N-doped carbon nanofiber matrix and the protected cobalt nanoparticles embedded in CNFs. The durability of the Co-PNCNFs catalyst demonstrates the potential for practical applications.

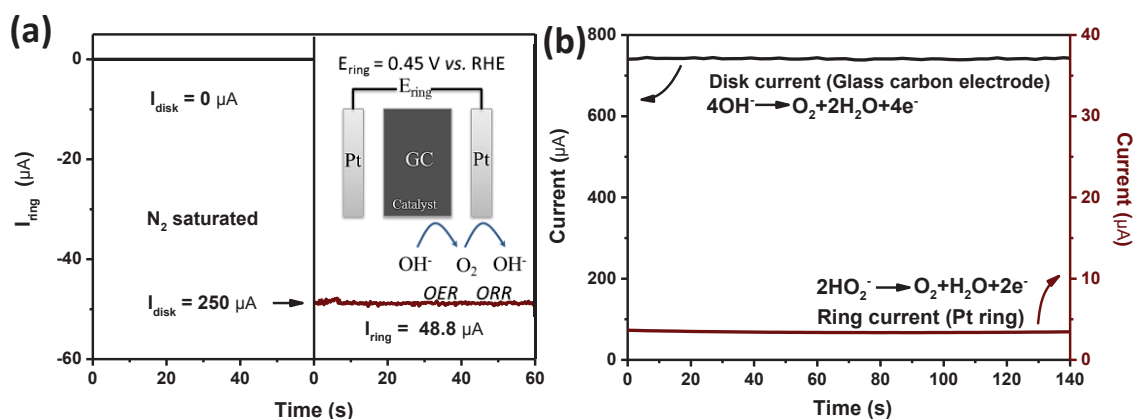


Figure 8-9 (a) The ring current of Co-PNCNFs on a RRDE (1600 rpm) in a N_2 -saturated 1 M KOH solution (ring potential: 0.45 V vs. RHE). (b) Disk and ring current of Co-PNCNFs on a RRDE (1600 rpm) with a disk potential of 1.55 V (vs. RHE) and ring potential of 1.50 V (vs. RHE) in 1 M KOH solution.

To ensure that the observed oxidation current in Figure 8-6(a) originates from oxygen evolution rather than other side reactions and to calculate the Faradaic efficiency, RRDE apparatus was applied in N_2 -saturated 1 M KOH solution, rendering a continuous OER (disk electrode)-ORR (ring electrode) process.^{269, 308} With the disk current fixed at 250 μA , O_2 molecules generated from the Co-PNCNFs catalyst, and the formed O_2 molecules were further reduced by sweeping across the surrounding Pt ring electrode with an ORR potential of 0.45 V vs. RHE. As shown in Figure 8-9(a), a ring

current of approximately $48.8 \mu\text{A}$ can be detected (RRDE collection efficiency = 0.2), corresponding to a Faradaic efficiency of 97.6% (see calculation details in the Experimental part). Furthermore, we have analyzed the content of the HO_2^- intermediates formed at the surface of Co-PNCNFs catalyst during the OER process by employing Pt ring electrode potential at 1.50 V vs. RHE (disk potential was fixed at 1.55 V vs. RHE). Figure 8-9(b) shows a relatively low ring current value ($\sim 3.3 \mu\text{A}$) compared to that of disk current ($\sim 740 \mu\text{A}$), suggesting that the formation of by-product (HO_2^-) is negligible and the OER reaction occurs via a desirable four-electron pathway for water oxidation, *i.e.* $4\text{OH}^- \rightarrow \text{O}_2 + 2\text{H}_2\text{O} + 4\text{e}^-$.

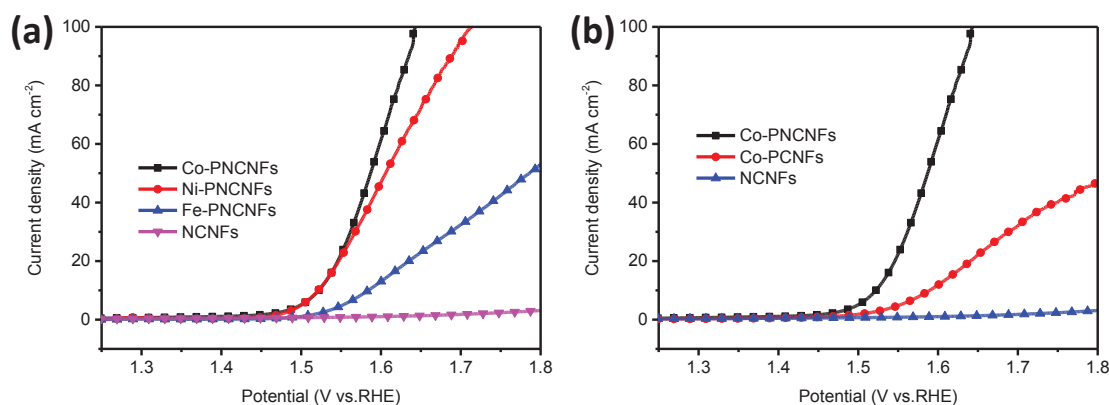


Figure 8-10 Catalytic activities of (a) Co-PNCNFs, Ni-PNCNFs, Fe-PNCNFs and pure NCNFs, and (b) Co-PNCNFs, Co-PCNFs and NCNFs. All these catalytic activity of CNFs based materials towards OER were tested in 1 M KOH solution, showing the electrocatalytic improvements promoted by metal or N functionalization.

The above mentioned results demonstrate that the Co-PNCNFs catalyst exhibits excellent electrocatalytic performance towards OER. Based on the aforementioned measurements and coupled with recent studies on nitrogen doped carbon materials or Co-based electrocatalysts, the following synergistic catalytic factors are proposed to elaborate the enhanced OER activity of the Co-PNCNFs catalyst. First, the unique one dimensional structure, as well as its porous architecture with high specific surface area,

provides high catalyst/electrolyte interfaces for oxygen evolution. Therefore, a large amount of active sites are generated, leading to the enhanced catalytic activities. Second, the cobalt/CNF core-shell structure benefits for the OER process in many aspects. Even though the metals (Co, Ni, Fe; the electrochemical performance of Ni-PNCNFs, Fe-PNCNFs are presented in Figure 8-10(a)) are not in direct contact with the electrolyte, they can influence the property of protective carbon towards catalytic processes. It is proposed that the catalytic activity might come from the structural and electronic interaction between the encapsulated metal and the protective carbon, and their intimate and direct contact further induce a high electronic conductivity, which promotes the OER activity.^{265, 267, 309, 310} Furthermore, the Co-PNCNFs catalyst is structurally stable in electrolyte because the metal nanoparticles are efficiently protected by encapsulated structure, so that outstanding long term performance can be achieved. Third, the positively charged nitrogen dopant in the carbon lattice could not only improve the interaction with reactant, but also induce asymmetrical charge distributions on the adjacent carbon atoms (facilitate a fast electron transfer for OER), resulting in the acceleration of the dynamics of oxygen evolution (the electrochemical performance of Co-PCNFs without nitrogen doping is presented in Figure 8-10(b)).^{165, 171, 311} Lastly, the encapsulated metallic cobalt nanoparticles and the nitrogen dopant synergistically affect the microstructure of the composite, not only by converting the inert carbon atoms into active sites, but also significantly improving the charge transport of electrodes, which efficiently reduces the reaction barrier and enhances the catalytic performance.

Co-PNCNFs have also shown efficient catalytic activity towards hydrogen evolution. The electrocatalytic activity of the Co-PNCNFs catalyst for HER was examined in 1 M KOH solution. According to the polarization curves (Figure 8-11(a)), it is evident that Co-PNCNFs exhibit acceptable catalytic activity towards HER. The

catalyst achieved 10 mA cm^{-2} at an overpotential of 249 mV, which is better than that of previously reported Co-NRCNTs (370 mV for 10 mA cm^{-2}) at the same condition.⁸⁷ Moreover, Co-PNCNFs displayed a smaller Tafel slope of 92 mV dec^{-1} (Figure 8-11(b)) than that of the pure NCNFs (213 mV dec^{-1}). These findings confirm the good electrocatalytic activity of Co-PNCNFs towards HER in alkaline solution. The catalytic stability was further evaluated by running continuous LSVs for 1000 cycles. Almost no change was observed from the polarization curves (Fig. S13).

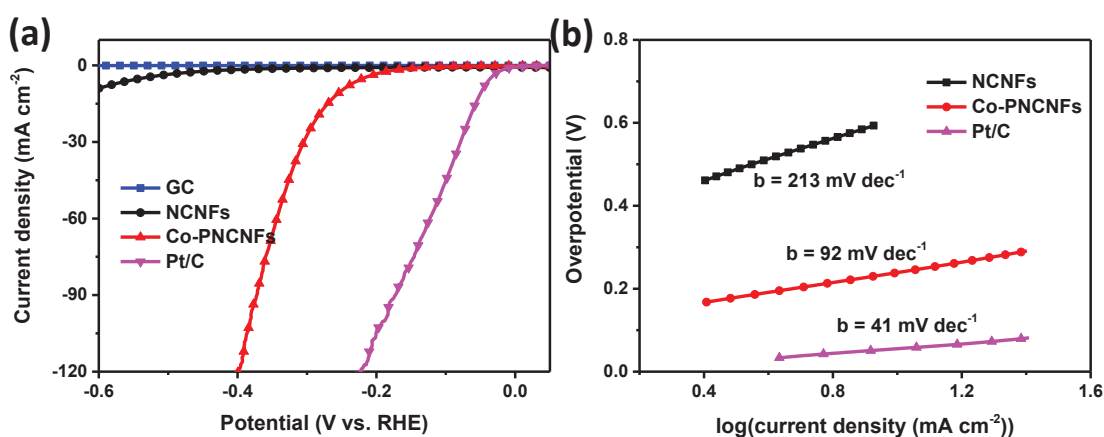


Figure 8-11 Electrochemical performance of the catalysts towards HER in 1 M KOH solution: (a) polarization curves for Co-PNCNFs, NCNFs, Pt/C and bare GC. (b) The corresponding Tafel plots.

The good catalytic activity and durability for both OER and HER suggest that the Co-PNCNFs composite is a highly efficient catalyst for the overall water splitting reaction in alkaline media. To test the feasibility, we fabricated the water splitting electrolyzer by applying Co-PNCNFs both as the anode and cathode in 1 M KOH solution, respectively (Figure 8-12(c)), the OER and HER performance of Co-PNCNFs deposited on Nickel foam are shown in Figure 8-12(a, b)). We observed water electrolysis with a current density of 10 mA cm^{-2} at 1.66 V at room temperature (Figure 8-12(d)). The durability of the electrolyzer was tested at 1.66 V in 1 M KOH solution. As shown in the inset of Figure 8-12(d), the cell exhibits excellent stability for the

overall water splitting. The high performance and long durability of the Co-PNCNFs catalyst in the alkaline electrolyzer provides a new strategy for developing non-precious efficient catalyst for the overall water splitting.

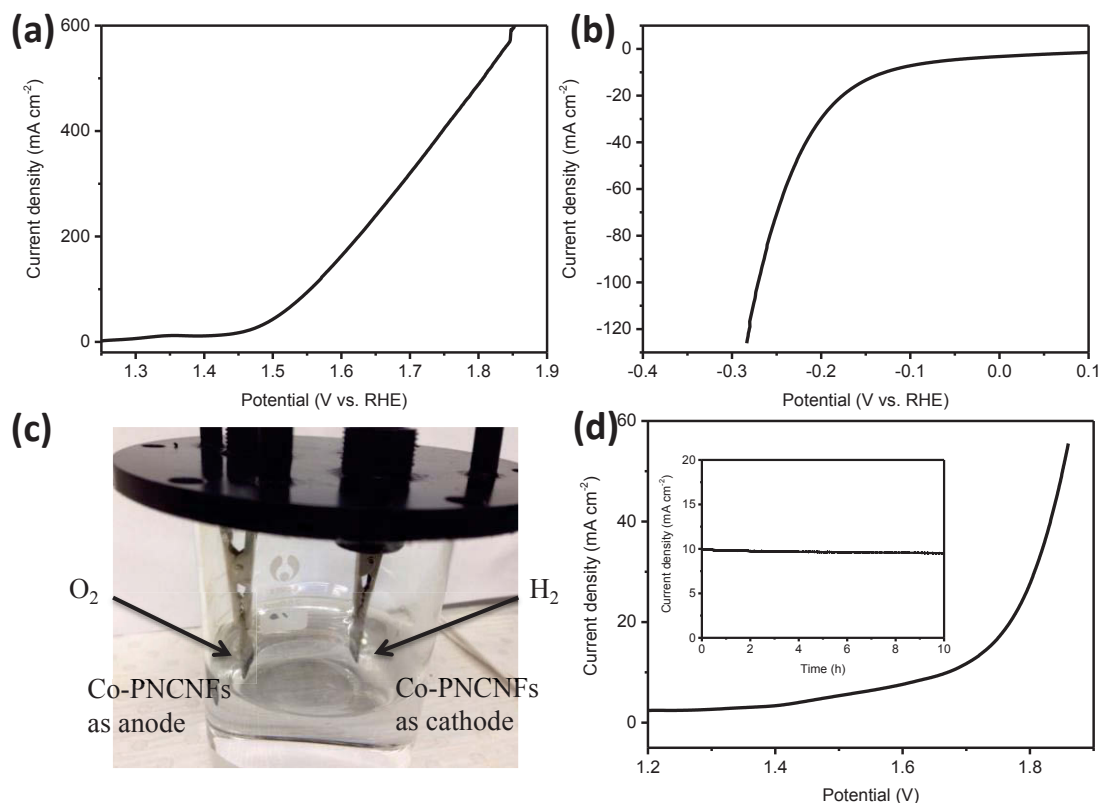


Figure 8-12 Electrochemical performance test of Co-PNCNFs deposited on nickel foam towards (a) OER and (b) HER in 1 M KOH solution. (c) Optical photograph of Co-PNCNFs based electrolyzer. (d) LSV of water electrolysis using Co-PNCNFs as both OER and HER catalysts. The inset shows the stability test at the potential of 1.66 V over 10 h.

8.4 Conclusions

In summary, the Co-PNCNFs composite with small cobalt nanoparticles embedded in N-doped porous carbon nanofibers was prepared by electrospinning and evaluated as a catalyst for OER and HER in alkaline solution. The excellent OER performance (high catalytic activity and good stability) was obtained, owing to the unique encapsulated and porous architecture. The nitrogen and cobalt bi-functionalization CNFs generates

active sites, which have a significant synergic effect on enhancing the catalytic activity. Moreover, the Co-PNCNFs composite also demonstrates a catalytic effect on the HER process in alkaline media. The excellent performance of the Co-PNCNFs composite towards both OER and HER makes it as an efficient catalyst for the overall water splitting. The alkaline electrolyzer achieves 10 mA cm^{-2} at a voltage of 1.66 V with a long durability. We believe that such transition metal embedded in low dimensional carbon matrix materials (e.g. Co-PNCNFs) can be practically applied as high-performance catalysts for overall water splitting.

Chapter 9 CONCLUSIONS

9.1 General Conclusion

This doctoral work explored a series of methods to design nanostructure catalysts for water splitting, including hydrothermal method; wet-chemical synthesis; chemical redox reaction; hard template method and electrospinning technique. We have designed MoS₂ based materials as the catalysts towards HER. We investigated transition metal oxides and transition metal carbides, especially cobalt-based oxides and iron carbide, as catalysts to reduce the OER energy barrier and to further accelerate the overall water splitting process. Finally, we developed carbon based material as a bifunctional catalyst to simultaneously generate H₂ and O₂ in alkaline solution. These nanostructured catalysts all exhibit excellent catalytic activity and stability towards water splitting.

9.1.1 MoS₂ nanosheets based material as a highly efficient catalyst for hydrogen evolution

We have prepared an active catalyst composed of MoS₂ nanosheets and 3D architectural GA (GA-MoS₂) by two-step hydrothermal method. The resultant material displays a well-organized structure with layer MoS₂ nanosheets uniformly distributed around the pores of GA, providing relatively large amounts of exposed edge sites for hydrogen evolution. The unique 3D architecture and large active surface areas lead to superior HER activity with low overpotential (100 mV) and high catalytic current density (95 mA cm⁻² at the overpotential of 200 mV). Moreover, GA-MoS₂ also exhibited good stability in acid solution, indicating the importance of the stable framework provided by 3D GA. The excellent electrochemical performance of GA-MoS₂ makes it a promising material for hydrogen evolution.

9.1.2 Cobalt oxide based material as a highly efficient catalyst for oxygen evolution

The unique sandwich-architecture graphene and Co_3O_4 (G- Co_3O_4) composite has been prepared. The unique sandwich-architecture leads to large amount loading of the active Co_3O_4 nanocrystals, resulting in ultrafine Co_3O_4 particles uniformly anchor onto both sides of graphene sheets. The graphene nanosheets acted as a binder to link neighboring Co_3O_4 particles together and also increased the conductivity of the composite. G- Co_3O_4 exhibited high catalytic activity towards OER both in alkaline solution (the current density of $j=10 \text{ mA cm}^{-2}$ at the overpotential of 313 mV) and neutral solution (a current density of $j=10 \text{ mA cm}^{-2}$ at the overpotential of 498 mV). The G- Co_3O_4 catalyst also exhibits good stability in the alkaline and neutral solutions, which is another important factor for energy conversion systems.

The composite, CoO nanoparticles are well wrapped by porous graphene (PGE-CoO), has been developed as catalyst for oxygen evolution. Graphene with highly porous structure was synthesized by a hard template method, and the 1D silica nanorods functionalized with surface methyl groups as the hard template. The results indicate that ultrafine CoO nanoparticles were uniformly dispersed and wrapped by porous graphene, which could efficiently avoid the corrosion during electrochemical test. The homogenous distribution of particles and porous structure of graphene enable the efficient utilization of catalysts. When tested as catalyst for OER, PGE-CoO showed low onset potential (504 mV vs. Ag/AgCl) and high current density (a current density of $j=10 \text{ mA cm}^{-2}$ at the overpotential of 348 mV). Besides the high catalytic activities, PGE-CoO electrocatalyst still remained a similar polarization curve to that in the initial cycle after long time cycles. PGE-CoO could be a promising electrocatalyst for oxygen evolution reaction.

The ultrathin CoMn_2O_4 nanosheets with abundant oxygen vacancies vertically aligned on cobalt/nitrogen co-functionalized CNFs ($\text{CoMn}_2\text{O}_4\text{-CoNC}$) has been prepared by a facile spontaneous redox reaction between CoNC and KMnO_4 solution. The well aligned architecture, coexistence of Mn and Co cations, abundant oxygen vacancies, and strong synergetic interaction are responsible for the outstanding electrochemical catalytic performance. When performed as an OER catalyst, $\text{CoMn}_2\text{O}_4\text{-CoNC}$ exhibited superior performance with high current density (an overpotential of only 307 mV to reach 10 mA cm^{-2}), low transfer resistance and long-time durability. This work paves the path for easy preparation of ternary structure catalysts to replace the benchmarking precious Ir/Ru OER catalysts.

9.1.3 Iron carbide based material as a highly efficient catalyst for oxygen evolution

Fe_3C encapsulated in nitrogen-enriched CNTs aligned on nitrogen doped CNFs ($\text{Fe}_3\text{C@NCNTs-NCNFs}$) had been prepared by the electrospinning technique. The as-prepared $\text{Fe}_3\text{C@NCNTs-NCNFs}$ composite displays uniquely aligned arrays and 3D hierarchical architecture, which exposes sufficient active sites and facilitates fast reaction kinetics towards OER. The encapsulated structure highly avoids the corrosion phenomenon during electrochemical test. When tested as a catalyst for water oxidation, it exhibits outstanding electrocatalytic activity, including a low onset potential (1.39 V vs. RHE), a high current density (10 mA cm^{-2} at the overpotential of 284 mV) and excellent stability, making $\text{Fe}_3\text{C@NCNTs-NCNFs}$ an efficient nonprecious metal catalyst for water oxidation.

9.1.4 Carbon based material as highly efficient bi-functional catalyst for water splitting

Cobalt nanoparticles embedded in porous nitrogen doped CNFs (Co-PNCNFs) has been prepared by electrospinning technique. The Co-PNCNFs composite displays a well-defined 3D networks associated with encapsulated and porous structure. The unique encapsulated structure could efficiently avoid the metal nanoparticles directly contact with the harsh environmental, protecting the metal nanoparticles from corrosion and aggregation during the catalytic process. The porous structure could provide more active sites for oxygen evolution and facilitate fast and versatile transport pathways for the electrolyte diffusion. The Co-PNCNFs composite demonstrates a catalytic effect on the HER and OER process in alkaline media. The excellent performance of the Co-PNCNFs composite towards both OER and HER makes it as an efficient catalyst for the overall water splitting. The alkaline electrolyzer achieves 10 mA cm^{-2} at a voltage of 1.66 V with a long durability. We believe that such transition metal embedded in low dimensional carbon matrix materials (e.g. Co-PNCNFs) can be practically applied as high-performance catalysts for overall water splitting.

9.2 Outlook

This thesis mainly concentrates on the synthesis of deliberately designed nanomaterials with novel architectures and their applications for water splitting. The preparation techniques presented in this thesis are also applicable to synthesize other nanostructure materials. Moreover, the characterization method (SEM, TEM, XRD, XPS, TGA, BET) and electrochemical measuring techniques, including linear sweep voltammograms (LSV), cyclic voltammetry (CV), electrochemical impedance spectra

(EIS) and stability test, reported in this thesis have large potentials to characterize and evaluate other nanomaterials for water splitting.

MoS₂ with vertically stacked S-Mo-S interlayer, is a typical two-dimensional material, which has garnered intensive interest as a potential catalyst for the electrochemical and photocatalytic hydrogen evolution. As we mentioned, the catalytic activity of MoS₂ towards HER are related to the density and reactivity of the active sites and the electrical transport. Therefore, by synthesizing single layer or double layer of MoS₂ can maximum expose the active sites for HER. Our strategy by combining MoS₂ and graphene aerogel efficiently enhanced the electron transportation, which can be applied for other carbon materials, such as carbon nanotube, mesoporous carbon sphere. Moreover, MoS₂ is an efficient catalyst for electrochemical hydrogen evolution, which means MoS₂ has the potential to act as co-catalyst for photocatalytic hydrogen evolution by combining with other semiconductors, such as TiO₂, Cu₂O, C₃N₄. We expect that MoS₂ could not only promote the separation of photoexcited electrons and holes but also offer more active sites for H₂ generation.

For the cobalt oxide (Co₃O₄, CoO), the experiment results have demonstrated that they show excellent catalytic performance towards OER when combined with graphene. This strategy can be applied to other transition metal oxides or even phosphides, sulfides, such as nickel oxide, cobalt phosphide, nickel phosphide. The unique sandwich-architected G-Co₃O₄ leads to large amount loading of the active Co₃O₄ nanocrystals and enhances electron transfer kinetics between the materials; the technique for its synthesis can be used to prepare other catalysts with unique sandwich-architecture by using surfactant. The porous graphene was prepared by using 1D silica nanorods as the template, which provides a good way to fabricate the porous structure carbon materials. The composite of G-CoO shows that ultrafine CoO nanoparticles were

uniformly dispersed and wrapped by porous graphene, which could efficiently avoid the corrosion during electrochemical test. This strategy paves a new way for designing catalysts with the encapsulated structure to avoid the corrosion phenomenon. Even though cobalt oxide and carbon composites have achieved high performance towards OER, the performance of pure cobalt oxide is not satisfied. Doping cobalt oxide with other elements, such as nitrogen, phosphorus could be a promising strategy for enhancing the conductivity of cobalt oxide, and thus improve the catalytic performance.

The electrospinning technique used in this thesis provides a way to produce nanofibers and nanowires on large-scale. The condition we used in our experiment could be applied to other materials, such as MoS₂-CNFs, WS₂-CNFs, CuO-CNFs. The electrospinning technique is undergoing renewed intense interest and current advances indicate a high potential of electrospun materials in energy related applications, including lithium/sodium ion batteries, supercapacitors, oxygen reduction reaction. Several challenges remain to be overcome before large scale usage of electrospun materials, and this is partly due to the fact that the process parameters affecting the electrospinning technique are still not fully understood. Thus, there are still limitations on the types of materials that can be synthesised by electrospinning. We need to explore the suitable process parameters for certain materials when we use the electrospinning technique.

Reference

1. Jacobson, M. Z. Review of solutions to global warming, air pollution, and energy security. *Energy & Environmental Science* 2009, 2, 148-173.
2. Han, S.; Wu, D.; Li, S.; Zhang, F.; Feng, X. Porous graphene materials for advanced electrochemical energy storage and conversion devices. *Advanced Materials* 2014, 26, 849-864.
3. Leslie, J. Dawn of the hydrogen age. *Wired October* 1997, 5.
4. Dunn, S. Hydrogen futures: toward a sustainable energy system. *International journal of hydrogen energy* 2002, 27, 235-264.
5. Rostrup-Nielsen, J. R. Fuels and energy for the future: the role of catalysis. *Catalysis reviews* 2004, 46, 247-270.
6. Turner, J. A. A realizable renewable energy future. *Science* 1999, 285, 687-689.
7. Cook, T. R.; Dogutan, D. K.; Reece, S. Y.; Surendranath, Y.; Teets, T. S.; Nocera, D. G. Solar energy supply and storage for the legacy and nonlegacy worlds. *Chemical reviews* 2010, 110, 6474-6502.
8. De Levie, R. The electrolysis of water. *Journal of Electroanalytical Chemistry* 1999, 476, 92-93.
9. Wang, J.; Zhong, H.-x.; Wang, Z.-l.; Meng, F.-l.; Zhang, X.-b. Integrated three-dimensional carbon paper/carbon tubes/cobalt-sulfide sheets as an efficient electrode for overall water splitting. *ACS nano* 2016, 10, 2342-2348.
10. Nai, J.; Yin, H.; You, T.; Zheng, L.; Zhang, J.; Wang, P.; Jin, Z.; Tian, Y.; Liu, J.; Tang, Z. Efficient electrocatalytic water oxidation by using amorphous Ni-Co double hydroxides nanocages. *Advanced Energy Materials* 2015, 5.
11. Pavel, C. C.; Cecconi, F.; Emiliani, C.; Santiccioli, S.; Scaffidi, A.; Catanorchi, S.; Comotti, M. Highly Efficient Platinum Group Metal Free Based Membrane-Electrode Assembly for Anion Exchange Membrane Water Electrolysis. *Angewandte Chemie* 2014, 126, 1402-1405.
12. Walter, M. G.; Warren, E. L.; McKone, J. R.; Boettcher, S. W.; Mi, Q.; Santori, E. A.; Lewis, N. S. Solar water splitting cells. *Chemical reviews* 2010, 110, 6446-6473.
13. Fletcher, S. Tafel slopes from first principles. *Journal of Solid State Electrochemistry* 2009, 13, 537-549.

14. Gao, M.-R.; Liang, J.-X.; Zheng, Y.-R.; Xu, Y.-F.; Jiang, J.; Gao, Q.; Li, J.; Yu, S.-H. An efficient molybdenum disulfide/cobalt diselenide hybrid catalyst for electrochemical hydrogen generation. *Nature communications* 2015, 6.
15. Bockris, J. M.; Potter, E. The mechanism of the cathodic hydrogen evolution reaction. *Journal of The Electrochemical Society* 1952, 99, 169-186.
16. Nørskov, J. K.; Bligaard, T.; Logadottir, A.; Kitchin, J.; Chen, J. G.; Pandelov, S.; Stimming, U. Trends in the exchange current for hydrogen evolution. *Journal of The Electrochemical Society* 2005, 152, J23-J26.
17. Hinnemann, B.; Moses, P. G.; Bonde, J.; Jørgensen, K. P.; Nielsen, J. H.; Horch, S.; Chorkendorff, I.; Nørskov, J. K. Biomimetic hydrogen evolution: MoS₂ nanoparticles as catalyst for hydrogen evolution. *Journal of the American Chemical Society* 2005, 127, 5308-5309.
18. Choi, W. I.; Wood, B. C.; Schwegler, E.; Ogitsu, T. Site-dependent free energy barrier for proton reduction on MoS₂ edges. *The Journal of Physical Chemistry C* 2013, 117, 21772-21777.
19. Trasatti, S. Work function, electronegativity, and electrochemical behaviour of metals: III. Electrolytic hydrogen evolution in acid solutions. *Journal of Electroanalytical Chemistry and Interfacial Electrochemistry* 1972, 39, 163-184.
20. Late, D. J.; Liu, B.; Matte, H. R.; Dravid, V. P.; Rao, C. Hysteresis in single-layer MoS₂ field effect transistors. *ACS nano* 2012, 6, 5635-5641.
21. Li, H.; Tsai, C.; Koh, A. L.; Cai, L.; Contryman, A. W.; Fragapane, A. H.; Zhao, J.; Han, H. S.; Manoharan, H. C.; Abild-Pedersen, F. Activating and optimizing MoS₂ basal planes for hydrogen evolution through the formation of strained sulphur vacancies. *Nature materials* 2016, 15, 48-53.
22. Yu, Y.; Huang, S.-Y.; Li, Y.; Steinmann, S. N.; Yang, W.; Cao, L. Layer-dependent electrocatalysis of MoS₂ for hydrogen evolution. *Nano letters* 2014, 14, 553-558.
23. Voiry, D.; Salehi, M.; Silva, R.; Fujita, T.; Chen, M.; Asefa, T.; Shenoy, V. B.; Eda, G.; Chhowalla, M. Conducting MoS₂ nanosheets as catalysts for hydrogen evolution reaction. *Nano letters* 2013, 13, 6222-6227.
24. Lukowski, M. A.; Daniel, A. S.; Meng, F.; Forticaux, A.; Li, L.; Jin, S. Enhanced hydrogen evolution catalysis from chemically exfoliated metallic

- MoS₂ nanosheets. *Journal of the American Chemical Society* 2013, 135, 10274-10277.
25. Xie, J.; Zhang, H.; Li, S.; Wang, R.; Sun, X.; Zhou, M.; Zhou, J.; Lou, X. W. D.; Xie, Y. Defect-rich MoS₂ ultrathin nanosheets with additional active edge sites for enhanced electrocatalytic hydrogen evolution. *Advanced materials* 2013, 25, 5807-5813.
 26. Li, Y.; Wang, H.; Xie, L.; Liang, Y.; Hong, G.; Dai, H. MoS₂ nanoparticles grown on graphene: an advanced catalyst for the hydrogen evolution reaction. *Journal of the American Chemical Society* 2011, 133, 7296-7299.
 27. Kong, D.; Wang, H.; Cha, J. J.; Pasta, M.; Koski, K. J.; Yao, J.; Cui, Y. Synthesis of MoS₂ and MoSe₂ films with vertically aligned layers. *Nano letters* 2013, 13, 1341-1347.
 28. Chen, Z.; Cummins, D.; Reinecke, B. N.; Clark, E.; Sunkara, M. K.; Jaramillo, T. F. Core-shell MoO₃-MoS₂ nanowires for hydrogen evolution: a functional design for electrocatalytic materials. *Nano letters* 2011, 11, 4168-4175.
 29. Zhang, N.; Gan, S.; Wu, T.; Ma, W.; Han, D.; Niu, L. Growth control of MoS₂ nanosheets on carbon cloth for maximum active edges exposed: an excellent hydrogen evolution 3D cathode. *ACS applied materials & interfaces* 2015, 7, 12193-12202.
 30. Shin, S.; Jin, Z.; Kwon, D. H.; Bose, R.; Min, Y.-S. High turnover frequency of hydrogen evolution reaction on amorphous MoS₂ thin film directly grown by atomic layer deposition. *Langmuir* 2015, 31, 1196-1202.
 31. Morales-Guio, C. G.; Hu, X. Amorphous molybdenum sulfides as hydrogen evolution catalysts. *Accounts of chemical research* 2014, 47, 2671-2681.
 32. Benck, J. D.; Hellstern, T. R.; Kibsgaard, J.; Chakthranont, P.; Jaramillo, T. F. Catalyzing the hydrogen evolution reaction (HER) with molybdenum sulfide nanomaterials. *ACS Catalysis* 2014, 4, 3957-3971.
 33. Yang, J.; Voiry, D.; Ahn, S. J.; Kang, D.; Kim, A. Y.; Chhowalla, M.; Shin, H. S. Two-Dimensional Hybrid Nanosheets of Tungsten Disulfide and Reduced Graphene Oxide as Catalysts for Enhanced Hydrogen Evolution. *Angewandte Chemie International Edition* 2013, 52, 13751-13754.
 34. Cheng, L.; Huang, W.; Gong, Q.; Liu, C.; Liu, Z.; Li, Y.; Dai, H. Ultrathin WS₂ nanoflakes as a high-performance electrocatalyst for the hydrogen

- evolution reaction. *Angewandte Chemie International Edition* 2014, 53, 7860-7863.
35. Choi, C. L.; Feng, J.; Li, Y.; Wu, J.; Zak, A.; Tenne, R.; Dai, H. WS₂ nanoflakes from nanotubes for electrocatalysis. *Nano Research* 2013, 6, 921-928.
 36. Wu, Z.; Fang, B.; Bonakdarpour, A.; Sun, A.; Wilkinson, D. P.; Wang, D. WS₂ nanosheets as a highly efficient electrocatalyst for hydrogen evolution reaction. *Applied Catalysis B: Environmental* 2012, 125, 59-66.
 37. Pu, Z.; Liu, Q.; Asiri, A. M.; Obaid, A. Y.; Sun, X. One-step electrodeposition fabrication of graphene film-confined WS₂ nanoparticles with enhanced electrochemical catalytic activity for hydrogen evolution. *Electrochimica Acta* 2014, 134, 8-12.
 38. Voiry, D.; Yamaguchi, H.; Li, J.; Silva, R.; Alves, D. C.; Fujita, T.; Chen, M.; Asefa, T.; Shenoy, V. B.; Eda, G. Enhanced catalytic activity in strained chemically exfoliated WS₂ nanosheets for hydrogen evolution. *Nature materials* 2013, 12, 850-855.
 39. Faber, M. S.; Lukowski, M. A.; Ding, Q.; Kaiser, N. S.; Jin, S. Earth-abundant metal pyrites (FeS₂, CoS₂, NiS₂, and their alloys) for highly efficient hydrogen evolution and polysulfide reduction electrocatalysis. *The Journal of Physical Chemistry C* 2014, 118, 21347-21356.
 40. Sun, R.; Chan, M.; Ceder, G. First-principles electronic structure and relative stability of pyrite and marcasite: Implications for photovoltaic performance. *Physical Review B* 2011, 83, 235311.
 41. Kong, D.; Cha, J. J.; Wang, H.; Lee, H. R.; Cui, Y. First-row transition metal dichalcogenide catalysts for hydrogen evolution reaction. *Energy & Environmental Science* 2013, 6, 3553-3558.
 42. Levy, R.; Boudart, M. Platinum-like behavior of tungsten carbide in surface catalysis. *science* 1973, 181, 547-549.
 43. Liao, L.; Wang, S.; Xiao, J.; Bian, X.; Zhang, Y.; Scanlon, M. D.; Hu, X.; Tang, Y.; Liu, B.; Girault, H. H. A nanoporous molybdenum carbide nanowire as an electrocatalyst for hydrogen evolution reaction. *Energy & Environmental Science* 2014, 7, 387-392.

44. Xiao, P.; Yan, Y.; Ge, X.; Liu, Z.; Wang, J.-Y.; Wang, X. Investigation of molybdenum carbide nano-rod as an efficient and durable electrocatalyst for hydrogen evolution in acidic and alkaline media. *Applied Catalysis B: Environmental* 2014, 154, 232-237.
45. Chen, W.-F.; Wang, C.-H.; Sasaki, K.; Marinkovic, N.; Xu, W.; Muckerman, J.; Zhu, Y.; Adzic, R. Highly active and durable nanostructured molybdenum carbide electrocatalysts for hydrogen production. *Energy & Environmental Science* 2013, 6, 943-951.
46. Hunt, S. T.; Nimmanwudipong, T.; Román-Leshkov, Y. Engineering Non-sintered, Metal-Terminated Tungsten Carbide Nanoparticles for Catalysis. *Angewandte Chemie International Edition* 2014, 53, 5131-5136.
47. Nikiforov, A.; Petrushina, I.; Christensen, E.; Alexeev, N.; Samokhin, A.; Bjerrum, N. WC as a non-platinum hydrogen evolution electrocatalyst for high temperature PEM water electrolyzers. *international journal of hydrogen energy* 2012, 37, 18591-18597.
48. Zhang, J.; Meng, X.; Zhao, J.; Zhu, Z. Construction of a $\text{Mo}_x\text{C}/\text{Ni}$ Network Electrode with Low Overpotential for Hydrogen Generation. *ChemCatChem* 2014, 6, 2059-2064.
49. Ge, C.; Jiang, P.; Cui, W.; Pu, Z.; Xing, Z.; Asiri, A. M.; Obaid, A. Y.; Sun, X.; Tian, J. Shape-controllable synthesis of Mo_2C nanostructures as hydrogen evolution reaction electrocatalysts with high activity. *Electrochimica Acta* 2014, 134, 182-186.
50. Vrubel, H.; Hu, X. Molybdenum boride and carbide catalyze hydrogen evolution in both acidic and basic solutions. *Angewandte Chemie* 2012, 124, 12875-12878.
51. Liu, Y.; Yu, G.; Li, G. D.; Sun, Y.; Asefa, T.; Chen, W.; Zou, X. Coupling Mo_2C with Nitrogen-Rich Nanocarbon Leads to Efficient Hydrogen-Evolution Electrocatalytic Sites. *Angewandte Chemie International Edition* 2015, 54, 10752-10757.
52. Wu, Z.; Yang, Y.; Gu, D.; Li, Q.; Feng, D.; Chen, Z.; Tu, B.; Webley, P. A.; Zhao, D. Silica-Templated Synthesis of Ordered Mesoporous Tungsten Carbide/Graphitic Carbon Composites with Nanocrystalline Walls and High Surface Areas via a Temperature-Programmed Carburization Route. *Small* 2009, 5, 2738-2749.

53. Giordano, C.; Erpen, C.; Yao, W.; Antonietti, M. Synthesis of Mo and W carbide and nitride nanoparticles via a simple “urea glass” route. *Nano letters* 2008, 8, 4659-4663.
54. Wang, G.; Campbell, S.; Calka, A.; Kaczmarek, W. Synthesis and structural evolution of tungsten carbide prepared by ball milling. *Journal of Materials Science* 1997, 32, 1461-1467.
55. Lu, J. L.; Li, Z. H.; Jiang, S. P.; Shen, P. K.; Li, L. Nanostructured tungsten carbide/carbon composites synthesized by a microwave heating method as supports of platinum catalysts for methanol oxidation. *Journal of Power Sources* 2012, 202, 56-62.
56. Cha, S. I.; Hong, S. H.; Ha, G. H.; Kim, B. K. Mechanical properties of WC–10Co cemented carbides sintered from nanocrystalline spray conversion processed powders. *International Journal of Refractory Metals and Hard Materials* 2001, 19, 397-403.
57. Essaki, K.; Rees, E.; Burstein, G. Influence of precursor preparation on the synthesis of WC under microwave irradiation. *Materials Letters* 2009, 63, 2185-2187.
58. Fan, X.; Zhou, H.; Guo, X. WC nanocrystals grown on vertically aligned carbon nanotubes: an efficient and stable electrocatalyst for hydrogen evolution reaction. *ACS nano* 2015, 9, 5125-5134.
59. Dong, S.; Chen, X.; Zhang, X.; Cui, G. Nanostructured transition metal nitrides for energy storage and fuel cells. *Coordination Chemistry Reviews* 2013, 257, 1946-1956.
60. Hargreaves, J. Heterogeneous catalysis with metal nitrides. *Coordination Chemistry Reviews* 2013, 257, 2015-2031.
61. Ham, D. J.; Lee, J. S. Transition metal carbides and nitrides as electrode materials for low temperature fuel cells. *Energies* 2009, 2, 873-899.
62. Chen, W. F.; Sasaki, K.; Ma, C.; Frenkel, A. I.; Marinkovic, N.; Muckerman, J. T.; Zhu, Y.; Adzic, R. R. Hydrogen-Evolution Catalysts Based on Non-Noble Metal Nickel–Molybdenum Nitride Nanosheets. *Angewandte Chemie International Edition* 2012, 51, 6131-6135.

63. Xie, J.; Li, S.; Zhang, X.; Zhang, J.; Wang, R.; Zhang, H.; Pan, B.; Xie, Y. Atomically-thin molybdenum nitride nanosheets with exposed active surface sites for efficient hydrogen evolution. *Chemical Science* 2014, 5, 4615-4620.
64. Youn, D. H.; Han, S.; Kim, J. Y.; Kim, J. Y.; Park, H.; Choi, S. H.; Lee, J. S. Highly active and stable hydrogen evolution electrocatalysts based on molybdenum compounds on carbon nanotube–graphene hybrid support. *ACS nano* 2014, 8, 5164-5173.
65. Chen, W.-F.; Muckerman, J. T.; Fujita, E. Recent developments in transition metal carbides and nitrides as hydrogen evolution electrocatalysts. *Chemical Communications* 2013, 49, 8896-8909.
66. Zhang, Y.; Ouyang, B.; Xu, J.; Chen, S.; Rawat, R. S.; Fan, H. J. 3D Porous Hierarchical Nickel–Molybdenum Nitrides Synthesized by RF Plasma as Highly Active and Stable Hydrogen-Evolution-Reaction Electrocatalysts. *Advanced Energy Materials* 2016, 6.
67. Liu, P.; Rodriguez, J. A. Catalysts for hydrogen evolution from the [NiFe] hydrogenase to the Ni₂P (001) surface: the importance of ensemble effect. *Journal of the American Chemical Society* 2005, 127, 14871-14878.
68. Xiao, P.; Sk, M. A.; Thia, L.; Ge, X.; Lim, R. J.; Wang, J.-Y.; Lim, K. H.; Wang, X. Molybdenum phosphide as an efficient electrocatalyst for the hydrogen evolution reaction. *Energy & Environmental Science* 2014, 7, 2624-2629.
69. Zhang, G.; Wang, G.; Liu, Y.; Liu, H.; Qu, J.; Li, J. Highly Active and Stable Catalysts of Phytic Acid-Derivative Transition Metal Phosphides for Full Water Splitting. *J. Am. Chem. Soc* 2016, 138, 14686-14693.
70. Xing, Z.; Liu, Q.; Asiri, A. M.; Sun, X. Closely interconnected network of molybdenum phosphide nanoparticles: a highly efficient electrocatalyst for generating hydrogen from water. *Advanced Materials* 2014, 26, 5702-5707.
71. Read, C. G.; Callejas, J. F.; Holder, C. F.; Schaak, R. E. General strategy for the synthesis of transition metal phosphide films for electrocatalytic hydrogen and oxygen evolution. *ACS applied materials & interfaces* 2016, 8, 12798-12803.
72. Oyama, S. T.; Gott, T.; Zhao, H.; Lee, Y.-K. Transition metal phosphide hydroprocessing catalysts: a review. *Catalysis Today* 2009, 143, 94-107.

73. Xu, Y.; Wu, R.; Zhang, J.; Shi, Y.; Zhang, B. Anion-exchange synthesis of nanoporous FeP nanosheets as electrocatalysts for hydrogen evolution reaction. *Chemical Communications* 2013, 49, 6656-6658.
74. Kibsgaard, J.; Jaramillo, T. F. Molybdenum Phosphosulfide: An Active, Acid-Stable, Earth-Abundant Catalyst for the Hydrogen Evolution Reaction. *Angewandte Chemie International Edition* 2014, 53, 14433-14437.
75. Saadi, F. H.; Carim, A. I.; Verlage, E.; Hemminger, J. C.; Lewis, N. S.; Soriaga, M. P. CoP as an acid-stable active electrocatalyst for the hydrogen-evolution reaction: Electrochemical synthesis, interfacial characterization and performance evaluation. *The Journal of Physical Chemistry C* 2014, 118, 29294-29300.
76. Wang, X.; Kolen'ko, Y. V.; Liu, L. Direct solvothermal phosphorization of nickel foam to fabricate integrated Ni₂P-nanorods/Ni electrodes for efficient electrocatalytic hydrogen evolution. *Chemical Communications* 2015, 51, 6738-6741.
77. Han, S.; Feng, Y.; Zhang, F.; Yang, C.; Yao, Z.; Zhao, W.; Qiu, F.; Yang, L.; Yao, Y.; Zhuang, X. Metal-Phosphide-Containing Porous Carbons Derived from an Ionic-Polymer Framework and Applied as Highly Efficient Electrochemical Catalysts for Water Splitting. *Advanced Functional Materials* 2015, 25, 3899-3906.
78. Popczun, E. J.; McKone, J. R.; Read, C. G.; Biacchi, A. J.; Wiltout, A. M.; Lewis, N. S.; Schaak, R. E. Nanostructured nickel phosphide as an electrocatalyst for the hydrogen evolution reaction. *Journal of the American Chemical Society* 2013, 135, 9267-9270.
79. Deng, J.; Ren, P.; Deng, D.; Bao, X. Enhanced electron penetration through an ultrathin graphene layer for highly efficient catalysis of the hydrogen evolution reaction. *Angewandte Chemie International Edition* 2015, 54, 2100-2104.
80. Kibsgaard, J.; Tsai, C.; Chan, K.; Benck, J. D.; Nørskov, J. K.; Abild-Pedersen, F.; Jaramillo, T. F. Designing an improved transition metal phosphide catalyst for hydrogen evolution using experimental and theoretical trends. *Energy & Environmental Science* 2015, 8, 3022-3029.
81. Tan, Y.; Wang, H.; Liu, P.; Shen, Y.; Cheng, C.; Hirata, A.; Fujita, T.; Tang, Z.; Chen, M. Versatile nanoporous bimetallic phosphides towards electrochemical water splitting. *Energy & Environmental Science* 2016, 9, 2257-2261.

82. Li, Y.; Zhang, H.; Jiang, M.; Kuang, Y.; Sun, X.; Duan, X. Ternary NiCoP nanosheet arrays: An excellent bifunctional catalyst for alkaline overall water splitting. *Nano Research* 2016, 9, 2251-2259.
83. Wang, X.-D.; Xu, Y.-F.; Rao, H.-S.; Xu, W.-J.; Chen, H.-Y.; Zhang, W.-X.; Kuang, D.-B.; Su, C.-Y. Novel porous molybdenum tungsten phosphide hybrid nanosheets on carbon cloth for efficient hydrogen evolution. *Energy & Environmental Science* 2016, 9, 1468-1475.
84. Sathe, B. R.; Zou, X.; Asefa, T. Metal-free B-doped graphene with efficient electrocatalytic activity for hydrogen evolution reaction. *Catalysis Science & Technology* 2014, 4, 2023-2030.
85. Zheng, Y.; Jiao, Y.; Li, L. H.; Xing, T.; Chen, Y.; Jaroniec, M.; Qiao, S. Z. Toward design of synergistically active carbon-based catalysts for electrocatalytic hydrogen evolution. *ACS nano* 2014, 8, 5290-5296.
86. Zheng, Y.; Jiao, Y.; Zhu, Y.; Li, L. H.; Han, Y.; Chen, Y.; Du, A.; Jaroniec, M.; Qiao, S. Z. Hydrogen evolution by a metal-free electrocatalyst. *Nature communications* 2014, 5.
87. Zou, X.; Huang, X.; Goswami, A.; Silva, R.; Sathe, B. R.; Mikmeková, E.; Asefa, T. Cobalt-Embedded Nitrogen-Rich Carbon Nanotubes Efficiently Catalyze Hydrogen Evolution Reaction at All pH Values. *Angewandte Chemie* 2014, 126, 4461-4465.
88. Gao, S.; Li, G.-D.; Liu, Y.; Chen, H.; Feng, L.-L.; Wang, Y.; Yang, M.; Wang, D.; Wang, S.; Zou, X. Electrocatalytic H₂ production from seawater over Co, N-codoped nanocarbons. *Nanoscale* 2015, 7, 2306-2316.
89. Deng, J.; Ren, P.; Deng, D.; Yu, L.; Yang, F.; Bao, X. Highly active and durable non-precious-metal catalysts encapsulated in carbon nanotubes for hydrogen evolution reaction. *Energy & Environmental Science* 2014, 7, 1919-1923.
90. Cui, W.; Liu, Q.; Cheng, N.; Asiri, A. M.; Sun, X. Activated carbon nanotubes: a highly-active metal-free electrocatalyst for hydrogen evolution reaction. *Chemical Communications* 2014, 50, 9340-9342.
91. Zhang, J.; Qu, L.; Shi, G.; Liu, J.; Chen, J.; Dai, L. N, P-Codoped Carbon Networks as Efficient Metal-free Bifunctional Catalysts for Oxygen Reduction and Hydrogen Evolution Reactions. *Angewandte Chemie* 2016, 128, 2270-2274.

92. Hou, Y.; Wen, Z.; Cui, S.; Ci, S.; Mao, S.; Chen, J. An Advanced Nitrogen-Doped Graphene/Cobalt-Embedded Porous Carbon Polyhedron Hybrid for Efficient Catalysis of Oxygen Reduction and Water Splitting. *Advanced Functional Materials* 2015, 25, 872-882.
93. Birss, V. I.; Damjanovic, A.; Hudson, P. Oxygen Evolution at Platinum Electrodes in Alkaline Solutions II. Mechanism of the Reaction. *Journal of The Electrochemical Society* 1986, 133, 1621-1625.
94. Dau, H.; Limberg, C.; Reier, T.; Risch, M.; Roggan, S.; Strasser, P. The mechanism of water oxidation: from electrolysis via homogeneous to biological catalysis. *ChemCatChem* 2010, 2, 724-761.
95. Kötz, R.; Stucki, S. Oxygen Evolution and Corrosion on Ruthenium-Iridium Alloys. *Journal of The Electrochemical Society* 1985, 132, 103-107.
96. Matsumoto, Y.; Yamada, S.; Nishida, T.; Sato, E. Oxygen Evolution on $\text{La}_{1-x}\text{Sr}_x\text{Fe}_{1-y}\text{Co}_y\text{O}_3$ Series Oxides. *Journal of The Electrochemical Society* 1980, 127, 2360-2364.
97. Dou, Y.; Liao, T.; Ma, Z.; Tian, D.; Liu, Q.; Xiao, F.; Sun, Z.; Kim, J. H.; Dou, S. X. Graphene-like holey Co_3O_4 nanosheets as a highly efficient catalyst for oxygen evolution reaction. *Nano Energy* 2016, 30, 267-275.
98. Zhuang, Z.; Sheng, W.; Yan, Y. Synthesis of Monodisperse $\text{Au}@ \text{Co}_3\text{O}_4$ Core-Shell Nanocrystals and Their Enhanced Catalytic Activity for Oxygen Evolution Reaction. *Advanced Materials* 2014, 26, 3950-3955.
99. Huang, J.; Chen, J.; Yao, T.; He, J.; Jiang, S.; Sun, Z.; Liu, Q.; Cheng, W.; Hu, F.; Jiang, Y. CoOOH nanosheets with high mass activity for water oxidation. *Angewandte Chemie* 2015, 127, 8846-8851.
100. Strickland, K.; Miner, E.; Jia, Q.; Tylus, U.; Ramaswamy, N.; Liang, W.; Sougrati, M.-T.; Jaouen, F.; Mukerjee, S. Highly active oxygen reduction non-platinum group metal electrocatalyst without direct metal-nitrogen coordination. *Nature communications* 2015, 6.
101. Wang, Y.; Zhou, T.; Jiang, K.; Da, P.; Peng, Z.; Tang, J.; Kong, B.; Cai, W. B.; Yang, Z.; Zheng, G. Reduced mesoporous Co_3O_4 nanowires as efficient water oxidation electrocatalysts and supercapacitor electrodes. *Advanced Energy Materials* 2014, 4.

102. Liu, Z. Q.; Cheng, H.; Li, N.; Ma, T. Y.; Su, Y. Z. ZnCo₂O₄ Quantum Dots Anchored on Nitrogen-Doped Carbon Nanotubes as Reversible Oxygen Reduction/Evolution Electrocatalysts. *Advanced Materials* 2016, 28, 3777-3784.
103. Maiyalagan, T.; Jarvis, K. A.; Therese, S.; Ferreira, P. J.; Manthiram, A. Spinel-type lithium cobalt oxide as a bifunctional electrocatalyst for the oxygen evolution and oxygen reduction reactions. *Nature communications* 2014, 5.
104. Tichenor, R. L. Nickel Oxides-Relation Between Electrochemical and Foreign Ion Content. *Industrial & Engineering Chemistry* 1952, 44, 973-977.
105. Troilius, G.; Alfelt, G. In *The migration of iron in alkaline nickel-cadmium cells with pocket electrodes*, Proceedings of the Fifth International Symposium on Power Sources, 1967; pp 337-348.
106. Munshi, M.; Tseung, A.; Parker, J. The dissolution of iron from the negative material in pocket plate nickel-cadmium batteries. *Journal of applied electrochemistry* 1985, 15, 711-717.
107. Corrigan, D. A. The catalysis of the oxygen evolution reaction by iron impurities in thin film nickel oxide electrodes. *Journal of the Electrochemical Society* 1987, 134, 377-384.
108. Kleinke, M.; Knobel, M.; Bonugli, L.; Teschke, O. Amorphous alloys as anodic and cathodic materials for alkaline water electrolysis. *International journal of hydrogen energy* 1997, 22, 759-762.
109. Potvin, E.; Brossard, L. Electrocatalytic activity of Ni-Fe anodes for alkaline water electrolysis. *Materials chemistry and physics* 1992, 31, 311-318.
110. Grande, W. C.; Talbot, J. B. Electrodeposition of Thin Films of Nickel-Iron II. Modeling. *Journal of the Electrochemical Society* 1993, 140, 675-681.
111. Ullal, Y.; Hegde, A. C. Electrodeposition and electro-catalytic study of nanocrystalline Ni-Fe alloy. *International Journal of Hydrogen Energy* 2014, 39, 10485-10492.
112. Kumar, M.; Awasthi, R.; Sinha, A.; Singh, R. New ternary Fe, Co, and Mo mixed oxide electrocatalysts for oxygen evolution. *international journal of hydrogen energy* 2011, 36, 8831-8838.
113. Cheng, Y.; Liu, C.; Cheng, H.-M.; Jiang, S. P. One-Pot Synthesis of Metal-Carbon Nanotubes Network Hybrids as Highly Efficient Catalysts for Oxygen

- Evolution Reaction of Water Splitting. *ACS applied materials & interfaces* 2014, 6, 10089-10098.
114. Trotochaud, L.; Ranney, J. K.; Williams, K. N.; Boettcher, S. W. Solution-cast metal oxide thin film electrocatalysts for oxygen evolution. *Journal of the American Chemical Society* 2012, 134, 17253-17261.
 115. Refait, P.; Abdelmoula, M.; Simon, L.; Génin, J.-M. R. Mechanisms of formation and transformation of Ni-Fe layered double hydroxides in and containing aqueous solutions. *Journal of Physics and Chemistry of Solids* 2005, 66, 911-917.
 116. Gong, M.; Li, Y.; Wang, H.; Liang, Y.; Wu, J. Z.; Zhou, J.; Wang, J.; Regier, T.; Wei, F.; Dai, H. An advanced Ni-Fe layered double hydroxide electrocatalyst for water oxidation. *J. Am. Chem. Soc* 2013, 135, 8452-8455.
 117. Tang, D.; Liu, J.; Wu, X.; Liu, R.; Han, X.; Han, Y.; Huang, H.; Liu, Y.; Kang, Z. Carbon quantum dot/NiFe layered double-hydroxide composite as a highly efficient electrocatalyst for water oxidation. *ACS applied materials & interfaces* 2014, 6, 7918-7925.
 118. Tang, C.; Wang, H. S.; Wang, H. F.; Zhang, Q.; Tian, G. L.; Nie, J. Q.; Wei, F. Spatially Confined Hybridization of Nanometer-Sized NiFe Hydroxides into Nitrogen-Doped Graphene Frameworks Leading to Superior Oxygen Evolution Reactivity. *Advanced Materials* 2015, 27, 4516-4522.
 119. Gorlin, Y.; Jaramillo, T. F. A bifunctional nonprecious metal catalyst for oxygen reduction and water oxidation. *Journal of the American Chemical Society* 2010, 132, 13612-13614.
 120. Su, H.-Y.; Gorlin, Y.; Man, I. C.; Calle-Vallejo, F.; Nørskov, J. K.; Jaramillo, T. F.; Rossmeisl, J. Identifying active surface phases for metal oxide electrocatalysts: a study of manganese oxide bi-functional catalysts for oxygen reduction and water oxidation catalysis. *Physical Chemistry Chemical Physics* 2012, 14, 14010-14022.
 121. Harriman, A.; Pickering, I. J.; Thomas, J. M.; Christensen, P. A. Metal oxides as heterogeneous catalysts for oxygen evolution under photochemical conditions. *Journal of the Chemical Society, Faraday Transactions 1: Physical Chemistry in Condensed Phases* 1988, 84, 2795-2806.

122. Song, F.; Hu, X. Ultrathin cobalt–manganese layered double hydroxide is an efficient oxygen evolution catalyst. *Journal of the American Chemical Society* 2014, 136, 16481-16484.
123. Wei, C.; Yu, L.; Cui, C.; Lin, J.; Wei, C.; Mathews, N.; Huo, F.; Sritharan, T.; Xu, Z. Ultrathin MnO₂ nanoflakes as efficient catalysts for oxygen reduction reaction. *Chemical Communications* 2014, 50, 7885-7888.
124. Meng, Y.; Song, W.; Huang, H.; Ren, Z.; Chen, S.-Y.; Suib, S. L. Structure–property relationship of bifunctional MnO₂ nanostructures: highly efficient, ultra-stable electrochemical water oxidation and oxygen reduction reaction catalysts identified in alkaline media. *Journal of the American Chemical Society* 2014, 136, 11452-11464.
125. Cheng, F.; Shen, J.; Peng, B.; Pan, Y.; Tao, Z.; Chen, J. Rapid room-temperature synthesis of nanocrystalline spinels as oxygen reduction and evolution electrocatalysts. *Nature chemistry* 2011, 3, 79-84.
126. Jiao, F.; Frei, H. Nanostructured cobalt and manganese oxide clusters as efficient water oxidation catalysts. *Energy & Environmental Science* 2010, 3, 1018-1027.
127. Takashima, T.; Hashimoto, K.; Nakamura, R. Inhibition of charge disproportionation of MnO₂ electrocatalysts for efficient water oxidation under neutral conditions. *Journal of the American Chemical Society* 2012, 134, 18153-18156.
128. Ge, X.; Liu, Y.; Goh, F. T.; Hor, T. A.; Zong, Y.; Xiao, P.; Zhang, Z.; Lim, S. H.; Li, B.; Wang, X. Dual-phase spinel MnCo₂O₄ and spinel MnCo₂O₄/nanocarbon hybrids for electrocatalytic oxygen reduction and evolution. *ACS applied materials & interfaces* 2014, 6, 12684-12691.
129. Ramírez, A.; Hillebrand, P.; Stellmach, D.; May, M. M.; Bogdanoff, P.; Fiechter, S. Evaluation of MnO_x, Mn₂O₃, and Mn₃O₄ Electrodeposited Films for the Oxygen Evolution Reaction of Water. *The Journal of Physical Chemistry C* 2014, 118, 14073-14081.
130. Chen, C.-F.; King, G.; Dickerson, R. M.; Papin, P. A.; Gupta, S.; Kellogg, W. R.; Wu, G. Oxygen-deficient BaTiO_{3-x} perovskite as an efficient bifunctional oxygen electrocatalyst. *Nano Energy* 2015, 13, 423-432.
131. Grimaud, A.; May, K. J.; Carlton, C. E.; Lee, Y.-L.; Risch, M.; Hong, W. T.; Zhou, J.; Shao-Horn, Y. Double perovskites as a family of highly active

- catalysts for oxygen evolution in alkaline solution. *Nature communications* 2013, 4.
132. Zhou, W.; Sunarso, J. Enhancing Bi-functional Electrocatalytic Activity of Perovskite by Temperature Shock: A Case Study of $\text{LaNiO}_{3-\delta}$. *The journal of physical chemistry letters* 2013, 4, 2982-2988.
 133. Zhu, Y.; Su, C.; Xu, X.; Zhou, W.; Ran, R.; Shao, Z. A universal and facile way for the development of superior bifunctional electrocatalysts for oxygen reduction and evolution reactions utilizing the synergistic effect. *Chemistry–A European Journal* 2014, 20, 15533-15542.
 134. Liu, R.; Liang, F.; Zhou, W.; Yang, Y.; Zhu, Z. Calcium-doped lanthanum nickelate layered perovskite and nickel oxide nano-hybrid for highly efficient water oxidation. *Nano Energy* 2015, 12, 115-122.
 135. Zhu, Y.; Zhou, W.; Chen, Y.; Yu, J.; Xu, X.; Su, C.; Tadé, M. O.; Shao, Z. Boosting oxygen reduction reaction activity of palladium by stabilizing its unusual oxidation states in perovskite. *Chemistry of Materials* 2015, 27, 3048-3054.
 136. Suntivich, J.; Gasteiger, H. A.; Yabuuchi, N.; Nakanishi, H.; Goodenough, J. B.; Shao-Horn, Y. Design principles for oxygen-reduction activity on perovskite oxide catalysts for fuel cells and metal–air batteries. *Nature chemistry* 2011, 3, 546-550.
 137. Hong, W. T.; Risch, M.; Stoerzinger, K. A.; Grimaud, A.; Suntivich, J.; Shao-Horn, Y. Toward the rational design of non-precious transition metal oxides for oxygen electrocatalysis. *Energy & Environmental Science* 2015, 8, 1404-1427.
 138. Malkhandi, S.; Yang, B.; Manohar, A.; Manivannan, A.; Prakash, G. S.; Narayanan, S. Electrocatalytic properties of nanocrystalline calcium-doped lanthanum cobalt oxide for bifunctional oxygen electrodes. *The journal of physical chemistry letters* 2012, 3, 967-972.
 139. Sunarso, J.; Torriero, A. A.; Zhou, W.; Howlett, P. C.; Forsyth, M. Oxygen reduction reaction activity of La-based perovskite oxides in alkaline medium: a thin-film rotating ring-disk electrode study. *The Journal of Physical Chemistry C* 2012, 116, 5827-5834.
 140. Haider, M. A.; Capizzi, A. J.; Murayama, M.; McIntosh, S. Reverse micelle synthesis of perovskite oxide nanoparticles. *Solid State Ionics* 2011, 196, 65-72.

141. Yuasa, M.; Sakai, G.; Shimanoe, K.; Teraoka, Y.; Yamazoe, N. Exploration of reverse micelle synthesis of carbon-supported LaMnO_3 . *Journal of The Electrochemical Society* 2004, 151, A1477-A1482.
142. Yuasa, M.; Shimanoe, K.; Teraoka, Y.; Yamazoe, N. High-performance oxygen reduction catalyst using carbon-supported La-Mn-based perovskite-type oxide. *Electrochemical and Solid-State Letters* 2011, 14, A67-A69.
143. Ovenstone, J.; Chan, K.; Ponton, C. Hydrothermal processing and characterisation of doped lanthanum chromite for use in SOFCs. *Journal of materials science* 2002, 37, 3315-3322.
144. Shao, Z.; Zhou, W.; Zhu, Z. Advanced synthesis of materials for intermediate-temperature solid oxide fuel cells. *Progress in Materials Science* 2012, 57, 804-874.
145. Mueller, D. N.; Machala, M. L.; Bluhm, H.; Chueh, W. C. Redox activity of surface oxygen anions in oxygen-deficient perovskite oxides during electrochemical reactions. *Nature communications* 2015, 6.
146. Suntivich, J.; May, K. J.; Gasteiger, H. A.; Goodenough, J. B.; Shao-Horn, Y. A perovskite oxide optimized for oxygen evolution catalysis from molecular orbital principles. *Science* 2011, 334, 1383-1385.
147. Guldi, D. M.; Rahman, G. A.; Sgobba, V.; Ehli, C. Multifunctional molecular carbon materials-from fullerenes to carbon nanotubes. *Chemical Society Reviews* 2006, 35, 471-487.
148. Bottari, G.; de la Torre, G.; Guldi, D. M.; Torres, T. Covalent and noncovalent phthalocyanine-carbon nanostructure systems: synthesis, photoinduced electron transfer, and application to molecular photovoltaics. *Chemical reviews* 2010, 110, 6768-6816.
149. Wasielewski, M. R. Photoinduced electron transfer in supramolecular systems for artificial photosynthesis. *Chemical Reviews* 1992, 92, 435-461.
150. Ostwald, W. 7, 995-1066 (1901). *Nature* 1902, 65, 522-526.
151. Lin, Y.; Finke, R. G. A More General Approach to Distinguishing "Homogeneous" from "Heterogeneous" Catalysis: Discovery of Polyoxoanion- and Bu_4N^+ -Stabilized, Isolable and Redissolvable, High-Reactivity Ir. approx. 190-450 Nanocluster Catalysts. *Inorganic Chemistry* 1994, 33, 4891-4910.

152. Widegren, J. A.; Finke, R. G. A review of the problem of distinguishing true homogeneous catalysis from soluble or other metal-particle heterogeneous catalysis under reducing conditions. *Journal of Molecular Catalysis A: Chemical* 2003, 198, 317-341.
153. Sala, X.; Romero, I.; Rodríguez, M.; Escriche, L.; Llobet, A. Molecular catalysts that oxidize water to dioxygen. *Angewandte Chemie International Edition* 2009, 48, 2842-2852.
154. Artero, V.; Fontecave, M. Solar fuels generation and molecular systems: is it homogeneous or heterogeneous catalysis? *Chemical Society Reviews* 2013, 42, 2338-2356.
155. Crabtree, R. H. Resolving heterogeneity problems and impurity artifacts in operationally homogeneous transition metal catalysts. *Chemical reviews* 2011, 112, 1536-1554.
156. Limburg, B.; Bouwman, E.; Bonnet, S. Molecular water oxidation catalysts based on transition metals and their decomposition pathways. *Coordination Chemistry Reviews* 2012, 256, 1451-1467.
157. Wasylenko, D. J.; Ganesamoorthy, C.; Borau-Garcia, J.; Berlinguette, C. P. Electrochemical evidence for catalytic water oxidation mediated by a high-valent cobalt complex. *Chemical Communications* 2011, 47, 4249-4251.
158. Chen, G.; Chen, L.; Ng, S. M.; Lau, T. C. Efficient Chemical and Visible-Light-Driven Water Oxidation using Nickel Complexes and Salts as Precatalysts. *ChemSusChem* 2014, 7, 127-134.
159. Mirzakułova, E.; Khatmullin, R.; Walpita, J.; Corrigan, T.; Vargas-Barbosa, N. M.; Vyas, S.; Oottikkal, S.; Manzer, S. F.; Hadad, C. M.; Glusac, K. D. Electrode-assisted catalytic water oxidation by a flavin derivative. *Nature chemistry* 2012, 4, 794-801.
160. Yang, L.; Jiang, S.; Zhao, Y.; Zhu, L.; Chen, S.; Wang, X.; Wu, Q.; Ma, J.; Ma, Y.; Hu, Z. Boron-doped carbon nanotubes as metal-free electrocatalysts for the oxygen reduction reaction. *Angewandte Chemie* 2011, 123, 7270-7273.
161. Lai, L.; Potts, J. R.; Zhan, D.; Wang, L.; Poh, C. K.; Tang, C.; Gong, H.; Shen, Z.; Lin, J.; Ruoff, R. S. Exploration of the active center structure of nitrogen-doped graphene-based catalysts for oxygen reduction reaction. *Energy & Environmental Science* 2012, 5, 7936-7942.

162. Wang, D.-W.; Su, D. Heterogeneous nanocarbon materials for oxygen reduction reaction. *Energy & Environmental Science* 2014, 7, 576-591.
163. Geng, D.; Chen, Y.; Chen, Y.; Li, Y.; Li, R.; Sun, X.; Ye, S.; Knights, S. High oxygen-reduction activity and durability of nitrogen-doped graphene. *Energy & Environmental Science* 2011, 4, 760-764.
164. Gong, K.; Du, F.; Xia, Z.; Durstock, M.; Dai, L. Nitrogen-doped carbon nanotube arrays with high electrocatalytic activity for oxygen reduction. *science* 2009, 323, 760-764.
165. Zhao, Y.; Nakamura, R.; Kamiya, K.; Nakanishi, S.; Hashimoto, K. Nitrogen-doped carbon nanomaterials as non-metal electrocatalysts for water oxidation. *Nature communications* 2013, 4.
166. Ma, T. Y.; Dai, S.; Jaroniec, M.; Qiao, S. Z. Graphitic carbon nitride nanosheet–carbon nanotube three-dimensional porous composites as high-performance oxygen evolution electrocatalysts. *Angewandte Chemie International Edition* 2014, 53, 7281-7285.
167. Shi, Y.; Zhang, B. Recent advances in transition metal phosphide nanomaterials: synthesis and applications in hydrogen evolution reaction. *Chem. Soc. Rev.* 2016, 45, 1529-1541.
168. Han, L.; Dong, S.; Wang, E. Transition-Metal (Co, Ni, and Fe)-Based Electrocatalysts for the Water Oxidation Reaction. *Advanced Materials* 2016.
169. Ma, W.; Ma, R.; Wang, C.; Liang, J.; Liu, X.; Zhou, K.; Sasaki, T. A superlattice of alternately stacked Ni–Fe hydroxide nanosheets and graphene for efficient splitting of water. *ACS nano* 2015, 9, 1977-1984.
170. Jiao, L.; Zhou, Y.-X.; Jiang, H.-L. Metal–organic framework-based CoP/reduced graphene oxide: high-performance bifunctional electrocatalyst for overall water splitting. *Chemical Science* 2016, 7, 1690-1695.
171. Jin, H.; Wang, J.; Su, D.; Wei, Z.; Pang, Z.; Wang, Y. In situ cobalt–cobalt oxide/N-doped carbon hybrids as superior bifunctional electrocatalysts for hydrogen and oxygen evolution. *J. Am. Chem. Soc* 2015, 137, 2688-2694.
172. Wang, X.; Li, W.; Xiong, D.; Petrovykh, D. Y.; Liu, L. Bifunctional nickel phosphide nanocatalysts supported on carbon fiber paper for highly efficient and stable overall water splitting. *Advanced Functional Materials* 2016, 26, 4067-4077.

173. Hou, Y.; Lohe, M. R.; Zhang, J.; Liu, S.; Zhuang, X.; Feng, X. Vertically oriented cobalt selenide/NiFe layered-double-hydroxide nanosheets supported on exfoliated graphene foil: an efficient 3D electrode for overall water splitting. *Energy & Environmental Science* 2016, 9, 478-483.
174. Wang, G.; Yang, J.; Park, J.; Gou, X.; Wang, B.; Liu, H.; Yao, J. Facile synthesis and characterization of graphene nanosheets. *The Journal of Physical Chemistry C* 2008, 112, 8192-8195.
175. Mak, K. F.; Lee, C.; Hone, J.; Shan, J.; Heinz, T. F. Atomically thin MoS₂: a new direct-gap semiconductor. *Physical Review Letters* 2010, 105, 136805.
176. Seo, J. w.; Jang, J. t.; Park, S. w.; Kim, C.; Park, B.; Cheon, J. Two-dimensional SnS₂ nanoplates with extraordinary high discharge capacity for lithium ion batteries. *Advanced Materials* 2008, 20, 4269-4273.
177. Wang, G.; Shen, X.; Yao, J.; Park, J. Graphene nanosheets for enhanced lithium storage in lithium ion batteries. *Carbon* 2009, 47, 2049-2053.
178. Zhou, G.; Wang, D.-W.; Li, F.; Zhang, L.; Li, N.; Wu, Z.-S.; Wen, L.; Lu, G. Q.; Cheng, H.-M. Graphene-wrapped Fe₃O₄ anode material with improved reversible capacity and cyclic stability for lithium ion batteries. *Chemistry of Materials* 2010, 22, 5306-5313.
179. Shi, Y.; Wang, Y.; Wong, J. I.; Tan, A. Y. S.; Hsu, C.-L.; Li, L.-J.; Lu, Y.-C.; Yang, H. Y. Self-assembly of hierarchical MoS_x/CNT nanocomposites (2 < x < 3): towards high performance anode materials for lithium ion batteries. *Scientific reports* 2013, 3, 2169.
180. Radisavljevic, B.; Radenovic, A.; Brivio, J.; Giacometti, i. V.; Kis, A. Single-layer MoS₂ transistors. *Nature nanotechnology* 2011, 6, 147-150.
181. Splendiani, A.; Sun, L.; Zhang, Y.; Li, T.; Kim, J.; Chim, C.-Y.; Galli, G.; Wang, F. Emerging photoluminescence in monolayer MoS₂. *Nano letters* 2010, 10, 1271-1275.
182. Joensen, P.; Frindt, R.; Morrison, S. R. Single-layer MoS₂. *Materials research bulletin* 1986, 21, 457-461.
183. Lee, C.; Yan, H.; Brus, L. E.; Heinz, T. F.; Hone, J.; Ryu, S. Anomalous lattice vibrations of single-and few-layer MoS₂. *ACS nano* 2010, 4, 2695-2700.
184. Lee, Y. H.; Zhang, X. Q.; Zhang, W.; Chang, M. T.; Lin, C. T.; Chang, K. D.; Yu, Y. C.; Wang, J. T. W.; Chang, C. S.; Li, L. J. Synthesis of Large-Area

- MoS₂ Atomic Layers with Chemical Vapor Deposition. *Advanced Materials* 2012, 24, 2320-2325.
185. Yan, Y.; Xia, B.; Xu, Z.; Wang, X. Recent development of molybdenum sulfides as advanced electrocatalysts for hydrogen evolution reaction. *ACS Catalysis* 2014, 4, 1693-1705.
 186. Wu, Z.; Fang, B.; Wang, Z.; Wang, C.; Liu, Z.; Liu, F.; Wang, W.; Alfantazi, A.; Wang, D.; Wilkinson, D. P. MoS₂ nanosheets: a designed structure with high active site density for the hydrogen evolution reaction. *Acs Catalysis* 2013, 3, 2101-2107.
 187. Chang, Y. H.; Lin, C. T.; Chen, T. Y.; Hsu, C. L.; Lee, Y. H.; Zhang, W.; Wei, K. H.; Li, L. J. Highly Efficient Electrocatalytic Hydrogen Production by MoS_x Grown on Graphene-Protected 3D Ni Foams. *Advanced materials* 2013, 25, 756-760.
 188. Liao, L.; Zhu, J.; Bian, X.; Zhu, L.; Scanlon, M. D.; Girault, H. H.; Liu, B. MoS₂ formed on mesoporous graphene as a highly active catalyst for hydrogen evolution. *Advanced Functional Materials* 2013, 23, 5326-5333.
 189. Zheng, X.; Xu, J.; Yan, K.; Wang, H.; Wang, Z.; Yang, S. Space-confined growth of MoS₂ nanosheets within graphite: the layered hybrid of MoS₂ and graphene as an active catalyst for hydrogen evolution reaction. *Chemistry of Materials* 2014, 26, 2344-2353.
 190. Zhao, Y.; Hu, C.; Hu, Y.; Cheng, H.; Shi, G.; Qu, L. A versatile, ultralight, nitrogen-doped graphene framework. *Angewandte Chemie* 2012, 124, 11533-11537.
 191. Worsley, M. A.; Pauzauskie, P. J.; Olson, T. Y.; Biener, J.; Satcher Jr, J. H.; Baumann, T. F. Synthesis of graphene aerogel with high electrical conductivity. *Journal of the American Chemical Society* 2010, 132, 14067-14069.
 192. Xu, Y.; Lin, Z.; Huang, X.; Liu, Y.; Huang, Y.; Duan, X. Flexible solid-state supercapacitors based on three-dimensional graphene hydrogel films. *ACS nano* 2013, 7, 4042-4049.
 193. Yin, H.; Zhang, C.; Liu, F.; Hou, Y. Hybrid of Iron Nitride and Nitrogen-Doped Graphene Aerogel as Synergistic Catalyst for Oxygen Reduction Reaction. *Advanced Functional Materials* 2014, 24, 2930-2937.

194. Wu, Z.-S.; Yang, S.; Sun, Y.; Parvez, K.; Feng, X.; Müllen, K. 3D nitrogen-doped graphene aerogel-supported Fe₃O₄ nanoparticles as efficient electrocatalysts for the oxygen reduction reaction. *Journal of the American Chemical Society* 2012, 134, 9082-9085.
195. Chen, S.; Duan, J.; Jaroniec, M.; Qiao, S. Z. Three-dimensional N-doped graphene hydrogel/NiCo double hydroxide electrocatalysts for highly efficient oxygen evolution. *Angewandte Chemie International Edition* 2013, 52, 13567-13570.
196. Chang, K.; Chen, W. L-cysteine-assisted synthesis of layered MoS₂/graphene composites with excellent electrochemical performances for lithium ion batteries. *ACS nano* 2011, 5, 4720-4728.
197. Kumar, B.; Asadi, M.; Pisasale, D.; Sinha-Ray, S.; Rosen, B. A.; Haasch, R.; Abiade, J.; Yarin, A. L.; Salehi-Khojin, A. Renewable and metal-free carbon nanofibre catalysts for carbon dioxide reduction. *Nature communications* 2013, 4.
198. Qin, P.; Fang, G.; Ke, W.; Cheng, F.; Zheng, Q.; Wan, J.; Lei, H.; Zhao, X. In situ growth of double-layer MoO₃/MoS₂ film from MoS₂ for hole-transport layers in organic solar cell. *Journal of Materials Chemistry A* 2014, 2, 2742-2756.
199. Xie, J.; Zhang, J.; Li, S.; Grote, F.; Zhang, X.; Zhang, H.; Wang, R.; Lei, Y.; Pan, B.; Xie, Y. Controllable disorder engineering in oxygen-incorporated MoS₂ ultrathin nanosheets for efficient hydrogen evolution. *Journal of the American Chemical Society* 2013, 135, 17881-17888.
200. Kong, D.; Wang, H.; Lu, Z.; Cui, Y. CoSe₂ nanoparticles grown on carbon fiber paper: an efficient and stable electrocatalyst for hydrogen evolution reaction. *Journal of the American Chemical Society* 2014, 136, 4897-4900.
201. McCrory, C. C.; Jung, S.; Peters, J. C.; Jaramillo, T. F. Benchmarking heterogeneous electrocatalysts for the oxygen evolution reaction. *Journal of the American Chemical Society* 2013, 135, 16977-16987.
202. Doyle, R. L.; Lyons, M. E. An electrochemical impedance study of the oxygen evolution reaction at hydrous iron oxide in base. *Physical Chemistry Chemical Physics* 2013, 15, 5224-5237.
203. Mao, S.; Wen, Z.; Huang, T.; Hou, Y.; Chen, J. High-performance bi-functional electrocatalysts of 3D crumpled graphene-cobalt oxide nanohybrids

- for oxygen reduction and evolution reactions. *Energy & Environmental Science* 2014, 7, 609-616.
204. Skirrow, F. Über Oxydation durch elektrolytisch abgeschiedenes Fluor. *Zeitschrift für anorganische Chemie* 1902, 33, 25-30.
 205. Shafirovich, V. Y.; Strelets, V. CATALYTIC-OXIDATION OF WATER BY COBALT COMPLEXES. *NOUVEAU JOURNAL DE CHIMIE-NEW JOURNAL OF CHEMISTRY* 1978, 2, 199-201.
 206. Lai, Y.-H.; Lin, C.-Y.; Lv, Y.; King, T. C.; Steiner, A.; Muresan, N. M.; Gan, L.; Wright, D. S.; Reisner, E. Facile assembly of an efficient CoO_x water oxidation electrocatalyst from Co-containing polyoxotitanate nanocages. *Chemical Communications* 2013, 49, 4331-4333.
 207. Hu, L.; Sun, K.; Peng, Q.; Xu, B.; Li, Y. Surface active sites on Co_3O_4 nanobelt and nanocube model catalysts for CO oxidation. *Nano Research* 2010, 3, 363-368.
 208. Grzelczak, M.; Zhang, J.; Pfrommer, J.; Hartmann, J. r.; Driess, M.; Antonietti, M.; Wang, X. Electro-and photochemical water oxidation on ligand-free Co_3O_4 nanoparticles with tunable sizes. *ACS Catalysis* 2013, 3, 383-388.
 209. Smith, W.; Hobson, A. The structure of cobalt oxide, Co_3O_4 . *Acta Crystallographica Section B: Structural Crystallography and Crystal Chemistry* 1973, 29, 362-363.
 210. Sickafus, K. E.; Wills, J. M.; Grimes, N. W. Structure of spinel. *Journal of the American Ceramic Society* 1999, 82, 3279-3292.
 211. Tüysüz, H.; Hwang, Y. J.; Khan, S. B.; Asiri, A. M.; Yang, P. Mesoporous Co_3O_4 as an electrocatalyst for water oxidation. *Nano Research* 2013, 6, 47-54.
 212. Esswein, A. J.; McMurdo, M. J.; Ross, P. N.; Bell, A. T.; Tilley, T. D. Size-dependent activity of Co_3O_4 nanoparticle anodes for alkaline water electrolysis. *The Journal of Physical Chemistry C* 2009, 113, 15068-15072.
 213. Rosen, J.; Hutchings, G. S.; Jiao, F. Ordered mesoporous cobalt oxide as highly efficient oxygen evolution catalyst. *Journal of the American Chemical Society* 2013, 135, 4516-4521.
 214. Koza, J. A.; He, Z.; Miller, A. S.; Switzer, J. A. Electrodeposition of Crystalline Co_3O_4 : A Catalyst for the Oxygen Evolution Reaction. *Chemistry of Materials* 2012, 24, 3567-3573.

215. Mu, Y.; Liang, H.; Hu, J.; Jiang, L.; Wan, L. Controllable Pt nanoparticle deposition on carbon nanotubes as an anode catalyst for direct methanol fuel cells. *The Journal of Physical Chemistry B* 2005, 109, 22212-22216.
216. Liu, Q.; Jin, J.; Zhang, J. NiCo₂S₄@ graphene as a bifunctional electrocatalyst for oxygen reduction and evolution reactions. *ACS applied materials & interfaces* 2013, 5, 5002-5008.
217. Liang, Y.; Wang, H.; Zhou, J.; Li, Y.; Wang, J.; Regier, T.; Dai, H. Covalent hybrid of spinel manganese–cobalt oxide and graphene as advanced oxygen reduction electrocatalysts. *Journal of the American Chemical Society* 2012, 134, 3517-3523.
218. Dai, H. Co₃O₄ nanocrystals on graphene as a synergistic catalyst for oxygen reduction reaction. 2011.
219. Suryanto, B. H.; Lu, X.; Zhao, C. Layer-by-layer assembly of transparent amorphous Co₃O₄ nanoparticles/graphene composite electrodes for sustained oxygen evolution reaction. *Journal of Materials Chemistry A* 2013, 1, 12726-12731.
220. Wu, J.; Xue, Y.; Yan, X.; Yan, W.; Cheng, Q.; Xie, Y. Co₃O₄ nanocrystals on single-walled carbon nanotubes as a highly efficient oxygen-evolving catalyst. *Nano Research* 2012, 5, 521-530.
221. Lu, X.; Zhao, C. Highly efficient and robust oxygen evolution catalysts achieved by anchoring nanocrystalline cobalt oxides onto mildly oxidized multiwalled carbon nanotubes. *Journal of Materials Chemistry A* 2013, 1, 12053-12059.
222. Lu, Y.; Lu, X.; Mayers, B. T.; Herricks, T.; Xia, Y. Synthesis and characterization of magnetic Co nanoparticles: A comparison study of three different capping surfactants. *Journal of Solid State Chemistry* 2008, 181, 1530-1538.
223. Sun, B.; Munroe, P.; Wang, G. Ruthenium nanocrystals as cathode catalysts for lithium-oxygen batteries with a superior performance. *Scientific reports* 2013, 3, 2247.
224. Yang, P.; Zhao, D.; Margolese, D. I.; Chmelka, B. F.; Stucky, G. D. Generalized syntheses of large-pore mesoporous metal oxides with semicrystalline frameworks. *Nature* 1998, 396, 152-155.

225. Gao, M.-R.; Cao, X.; Gao, Q.; Xu, Y.-F.; Zheng, Y.-R.; Jiang, J.; Yu, S.-H. Nitrogen-doped graphene supported CoSe₂ nanobelt composite catalyst for efficient water oxidation. *ACS nano* 2014, 8, 3970-3978.
226. Duan, J.; Zheng, Y.; Chen, S.; Tang, Y.; Jaroniec, M.; Qiao, S. Mesoporous hybrid material composed of Mn₃O₄ nanoparticles on nitrogen-doped graphene for highly efficient oxygen reduction reaction. *Chemical Communications* 2013, 49, 7705-7707.
227. Chou, N. H.; Ross, P. N.; Bell, A. T.; Tilley, T. D. Comparison of Cobalt-based Nanoparticles as Electrocatalysts for Water Oxidation. *ChemSusChem* 2011, 4, 1566-1569.
228. Minguzzi, A.; Fan, F.-R. F.; Vertova, A.; Rondinini, S.; Bard, A. J. Dynamic potential–pH diagrams application to electrocatalysts for water oxidation. *Chemical Science* 2012, 3, 217-229.
229. Nakagawa, T.; Beasley, C. A.; Murray, R. W. Efficient electro-oxidation of water near its reversible potential by a mesoporous IrO_x nanoparticle film. *The Journal of Physical Chemistry C* 2009, 113, 12958-12961.
230. Xiao, J.; Mei, D.; Li, X.; Xu, W.; Wang, D.; Graff, G. L.; Bennett, W. D.; Nie, Z.; Saraf, L. V.; Aksay, I. A. Hierarchically porous graphene as a lithium–air battery electrode. *Nano letters* 2011, 11, 5071-5078.
231. Jiang, D.-e.; Cooper, V. R.; Dai, S. Porous graphene as the ultimate membrane for gas separation. *Nano letters* 2009, 9, 4019-4024.
232. Li, Y.; Li, Z.; Shen, P. K. Simultaneous Formation of Ultrahigh Surface Area and Three-Dimensional Hierarchical Porous Graphene-Like Networks for Fast and Highly Stable Supercapacitors. *Advanced Materials* 2013, 25, 2474-2480.
233. Huang, X.; Qian, K.; Yang, J.; Zhang, J.; Li, L.; Yu, C.; Zhao, D. Functional nanoporous graphene foams with controlled pore sizes. *Advanced Materials* 2012, 24, 4419-4423.
234. Yang, S.; Feng, X.; Ivanovici, S.; Müllen, K. Fabrication of graphene-encapsulated oxide nanoparticles: towards high-performance anode materials for lithium storage. *Angewandte Chemie* 2010, 122, 8586-8589.
235. Chen, Z.; Ren, W.; Gao, L.; Liu, B.; Pei, S.; Cheng, H.-M. Three-dimensional flexible and conductive interconnected graphene networks grown by chemical vapour deposition. *Nature materials* 2011, 10, 424-428.

236. Ito, Y.; Tanabe, Y.; Qiu, H. J.; Sugawara, K.; Heguri, S.; Tu, N. H.; Huynh, K. K.; Fujita, T.; Takahashi, T.; Tanigaki, K. High-Quality Three-Dimensional Nanoporous Graphene. *Angewandte Chemie International Edition* 2014, 53, 4822-4826.
237. Sohn, K.; Na, Y. J.; Chang, H.; Roh, K.-M.; Jang, H. D.; Huang, J. Oil absorbing graphene capsules by capillary molding. *Chemical Communications* 2012, 48, 5968-5970.
238. Wang, Z.-L.; Xu, D.; Wang, H.-G.; Wu, Z.; Zhang, X.-B. In situ fabrication of porous graphene electrodes for high-performance energy storage. *ACS nano* 2013, 7, 2422-2430.
239. Zhou, D.; Cui, Y.; Xiao, P.-W.; Jiang, M.-Y.; Han, B.-H. A general and scalable synthesis approach to porous graphene. *Nature communications* 2014, 5.
240. Qiu, L.; Liu, J. Z.; Chang, S. L.; Wu, Y.; Li, D. Biomimetic superelastic graphene-based cellular monoliths. *Nature communications* 2012, 3, 1241.
241. Wu, Z.-S.; Sun, Y.; Tan, Y.-Z.; Yang, S.; Feng, X.; Müllen, K. Three-dimensional graphene-based macro-and mesoporous frameworks for high-performance electrochemical capacitive energy storage. *Journal of the American Chemical Society* 2012, 134, 19532-19535.
242. Sun, H.; Xu, Z.; Gao, C. Multifunctional, ultra-flyweight, synergistically assembled carbon aerogels. *Advanced Materials* 2013, 25, 2554-2560.
243. Sun, B.; Huang, X.; Chen, S.; Munroe, P.; Wang, G. Porous graphene nanoarchitectures: an efficient catalyst for low charge-overpotential, long life, and high capacity lithium–oxygen batteries. *Nano letters* 2014, 14, 3145-3152.
244. Deng, Y.; Wei, J.; Sun, Z.; Zhao, D. Large-pore ordered mesoporous materials templated from non-Pluronic amphiphilic block copolymers. *Chemical Society Reviews* 2013, 42, 4054-4070.
245. Ma, T.-Y.; Liu, L.; Yuan, Z.-Y. Direct synthesis of ordered mesoporous carbons. *Chemical Society Reviews* 2013, 42, 3977-4003.
246. Liu, J.; Yang, T.; Wang, D.-W.; Lu, G. Q. M.; Zhao, D.; Qiao, S. Z. A facile soft-template synthesis of mesoporous polymeric and carbonaceous nanospheres. *Nature communications* 2013, 4.

247. Huang, X.; Zhao, Y.; Ao, Z.; Wang, G. Micelle-template synthesis of nitrogen-doped mesoporous graphene as an efficient metal-free electrocatalyst for hydrogen production. *Scientific reports* 2014, 4, 7557.
248. Huang, X.; Sun, B.; Li, K.; Chen, S.; Wang, G. Mesoporous graphene paper immobilised sulfur as a flexible electrode for lithium–sulfur batteries. *Journal of Materials Chemistry A* 2013, 1, 13484-13489.
249. Sun, Y.; Hu, X.; Luo, W.; Huang, Y. Self-assembled mesoporous CoO nanodisks as a long-life anode material for lithium-ion batteries. *Journal of Materials Chemistry* 2012, 22, 13826-13831.
250. Yuan, C.; Wu, H. B.; Xie, Y.; Lou, X. W. D. Mixed transition-metal oxides: design, synthesis, and energy-related applications. *Angewandte Chemie International Edition* 2014, 53, 1488-1504.
251. Staszak-Jirkovský, J.; Malliakas, C. D.; Lopes, P. P.; Danilovic, N.; Kota, S. S.; Chang, K.-C.; Genorio, B.; Strmcnik, D.; Stamenkovic, V. R.; Kanatzidis, M. G. Design of active and stable Co-Mo-S_x chalcogels as pH-universal catalysts for the hydrogen evolution reaction. *Nature materials* 2016, 15, 197-203.
252. Cao, B.; Veith, G. M.; Neuefeind, J. C.; Adzic, R. R.; Khalifah, P. G. Mixed close-packed cobalt molybdenum nitrides as non-noble metal electrocatalysts for the hydrogen evolution reaction. *Journal of the American Chemical Society* 2013, 135, 19186-19192.
253. Yang, Y.; Fei, H.; Ruan, G.; Xiang, C.; Tour, J. M. Efficient electrocatalytic oxygen evolution on amorphous nickel–cobalt binary oxide nanoporous layers. *ACS nano* 2014, 8, 9518-9523.
254. Browne, M. P.; Nolan, H.; Duesberg, G. S.; Colavita, P. E.; Lyons, M. E. Low-Overpotential High-Activity Mixed Manganese and Ruthenium Oxide Electrocatalysts for Oxygen Evolution Reaction in Alkaline Media. *ACS Catalysis* 2016, 6, 2408-2415.
255. Chen, S.; Duan, J.; Vasileff, A.; Qiao, S. Z. Size Fractionation of Two-Dimensional Sub-Nanometer Thin Manganese Dioxide Crystals towards Superior Urea Electrocatalytic Conversion. *Angewandte Chemie* 2016, 128, 3868-3872.

256. Jung, Y.; Shen, J.; Sun, Y.; Cha, J. J. Chemically synthesized heterostructures of two-dimensional molybdenum/tungsten-based dichalcogenides with vertically aligned layers. *ACS nano* 2014, 8, 9550-9557.
257. Li, L.; Feng, X.; Nie, Y.; Chen, S.; Shi, F.; Xiong, K.; Ding, W.; Qi, X.; Hu, J.; Wei, Z. Insight into the effect of oxygen vacancy concentration on the catalytic performance of MnO₂. *ACS Catalysis* 2015, 5, 4825-4832.
258. Luo, Z.; Miao, R.; Huan, T. D.; Mosa, I. M.; Poyraz, A. S.; Zhong, W.; Cloud, J. E.; Kriz, D. A.; Thanneeru, S.; He, J. Mesoporous MoO_{3-x} Material as an Efficient Electrocatalyst for Hydrogen Evolution Reactions. *Advanced Energy Materials* 2016, 6.
259. Wu, R.; Zhang, J.; Shi, Y.; Liu, D.; Zhang, B. Metallic WO₂-carbon mesoporous nanowires as highly efficient electrocatalysts for hydrogen evolution reaction. *Journal of the American Chemical Society* 2015, 137, 6983-6986.
260. Veal, B. W.; Kim, S. K.; Zapol, P.; Iddir, H.; Baldo, P. M.; Eastman, J. A. Interfacial control of oxygen vacancy doping and electrical conduction in thin film oxide heterostructures. *Nature communications* 2016, 7.
261. Yu, N.; Yin, H.; Zhang, W.; Liu, Y.; Tang, Z.; Zhu, M. Q. High-Performance Fiber-Shaped All-Solid-State Asymmetric Supercapacitors Based on Ultrathin MnO₂ Nanosheet/Carbon Fiber Cathodes for Wearable Electronics. *Advanced Energy Materials* 2016, 6.
262. Chen, Y.; Zhang, Y.; Geng, D.; Li, R.; Hong, H.; Chen, J.; Sun, X. One-pot synthesis of MnO₂/graphene/carbon nanotube hybrid by chemical method. *Carbon* 2011, 49, 4434-4442.
263. Liang, X.; Hart, C.; Pang, Q.; Garsuch, A.; Weiss, T.; Nazar, L. F. A highly efficient polysulfide mediator for lithium-sulfur batteries. *Nature communications* 2015, 6.
264. Kim, J. G.; Kim, Y.; Noh, Y.; Kim, W. B. MnCo₂O₄ nanowires anchored on reduced graphene oxide sheets as effective bifunctional catalysts for Li-O₂ battery cathodes. *ChemSusChem* 2015, 8, 1752-1760.
265. Cui, X.; Ren, P.; Deng, D.; Deng, J.; Bao, X. Single layer graphene encapsulating non-precious metals as high-performance electrocatalysts for water oxidation. *Energy & Environmental Science* 2016, 9, 123-129.

266. Bao, J.; Zhang, X.; Fan, B.; Zhang, J.; Zhou, M.; Yang, W.; Hu, X.; Wang, H.; Pan, B.; Xie, Y. Ultrathin Spinel-Structured Nanosheets Rich in Oxygen Deficiencies for Enhanced Electrocatalytic Water Oxidation. *Angewandte Chemie* 2015, 127, 7507-7512.
267. Xia, B. Y.; Yan, Y.; Li, N.; Wu, H. B.; Lou, X. W. D.; Wang, X. A metal-organic framework-derived bifunctional oxygen electrocatalyst. *Nature Energy* 2016, 1, 15006.
268. Li, J.-S.; Wang, Y.; Liu, C.-H.; Li, S.-L.; Wang, Y.-G.; Dong, L.-Z.; Dai, Z.-H.; Li, Y.-F.; Lan, Y.-Q. Coupled molybdenum carbide and reduced graphene oxide electrocatalysts for efficient hydrogen evolution. *Nature communications* 2016, 7.
269. Ma, T. Y.; Cao, J. L.; Jaroniec, M.; Qiao, S. Z. Interacting Carbon Nitride and Titanium Carbide Nanosheets for High-Performance Oxygen Evolution. *Angewandte Chemie International Edition* 2016, 55, 1138-1142.
270. Qi, J.; Zhang, W.; Xiang, R.; Liu, K.; Wang, H. Y.; Chen, M.; Han, Y.; Cao, R. Porous nickel-iron oxide as a highly efficient electrocatalyst for oxygen evolution reaction. *Advanced Science* 2015, 2.
271. Yang, J.; Zhu, G.; Liu, Y.; Xia, J.; Ji, Z.; Shen, X.; Wu, S. Fe₃O₄-Decorated Co₉S₈ Nanoparticles In Situ Grown on Reduced Graphene Oxide: A New and Efficient Electrocatalyst for Oxygen Evolution Reaction. *Advanced Functional Materials* 2016, 26, 4712-4721.
272. Sun, C.; Dong, Q.; Yang, J.; Dai, Z.; Lin, J.; Chen, P.; Huang, W.; Dong, X. Metal-organic framework derived CoSe₂ nanoparticles anchored on carbon fibers as bifunctional electrocatalysts for efficient overall water splitting. *Nano Research* 2016, 9, 2234-2243.
273. Yang, H.; Zhang, Y.; Hu, F.; Wang, Q. Urchin-like CoP nanocrystals as hydrogen evolution reaction and oxygen reduction reaction dual-electrocatalyst with superior stability. *Nano letters* 2015, 15, 7616-7620.
274. Jiang, P.; Liu, Q.; Liang, Y.; Tian, J.; Asiri, A. M.; Sun, X. A Cost-Effective 3D Hydrogen Evolution Cathode with High Catalytic Activity: FeP Nanowire Array as the Active Phase. *Angewandte Chemie International Edition* 2014, 53, 12855-12859.

275. Chen, P.; Xu, K.; Fang, Z.; Tong, Y.; Wu, J.; Lu, X.; Peng, X.; Ding, H.; Wu, C.; Xie, Y. Metallic Co₄N porous nanowire arrays activated by surface oxidation as electrocatalysts for the oxygen evolution reaction. *Angewandte Chemie* 2015, 127, 14923-14927.
276. Swesi, A.; Masud, J.; Nath, M. Nickel selenide as a high-efficiency catalyst for oxygen evolution reaction. *Energy & Environmental Science* 2016, 9, 1771-1782.
277. Fan, X.; Peng, Z.; Ye, R.; Zhou, H.; Guo, X. M₃C (M: Fe, Co, Ni) nanocrystals encased in graphene nanoribbons: An active and stable bifunctional electrocatalyst for oxygen reduction and hydrogen evolution reactions. *ACS nano* 2015, 9, 7407-7418.
278. Hu, Y.; Jensen, J. O.; Zhang, W.; Martin, S.; Chenitz, R.; Pan, C.; Xing, W.; Bjerrum, N. J.; Li, Q. Fe₃C-based oxygen reduction catalysts: synthesis, hollow spherical structures and applications in fuel cells. *Journal of Materials Chemistry A* 2015, 3, 1752-1760.
279. Lee, J. S.; Park, G. S.; Kim, S. T.; Liu, M.; Cho, J. A highly efficient electrocatalyst for the oxygen reduction reaction: N-doped ketjenblack incorporated into Fe/Fe₃C-functionalized melamine foam. *Angewandte Chemie* 2013, 125, 1060-1064.
280. Yang, W.; Liu, X.; Yue, X.; Jia, J.; Guo, S. Bamboo-like carbon nanotube/Fe₃C nanoparticle hybrids and their highly efficient catalysis for oxygen reduction. *Journal of the American Chemical Society* 2015, 137, 1436-1439.
281. Barman, B. K.; Nanda, K. K. Prussian blue as a single precursor for synthesis of Fe/Fe₃C encapsulated N-doped graphitic nanostructures as bi-functional catalysts. *Green Chemistry* 2016, 18, 427-432.
282. Li, J.-S.; Li, S.-L.; Tang, Y.-J.; Han, M.; Dai, Z.-H.; Bao, J.-C.; Lan, Y.-Q. Nitrogen-doped Fe/Fe₃C@ graphitic layer/carbon nanotube hybrids derived from MOFs: efficient bifunctional electrocatalysts for ORR and OER. *Chemical Communications* 2015, 51, 2710-2713.
283. Xie, X.; Kretschmer, K.; Zhang, J.; Sun, B.; Su, D.; Wang, G. Sn@ CNT nanopillars grown perpendicularly on carbon paper: a novel free-standing anode for sodium ion batteries. *Nano Energy* 2015, 13, 208-217.

284. Feng, J. X.; Ye, S. H.; Xu, H.; Tong, Y. X.; Li, G. R. Design and Synthesis of FeOOH/CeO₂ Heterolayered Nanotube Electrocatalysts for the Oxygen Evolution Reaction. *Advanced Materials* 2016, 28, 4698-4703.
285. Jeong, I.; Lee, J.; Joseph, K. V.; Lee, H. I.; Kim, J. K.; Yoon, S.; Lee, J. Low-cost electrospun WC/C composite nanofiber as a powerful platinum-free counter electrode for dye sensitized solar cell. *Nano Energy* 2014, 9, 392-400.
286. Zhang, C.-L.; Yu, S.-H. Spraying functional fibres by electrospinning. *Materials Horizons* 2016, 3, 266-269.
287. Jiang, W.-J.; Gu, L.; Li, L.; Zhang, Y.; Zhang, X.; Zhang, L.-J.; Wang, J.-Q.; Hu, J.-S.; Wei, Z.; Wan, L.-J. Understanding the High Activity of Fe–N–C Electrocatalysts in Oxygen Reduction: Fe/Fe₃C Nanoparticles Boost the Activity of Fe–N_x. *Journal of the American Chemical Society* 2016, 138, 3570-3578.
288. Yu, X.-Y.; Feng, Y.; Guan, B.; Lou, X. W. D.; Paik, U. Carbon coated porous nickel phosphides nanoplates for highly efficient oxygen evolution reaction. *Energy & Environmental Science* 2016, 9, 1246-1250.
289. Chen, S.; Duan, J.; Tang, Y.; Jin, B.; Qiao, S. Z. Molybdenum sulfide clusters-nitrogen-doped graphene hybrid hydrogel film as an efficient three-dimensional hydrogen evolution electrocatalyst. *Nano Energy* 2015, 11, 11-18.
290. Chen, W. F.; Schneider, J. M.; Sasaki, K.; Wang, C. H.; Schneider, J.; Iyer, S.; Iyer, S.; Zhu, Y.; Muckerman, J. T.; Fujita, E. Tungsten carbide–nitride on graphene nanoplatelets as a durable hydrogen evolution electrocatalyst. *ChemSusChem* 2014, 7, 2414-2418.
291. Wang, S.; Wang, J.; Zhu, M.; Bao, X.; Xiao, B.; Su, D.; Li, H.; Wang, Y. Molybdenum-carbide-modified nitrogen-doped carbon vesicle encapsulating nickel nanoparticles: a Highly efficient, low-cost catalyst for hydrogen evolution reaction. *J. Am. Chem. Soc* 2015, 137, 15753-15759.
292. Jahan, M.; Liu, Z.; Loh, K. P. A Graphene Oxide and Copper-Centered Metal Organic Framework Composite as a Tri-Functional Catalyst for HER, OER, and ORR. *Advanced Functional Materials* 2013, 23, 5363-5372.
293. Hou, Y.; Li, J.; Wen, Z.; Cui, S.; Yuan, C.; Chen, J. Co₃O₄ nanoparticles embedded in nitrogen-doped porous carbon dodecahedrons with enhanced electrochemical properties for lithium storage and water splitting. *Nano Energy* 2015, 12, 1-8.

294. Liu, X.; Chang, Z.; Luo, L.; Xu, T.; Lei, X.; Liu, J.; Sun, X. Hierarchical Zn_xCo_{3-x}O₄ Nanoarrays with High Activity for Electrocatalytic Oxygen Evolution. *chemistry of Materials* 2014, 26, 1889-1895.
295. Rafailović, L. D.; Gammer, C.; Rentenberger, C.; Trišović, T.; Kleber, C.; Karnthaler, H. P. Enhanced oxygen evolution and reduction reactions of porous ternary NiCoFe foam electrodes prepared by dynamic hydrogen template deposition. *Nano Energy* 2013, 2, 523-529.
296. Wu, G.; More, K. L.; Johnston, C. M.; Zelenay, P. High-performance electrocatalysts for oxygen reduction derived from polyaniline, iron, and cobalt. *Science* 2011, 332, 443-447.
297. Ren, J.; Antonietti, M.; Feller, T. P. Efficient water splitting using a simple Ni/N/C paper electrocatalyst. *Advanced Energy Materials* 2015, 5.
298. Zhou, W.; Zhou, J.; Zhou, Y.; Lu, J.; Zhou, K.; Yang, L.; Tang, Z.; Li, L.; Chen, S. N-doped carbon-wrapped cobalt nanoparticles on N-doped graphene nanosheets for high-efficiency hydrogen production. *Chemistry of Materials* 2015, 27, 2026-2032.
299. Kumar, P. S.; Sundaramurthy, J.; Sundarajan, S.; Babu, V. J.; Singh, G.; Allakhverdiev, S. I.; Ramakrishna, S. Hierarchical electrospun nanofibers for energy harvesting, production and environmental remediation. *Energy & Environmental Science* 2014, 7, 3192-3222.
300. Yu, Y.; Gu, L.; Zhu, C.; Van Aken, P. A.; Maier, J. Tin nanoparticles encapsulated in porous multichannel carbon microtubes: preparation by single-nozzle electrospinning and application as anode material for high-performance Li-based batteries. *Journal of the American Chemical Society* 2009, 131, 15984-15985.
301. Cavaliere, S.; Subianto, S.; Savych, I.; Jones, D. J.; Rozière, J. Electrospinning: designed architectures for energy conversion and storage devices. *Energy & Environmental Science* 2011, 4, 4761-4785.
302. Zhu, H.; Du, M.; Zhang, M.; Zou, M.; Yang, T.; Wang, S.; Yao, J.; Guo, B. S-rich single-layered MoS₂ nanoplates embedded in N-doped carbon nanofibers: efficient co-electrocatalysts for the hydrogen evolution reaction. *Chemical Communications* 2014, 50, 15435-15438.
303. Ito, Y.; Cong, W.; Fujita, T.; Tang, Z.; Chen, M. High Catalytic Activity of Nitrogen and Sulfur Co-Doped Nanoporous Graphene in the Hydrogen

- Evolution Reaction. *Angewandte Chemie International Edition* 2015, 54, 2131-2136.
304. Deng, D.; Yu, L.; Chen, X.; Wang, G.; Jin, L.; Pan, X.; Deng, J.; Sun, G.; Bao, X. Iron encapsulated within pod-like carbon nanotubes for oxygen reduction reaction. *Angewandte Chemie International Edition* 2013, 52, 371-375.
 305. Liang, H.; Meng, F.; Cabán-Acevedo, M.; Li, L.; Forticaux, A.; Xiu, L.; Wang, Z.; Jin, S. Hydrothermal continuous flow synthesis and exfoliation of NiCo layered double hydroxide nanosheets for enhanced oxygen evolution catalysis. *Nano letters* 2015, 15, 1421-1427.
 306. Lin, X.; Li, X.; Li, F.; Fang, Y.; Tian, M.; An, X.; Fu, Y.; Jin, J.; Ma, J. Precious-metal-free Co-Fe-O_x coupled nitrogen-enriched porous carbon nanosheets derived from Schiff-base porous polymers as superior electrocatalysts for the oxygen evolution reaction. *Journal of Materials Chemistry A* 2016, 4, 6505-6512.
 307. Wang, H.; Lu, Z.; Kong, D.; Sun, J.; Hymel, T. M.; Cui, Y. Electrochemical tuning of MoS₂ nanoparticles on three-dimensional substrate for efficient hydrogen evolution. *ACS nano* 2014, 8, 4940-4947.
 308. Tavakkoli, M.; Kallio, T.; Reynaud, O.; Nasibulin, A. G.; Sainio, J.; Jiang, H.; Kauppinen, E. I.; Laasonen, K. Maghemite nanoparticles decorated on carbon nanotubes as efficient electrocatalysts for the oxygen evolution reaction. *Journal of Materials Chemistry A* 2016, 4, 5216-5222.
 309. Pan, X.; Bao, X. The effects of confinement inside carbon nanotubes on catalysis. *Accounts of chemical research* 2011, 44, 553-562.
 310. Fei, H.; Yang, Y.; Peng, Z.; Ruan, G.; Zhong, Q.; Li, L.; Samuel, E. L.; Tour, J. M. Cobalt nanoparticles embedded in nitrogen-doped carbon for the hydrogen evolution reaction. *ACS applied materials & interfaces* 2015, 7, 8083-8087.
 311. Dou, S.; Tao, L.; Huo, J.; Wang, S.; Dai, L. Etched and doped Co₉S₈/graphene hybrid for oxygen electrocatalysis. *Energy & Environmental Science* 2016, 9, 1320-1326.